Determination of nuclear matter radii of Ca isotopes across the neutron magic number $N = 28$ via interaction cross section measurements

Doctoral Dissertation
by
Masaomi Tanaka

2018

Department of Physics,
Graduate School of Science,
Osaka University

Abstract

Interaction cross sections $\sigma_{\rm I}$ for $^{42-51}$Ca and their neighboring nuclides $^{40-48}$K and $^{44-46}$Sc on a natural carbon target at around 270 MeV/nucleon have been measured at the Radioactive Isotope Beam Factory (RIBF) at RIKEN by using the BigRIPS fragment separator. The present $\sigma_{\rm I}$ data are the first systematic ones along the isotopic chain in Ca mass region. Based on the Glauber-type calculation with the modified optical limit approximation, the root-mean-square matter radii $\langle r^2\rangle_{\rm m}^{1/2}$ were successfully deduced.

For Ca isotopes, significant enhancements of $\langle r^2\rangle_{\rm m}^{1/2}$ compared to the systematics of spherical nuclear radii have been observed in the region beyond the neutron magic number $N = 28$. These enhancements were examined with several models. Within the simple single particle model, a significant core enlargement is required to explain the systematics of the present experimental $\langle r^2\rangle_{\rm m}^{1/2}$ for $^{49-51}$Ca. On the other hand, the Hartree Fock calculations indicate that the enhancement is due to the rapid increase of surface diffuseness. Although the origin of significantly large enhancements of experimental results has not been elucidated in the microscopic level yet, this may be related to the spin-orbit force.

We also obtained the neutron skin thicknesses $r_{\rm np}$ from the deduced $\langle r^2\rangle_{\rm m}^{1/2}$ incorporating the previously measured charge radii. By using the obtained $r_{\rm np}$ for Ca isotopes, the sensitivity to the EOS parameter L was examined with the help of mean field calculations. Adopting the relative values of $r_{\rm np}$, we show that the present data have a sensitivity of 30 MeV precision to determine L without a fatal systematic error. Present $r_{\rm np}$ which were directly determined from the experimental proton and matter radii in the wide range of $0.05 < \delta < 0.22$ are more reliable compared to the previous experimental studies mainly with the indirect method. Nuclear structure theories which can explain quantitatively the evolution of nuclear radii for Ca isotopes including $^{49-51}$Ca and enable us to extract a reliable L value from the present directly-determined $r_{\rm np}$ are anticipated.

Acknowledgements

The author would like to express his gratitude to all of those who have helped to make this work successful.

Associate Prof. M. Fukuda, for his many fruitful advices and enthusiastic guidance to complete this work.

Assistant Prof. M. Takechi at Niigata University, for giving the chance to taking part in the experiment and to analyze the experimental data as well as her fruitful advices, discussions, and collaborations on the whole of this work.
Associate Prof. D. Nishimura at Tokyo City University, not only for his fruitful advices, discussions, and collaborations on the whole of this work but also for his constant encouragement.

Associate Prof. K. Matsuta, for his valuable advices and constant encouragement.
Assistant Prof. M. Mihara, for his valuable advices and constant encouragement.

Prof. Y. Kuno, for his support on the submittal of this thesis.

Prof. T. Suzuki at Saitama University, for his supports and advices during the experiment.
Associate Prof. T. Yamaguchi at Saitama University, for his supports and advices during the experiment.
Associate Prof. T. Ohtsubo at Niigata University, for his supports and advices during the experiment.
Associate Prof. T. Izumikawa at Niigata University, for his supports and advices during the experiment.
Prof. A. Ozawa at Tsukuba University, for his supports and advices during the experiment.
Assistant Prof. T. Moriguchi at Tsukuba University, for his supports and advices during the experiment.
Assistant Prof. S. Suzuki at Tsukuba University, for his supports and advices during the experiment.
Lecturer H.J. Ong at RCNP (Research Center for Nuclear Physics), Osaka University, for his fruitful discussions and advices to this work.

Assistant Prof. S. Ebata at Tokyo Institute of Technology, for his supports

on the theoretical calculations.
Lecturer. W. Horiuchi at Hokkaido University, for his supports on the theoretical calculations.

Mr. K. Iwamoto, M. Wakabayashi, Y. Kamisho, Y. Morita, J. Ohno, R. Kambe, S. Shinozaki, K. Watanabe, S. Yamaoka, H. Du, J. Shimaya, Y. Tanaka, S. Kambayashi, K. Ohnishi, T. Sugihara, S. Yagi, T. Hori, S. Nakamura, R. Yanagihara at Osaka University, for their collaborations and discussions.

Mr. A. Honma and N. Kanda at Niigata University, for their collaborations and discussions.

Finally, The author would like to thank all of the collaborators of the experiment at RIBF, RIKEN.

This work was supported by Grant-in-Aid for JSPS Research Fellow (No. 15J01446).

Contents

1 Introduction **1**
- 1.1 Nuclear Size . . . 1
- 1.2 Nuclear Structure of Calcium Isotopes . . . 3
- 1.3 Neutron Skin Thickness and Its Impact on Equation of State . 6
- 1.4 Thesis Objectives . . . 11

2 Cross Sections and Nuclear Radii **12**
- 2.1 Definition of Interaction Cross Section σ_{I} . . . 12
- 2.2 Classical Description of Reaction Cross Section . . . 13
- 2.3 Scattering Theory . . . 15
- 2.4 Eikonal Approximation . . . 18
- 2.5 Glauber Theory . . . 20
  - 2.5.1 General Description of Glauber Theory . . . 20
  - 2.5.2 Input Parameters for Calculation of Reaction Cross Section . . . 25
  - 2.5.3 Optical Limit Approximation (OLA) . . . 26
  - 2.5.4 Modified Optical Limit Approximation (MOL) . . . 28
- 2.6 Effect of Fermi Motion . . . 29
- 2.7 Effects of Electromagnetic Interaction . . . 31

3 Experiment **35**
- 3.1 Transmission Method . . . 35
- 3.2 Experimental Facility . . . 38
  - 3.2.1 Accelerators . . . 38
  - 3.2.2 BigRIPS Fragment Separator . . . 40
- 3.3 Production and Separation of Secondary Beams . . . 43
  - 3.3.1 Production of Secondary Beams . . . 43
  - 3.3.2 Separation of Secondary Beams at the 1st Stage of BigRIPS . . . 46
- 3.4 Particle Identification at 2nd Stage of BigRIPS . . . 49
- 3.5 Beam Line Information . . . 54
- 3.6 Reaction Target . . . 55
- 3.7 Detectors . . . 57
  - 3.7.1 Setup . . . 57
  - 3.7.2 Plastic Scintillation Counter (PL) . . . 61
  - 3.7.3 Multi-Sampling Ionization Chamber (IC) . . . 63
  - 3.7.4 Parallel Plate Avalanche Counter (PPAC) . . . 65
- 3.8 Data Acquisition System (DAQ) . . . 66

4 Data Analysis **67**
4.1 Analysis Before Reaction Target . . . 67
4.1.1 Pileup Rejection . . . 67
4.1.2 Background Removal . . . 70
4.1.3 Particle Selection in A/Q_{F3F5} vs Z_{F3IC} Spectrum . . . 73
4.2 Analysis after Reaction Target . . . 79
4.2.1 Identification of Z . . . 80
4.2.2 Identification of A/Q . . . 81
4.3 Target-Out Measurement . . . 83
4.4 Emittance Cut . . . 85
4.5 Determination of Target Profile . . . 89
4.6 Estimation of Systematic Error . . . 92
4.6.1 Dependence of Gate Width . . . 92
4.6.2 Emittance Cut Dependence . . . 94
4.6.3 Multiple Scattering . . . 95
4.6.4 Reproducibility of Beam Profile in F7 between Target-in and Target-out Measurements . . . 97
4.6.5 Large-Angle Scattering via Elastic Process . . . 99
4.6.6 Charge State . . . 99
4.7 Derivation of Interaction Cross Section . . . 102
4.8 Experimental Results . . . 104

5 Discussion **106**
5.1 Deduction of RMS Matter Radii . . . 106
5.1.1 Nucleon Density Distribution of Target Nucleus ^{12}C . . . 106
5.1.2 Model Functions of Density Distributions of Projectile Nuclei . . . 107
5.1.3 Deduced RMS Radii $\langle r^2\rangle^{1/2}$ and Neutron Skin Thickness r_{np} . . . 115
5.2 Evolution of Nuclear Radii . . . 118
5.2.1 Comparison to Results of Hadron Elastic Scattering . . . 118
5.2.2 Mass Number Dependence . . . 120
5.2.3 Contribution of Quadrupole Deformation . . . 122
5.2.4 Enhancement Mechanism of Nuclear Radii beyond $N = 28$ . . . 127
5.3 Derivation of L . . . 143
5.3.1 Correlation between r_{np} and L . . . 145
5.3.2 Sensitivity of r_{np} to L . . . 149

6 Summary **156**
6.1 Summary 156
6.2 Future Prospect 157
6.2.1 Nuclear Structure 157
6.2.2 Equation of State 158

A Derivation Formula of Interaction Cross Section **167**

B Mass number dependence of matter radii for stable nuclei **170**

C PID Spectra **171**

D Transmission Distribution **204**

1 Introduction

1.1 Nuclear Size

The size of a nucleus is one of the most fundamental quantities to characterize nuclear properties. There have been many efforts to measure the nuclear size, which is too small – about 10^{-14} m – to be seen by the usual methods such as using a microscope. Conventionally, charge radii or charge distributions of stable nuclei have been determined by measuring the electron elastic scattering and the transition energy of muonic atom, whereas nuclear matter radii or distributions have been determined only by elastic scatterings with hadronic probes. Owing to a large number of studies on the nuclear sizes of stable nuclei, the following properties have been revealed:

- The nuclear radius R depends on their own mass number A as $R = r_0 A^{1/3}$.
- The diffuseness parameters of nuclear density are about 0.5-0.7 fm in stable nuclei.
- The point-proton density is similar to the point-neutron one.

Since 1980's, it became possible for nuclear physics experimentalists to access unstable nuclei far from the beta-stability line due to the remarkable development on the production technique of unstable nuclei. This advancement resulted in the discovery of some exotic nuclear structures which are beyond the conventional knowledge of stable nuclei. The interaction cross section $\sigma_{\rm I}$ measurements, for instance, have made significant contributions to unstable nuclear physics. By measuring $\sigma_{\rm I}$ at Lawrence Berkeley Laboratory (LBL), I. Tanihata *et al.* deduced interaction radii $R_{\rm I}$ of nuclei whose atomic numbers are from $Z = 2$ (Helium) to $Z = 5$ (Boron) [TA85a]. The extraordinary large enhancements of $R_{\rm I}$ were found in very neutron-rich ^{11}Li and ^{14}Be nuclei (Fig. 1-1(a)). This discovery pointed to the existence of the neutron-halo structure in some neutron-rich nuclei. In the early 2010's, M. Takechi *et al.* found the enhancement of $\sigma_{\rm I}$ due to the deformation effect in Ne and Mg isotopes which are located in the "island of inversion" [TA12, TA14]. Moreover, they also discovered the deformed-halo structure in ^{29,31}Ne and ^{37}Mg, whose halo structures arise due to the large contribution of smaller orbital angular momentum in their valence neutron caused by the deformation effect. These deformed-halo structures have been studied from the theoretical approaches [MI12, WAT14].

In parallel with the neutron-halo discoveries, T. Suzuki *et al.* found the neutron-skin structure in neutron-rich Na isotopes by measuring $\sigma_{\rm I}$ [SU95].

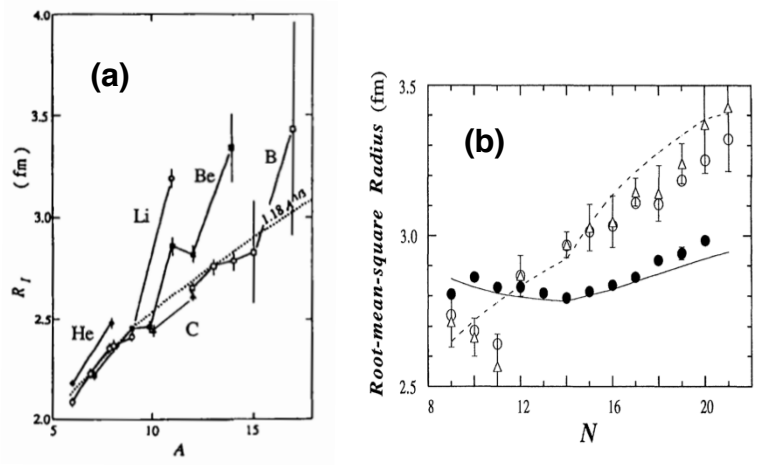

Figure 1-1: (a) Interaction radii $R_{\rm I}$ for He, Li, Be, and B isotopes [TA89]. (b) Root-mean-square neutron (open) and proton (closed) radii of Na isotopes [SU95]. These figure are taken from Refs. [TA89, SU95].

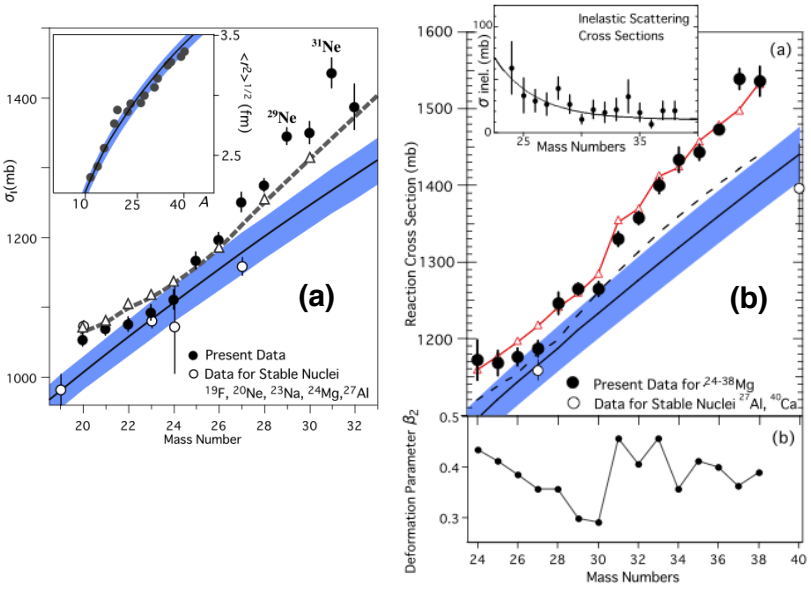

Figure 1-2: (a) Interaction cross sections $\sigma_{\rm I}$ for Ne isotopes [TA12] and (b) reaction cross section $\sigma_{\rm R}$ for Mg ones [TA14] on C target. In the neutron-rich nuclei, $\sigma_{\rm I}$ are larger than the systematics of ones of stable nuclei (black line and blue band) due to the deformation effect. Large enhancements can be seen at ^{29,31}Ne and ^{37}Mg, which correspond to the deformed-halo nuclei. These figures are taken from Refs. [TA12, TA14].

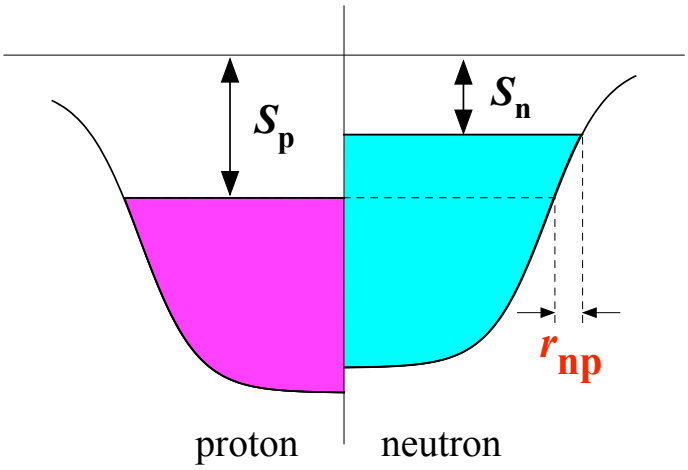

Figure 1-3: Schematic description of the correlation between $r_{\rm np}$ and $S_{\rm p} - S_{\rm n}$.

In this structure, a layer consisting of only neutrons emerges at the nuclear surface. The neutron-skin thickness $r_{\rm np}$ is defined as the difference between the point-proton and point-neutron root-mean-square (RMS) radii $\langle r^2 \rangle_{\rm p,n}^{1/2}$:

$$r_{\rm np} \equiv \langle r^2 \rangle_{\rm n}^{1/2} - \langle r^2 \rangle_{\rm p}^{1/2}. \tag{1.1}$$

The emergence of neutron-skin structure is often interpreted as due to the difference between proton and neutron separation energies $S_{\rm p} - S_{\rm n}$ as shown in Fig. 1-3 [TA92, SU95].

1.2 Nuclear Structure of Calcium Isotopes

The Ca isotopic chain has two well-known traditional doubly magic nuclei ^{40}Ca and ^{48}Ca. Very recently, two new magic numbers at $N = 32$ and $N = 34$ have been suggested experimentally from masses of ^{53,54}Ca [WI13] and excitation energies of the 1st 2^+ state $E(2_1^+)$ [ST13]. Many theoretical works using different approaches have been reported to explain the emergence of these neutron magic numbers – called the shell evolution, which include not only newly established ($N = 32, 34$) but also traditional ($N = 20, 28$) magic numbers. J.D. Holt *et al.* reproduced the $N = 28$ magicity, which can not be explained with the microscopic two-body (NN) interaction, by introducing the three-body ($3N$) forces [HO12]. In addition, theoretical calculations with the $NN + 3N$ forces also explained the N dependences on the masses and $E(2_1^+)$. Meanwhile, in the shell-model approach, the large shell gaps in the $N = 32, 34$ are reproduced by reducing the attractive tensor force between the $1f_{7/2}$ proton orbital and the $1f_{5/2}$ neutron one [OH05, ST13]. This shell

model calculation also explains the existence of the $N = 32$ magicity in Ti [JA02, DI05, LI04] and Cr [CH68, BU05, PR01] isotopes which, unlike Ca, do not have the large shell gap in the $N = 34$ (Fig. 1 of Ref. [ST13]). Hence, the Ca isotopic chain has attracted attention from both experimental and theoretical aspects.

Nuclear radii of Ca isotopes also have received a great deal of attention. Although ^{48}Ca has 8 neutrons more than ^{40}Ca, both isotopes have almost the same charge radii [PA84]. While this has been explained qualitatively by taking the cross shell excitation from *sd* to *pf* shell into account, it has not been reproduced at the microscopical level yet. Recently, the charge radii of $^{40-52}$Ca as shown in Fig. 1-4(a) were measured by the optical isotope-shift methods with the high-resolution bunched-beam collinear laser spectroscopy [GA16]. The measured charge radii increase unexpectedly beyond $N = 28$, which has been also found in neighboring potassium isotopes [KR14]. This growth of charge radii from ^{48}Ca to ^{52}Ca cannot be explained quantitatively with several theoretical calculations including the density functional theories (DFT) with several interactions, the configuration interaction (CI) calculations obtained from large-scale shell model calculations with the mean field theory, and the *ab initio* coupled-cluster calculations with SRG1 and SRG2 interactions (Fig. 1-4(b)) [GA16]. The *ab initio* calculation with the recently developed chiral effective field theory interaction NNLO$_{\rm sat}$ [EK15], which was obtained by reproducing charge radii and binding energies up to $A \sim 25$ can reproduce charge radii below ^{48}Ca accurately, and the radii beyond $N = 28$ relatively well. On the other hand, matter radii (or neutron radii) of Ca isotopes were deduced only for stable nuclei ^{40,42,44,48}Ca by the elastic scattering with hadronic probes such as the proton, α, and pion [FR68, AL76, AL77, CH77, RA81, AL82, BO84]. However, these results in the same nucleus are inconsistent with each other beyond the quoted errors, and hence it is difficult to discuss the evolution of matter radii in the Ca isotopic chain. In terms of the neutron skin thickness, the *ab initio* calculation with the NNLO$_{\rm sat}$ interaction predicts a smaller neutron skin thickness than the DFT calculation[HA16]. Thus, in order to understand the evolution of nuclear radii in the vicinity of $N = 28$, more precise and systematic measurements of matter radii are desired.

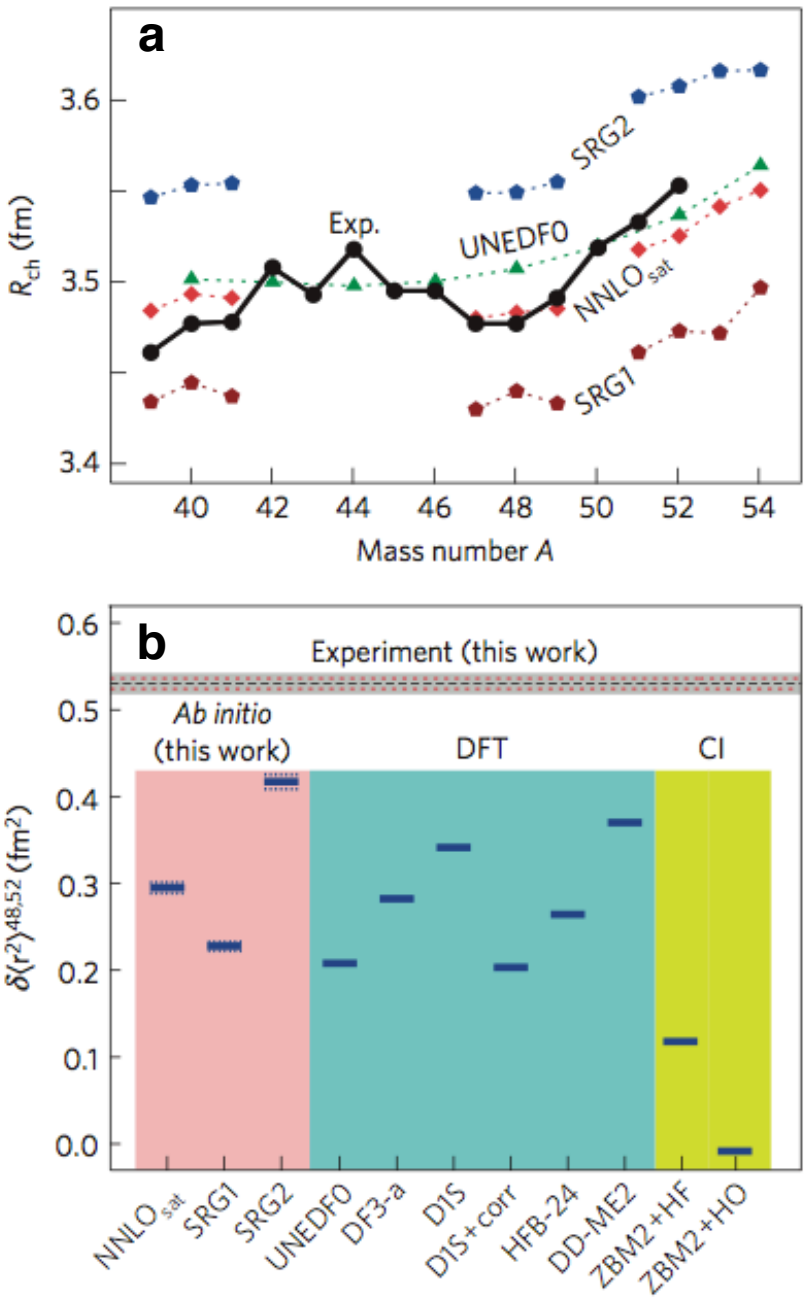

Figure 1-4: (a) Charge radii of $^{39-52}$Ca [GA16] (black-filled circles) in comparison with the *ab initio* calculations and the DFT calculation (UNEDF0). (b) The difference of charge radii between ^{48}Ca and ^{52}Ca in comparison with the *ab initio*, DFT, and CI calculations obtained from the large-space shell model calculation in harmony with the mean field theory [GA16]. This figure is taken from Ref. [GA16].

1.3 Neutron Skin Thickness and Its Impact on Equation of State

An equation of state (EOS) of nuclear matter describes the energy density of the nuclear matter system. The energy density e depends on the density ρ and the relative neutron excess $\delta = (N - Z)/A$ as

$$e(\rho, \delta) = e(\rho, 0) + c_{\rm sym}(\rho)\delta^2 + \mathcal{O}(\delta^4), \tag{1.2}$$

where $e(\rho, 0)$ is the EOS of symmetric nuclear matter and $c_{\rm sym}(\rho)$ is the density-dependent symmetry energy coefficient. In general, the EOS of nuclear matter is expressed by a quadratic expansion around the saturation density ρ_0 as

$$e(\rho, 0) \simeq e_0 + \frac{1}{2}K_0\epsilon^2, \tag{1.3}$$

$$c_{\rm sym}(\rho) \simeq J - L\epsilon + \frac{1}{2}K_{\rm sym}\epsilon^2, \tag{1.4}$$

where ϵ is the relative density defined by

$$\epsilon \equiv -\frac{1}{3}\frac{\rho - \rho_0}{\rho_0}. \tag{1.5}$$

The EOS parameters in Eqs. (1.3) and (1.4) are defined as

$$\begin{aligned} K_0 &\equiv 9\rho_0^2 \left.\frac{\partial^2 e(\rho, 0)}{\partial \rho^2}\right|_{\rho_0}, \\ J &\equiv c_{\rm sym}(\rho_0), \\ L &\equiv 3\rho_0 \left.\frac{\partial c_{\rm sym}(\rho)}{\partial \rho}\right|_{\rho_0}, \\ K_{\rm sym} &\equiv 9\rho_0^2 \left.\frac{\partial^2 c_{\rm sym}(\rho)}{\partial \rho^2}\right|_{\rho_0}. \end{aligned} \tag{1.6}$$

Therefore, the EOS is characterized by the following parameters:

ρ_0	: saturation density of the symmetric nuclear matter,
e_0	: energy per particle of the symmetric nuclear matter,
K_0	: incompressibility of the symmetric nuclear matter,
J	: symmetry energy at saturation density,
L	: slope of the symmetry energy coefficient at saturation density,
$K_{\rm sym}$	: curvature of the symmetry energy coefficient at saturation density.

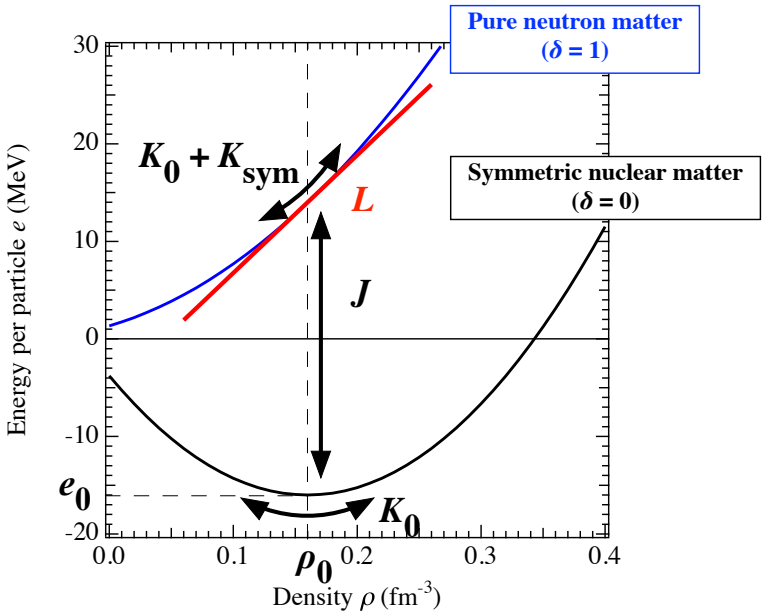

Figure 1-5: Equation of state of symmetric (black line) and pure neutron matter (blue line).

The EOS of nuclear matter system governs not only nuclear physics but also the structure of neutron star. For example, the correlation between mass and radius of neutron stars can be obtained by the EOS using the Tolman-Oppenheimer-Volkov (TOV) equation [LI11]. Moreover, the understanding of neutron star's property is important for the elucidation of the mechanism of supernova explosion. In Fig. 1-5, we show the EOS for the symmetric nuclear matter ($\delta = 0$) and the pure neutron matter ($\delta = 1$) together with the role of each parameter. In order to determine the EOS parameters, both terrestrial nuclear physics experiments and astrophysical observations have been performed. In the EOS of symmetric nuclear matter, ρ_0 and e_0 have been determined precisely by masses and charge radii of stable nuclei [II04]. The parameter K_0 has been determined by the isoscalar giant monopole resonance via α-inelastic scattering in medium-heavy nuclei as $K_0 = 231 \pm 5$ MeV [YO99]. The symmetry energy (isovector) term, on the other hand, had not been determined precisely. Although J has been determined precisely as 30 ± 4 MeV from nuclear masses [CH10], L and $K_{\rm sym}$ have large uncertainties, namely $L = 20$ MeV to 110 MeV [CH10] and $K_{\rm sym} = -550 \pm 100$ MeV [LI07], respectively. Therefore, the precise determination of L and $K_{\rm sym}$ are the keys to the elucidation of the EOS of asymmetric nuclear system around the saturation density.

Although several nuclear physics experiments and astrophysical observa-

tions have been performed to determine L, the results have large uncertainties and are inconsistent with each other. The measurement of $r_{\rm np}$ is one of the most hopeful experimental methods to determine L. In the compressible droplet model [CE09, WA09], the neutron-skin thickness $r_{\rm np}$ of a nucleus can be written as

$$r_{\rm np}(\delta) \simeq \sqrt{\frac{3}{5}}\left(\frac{3}{2}r_0\frac{J}{Q}\frac{\delta-\frac{1}{20}\frac{e^2}{r_0}\frac{Z}{J}A^{-1/3}}{1+\frac{9}{4}\frac{J}{Q}A^{-1/3}}\right)-\sqrt{\frac{3}{5}}\frac{e^2}{70J}Z+r_{\rm np}^{\rm surface}, \tag{1.7}$$

where r_0 is the nuclear radius constant (~ 1.2 fm), J is the symmetry energy at ρ_0, and Q is the surface stiffness which represents the resistance to the enlargement of nuclear radius. In Eq. (1.7), the second and third terms represent the contribution of Coulomb force and the one resulting from the difference of the surface diffusenesses between proton and neutron densities, respectively. The neutron-skin thickness in Eq. (1.7) depends on J/Q. M. Warda *et al.* found the following correlation between J/Q and L by the mean field calculations with several effective interactions [WA09]:

$$L = l_0\frac{J}{Q}+l_1 \ [\text{MeV}], \tag{1.8}$$

$$\begin{aligned} 139 < l_0 < 150 \ [\text{MeV}], \\ -57 < l_1 < -52 \ [\text{MeV}]. \end{aligned} \tag{1.9}$$

Therefore, $r_{\rm np}$ is almost proportional to L. On the other hand, from the point of view of thermodynamics, the energy E, pressure P, and volume V of a system are related by $P=-\partial E/\partial V$, so that the pressure of a neutron matter at the saturation density $P_{\rm n}(\rho_0)$ can be derived as

$$P_{\rm n}(\rho_0) = \rho_0^2\frac{\partial e(\rho,\delta=1)}{\partial\rho}\bigg|_{\rho_0} = \frac{L}{3\rho_0}. \tag{1.10}$$

Hence, we can interpret L as the pressure of the neutron matter. The schematic relation between $r_{\rm np}$ and L is shown in Fig. 1-6. For example, when L is large, which corresponds to a soft surface (small Q) or a solid saturation density (large J), the size of the neutron density increases due to the large pressure, resulting in a thick neutron skin at the nuclear surface.

The main experimental method so far to extract $r_{\rm np}$ for the determination of L is the measurement of E1 resonance excitation. Sine the E1 excitation is an isovector oscillation mode due to the different responses of protons and neutrons, the difference between proton and neutron density distributions can be probed. In the stable Sn isotopes and ^{208}Pb, $r_{\rm np}$ were derived via

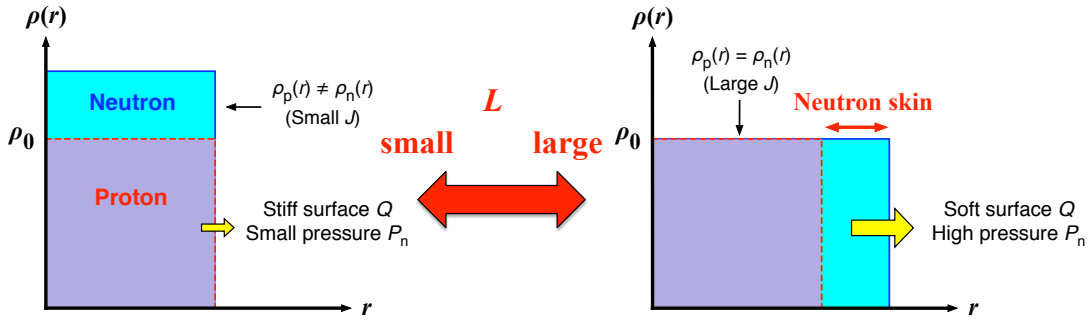

Figure 1-6: Schematic view of the correlation between L and $r_{\rm np}$.

the measurements of isovector giant dipole resonance (IVGDR) and the low-energy E1 excitation mode called pygmy dipole resonance (PDR), which is the oscillation mode between the neutron skin part and the isospin symmetric core. Moreover, recently, the nuclear polarizabilities $\alpha_{\rm D}$ derived by the complete measurement of E1 response were reported and used to obtain $r_{\rm np}$ in a few nuclei such as ^{48}Ca [BI17], ^{68}Ni [RO13], ^{120}Sn [HA15], and ^{208}Pb [TA11]. Although there are other experimental methods such as ones that use an antiprotonic atom [TR01, JA04] and the coherent pion photoproduction [TAR14], these methods including the E1 excitation are indirect measurements of $r_{\rm np}$. The direct determination of $r_{\rm np}$ was attempted by the parity violating elastic electron scattering of ^{208}Pb [AB12]. However, precise determination of $r_{\rm np}$ cannot be achieved yet because of the limited statistics. So far, the direct determination of $r_{\rm np}$ of Sn isotopes and ^{208}Pb has been done only by the proton elastic scattering [TE08, ZE10].

For the isotopic chain of Sn which has several stable isotopes, the $r_{\rm np}$'s have been obtained through several experiments. However, there are systematic deviations among respective measurements in the same nuclei as shown in Fig. 1-7. This figure also shows that $r_{\rm np}$ at large δ has a high sensitivity to L. However, in the conventional methods to measure $r_{\rm np}$'s, only stable nuclei were treated besides the very limited cases such as ^{68}Ni (PDR[WI11] and $\alpha_{\rm D}$ [RO13]) and ^{130,132}Sn (PDR [KL07]). Therefore, in order to determine L precisely, the measurement of $r_{\rm np}$ in a wide range of δ, which also include unstable nuclei by the direct method is strongly desirable. From this point of view, the application of direct extraction of $r_{\rm np}$ from the matter radii determined by $\sigma_{\rm I}$ in combination with the charge radius by the optical isotope shift as performed on Na isotopes by T. Suzuki (Fig. 1-4 (b)) [SU95] is suitable.

It is suggested that Eq. (1.4) is valid between about $\rho_0/2$ and $2\rho_0$ with less than 5% discrepancy [PI09]. When the density is within $\rho_0/2 < \rho < 2\rho_0$,

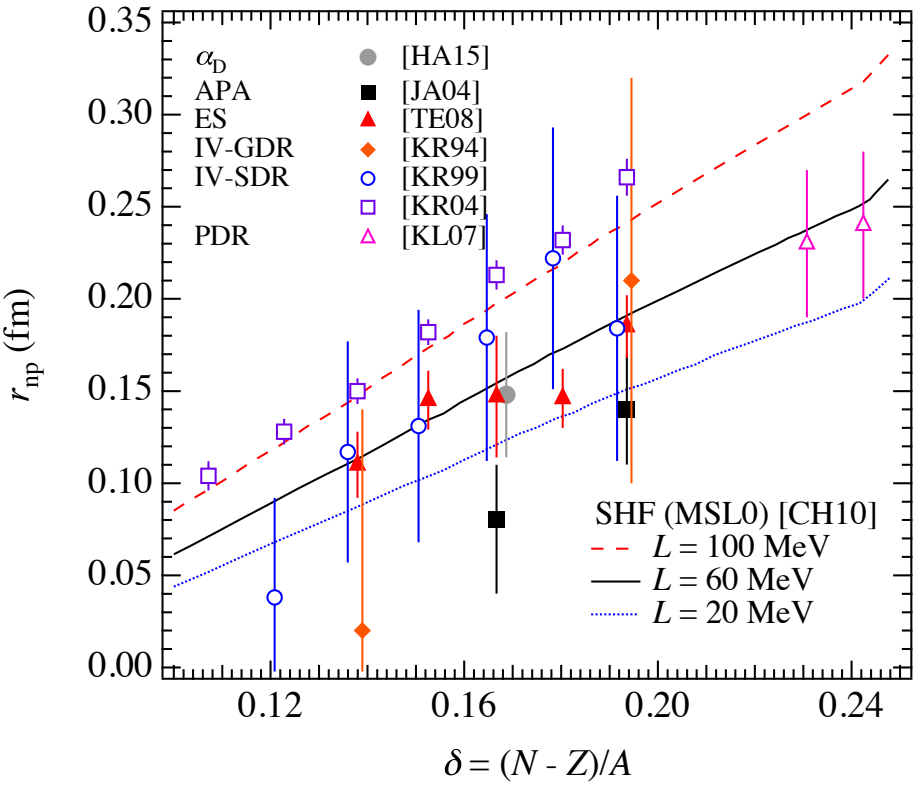

Figure 1-7: Previous experimental results of $r_{\rm np}$ of Sn isotopes as a function of δ. The closed gray circle show the dipole polarizability $\alpha_{\rm D}$ [HA15] and closed black squares show the antiprotonic atoms (APA) [TR01, JA04]. The results of proton elastic scattering (ES) [TE08] and isovector giant dipole resonance (IVGDR) [KR94] are represented by closed red squares and closed orange diamonds, respectively. There are two experimental results of the isovector spin dipole resonance (IV-SDR) shown by open blue circles [KR99] and open purple squares [KR04], respectively. The results of pigmy dipole resonance (PDR) of unstable nuclei ^{130,132}Sn are plotted by open pink triangles. The Skyrme-Hartree-Fock (SHF) calculations using MSL0 interactions with $L = 20, 60, 100$ MeV [CH10] are also shown by the blue dotted, black solid, and red dashed lines, respectively.

the correlation of $a_{\rm sym}(A) \simeq c_{\rm sym}(\rho)$, where $a_{\rm sym}(A)$ represents the symmetry energy of a nucleus whose mass number is A, can hold even down to medium-mass nuclei such as $A \sim 40$ [CE09].

1.4 Thesis Objectives

In order to understand the evolution of nuclear radii in the Ca isotopic chain and determine the EOS parameter L from $r_{\rm np}$ extracted by the direct method in a wide region of δ, we measured $\sigma_{\rm I}$ in the Ca region. In this thesis, we show the first experimental results of $\sigma_{\rm I}$ for $^{42-51}$Ca and their neighboring nuclei $^{40-48}$K and $^{44-46}$Sc, whose charge radii are already known via isotope shift measurements. The previous $\sigma_{\rm I}$ measurements were mainly performed for nuclei lighter than Ar isotopes, while the present study is the first $\sigma_{\rm I}$ measurement in the vicinity of $N = 28$. The matter radii were derived from the measured $\sigma_{\rm I}$ based on the Glauber theory. Moreover, $r_{\rm np}$ were also obtained from the present matter radii and the corresponding charge radii in the region of $0.05 < \delta < 0.22$.

In Chapter 2, we describe the relation between $\sigma_{\rm I}$ and the matter radius based on the Glauber theory. The experimental method, facility, and detectors are presented in Chapter 3. The data analysis to extract $\sigma_{\rm I}$ and the obtained $\sigma_{\rm I}$ are summarized in Chapter 4. Then, in Chapter 5, the matter radius and $r_{\rm np}$ are derived. The discussion of the evolution of nuclear radii in the Ca isotopic chain and the extraction of the EOS parameter L are also shown in Chapter 5. Finally, the summary and the future prospects are mentioned in Chapter 6.

2 Cross Sections and Nuclear Radii

2.1 Definition of Interaction Cross Section σ_{I}

Reaction cross sections σ_{R} and interaction cross sections σ_{I} are sensitive to nuclear radii and density distributions. In 1985, I. Tanihata *et al.* measured σ_{I} by using unstable nuclear beams, then deduced radii of unstable nuclei [TA85a, TA85b]. This experiment led to the beginning of unstable nuclear beam physics.

The σ_{R} is defined by the subtraction of total elastic scattering cross section σ_{el} from total cross section σ_{tot}:

$$\sigma_{\mathrm{R}} \equiv \sigma_{\mathrm{tot}} - \sigma_{\mathrm{el}}. \tag{2.1}$$

In other words, σ_{R} is a cross section of all inelastic collisions.

The σ_{I} is defined as the nuclide-changing cross sections. Therefore, σ_{I} is connected to σ_{R} as

$$\sigma_{\mathrm{I}} \equiv \sigma_{\mathrm{R}} - \sigma_{\mathrm{inel}}, \tag{2.2}$$

where σ_{inel} is a cross section of inelastic process in which the projectile does not change its nuclide. In a high-energy collision, the inelastic scatterings to bound states in the projectile can hardly occur because the incident energy is much higher than the Fermi energy of projectile nucleus. Hence, the σ_{I} is nearly equal to σ_{R} within a few % difference for the energy larger than several hundred MeV/nucleon [OG92].

Moreover, σ_{I} which is the nuclide-changing reactions can be classified whether the atomic number Z of fragment nucleus changes or not. The cross section of charge-changing process is called charge-changing cross section σ_{CC}, while the cross section of neutron removal reaction where Z is not changed is called neutron removal cross section $\sigma_{-\mathrm{xn}}$. In consequence, σ_{R} can be written by

$$\begin{aligned} \sigma_{\mathrm{R}} &= \sigma_{\mathrm{I}} + \sigma_{\mathrm{inel}} \\ &= \sigma_{\mathrm{CC}} + \sigma_{-\mathrm{xn}} + \sigma_{\mathrm{inel}}. \end{aligned} \tag{2.3}$$

In the present study, we measured σ_{I} at approximately 270 MeV/nucleon. In such energy region, σ_{inel} is so small compared to σ_{I} (for example, at most 2% for $^{24-38}$Mg+^{12}C at $\sim$ 240 MeV/nucleon [TA14]) that the condition $\sigma_{\mathrm{I}} \simeq \sigma_{\mathrm{R}}$ is fulfilled. For this reason, in the following subsections, we show the relation between the nuclear radius and σ_{R} on behalf of σ_{I}.

2.2 Classical Description of Reaction Cross Section

In a classical picture, σ_{R} can be considered in the framework of very simple geometrical model as shown in Fig. 2-1. This is called a black disk model. In this model, a reaction always occurs when the projectile and target nuclei overlap each other. Therefore, σ_{R} can be defined as

$$\sigma_{\mathrm{R}} \equiv \pi(R_{\mathrm{P}} + R_{\mathrm{T}})^2, \tag{2.4}$$

where R_{P} and R_{T} are radii of projectile and target nuclei, respectively. If a nucleus whose radius is known is adopted as a target, R_{P} can be derived via σ_{R}. Kox *et al.* measured σ_{R} for several projectile-target systems in the wide energy range of 10 to 300 MeV/nucleon [KO84, KO87]. These systematic data led to the empirical formula of σ_{R} as follows:

$$\sigma_{\mathrm{R}} = \pi {r_0}^2 \left(A_{\mathrm{P}}^{1/3} + A_{\mathrm{T}}^{1/3} + a\frac{A_{\mathrm{P}}^{1/3} A_{\mathrm{T}}^{1/3}}{A_{\mathrm{P}}^{1/3} + A_{\mathrm{T}}^{1/3}} - c(E) \right)^2 \times \left(1 - \frac{B_{\mathrm{C}}}{E_{\mathrm{CM}}} \right), \tag{2.5}$$

A_{P}	:	mass number of projectile nucleus,
A_{T}	:	mass number of target nucleus,
B_{C}	:	Coulomb barrier energy,
E_{CM}	:	kinetic energy in the Center-of-Mass system,
r_0, a	:	constants ($r_0 = 1.1$ fm, $a = 1.85$),

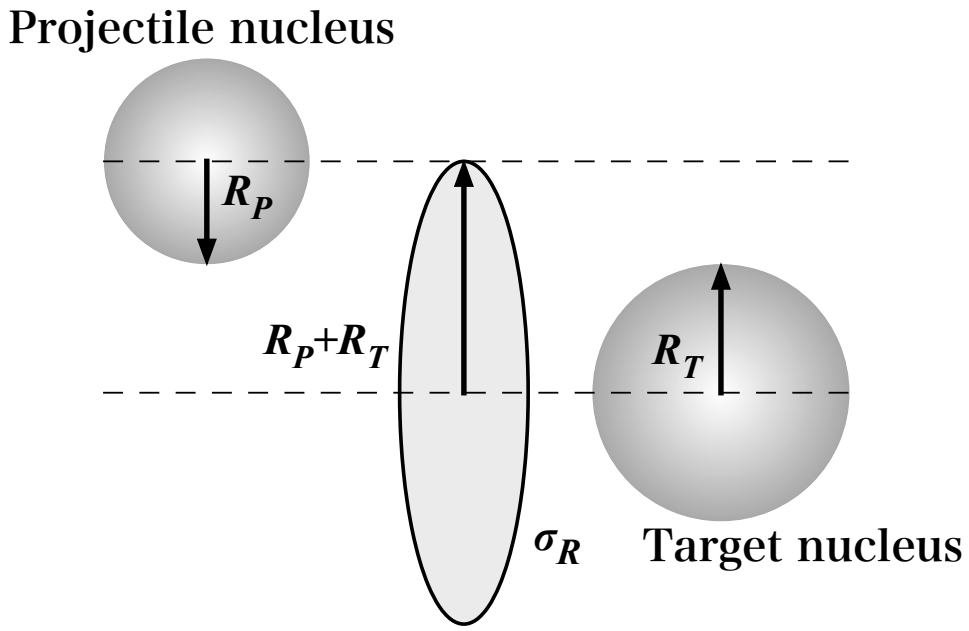

Figure 2-1: Geometrical model of σ_{R}

where $c(E)$ represents a transparency of nuclear surface as shown in Fig. 2-2. For $E_{\mathrm{CM}} < 100$ MeV/nucleon, a significant decrease of $c(E)$ can be seen, which corresponds to a high sensitivity to the surface region of nucleus. When a nucleus-nucleus reaction is depicted by the superposition of nucleon-nucleon collisions, the energy dependence of $\sigma_{\mathrm{R}}(E)$ results from that of nucleon-nucleon total cross section $\sigma_{\mathrm{NN}}(E)$. The optical-limit approximation of Glauber theory explained in Sec. 2.5 is also based on such a description.

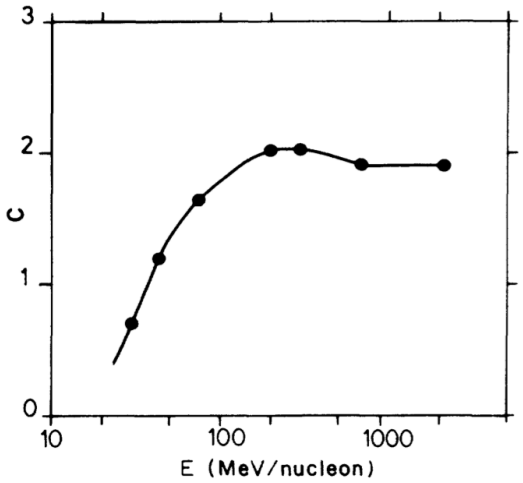

Figure 2-2: Energy dependence of $c(E)$ [KO87]. This figure is taken from Ref. [KO87].

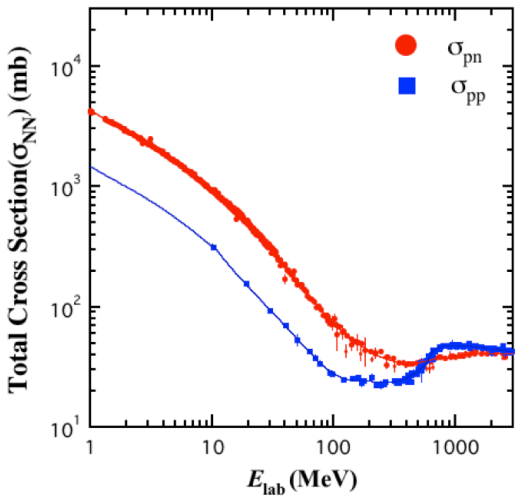

Figure 2-3: Energy dependence of $\sigma_{\mathrm{NN}}(E)$ [NA10]. This figure is taken from Ref. [NI11].

2.3 Scattering Theory

In a three-dimensional scattering theory, a Schrödinger equation for a particle with mass m in a spherically symmetric potential can be written as

$$\left[-\frac{\hbar^2}{2m}\nabla^2\psi + V(r)\psi\right] = i\hbar\frac{\partial\psi}{\partial t}. \tag{2.6}$$

When this potential $V(r)$ has a finite range a, the solution of Eq. (2.6) for $r > a$ is a plane wave as

$$\psi(\boldsymbol{r}) = e^{ikz} \tag{2.7}$$

with

$$k \equiv \sqrt{2mE/\hbar^2}. \tag{2.8}$$

This solution represents an incident wave function. After interacting with a target nucleus, the scattering results in an outgoing spherical wave, whose amplitude decreases as a function of r. Therefore, the wave function after scattering can be expressed by the superposition of incident wave and scattered one given by

$$\psi(\boldsymbol{r}) = e^{ikz} + f(\theta)\frac{e^{ik'r}}{r}, \tag{2.9}$$

where $f(\theta)$ is a scattering amplitude, and k' is a wave number for the scattered wave. Since it is assumed that $V(r)$ has the spherical symmetry, $f(\theta)$ do not depend on ϕ but only θ. Probability currents of incident and scattered waves are given by

$$j_{\text{inc}} = \frac{\hbar k}{m}, \tag{2.10}$$

$$j_{\text{scatt}} = \frac{\hbar k'}{mr^2}|f(\theta)|^2 + \mathcal{O}(r^{-3}). \tag{2.11}$$

Hence, the number of outgoing particles per solid angle ($d\Omega = dS/r^2$) per time $dN/d\Omega$ can be derived as

$$\frac{dN}{d\Omega} = r^2 \cdot j_{\text{scatt}} = \frac{\hbar k'}{m}|f(\theta)|^2. \tag{2.12}$$

In the case of elastic scattering, k is equal to k', so that a differential cross section $d\sigma/d\Omega$ is derived as

$$\begin{aligned}\frac{d\sigma}{d\Omega} &= \frac{1}{j_{inc}}\frac{dN}{d\Omega} \\ &= \frac{k'}{k}|f(\theta)|^2 \\ &= |f(\theta)|^2\end{aligned} \tag{2.13}$$

In other words, elastic scattering differential cross section measurements enable us to derive $f(\theta)$.

In order to clarify $\psi(r)$, the following equation has to be solved:

$$\left[\nabla^2 + k'^2\right] \psi(\boldsymbol{r}) = \frac{2m}{\hbar^2} V(r)\psi(\boldsymbol{r}) \tag{2.14}$$

The homogeneous solution of this equation is equal to the plane wave e^{ikz}, while the inhomogeneous solution can be represented with the Green function $G(\boldsymbol{r} - \boldsymbol{r'})$. As a result, the general solution is written by

$$\psi(\boldsymbol{r}) = e^{ikz} + \frac{2m}{\hbar^2} \int G(\boldsymbol{r} - \boldsymbol{r'}) V(\boldsymbol{r'}) \psi(\boldsymbol{r'}) d^3 r'. \tag{2.15}$$

The Green function fulfills the following equation:

$$\left[\nabla^2 + k'^2\right] G(\boldsymbol{r} - \boldsymbol{r'}) = \delta(\boldsymbol{r} - \boldsymbol{r'}), \tag{2.16}$$

where $\delta(\boldsymbol{r} - \boldsymbol{r'})$ is a delta function. This Green function can be derived with the Fourier transformation as

$$G(\boldsymbol{r} - \boldsymbol{r'}) = \frac{1}{(2\pi)^3} \int e^{i\boldsymbol{q}\cdot(\boldsymbol{r}-\boldsymbol{r'})} G'(\boldsymbol{q}) d^3 q, \tag{2.17}$$

$$\delta(\boldsymbol{r} - \boldsymbol{r'}) = \frac{1}{(2\pi)^3} \int e^{i\boldsymbol{q}\cdot(\boldsymbol{r}-\boldsymbol{r'})} d^3 q. \tag{2.18}$$

Substituting Eqs. (2.17) and (2.18) into Eq. (2.16), the following equation is given as

$$\begin{aligned} &\frac{1}{(2\pi)^3} \int (-\boldsymbol{q}^2 + \boldsymbol{k'}^2) e^{i\boldsymbol{q}\cdot(\boldsymbol{r}-\boldsymbol{r'})} G'(\boldsymbol{q}) d^3 q = \frac{1}{(2\pi)^3} \int e^{i\boldsymbol{q}\cdot(\boldsymbol{r}-\boldsymbol{r'})} d^3 q, \\ &\frac{1}{(2\pi)^3} \int \left\{(-\boldsymbol{q}^2 + \boldsymbol{k'}^2) G'(\boldsymbol{q}) - 1\right\} e^{i\boldsymbol{q}\cdot(\boldsymbol{r}-\boldsymbol{r'})} d^3 q = 0. \end{aligned} \tag{2.19}$$

From Eq. (2.19), the Green function can be derived as

$$G'(\boldsymbol{q}) = \frac{1}{k'^2 - q^2}, \tag{2.20}$$

$$\begin{aligned} G(\boldsymbol{r} - \boldsymbol{r'}) &= \frac{1}{(2\pi)^3} \int \frac{e^{i\boldsymbol{q}\cdot(\boldsymbol{r}-\boldsymbol{r'})}}{k'^2 - q^2} d^3 q \\ &= -\frac{1}{4\pi} \frac{e^{ik'|\boldsymbol{r}-\boldsymbol{r'}|}}{|\boldsymbol{r} - \boldsymbol{r'}|} \end{aligned} \tag{2.21}$$

The wave function $\psi(\boldsymbol{r})$ can be obtained by substituting Eq. (2.21) into Eq. (2.15):

$$\psi(\boldsymbol{r}) = e^{ikz} - \frac{1}{4\pi}\frac{2m}{\hbar^2}\int \frac{e^{ik'|\boldsymbol{r}-\boldsymbol{r'}|}}{|\boldsymbol{r}-\boldsymbol{r'}|}V(\boldsymbol{r'})\psi(\boldsymbol{r'})d^3r'. \tag{2.22}$$

Therefore, the derivation of $\psi(\boldsymbol{r})$ corresponds to solving the integral equation given by Eq. (2.22). In order to obtain $f(\theta)$ from Eq. (2.22), we compare the asymptotic form of Eq. (2.22) in the limit of $r \to \infty$ with Eq. (2.9). In such a limit, $|\boldsymbol{r'}|/|\boldsymbol{r}|$ is so small compared to 1 that the following approximation forms can be adopted:

$$k'|\boldsymbol{r}-\boldsymbol{r'}| \simeq k'r - \boldsymbol{k'}\cdot\boldsymbol{r'}, \tag{2.23}$$

$$\frac{1}{|\boldsymbol{r}-\boldsymbol{r'}|} \simeq \frac{1}{r}. \tag{2.24}$$

Taking Eqs. (2.23) and (2.24) into consideration, Eq. (2.22) can be converted to:

$$\begin{aligned}\psi(\boldsymbol{r}) &= e^{ikz} - \frac{1}{4\pi}\frac{2m}{\hbar^2}\int \frac{e^{ik'r}e^{-i\boldsymbol{k'}\cdot\boldsymbol{r'}}}{r}V(\boldsymbol{r'})\psi(\boldsymbol{r'})d^3r' \\ &= e^{ikz} + \left\{-\frac{1}{4\pi}\frac{2m}{\hbar^2}\int e^{-i\boldsymbol{k'}\cdot\boldsymbol{r'}}V(\boldsymbol{r'})\psi(\boldsymbol{r'})d^3r'\right\}\frac{e^{ik'r}}{r}.\end{aligned} \tag{2.25}$$

Finally, the scattering amplitude $f(\theta)$ can be obtained from the comparison of Eq. (2.25) to Eq. (2.9) as

$$f(\theta) = -\frac{1}{4\pi}\frac{2m}{\hbar^2}\int e^{-i\boldsymbol{k'}\cdot\boldsymbol{r'}}V(\boldsymbol{r'})\psi(\boldsymbol{r'})d^3r'. \tag{2.26}$$

2.4 Eikonal Approximation

We have to obtain the wave function $\psi(\boldsymbol{r})$ so as to derive the scattering amplitude $f(\theta)$. In Sec. 2.3, we define the wave function as a superposition of incident plane wave and scattered spherical one. Then, we redefine the solution of Schrödinger equation with a deviation of incident plane wave $\psi'(\boldsymbol{r})$:

$$\psi(\boldsymbol{r}) \equiv e^{ikz}\psi'(\boldsymbol{r}) \tag{2.27}$$

By substituting Eq. (2.27) into the Schrödinger equation, the following equation is obtained:

$$\left[-\frac{\hbar^2}{2m}\nabla^2\left(e^{ikz}\psi'(\boldsymbol{r})\right) + V(r)e^{ikz}\psi'(\boldsymbol{r})\right] = Ee^{ikz}\psi'(\boldsymbol{r}) \tag{2.28}$$

In the left-hand side of Eq. (2.28), the first term can be converted to

$$\nabla^2\{e^{ikz}\psi'(\boldsymbol{r})\} = e^{ikz}\left(-k^2\psi'(\boldsymbol{r}) + 2ik\frac{\partial}{\partial z}\psi'(\boldsymbol{r}) + \nabla^2\psi'(\boldsymbol{r})\right). \tag{2.29}$$

Hence, the deviation $\psi'(\boldsymbol{r})$ fulfills the following equation:

$$\left(vp_z + \frac{\boldsymbol{p}^2}{2m} + V(r)\right)\psi'(\boldsymbol{r}) = 0 \tag{2.30}$$

with

$$\begin{aligned} p_z &= -i\hbar\frac{\partial}{\partial z}, \\ p^2 &= -\hbar^2\nabla^2, \\ v &= \frac{\hbar k}{m}. \end{aligned} \tag{2.31}$$

In the eikonal approximation, though the scattered wave is distorted by the potential V, this distortion results in only the slight change of wave function. Namely, the eikonal approximation is assumed to the following conditions:

- The potential depth V is quite shallow compared to the incident energy E:

$$1 \gg \frac{|V|}{E}. \tag{2.32}$$

- The change of potential amplitude per one wavelength of the scattered wave is quite small:

$$a \gg \frac{1}{k}, \tag{2.33}$$

where a is a potential width.

Above conditions are valid in the high energy region. In the eikonal approximation, the secondary deviation in Eq. (2.30) is negligible, so that Eq. (2.30) can be reduced as

$$-i\hbar v \frac{\partial}{\partial z}\psi'(\boldsymbol{r}) + V(r)\psi'(\boldsymbol{r}) = 0. \tag{2.34}$$

By solving this equation with the initial condition $\lim_{z\to-\infty}\psi'(\boldsymbol{r}) = 1$, we can obtain the following expression:

$$\psi'(\boldsymbol{r}) = \exp\left[-\frac{i}{\hbar v}\int_{-\infty}^{z} V(\boldsymbol{b} + z'\boldsymbol{e_z})dz'\right], \tag{2.35}$$

where we adopt cylindrical coordinates as $\boldsymbol{r} \equiv (\boldsymbol{b}, z)$. Now, we introduce a phase shift function $\chi(\boldsymbol{b})$ defined by

$$\chi(\boldsymbol{b}) = -\frac{1}{\hbar v}\int_{-\infty}^{\infty} V(\boldsymbol{b} + z'\boldsymbol{e_z})dz'. \tag{2.36}$$

Therefore, the wave function can be expressed as

$$\psi(\boldsymbol{r}) = \exp\left[i\left\{kz + \chi(\boldsymbol{b})\right\}\right]. \tag{2.37}$$

Although this expression has an invalid asymptotic form in the limit of $r \to \infty$, it works as a good approximation nearby the potential. Equation (2.34) can be converted with Eq. (2.36) to

$$i\hbar v\left(e^{i\chi(\boldsymbol{b})} - 1\right) = \int_{-\infty}^{\infty}\left[V(r)\exp\left\{-\frac{i}{\hbar v}\int_{-\infty}^{z} V(\boldsymbol{b} + z'\boldsymbol{e_z})dz'\right\}\right]dz. \tag{2.38}$$

By substituting Eq. (2.38) into Eq. (2.26), the scattering amplitude $f(\theta)$ can also be represented as

$$f(\theta) = \frac{ik}{2\pi}\int d\boldsymbol{b'}e^{-i\boldsymbol{q}\cdot\boldsymbol{b'}}(1 - e^{i\chi(\boldsymbol{b})}). \tag{2.39}$$

When $|\chi(\boldsymbol{b})|$ is much smaller than 1, the scattering amplitude with the eikonal approximation is equal to that with the Born approximation.

2.5 Glauber Theory

Glauber utilized the eikonal approximation in harmony with an adiabatic approximation in order to depict nuclear-nuclear collisions as superpositions of nucleon-nucleon collisions between nucleons composing the colliding nuclei. In the adiabatic approximation, it is assumed that the nuclear excitation energy can be negligible, which is also valid in a high energy region. This framework is called the Glauber theory. In this section, we briefly explain the Glauber theory with the optical limit approximation (OLA) in Sec. 2.5.2 and the modified optical limit approximation (MOL) in Sec. 2.5.4, respectively. The detailed description of Glauber theory can be seen in Refs. [SU03, SU08].

2.5.1 General Description of Glauber Theory

Nucleon-Nucleus Scattering

A Hamiltonian of target nucleus H_{T} fulfills the following eigenequation:

$$H_{\mathrm{T}}\Psi_\alpha = E_\alpha \Psi_\alpha, \tag{2.40}$$

where Ψ is an eigenfunction, E is an eigenvalue, and subscript α denotes a state, respectively. First, we calculate a transition probability from the grand state ($\alpha = 0$) to the state α. In the relative coordinates, the Hamiltonian of the system which consists of an incident nucleon and a target nucleus with mass number A is given by

$$H = \frac{\boldsymbol{p}^2}{2\mu} + H_{\mathrm{T}} + \sum_{i=1}^{A} V(\boldsymbol{r} - \boldsymbol{r}_i), \tag{2.41}$$

where μ is a reduced mass, $\boldsymbol{p}$ a relative momentum, $\boldsymbol{r}_i$ the coordinates of i-th nucleon in the target, and $V(\boldsymbol{r} - \boldsymbol{r}_i)$ an interaction potential between an incident nucleon and nucleon in the target, respectively. When the wave function after scattering is defined as

$$\psi(\boldsymbol{r}, \boldsymbol{r}_1, \ldots, \boldsymbol{r}_A) \equiv e^{ikz}\Psi(\boldsymbol{r}, \boldsymbol{r}_1, \ldots, \boldsymbol{r}_A), \tag{2.42}$$

The Schrödinger equation is written in analogy with Eq. (2.29) by

$$\left[vp_z + \frac{\boldsymbol{p}^2}{2m} + (H_T - E_0) + V(r) \right] \Psi(\boldsymbol{r}, \boldsymbol{r}_1, \ldots, \boldsymbol{r}_A) = 0. \tag{2.43}$$

In the left-hand side of Eq. (2.43), the second term can be ignored based on the eikonal approximation. On the other hand, the eigenvalue of the third term on the left-hand side of Eq. (2.43) corresponds to the excitation

energy of target nucleus. Based on the adiabatic approximation, this term can be negligible compared to vp_z. The wave function $\Psi(\boldsymbol{r}, \boldsymbol{r}_1, \ldots, \boldsymbol{r}_A)$ can be derived with the initial condition $\lim_{z\to-\infty}\Psi = \Psi_0$ as

$$\Psi(\boldsymbol{r}, \boldsymbol{r}_1, \ldots, \boldsymbol{r}_A) = \exp\left[-\frac{i}{\hbar v}\int_{-\infty}^{z}\sum_{i=1}^{A} V(\boldsymbol{b} + z'\boldsymbol{e_z} - \boldsymbol{r}_i)dz'\right]\Psi_0(\boldsymbol{r}, \boldsymbol{r}_1, \ldots, \boldsymbol{r}_A). \tag{2.44}$$

Therefore, the scattering amplitude to the state α, $f(\theta)_\alpha$, can be derived in the similar procedure to derive Eq. (2.39) as

$$f(\theta)_\alpha = \frac{ik}{2\pi}\int d\boldsymbol{b}\langle\Psi_\alpha|e^{-i\boldsymbol{q}\cdot\boldsymbol{b}}(1 - e^{i\sum_{i=1}^{A}\chi(\boldsymbol{b}-\boldsymbol{s}_i)})|\Psi_0\rangle, \tag{2.45}$$

where $\boldsymbol{s}_i \equiv (x_i, y_i)$ is the coordinates on a plane perpendicular to the axis of beam direction. The coordinates $\boldsymbol{b} - \boldsymbol{s}_i$ correspond to the impact parameter between the incident particle and the i-th internucleon as shown in Fig. 2-4. The cross section to the state α is obtained as

$$\begin{aligned}\sigma_\alpha &= \int d\Omega|f_\alpha(\theta)|^2 \\ &= \int \frac{d\boldsymbol{q}}{k^2}\left|\frac{ik}{2\pi}\int d\boldsymbol{b}\langle\Psi_\alpha|e^{-i\boldsymbol{q}\cdot\boldsymbol{b}}(1 - e^{i\sum_{i=1}^{A}\chi(\boldsymbol{b}-\boldsymbol{s}_i)})|\Psi_0\rangle\right|^2 \\ &= \int d\boldsymbol{b}\left|\langle\Psi_\alpha|\left(1 - \exp\left\{i\sum_{i=1}^{A}\chi(\boldsymbol{b}-\boldsymbol{s}_i)\right\}\right)|\Psi_0\rangle\right|^2,\end{aligned} \tag{2.46}$$

where the Fourier transformation of the delta function is used:

$$(2\pi)^2\delta(\boldsymbol{b} - \boldsymbol{b'}) = \int e^{i\boldsymbol{q}\cdot(\boldsymbol{b}-\boldsymbol{b'})}d\boldsymbol{q}. \tag{2.47}$$

We can derive the cross sections to any states with Eq. (2.46). The elastic scattering cross section $\sigma_{\rm el}$, where the final state is $\alpha = 0$, is given by

$$\sigma_{\rm el} = \int d\boldsymbol{b}\left|1 - \langle\Psi_0|\exp\left\{i\sum_{i=1}^{A}\chi(\boldsymbol{b}-\boldsymbol{s}_i)\right\}|\Psi_0\rangle\right|^2. \tag{2.48}$$

On the other hand, the total cross section $\sigma_{\rm tot}$ can be derived based on the optical theorem as

$$\begin{aligned}\sigma_{\rm tot} &= \frac{4\pi}{k}{\rm Im}f_{\alpha=0}(\theta = 0) \\ &= 2\int d\boldsymbol{b}\langle\Psi_0|\left(1 - {\rm Re}\exp\left\{i\sum_{i=1}^{A}\chi(\boldsymbol{b}-\boldsymbol{s}_i)\right\}\right)|\Psi_0\rangle.\end{aligned} \tag{2.49}$$

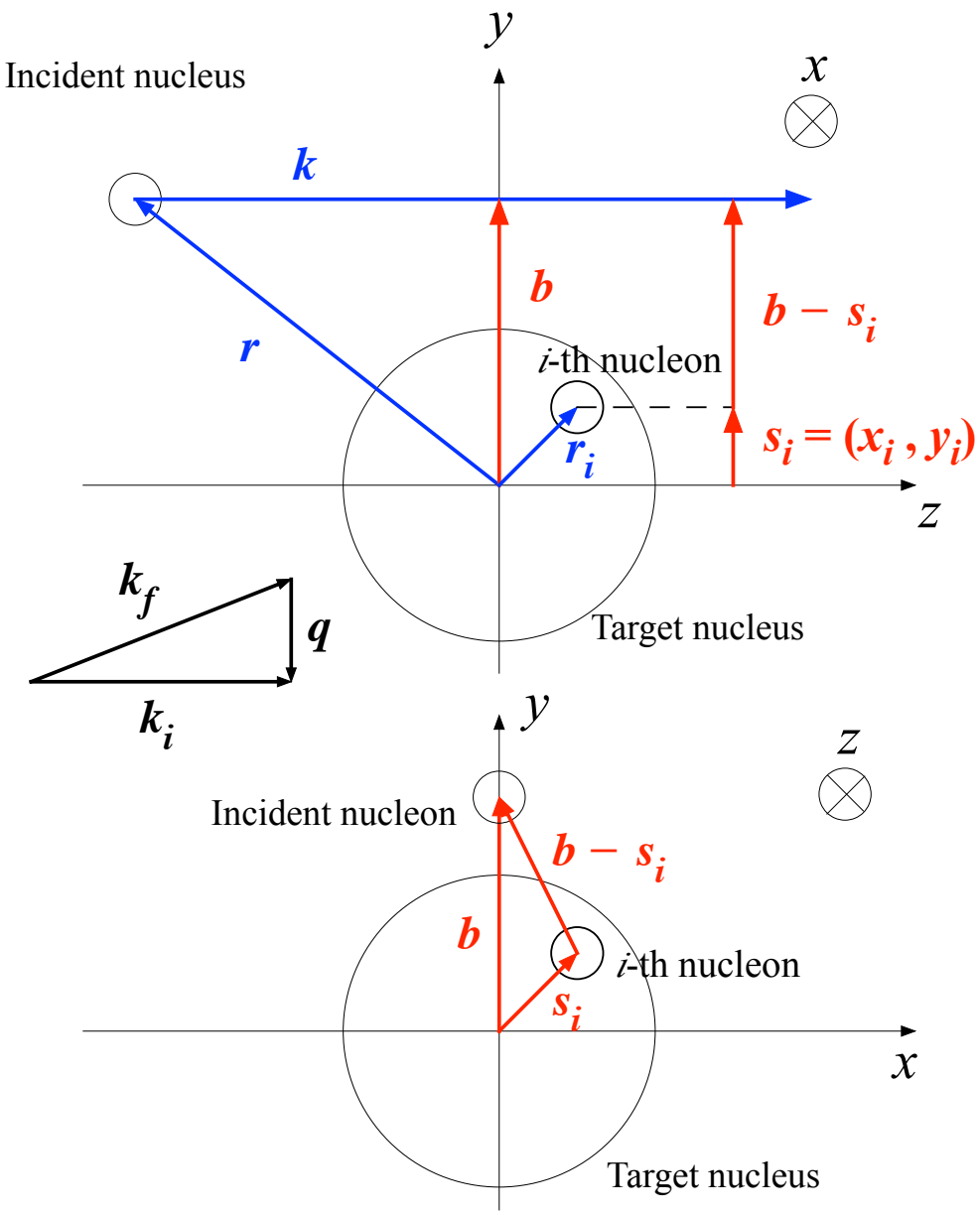

Figure 2-4: Geometrical configuration of each quantity in the nucleon-nucleus scattering.

By the combination of Eqs. (2.48) and (2.49), $\sigma_{\rm R}$ can be obtained as

$$\begin{aligned}\sigma_{\rm R} \equiv& \sigma_{\rm tot} - \sigma_{\rm el} \\ =& 2\int d\boldsymbol{b}\langle\Psi_0|\left(1 - {\rm Re}\exp\left\{i\sum_{i=1}^{A}\chi(\boldsymbol{b}-\boldsymbol{s}_i)\right\}\right)|\Psi_0\rangle \\ &- \int d\boldsymbol{b}\left|1 - \langle\Psi_0|\exp\left\{i\sum_{i=1}^{A}\chi(\boldsymbol{b}-\boldsymbol{s}_i)\right\}|\Psi_0\rangle\right|^2 \\ =& \int d\boldsymbol{b}\left(1 - \left|\langle\Psi_0|\exp\left\{i\sum_{i=1}^{A}\chi(\boldsymbol{b}-\boldsymbol{s}_i)\right\}|\Psi_0\rangle\right|^2\right).\end{aligned} \tag{2.50}$$

Nucleus-Nucleus Scattering

Next, we expand the discussion of nucleon-nucleus scattering to that of nucleus-nucleus scattering. In analogy with Eq. (2.45), the scattering amplitude $f_{\alpha,\beta}(\theta)$ from the ground state $|\Psi_0^{\rm P}\Psi_0^{\rm T}\rangle$ to the final state $\langle\Psi_\alpha^{\rm P}\Psi_\beta^{\rm T}|$ which consists of the state of projectile nucleus α and that of target nucleus β is given by

$$f_{\alpha,\beta}(\theta) = \frac{iK}{2\pi}\int d^2\boldsymbol{b}\langle\Psi_\alpha^{\rm P}\Psi_\beta^{\rm T}|e^{-i\boldsymbol{q}\cdot\boldsymbol{b}}(1 - e^{i\sum_i\sum_j\chi(\boldsymbol{b}+\boldsymbol{s}_i^{\rm P}-\boldsymbol{s}_j^{\rm T})})|\Psi_0^{\rm P}\Psi_0^{\rm T}\rangle, \tag{2.51}$$

where K is a relative wave number. The geometrical configuration of nucleus-nucleus scattering is shown in Fig. 2-5. Based on Eqs. (2.46) - (2.50), we can derive $\sigma_{\rm R}$ for the nucleus-nucleus system as follows:

$$\begin{aligned}\sigma_{\rm R} =& \sigma_{\rm total} - \sigma_{\rm ela=00} \\ =& 2\int d\boldsymbol{b}\langle\Psi_0^{\rm P}\Psi_0^{\rm T}|\left(1 - {\rm Re}\exp\left\{i\sum_i\sum_j\chi(\boldsymbol{b}+\boldsymbol{s}_i^{\rm P}-\boldsymbol{s}_j^{\rm T})\right\}\right)|\Psi_0^{\rm P}\Psi_0^{\rm T}\rangle \\ &- \int d\boldsymbol{b}\left|1 - \langle\Psi_0^{\rm P}\Psi_0^{\rm T}|\exp\left\{i\sum_i\sum_j\chi(\boldsymbol{b}+\boldsymbol{s}_i^{\rm P}-\boldsymbol{s}_j^{\rm T})\right\}|\Psi_0^{\rm P}\Psi_0^{\rm T}\rangle\right|^2 \\ =& \int d\boldsymbol{b}\left(1 - \left|\langle\Psi_0^{\rm P}\Psi_0^{\rm T}|\exp\left\{i\sum_i\sum_j\chi(\boldsymbol{b}+\boldsymbol{s}_i^{\rm P}-\boldsymbol{s}_j^{\rm T})\right\}|\Psi_0^{\rm P}\Psi_0^{\rm T}\rangle\right|^2\right).\end{aligned} \tag{2.52}$$

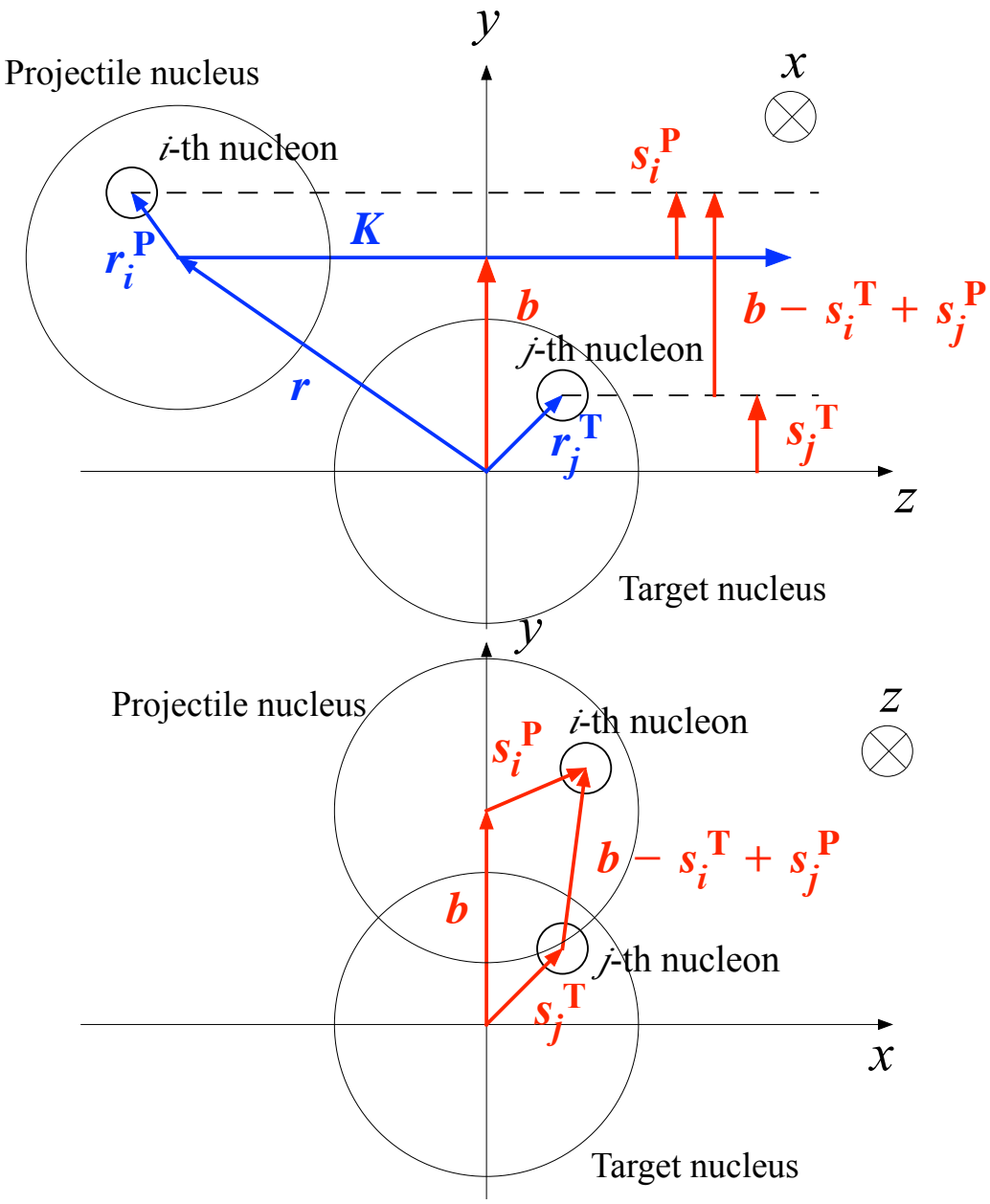

Figure 2-5: Geometrical configuration of each quantity in the nucleus-nucleus scattering.

2.5.2 Input Parameters for Calculation of Reaction Cross Section

The derivation of $\sigma_{\rm R}$ based on Eq. (2.52) needs the following quantities:

- Phase-shift function $\chi(\boldsymbol{b})$
- Ground-state wave function of projectile nucleus $|\Psi_0^{\rm P}\rangle$
- Ground-state wave function of target nucleus $|\Psi_0^{\rm T}\rangle$

Although $\chi(\boldsymbol{b})$ should be essentially calculated from the bare nuclear force, the strict calculation is quite difficult due to the unresolved characteristics of nuclear force itself. Therefore, we introduce the profile function defined as

$$\Gamma(\boldsymbol{b}) \equiv 1 - e^{i\chi(\boldsymbol{b})}. \tag{2.53}$$

The scattering amplitude given by Eq. (2.39) is expressed with $\Gamma(\boldsymbol{b})$ by

$$\begin{aligned} f(\theta) &= \frac{ik}{2\pi}\int d\boldsymbol{b} e^{-i\boldsymbol{q}\cdot\boldsymbol{b}}(1 - e^{i\chi(\boldsymbol{b})}) \\ &= \frac{ik}{2\pi}\int d\boldsymbol{b} e^{-i\boldsymbol{q}\cdot\boldsymbol{b}}\Gamma(\boldsymbol{b}), \end{aligned} \tag{2.54}$$

which means that $\Gamma(\boldsymbol{b})$ is related to the scattering amplitude with the Fourier transformation. The $\Gamma(\boldsymbol{b})$ is often parametrized as

$$\Gamma(\boldsymbol{b}, E) = \frac{1 - i\alpha}{2}\frac{\sigma_{\rm NN}^{\rm tot}(E)}{2\pi\beta}\exp(-\frac{\boldsymbol{b}^2}{2\beta}), \tag{2.55}$$

where $\sigma_{\rm NN}^{\rm tot}(E)$ is a nucleon-nucleon total cross section, α a ratio of the real to the imaginary part of nucleon-nucleon scattering amplitude, and β a slope parameter of the nucleon-nucleon elastic differential cross section. Ultimately, the β has a meaning of the effective range of nuclear force. The angular distribution of nucleon-nucleon elastic scattering enables us to deduce β owing to its dependence of $e^{-\beta q^2/2}$, while the combination of $\sigma_{\rm ela}^{\rm NN}$ and $\sigma_{\rm NN}^{\rm tot}$ provides the following relationship:

$$\sigma_{\rm ela}^{\rm NN} = \int d\boldsymbol{b}|\Gamma(\boldsymbol{b})|^2 = \frac{1 + \alpha^2}{16\pi\beta^2}(\sigma_{\rm NN}^{\rm tot})^2. \tag{2.56}$$

Since the hadron production channels are closed below $E < 300$ MeV/nucleon, Eq. (2.56) can be reduced with $\sigma_{\rm ela}^{NN} = \sigma_{NN}^{\rm tot}$ as

$$\beta = \sqrt{\frac{(1 + \alpha^2)\sigma_{NN}^{\rm tot}}{16\pi}}. \tag{2.57}$$

In the zero-range limit given by $\beta \to 0$, $\Gamma(\boldsymbol{b})$ can be expressed by the quite simple form as

$$\Gamma(\boldsymbol{b}) = \frac{1 - i\alpha}{2} \sigma_{NN}^{\mathrm{tot}}(E) \delta(\boldsymbol{b}). \tag{2.58}$$

On the other hand, a density distribution $\rho(\boldsymbol{r})$ which consists of A nucleons is defined as

$$\begin{aligned}
\rho(\boldsymbol{r}) &= \left\langle \Psi \left| \sum_{i=1}^{A} \delta(\boldsymbol{r} - \boldsymbol{r}_i) \right| \Psi \right\rangle \\
&= \int d\boldsymbol{r}_1 \ldots \int d\boldsymbol{r}_i \ldots \int d\boldsymbol{r}_A \left| \sum_{i=1}^{A} \delta(\boldsymbol{r} - \boldsymbol{r}_i) \Psi(\boldsymbol{r}_1, \ldots, \boldsymbol{r}_i, \ldots, \boldsymbol{r}_A) \right|^2 \\
&= \int d\boldsymbol{r}_1 \ldots \int d\boldsymbol{r}_i \ldots \int d\boldsymbol{r}_A \sum_{i=1}^{A} \delta(\boldsymbol{r} - \boldsymbol{r}_i) \prod_{i=1}^{A} n(\boldsymbol{r}_i) \\
&= \sum_{i=1}^{A} n_i(\boldsymbol{r}),
\end{aligned} \tag{2.59}$$

where $n_i(\boldsymbol{r})$ is a probability density distribution of i-th nucleon in the nucleus. Hence, instead of $\chi(\boldsymbol{b})$, $|\Psi_0^{\mathrm{P}}\rangle$, and $|\Psi_0^{\mathrm{T}}\rangle$, we can utilize $\Gamma(\boldsymbol{b})$, $\rho^{\mathrm{P}}(\boldsymbol{r})$, and $\rho^{\mathrm{T}}(\boldsymbol{r})$ to calculate σ_{R}.

2.5.3 Optical Limit Approximation (OLA)

The calculation of σ_{R} is quite complicated due to the second term of function to be integrated in Eqs. (2.50) and (2.52). Although these calculations can be performed with the Monte Carlo integration [VA02], several approximations such as the optical limit approximation (OLA) and the modified optical limit approximation (MOL) are commonly utilized. In the nucleus-nucleus scattering, the cumulant expansion theorem enables us to expand the second term of the function to be integrated in Eq. (2.52) as shown below:

$$\begin{aligned}
&\left\langle \Psi_0^{\mathrm{P}} \Psi_0^{\mathrm{T}} \left| \exp\left\{ i \sum_i \sum_j \chi(\boldsymbol{b} + \boldsymbol{s}_i^{\mathrm{P}} - \boldsymbol{s}_j^{\mathrm{T}}) \right\} \right| \Psi_0^{\mathrm{P}} \Psi_0^{\mathrm{T}} \right\rangle \\
&= \left\langle \Psi_0^{\mathrm{P}} \Psi_0^{\mathrm{T}} \left| \prod_{i=1}^{A_{\mathrm{P}}} \prod_{j=1}^{A_{\mathrm{T}}} \{1 - \Gamma(\boldsymbol{b} + \boldsymbol{s}_i^{\mathrm{P}} - \boldsymbol{s}_j^{\mathrm{T}})\} \right| \Psi_0^{\mathrm{P}} \Psi_0^{\mathrm{T}} \right\rangle \\
&\simeq \exp\left(\mu_1 + \mu_2 - \frac{1}{2} \mu_1^2 \right).
\end{aligned} \tag{2.60}$$

Here, μ_1 and μ_2 are defined by

$$\begin{aligned}\mu_1 &\equiv -\left\langle \Psi_0^{\mathrm{P}}\Psi_0^{\mathrm{T}} \left| \sum_{i=1}^{A_{\mathrm{P}}}\sum_{j=1}^{A_{\mathrm{T}}} \Gamma(\boldsymbol{b}+\boldsymbol{s}^{\mathrm{P}}-\boldsymbol{s}^{\mathrm{T}}) \right| \Psi_0^{\mathrm{P}}\Psi_0^{\mathrm{T}} \right\rangle \\ &= -\iint d\boldsymbol{r}^{\mathrm{P}} d\boldsymbol{r}^{\mathrm{T}} \rho^{\mathrm{P}}(\boldsymbol{r}^{\mathrm{P}})\rho^{\mathrm{T}}(\boldsymbol{r}^{\mathrm{T}})\Gamma(\boldsymbol{b}+\boldsymbol{s}_i^{\mathrm{P}}-\boldsymbol{s}_j^{\mathrm{T}}),\end{aligned} \tag{2.61}$$

$$\mu_2 \equiv \left\langle \Psi_0^{\mathrm{P}}\Psi_0^{\mathrm{T}} \left| \sum_{i=1}^{A_{\mathrm{P}}}\sum_{j=1}^{A_{\mathrm{T}}}\sum_{k=1}^{A_{\mathrm{P}}}\sum_{l=1}^{A_{\mathrm{P}}} \Gamma(\boldsymbol{b}+\boldsymbol{s}_i^{\mathrm{P}}-\boldsymbol{s}_j^{\mathrm{T}})\Gamma(\boldsymbol{b}+\boldsymbol{s}_k^{\mathrm{P}}-\boldsymbol{s}_l^{\mathrm{T}}) \right| \Psi_0^{\mathrm{P}}\Psi_0^{\mathrm{T}} \right\rangle. \tag{2.62}$$

In the optical limit approximation (OLA), the first term of Eq. (2.60) μ_1 is only taken into account:

$$\begin{aligned}\sigma_{\mathrm{R}}^{\mathrm{OLA}} &= \int d\boldsymbol{b}\left(1-\exp\left[-2\int d^2\boldsymbol{s}^{\mathrm{P}}\rho_z^P(\boldsymbol{s}^{\mathrm{P}})\int d^2\boldsymbol{s}^{\mathrm{T}}\rho_z^{\mathrm{T}}(\boldsymbol{s}^{\mathrm{T}})\mathrm{Re}\Gamma(\boldsymbol{b}+\boldsymbol{s}^{\mathrm{P}}-\boldsymbol{s}^{\mathrm{T}})\right]\right) \\ &= \int d\boldsymbol{b}(1-T(\boldsymbol{b})),\end{aligned} \tag{2.63}$$

with

$$T(\boldsymbol{b}) \equiv \exp\left[-2\int d^2\boldsymbol{s}^{\mathrm{P}}\rho_z^P(\boldsymbol{s}^{\mathrm{P}})\int d^2\boldsymbol{s}^{\mathrm{T}}\rho_z^{\mathrm{T}}(\boldsymbol{s}^{\mathrm{T}})\mathrm{Re}\Gamma(\boldsymbol{b}+\boldsymbol{s}^{\mathrm{P}}-\boldsymbol{s}^{\mathrm{T}})\right], \tag{2.64}$$

where $T(\boldsymbol{b})$ is called a transparency function, $\rho_z^{\mathrm{P}}(\boldsymbol{s}_{\mathrm{P}})$ and $\rho_z^{\mathrm{T}}(\boldsymbol{s}_{\mathrm{T}})$ represent density distributions of projectile and target integrated on the beam direction, respectively:

$$\rho_z^{\mathrm{P,T}}(\boldsymbol{s}^{\mathrm{P,T}}) = \int dz\rho^{\mathrm{P,T}}(\boldsymbol{r}^{\mathrm{P,T}}). \tag{2.65}$$

By substituting Eq. (2.58) into with Eq. (2.63), the zero range optical limit approximation (ZROLA) can be obtained as

$$\sigma_R^{\mathrm{ZROLA}} = \int\left(1-\exp\left[-\sum_{i,j=p,n}\sigma_{ij}(E)\int d^2\boldsymbol{s}^{\mathrm{P}}\rho_{i,z}^{\mathrm{P}}(\boldsymbol{s}^{\mathrm{P}})\rho_{j,z}^{\mathrm{T}}(\boldsymbol{b}+\boldsymbol{s}^{\mathrm{P}})\right]\right)d\boldsymbol{b}. \tag{2.66}$$

2.5.4 Modified Optical Limit Approximation (MOL)

Y. Suzuki *et al.* improved the OLA calculation in order to take the multiple scattering effect into consideration [SU03]. Equation (2.61) is modified as

$$\begin{aligned}\mu_1 &= -\iint d^2\boldsymbol{s}^{\mathrm{P}} d^2\boldsymbol{s}^{\mathrm{T}} \rho^{\mathrm{P}}(\boldsymbol{s}^{\mathrm{P}})\rho^{\mathrm{T}}(\boldsymbol{s}^{\mathrm{T}})\Gamma(\boldsymbol{b}+\boldsymbol{s}_i^{\mathrm{P}}-\boldsymbol{s}_j^{\mathrm{T}}) \\ &\to -\int d^2\boldsymbol{s}^{P}\rho_z^{P}(\boldsymbol{s}^{P})\Gamma_{\mathrm{NT}}(\boldsymbol{b}+\boldsymbol{s}^{P}),\end{aligned} \tag{2.67}$$

where the profile function for nucleon-nucleus system Γ_{NT} is introduced. In analogy with Eq. (2.60), Γ_{NT} is given based on the Cumulant expansion theorem by

$$\begin{aligned}\Gamma_{\mathrm{NT}} &= 1-\langle\Psi_0^{\mathrm{T}}|\prod_{j=1}^{A_{\mathrm{T}}}\left[1-\Gamma(\boldsymbol{b}-\boldsymbol{s}_j^{\mathrm{T}})\right]|\Psi_0^{\mathrm{T}}\rangle \\ &= 1-\exp\left[-\int d^2\boldsymbol{s}^{\mathrm{T}}\rho_z^{\mathrm{T}}(\boldsymbol{s}^{\mathrm{T}})\Gamma(\boldsymbol{b}-\boldsymbol{s}^{\mathrm{T}})\right].\end{aligned} \tag{2.68}$$

Therefore, the modified optical limit approximation (MOL) calculation is written as

$$\sigma_{\mathrm{R}}^{\mathrm{MOL}} = \int d\boldsymbol{b}\left(1-\exp\left[-2\int d^2\boldsymbol{s}^{\mathrm{P}}\rho_z^{\mathrm{P}}(\boldsymbol{s}^{\mathrm{P}})\left[1-\exp\left\{-\int d^2\boldsymbol{s}^{\mathrm{T}}\rho_z^{\mathrm{T}}(\boldsymbol{s}^{\mathrm{T}})\Gamma(\boldsymbol{b}+\boldsymbol{s}^{\mathrm{P}}-\boldsymbol{s}^{\mathrm{T}})\right\}\right]\right]\right). \tag{2.69}$$

This equation should also have the symmetrical form to the replacement of projectile and target, so that Eq. (2.69) is improved as,

$$\sigma_{\mathrm{R}}^{\mathrm{SMOL}} = \int d\boldsymbol{b}\left(1-\exp\left[-\frac{A_{\text{P-T}}+A_{\text{T-P}}}{2}\right]\right), \tag{2.70}$$

with

$$A_{\text{P-T}} = \int d^2\boldsymbol{s}^{\mathrm{P}}\rho_z^{\mathrm{P}}(\boldsymbol{s}^{\mathrm{P}})\left(1-\exp\left[-\int d^2\boldsymbol{s}^{\mathrm{T}}\rho_z^{\mathrm{T}}(\boldsymbol{s}^{\mathrm{T}})\Gamma(\boldsymbol{b}+\boldsymbol{s}^{\mathrm{P}}-\boldsymbol{s}^{\mathrm{T}})\right]\right), \tag{2.71}$$

$$A_{\text{T-P}} = \int d^2\boldsymbol{s}^{\mathrm{T}}\rho_z^{\mathrm{T}}(\boldsymbol{s}^{\mathrm{T}})\left(1-\exp\left[-\int d^2\boldsymbol{s}^{\mathrm{P}}\rho_z^{\mathrm{P}}(\boldsymbol{s}^{\mathrm{P}})\Gamma(\boldsymbol{b}+\boldsymbol{s}^{\mathrm{T}}-\boldsymbol{s}^{\mathrm{P}})\right]\right). \tag{2.72}$$

2.6 Effect of Fermi Motion

In the conventional Glauber calculation, the bare nucleon-nucleon total cross section $\sigma_{\rm NN}^{\rm bare}$ has been applied as a $\sigma_{\rm NN}$. Meanwhile, nucleons are moving intrinsically in the nucleus due to the uncertainty principle. The momentum of this Fermi motion is negligibly small in the high energy collision, so that we can ignore this intrinsic effect. Thus, the conventional Glauber calculation works fairly well above $E = 300$ MeV/nucleon, which is consistent with the validity of assumption for the eikonal approximation.

M. Takechi *et al.* developed the Glauber calculation which is applicable in the wide energy region by introducing the Fermi motion effect explicitly in $\sigma_{\rm NN}^{\rm bare}$ [TA05].

Momentum distributions of intrinsic nucleon are given by

$$P_{\rm P}(\Delta p_{\rm P}) = A \exp\left(-\frac{{\Delta p_{\rm P}}^2}{2\langle {p_{\rm P}}^2\rangle}\right), \tag{2.73}$$

$$P_{\rm T}(\Delta p_{\rm T}) = A \exp\left(-\frac{{\Delta p_{\rm T}}^2}{2\langle {p_{\rm T}}^2\rangle}\right), \tag{2.74}$$

where subscripts "P" and "T" represent projectile and target, respectively. The width of momentum distribution $\sqrt{\langle p^2\rangle}$ has been determined as 90 MeV/c for stable nuclei [GO74]. The momentum distribution of relative momentum $p_{\rm nucleon}$ is obtained by the Galilean transformation as

$$P(p_{\rm nucleon}) = \frac{1}{\sqrt{2\pi\langle p^2\rangle}} \exp\left[-\frac{\left(p_{\rm nucleon} - \sqrt{E_{\rm proj}(E_{\rm proj}+2m_0c^2)}\right)^2}{2\langle p^2\rangle}\right] \tag{2.75}$$

with

$$p_{\rm nucleon} = p_{\rm proj} + \Delta p_{\rm P} - \Delta p_{\rm T}, \tag{2.76}$$

$$\langle p^2\rangle = \langle {p_{\rm P}}^2\rangle + \langle {p_{\rm T}}^2\rangle, \tag{2.77}$$

where $E_{\rm proj}$ is a beam energy. Therefore, the effective momentum distribution taking the Fermi motion into account can be derived by folding $\sigma_{\rm NN}^{\rm bare}$ with the relative momentum distribution:

$$\sigma_{\rm NN}^{\rm eff} = \int_{-\infty}^{\infty} dp_{\rm nucleon} \sigma_{NN}^{\rm bare}(E_{\rm nucleon}) P(p_{\rm nucleon}). \tag{2.78}$$

Figure 2-6 shows $\sigma_{\rm NN}^{\rm eff}$ and $\sigma_{\rm NN}^{\rm bare}$ as a function of beam energy. The Fermi motion effect increases the $\sigma_{\rm NN}$ especially below $E = 200$ MeV/nucleon. This modification together with MOL calculation enables us to explain completely

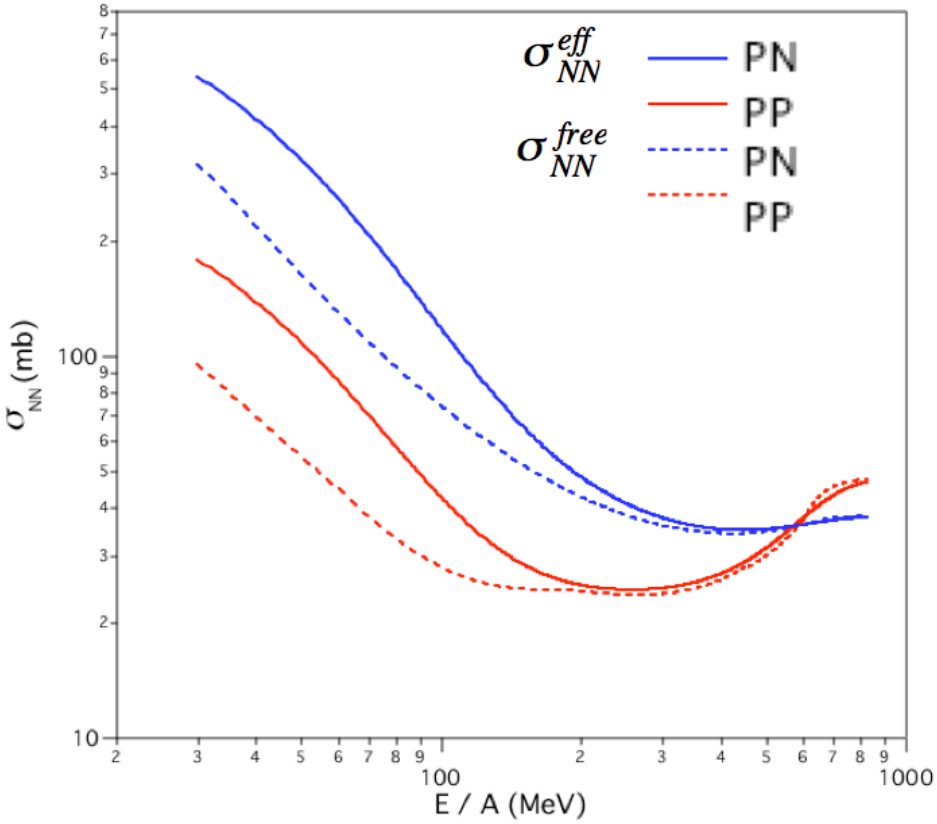

Figure 2-6: Nucleon-nucleon total cross section as a function of beam energy with and without the Fermi motion effect [TA05]. This figure is taken from Ref. [TA05].

the energy dependence of σ_R not only for ^{12}C on ^{9}Be, ^{12}C, and ^{27}Al targets system but also for such a system with an unstable nucleus as ^{11}Be and ^{8}B on ^{9}Be, ^{12}C, and ^{27}Al targets in the wide energy range between a few tens MeV and about 1 GeV [TA05].

2.7 Effects of Electromagnetic Interaction

The Glauber calculation describes only nuclear scattering processes, while the experimental $\sigma_{\rm R}$ results not only from nuclear interaction but also from electromagnetic interaction. Therefore, we take electromagnetic interaction effects into consideration in addition to the Glauber calculation from the following points of view.

Coulomb Deflection

The Coulomb repulsion interacting between projectile and target nuclei make the trajectory of projectile nucleus deflect as illustrated in Fig. 2-7. From the angular momentum and energy conservation laws, the following equations are obtained:

$$vb = v'b', \tag{2.79}$$

$$\frac{1}{2}\mu v^2 = \frac{1}{2}\mu v'^2 + E_{\rm B}, \tag{2.80}$$

where μ is a reduced mass, v and v' respective velocities before and after the interaction, and $E_{\rm B}$ a Coulomb barrier, respectively. The $E_{\rm B}$ is obtained from the Coulomb's law as follows:

$$E_{\rm B} = \frac{e^2}{4\pi\varepsilon}\frac{Z^{\rm P}Z^{\rm T}}{R_{\rm P}+R_{\rm T}} = \alpha\hbar c\frac{Z^{\rm P}Z^{\rm T}}{\sqrt{\sigma_{\rm R}^{\rm uncorr}/\pi}} \simeq 1.44\frac{Z^{\rm P}Z^{\rm T}}{\sqrt{\sigma_{\rm R}^{\rm uncorr}[{\rm fm}^2]/\pi}}, \tag{2.81}$$

where $\sigma_{\rm R}^{\rm uncorr}$ is a reaction cross section without deflection correction. If we assume that the reduction of $\sigma_{\rm R}$ depends on the ratio of impact parameter b/b', the correction factor $c_{\rm defl}(E)$ can be derived with $E_{\rm CM} \equiv \mu v^2/2$ as

$$\begin{aligned} c(E) &= \left(\frac{b}{b'}\right)^2 = 1 - \frac{E_{\rm B}}{E_{\rm CM}}, \\ \sigma_{\rm R}^{\rm cor}(E) &= c_{\rm defl}(E)\sigma_{\rm R}^{\rm uncorr}(E). \end{aligned} \tag{2.82}$$

Therefore, the Coulomb deflection effect reduces $\sigma_{\rm R}^{\rm uncorr}$. Fig. 2-8 shows $c(E)$ for ${}^{A}{\rm X} + {}^{12}{\rm C}$ system as a function of projectile mass number. In the present study, the projectile mass number is in $A \sim 40$ region and its bombarding energy is about 280 MeV/nucleon, which results in a slight reduction (approximately 1.1%) of $\sigma_{\rm R}$.

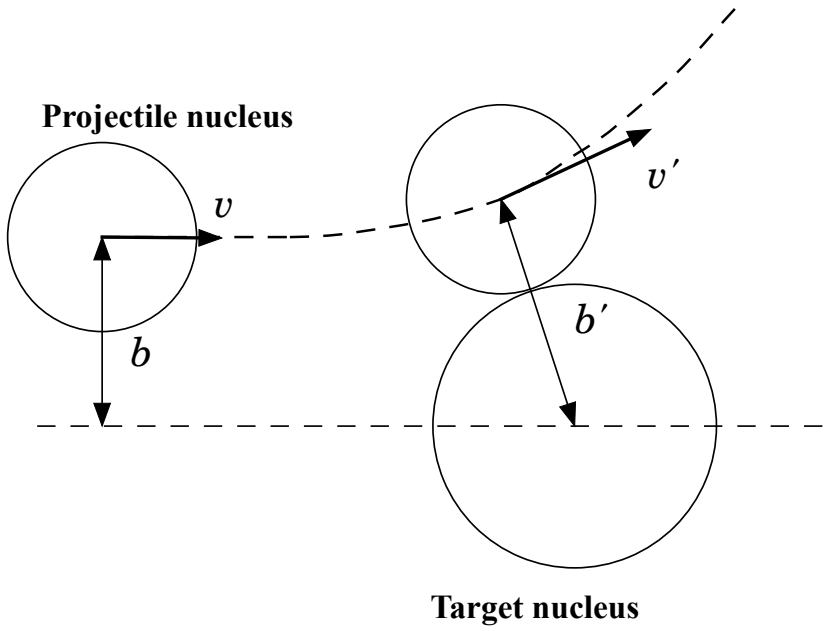

Figure 2-7: Schematic view of the deflection effect.

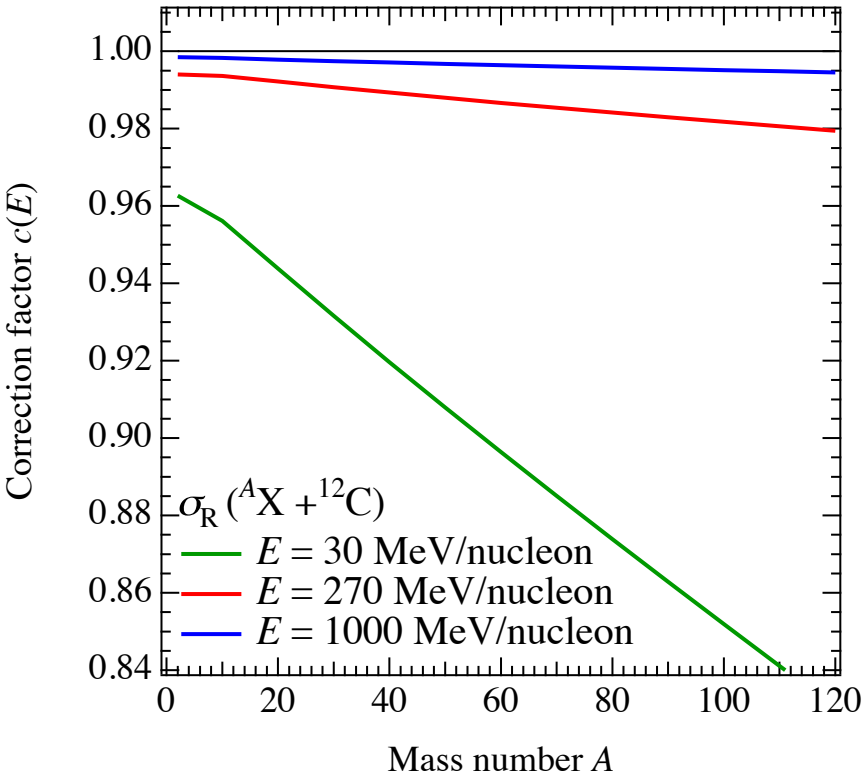

Figure 2-8: Correction factor $c_{\mathrm{defl}}(E)$ as a function of projectile mass number A.

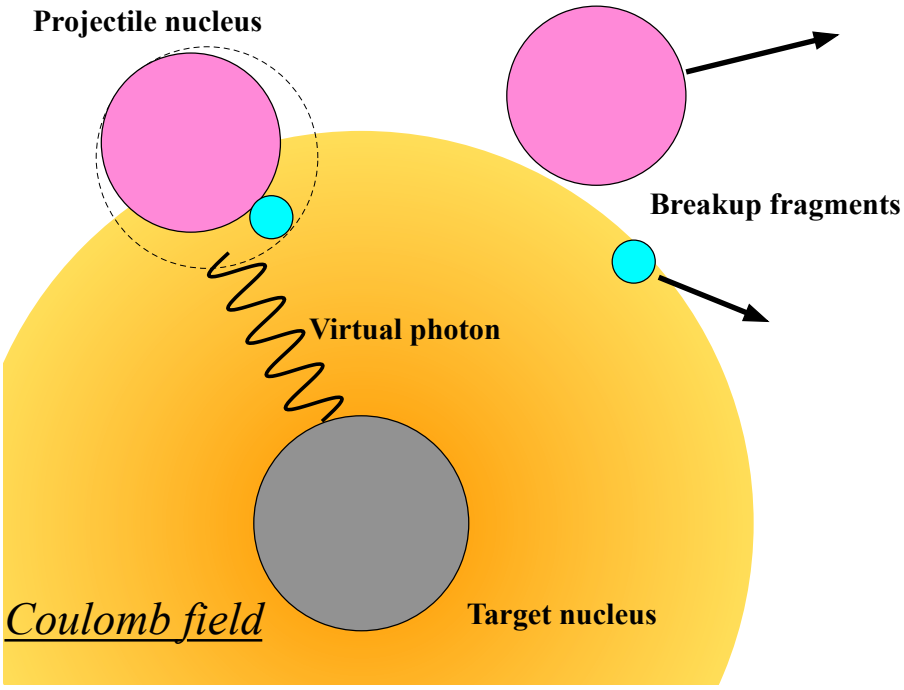

Figure 2-9: Schematic view of electromagnetic dissociation.

Electromagnetic Dissociation

The electromagnetic dissociation (EMD) also contributes to σ_{R}. The EMD occurs when the projectile nucleus absorbs virtual photons emitted from the electromagnetic field of target nucleus, that is, this contribution is large when a heavy target is employed. The EMD cross section σ_{EMD} depends on the photodissociation cross section $\sigma_\gamma(E_\gamma)$ by a photon with its energy E_γ and the virtual photon spectrum $N_\gamma(E_\gamma)$:

$$\sigma_{\mathrm{EMD}} = \int_0^\infty dE_\gamma N_\gamma(E_\gamma)\sigma_\gamma(E_\gamma). \tag{2.83}$$

The virtual photon spectrum $N_\gamma(E_\gamma)$ strongly depends on the target atomic number and the incident beam energy.

In general, the main contribution to the photodissociation process is an E1 transition because it is the lowest multiplicity in the electric interaction. The other component is much smaller than the E1 process, so that we consider only the E1 transition. The $\sigma_\gamma(E_\gamma)$ of $\mathrm{A}(\gamma, n)\mathrm{B}$ process can be derived from that of its inverse direct radiative capture reaction $\mathrm{B}(n, \gamma)\mathrm{A}$ under the law of time reversal invariance. Respective cross sections are connected through

the detailed balance theorem [BA86].

$$\sigma_{\mathrm{A}(\gamma,n)\mathrm{B}} = \frac{(2I_{\mathrm{B}}+1)(2I_n+1)}{2(2I_{\mathrm{A}}+1)}\frac{k_n^2}{k_\gamma^2}\sigma_{\mathrm{B}(n,\gamma)\mathrm{A}}, \tag{2.84}$$

where I_{A} is the spin of nucleus A, I_{B} that of nucleus B, I_n that of neutron, k_n the relative wave number of neutron, and k_γ that of emitted photon, respectively. The cross section of $\mathrm{B}(n,\gamma)\mathrm{A}$ process $\sigma_{\mathrm{B}(n,\gamma)\mathrm{A}}$ is obtained by

$$\sigma_{\mathrm{B}(n,\gamma)\mathrm{A}} = 0.0716\mu^{3/2}\left(1-\frac{Z_{\mathrm{B}}}{Z_{\mathrm{A}}}\right)^2\frac{E_\gamma^3}{E_n^3}\frac{(2I_{\mathrm{A}}+1)(2I_i+1)}{(2I_{\mathrm{B}}+1)(2I_f+1)}(l_i010|l_f0)^2R^2_{l_i1l_f}, \tag{2.85}$$

μ	reduced mass of the B+n system,
A_{B}	mass number of the nucleus B,
Z_{B}	atomic number of the nucleus B,
E_p	kinetic energy of neutron in center of mass system,
E_γ	kinetic energy of emitted photon in center of mass system,
l_i, l_f	orbital angular momenta of the initial and final state,
$(l_i010\|l_f0)$	Clebsch-Gordan coefficient for E1 transition,
$R_{l_i1l_f}$	radial matrix element for E1 operator.

From Eqs. (2.84) and (2.85), we calculated σ_γ for one-neutron emission process. The $N_\gamma(E_\gamma)$ was calculated with the point-charge approximation based on the Weizacker and William's method [BA86].

In the case of ^{43}Ca on ^{12}C at 270 MeV/nucleon, the EMD cross section for one-neutron emission E1 process is estimated as approximately 0.1 mb, which corresponds to only 8×10^{-3} % compared to σ_{I}. The transition of EMD for multi-nucleon emission process is also expected to be negligible. Therefore, we did not consider the EMD contribution.

3 Experiment

3.1 Transmission Method

Interaction cross sections σ_I were measured by the transmission method. This method is a more direct method compared to another experimental method such as the one using measurement of γ-rays emitted as a consequence of the reaction [SA89]. This is because particles are detected and identified directly with less ambiguity in the transmission method.

In the transmission method, a cross section is derived from the attenuation of the number of incident particles on a target whose thickness is known. Particle detectors are installed before and after the target as shown in Fig. 3-1. The number of incoming particles N_1 is counted by the upstream detector and that of non-reacted particles N_2 by the downstream detector, respectively. In σ_I measurements, the definition of N_2 means the number of non-nuclide-changing particles.

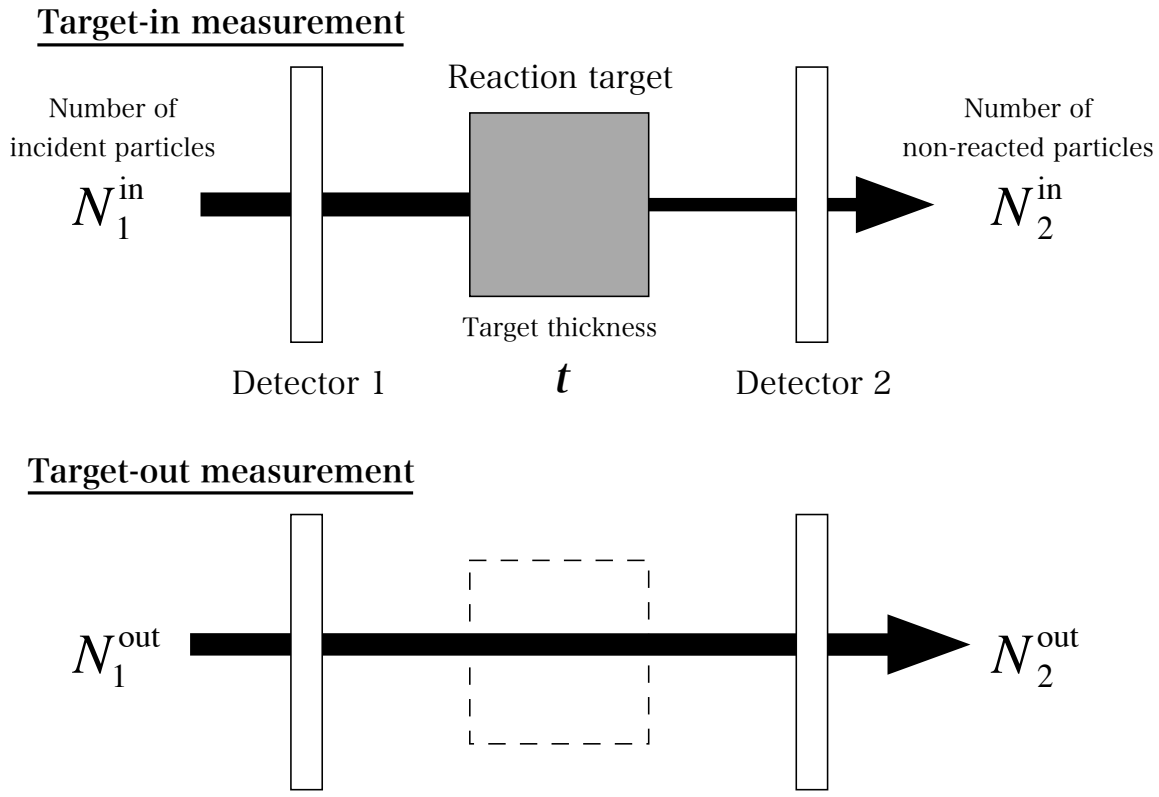

Figure 3-1: Principle of the transmission method

The attenuation of particles is described as

$$\frac{dN}{dx} = -\sigma_{\mathrm{I}} \left(\frac{\rho N_A}{A} \right) N, \tag{3.1}$$

N	: the number of non-reacted particles,
x	: length along the beam axis in the target,
ρ	: target density,
N_A	: the Avogadro number,
A	: atomic weight.

Here, $\rho N_A/A$ represents the number of target nuclei per unit area. By solving this equation, the following relation is derived:

$$\begin{aligned} N_2 &= N_1 \exp\left(-\sigma_{\mathrm{I}} t\right), \\ t &= \frac{\rho N_A}{A} x. \end{aligned} \tag{3.2}$$

Therefore, we can derive σ_{I} by the following equation:

$$\sigma_{\mathrm{I}} = -\frac{1}{t} \ln \left(\frac{N_2}{N_1} \right). \tag{3.3}$$

In fact, a non-reaction rate $R \equiv N_2/N_1$ is less than 1 even in the measurement without target since particles are also reacted in detectors. Taking this effect into account, Eq. (3.3) for the target-in and target-out measurements can be converted to

$$\sigma_{\mathrm{I}} t + \sigma_{\mathrm{I}}^{\mathrm{Det1}} t^{\mathrm{Det1}} + \sigma_{\mathrm{I}}^{\mathrm{Det2}} t^{\mathrm{Det2}} = -\ln R_{\mathrm{in}}, \tag{3.4}$$

$$\sigma_{\mathrm{I}}^{\mathrm{Det1}} t^{\mathrm{Det1}} + \left\{ (1+\alpha) \sigma_{\mathrm{I}}^{\mathrm{Det2}} \right\} t^{\mathrm{Det2}} = -\ln R_{\mathrm{out}}, \tag{3.5}$$

where $\sigma_{\mathrm{I}}^{\mathrm{Det1/2}}$ are interaction cross sections on detectors, $t^{\mathrm{Det1/2}}$ are thicknesses of detectors, and α is an enhancement factor of $\sigma_{\mathrm{I}}^{\mathrm{Det2}}$ resulting from the change of bombarding energy between target-in and target-out measurements. From Eqs. (3.4) and (3.5), the following equation is deduced:

$$\sigma_{\mathrm{I}} = -\frac{1}{t} \ln \left(\frac{R_{\mathrm{in}}}{R_{\mathrm{out}}} \right) - \alpha \frac{t^{\mathrm{Det2}}}{t} \sigma_{\mathrm{I}}^{\mathrm{Det2}}. \tag{3.6}$$

In cross section measurements, the effect of the second term on σ_{I} is generally so small that we can ignore this term. Therefore, σ_{I} can be derived as

$$\sigma_{\mathrm{I}} = -\frac{1}{t} \ln \left(\frac{R_{\mathrm{in}}}{R_{\mathrm{out}}} \right). \tag{3.7}$$

The relative error of σ_{I} can be written as

$$\left(\frac{\Delta\sigma_{\mathrm{I}}}{\sigma_{\mathrm{I}}}\right)^2 = \frac{1}{\sigma_{\mathrm{I}}^2 t^2}\left(\frac{1-R_{\mathrm{in}}}{N_1^{\mathrm{in}}R_{\mathrm{in}}} + \frac{1-R_{\mathrm{out}}}{N_1^{\mathrm{out}}R_{\mathrm{out}}}\right) + \left(\frac{\Delta t}{t}\right)^2, \tag{3.8}$$

where the following relationship is used:

$$\frac{\Delta R}{R} = \frac{\frac{\sqrt{N_1 R(1-R)}}{N_1}}{R} = \sqrt{\frac{1-R}{N_1 R}}. \tag{3.9}$$

When $(1-R)/R$ is quite small compared to 1, the relative error of R can be reduced as

$$\sqrt{\frac{1-R}{N_1 R}} \sim \sqrt{\frac{1}{N_1 - N_2}}, \tag{3.10}$$

which means $(1-R)$ approximately follows a gaussian distribution.

3.2 Experimental Facility

In the present study, experiments were performed at the RIKEN Radioactive Isotope Beam Factory (RIBF). Figure 3-2 shows a bird's eye view of the RIBF facility. At the RIBF, heavy ion beams are accelerated by an accelerator complex consisting of a linear accelerator and four ring cyclotrons. By the accelerator complex, Uranium-238 ^{238}U beams are accelerated up to 345 MeV/nucleon. Moreover, this facility supplies high intense ^{238}U beams as approximately 60 pnA. These intense ^{238}U beams enable us to produce many kinds of unstable nuclei which contain those far from the beta-stability line. Produced heavy ion beams of exotic nuclei are separated by the following superconducting isotope separator, called BigRIPS, then transported to the several unique equipments. Thus, the RIBF facility is one of the best platforms for nuclear physics experiments for exotic nuclear structures and reactions in the world. By taking advantage of this ability, 83 new isotopes have been found from 2006, the first operation of RIBF facility, to 2017 [OH08, KA09, OH10, SU13, HE13, LO15, BL16, CE16, SUM17, SUZ17].

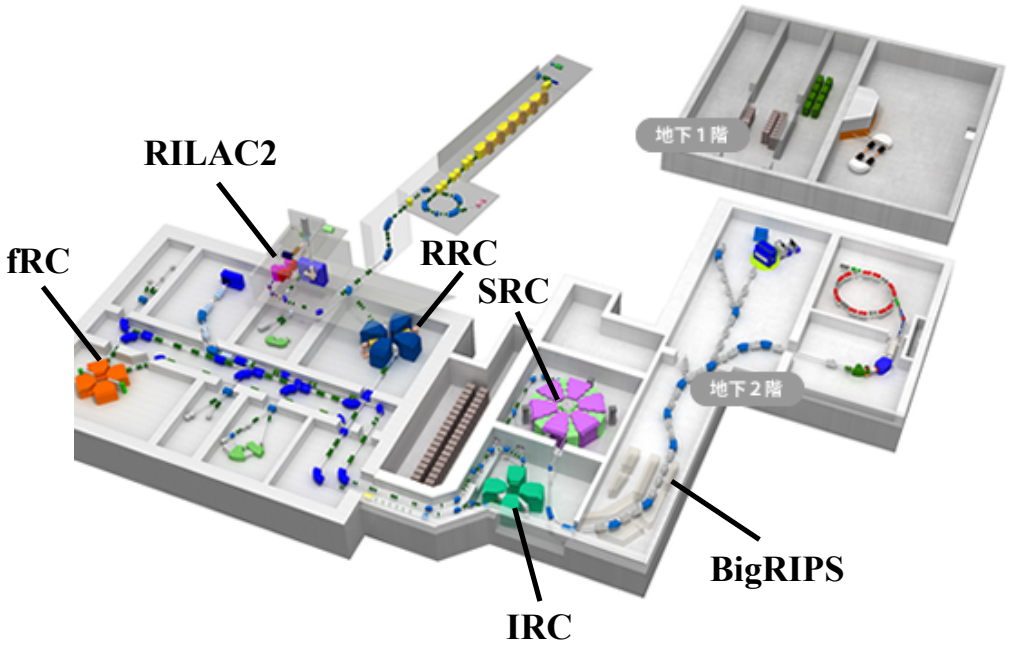

Figure 3-2: A bird's eye view of RIBF facility [BigRIPS1].

3.2.1 Accelerators

At the RIBF facility, the complex consists of following accelerators.

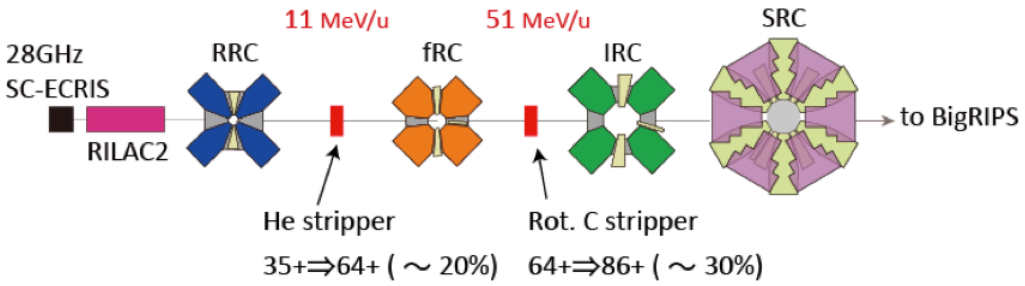

Figure 3-3: Acceleration scheme [IM16]. This figure is taken from Ref. [IM16].

RILAC2	: RIKEN Heavy Ion LINAC2
RRC	: RIKEN Ring Cyclotron
fRC	: Fixed-frequency Ring Cyclotron
IRC	: Intermediate-stage Ring Cyclotron
SRC	: Superconducting Ring Cyclotron

In the present study, ^{238}U was used as a primary beam. The ^{238}U primary beam was accelerated up to 345 MeV/u by the RILAC2, RRC, fRC, IRC, and SRC as shown in Fig. 3-3 with 18.25 MHz frequency. The specification of each accelerator is summarized in Table 3-1. A 28-GHz superconducting electron cyclotron resonance ion source was used to produce highly charged ^{238}U ions. In order to convert charge state of beams, two charge strippers were installed. A Helium gas stripper was installed as a first charge stripper between RRC and fRC. A rotating carbon-foil stripper was used as a second charge stripper between fRC and IRC. The charge state of ^{238}U is converted as $35^+ \rightarrow 64^+ \rightarrow 86^+$ with the 6% total converting efficiency [IM16].

Table 3-1: Specification of each accelerator in accelerating ^{238}U beams.

Accelerator	K value (MeV)	RF frequency (MHz)	Charge state	Energy (MeV/nucleon)
RILAC2	-	36.50	35+	0.68
RRC	540	18.25	35+	11
fRC	570	54.75	64+	50
IRC	980	36.50	86+	114
SRC	2600	36.50	86+	345

3.2.2 BigRIPS Fragment Separator

Accelerated ^{238}U beams are transported to the BigRIPS separator. The schematic drawing of BigRIPS separator is shown in Fig. 3-4. Secondary beams are produced by bombarding ^{238}U beams on a rotating Beryllium (Be) production target installed at F0 focal plane. The BigRIPS separator consists of two stages. Produced secondary beams are separated roughly between F0 and F3 focal planes. This part is called the first stage. In the second stage between F3 and F7, secondary beams are tagged according to their atomic number Z and mass-to-charge ratio A/Q in event-by-event mode. Since the BigRIPS separator has 14 superconducting quadrupole triplets (STQ), it has a large angular acceptance besides its large momentum acceptance. The specification of the BigRIPS separator is summarized in Table 3-2. We also show the ion optics of BigRIPS separator in Fig. 3-5.

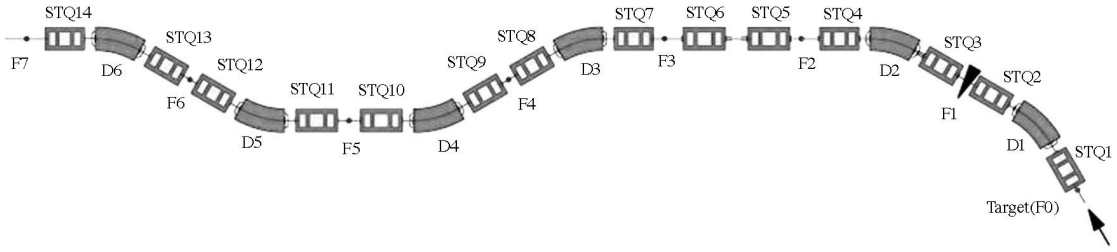

Figure 3-4: Schematic of BigRIPS [BigRIPS3].

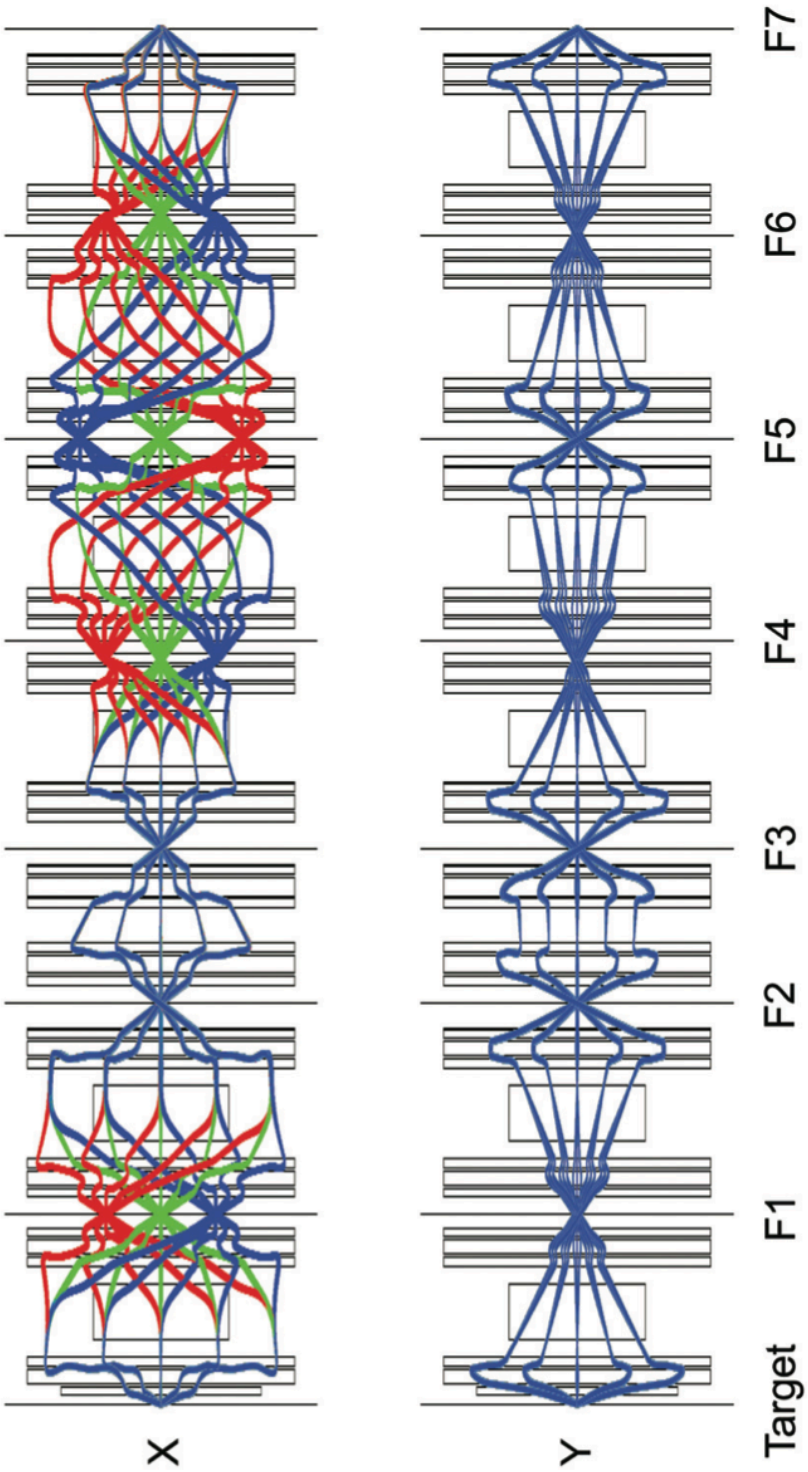

Figure 3-5: First-order ion optics of BigRIPS [KU12]. "X" and "Y" mean Horizontal and Vertical, respectively. This figure is taken from Ref. [KU12].

Table 3-2: Specification of BigRIPS separator.

	1st stage	2nd stage
Configuration	F0-STQ1-D1-STQ2-F1-STQ3-D2-STQ4-F2-STQ5-STQ6-F3	F3-STQ7-D3-STQ8-F4-STQ9-D4-STQ10-F5-STQ11-D5-STQ12-F6-STQ13-D6-STQ14-F7
Momentum acceptance	±3%	±3%
Horizontal angular acceptance	±40 mrad	±40 mrad
Vertical angular acceptance	±50 mrad	±50 mrad
Maximum rigidity	9 Tm	9 Tm
Total path length	77 m (F0 - F7)	
Momentum dispersion	−2.31 cm/%	3.3 cm/%
Momentum dispersive focal plane	F1	F4, F5, F6
Doubly Achromatic focal plane	F2, F3	F7

3.3 Production and Separation of Secondary Beams

3.3.1 Production of Secondary Beams

Generally, there are two types of production method of secondary beams. One is the Isotope Separator On-Line (ISOL) type and the other is the In-flight type. The RIBF facility is one of the In-flight facilities. Compared to the ISOL type, In-flight type can produce secondary beams not depending on their chemical properties and lifetimes. In the In-flight facility, secondary beams are produced by the projectile fragmentation (PF) or the in-flight fission (IFF) reactions.

The PF reaction mechanism is well described by the participant-spectator model shown in Fig. 3-6(a). By a peripheral collision between an incident and target nuclei, nucleons in the overlap region are abraded. The produced projectile fragment goes away with almost the same velocity β_{F} as the incident one β_{P}. The momentum distribution of fragment reflects the sum of Fermi motions of abraded nucleons in the incident nucleus. Goldhaber pointed out that the width of momentum distribution can be written as

$$\sigma = \sigma_0 \sqrt{\frac{A_{\mathrm{F}}(A_{\mathrm{P}} - A_{\mathrm{F}})}{A_{\mathrm{P}} - 1}}, \tag{3.11}$$

where $\sigma_0 = 90$ MeV/c, A_{P} is the mass number of projectile nucleus, and A_{F} is that of fragment nucleus, respectively [GO74].

On the other hand, The IFF reaction mechanism can be understood with the schematic drawing shown in Fig. 3-6(b). When a heavy projectile such as ^{238}U bombards a light-mass target, a fissile fragment is produced by the nuclear interaction. Finally, a fission fragment is produced as a result of the nuclear fission of produced fissile fragment. This process is called the abrasion-fission process, while the IFF reaction with a heavy-mass target is called the Coulomb fission reaction. In the Coulomb fission process, the incident projectile is excited by the Coulomb interaction with the target nucleus followed by a probable fission.

As an example, we estimated production cross sections of Ca isotopes with a combination of 345 MeV/u ^{238}U beam and 1 mm thick Be target by using the LISE++ [LISE] which is a simulation program for the secondary beam production in several reaction mechanisms with the fragment separator. Calculated production cross sections of Ca isotopes with the empirical cross section formula EPAX3.1a [SU12] are shown in Fig. 3-7. The PF and IFF reactions compete in the production of $^{42-51}$Ca which are ones of the mainly present research subjects. According to the calculation, nuclei located far from the beta-stability line are mainly produced by the IFF reaction, while

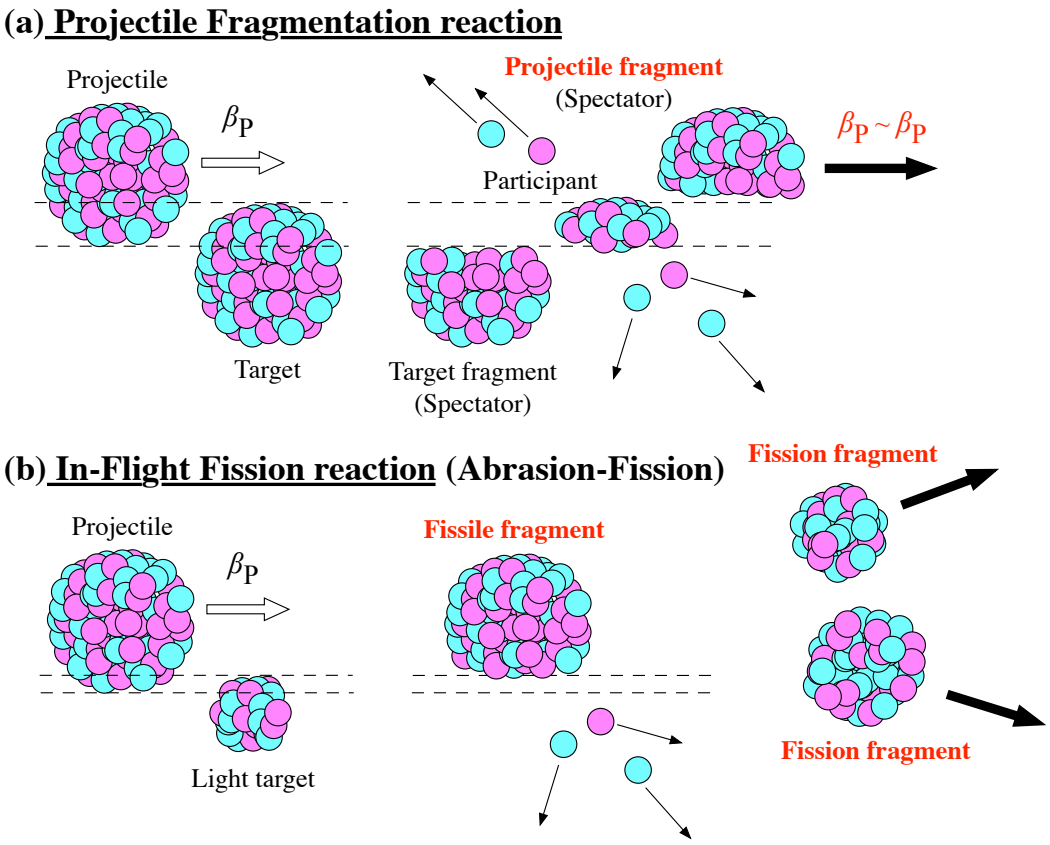

Figure 3-6: Schematic of Projectile Fragmentation reaction.

nuclei located near the beta-stability line by the PF reaction. In terms of the phase-space distributions of produced nuclei, both reactions have different properties. Figure 3-7 shows the angular and momentum distributions of ^{43}Ca in both reactions. The IFF reaction has broader distributions due to the two-body reaction with a Q value of 100-200 MeV, while fragments produced in the PF reaction has a three-dimensional Gaussian distribution in the phase space with a fairly narrow width. The BigRIPS separator can transmit even the broad beams from the IFF reaction with the large angular and momentum acceptance.

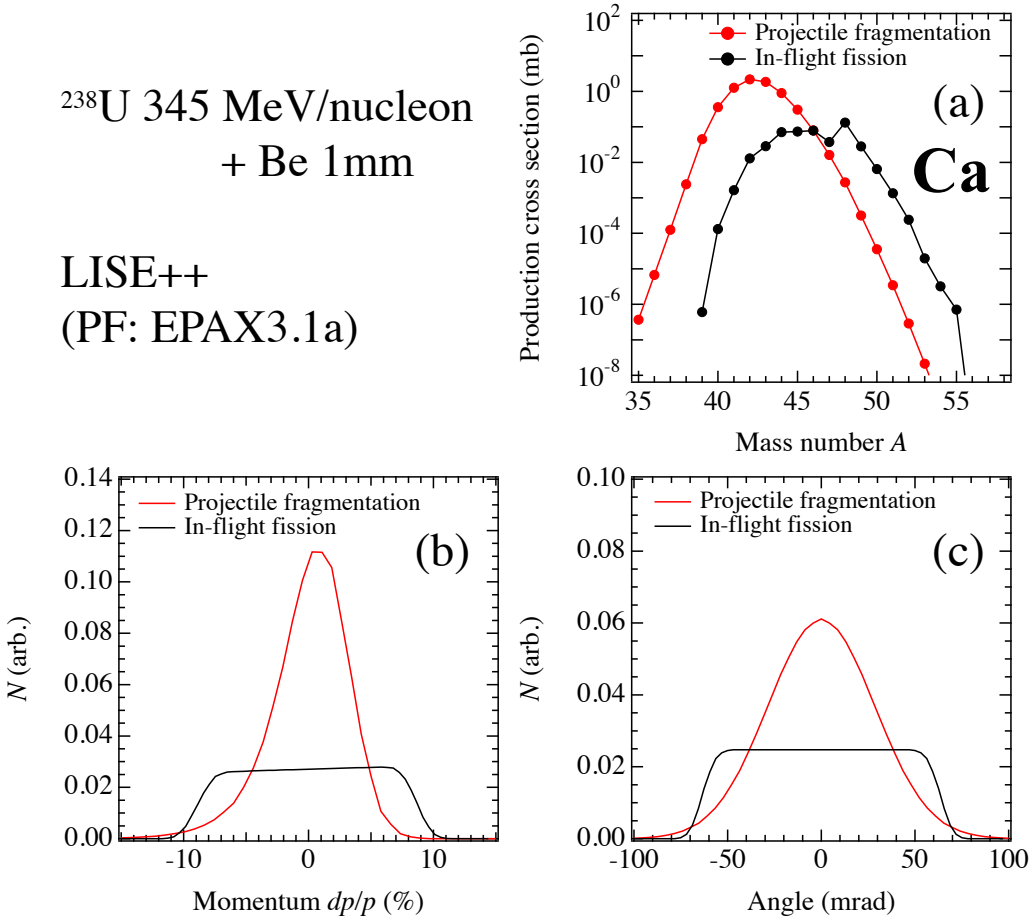

Figure 3-7: A comparison between the PF (red) and the IFF (black) reaction in ^{238}U 345 MeV/u + Be 1 mm $\rightarrow$ ^{A}Ca. (a): Production cross sections of Ca isotopes predicted from LISE++ [LISE] with the EPAX3.1a empirical cross section formula [SU12]. (b): Momentum distributions of produced ^{43}Ca. (c) angular distributions of produced ^{43}Ca.

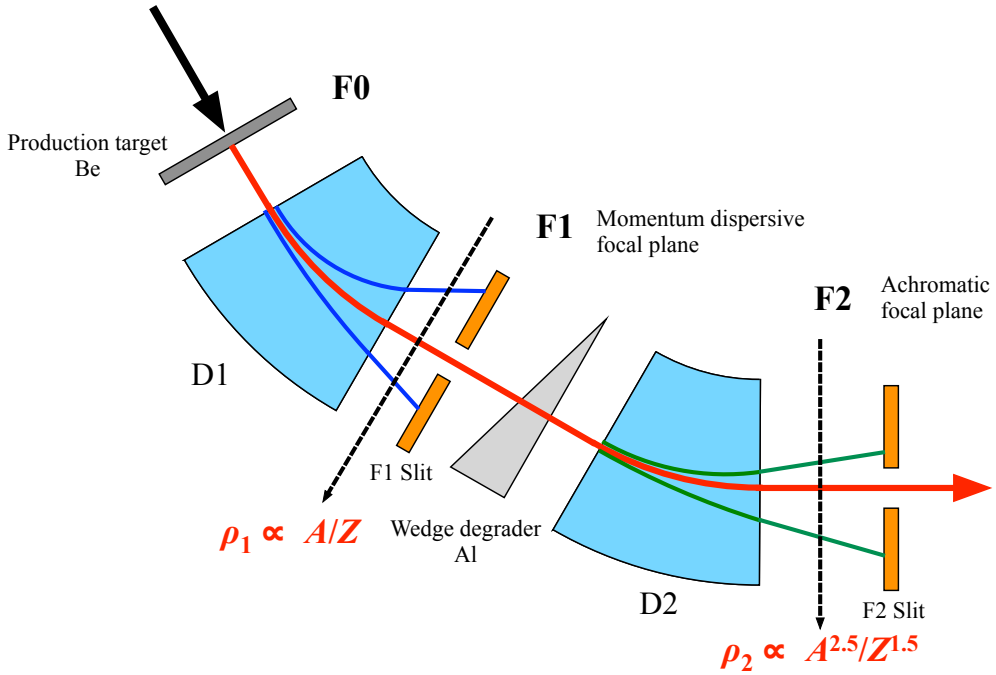

Figure 3-8: Schematic drawing of the separation of secondary beams at 1st stage of BigRIPS.

3.3.2 Separation of Secondary Beams at the 1st Stage of BigRIPS

At the first stage of BigRIPS separator, secondary beams are separated by the $B\rho$-ΔE-$B\rho$ method. Figure 3-8 shows the schematic view of the first stage of BigRIPS separator, which consists of two dipole magnets called D1 and D2, slits at F1 and F2, and a wedge-shaped energy degrader at F1.

The magnetic rigidity $B\rho$ can be expressed by the equilibrium between the Lorentz and centrifugal forces as below:

$$B\rho = \frac{u}{c}\frac{A}{Ze}\beta\gamma, \tag{3.12}$$

where u is the unified atomic mass unit which is equal to 931.494 MeV/c^2, c is the speed of light, A and Z are the mass number and atomic number of the objective nuclide, β is a relative speed compared to c, and γ is a Lorentz factor, respectively. The velocity spread of produced secondary beams is so small that the magnetic rigidity analyzed at D1 magnet is almost proportional to A/Z:

$$B\rho_1 \propto \frac{A}{Z}. \tag{3.13}$$

After analyzing $B\rho_1$, A/Z of secondary beams can be confined roughly by F1

slit. Therefore by selecting $B\rho_1$ with F1 slit, A/Z of secondary beams can be roughly analyzed. However, nuclei which have the same $(A/Z)\beta\gamma$ as the objective nuclide can contaminate by this selection only. Hence, secondary beams are further purified by the following analysis consisting of the wedge-shaped degrader and D2 magnet.

The range of charged particle R can be empirically expressed as

$$R(A, Z, E) = k\frac{A}{Z^2}E^\gamma, \tag{3.14}$$

where A is a mass number, Z an atomic number, E a kinetic energy per nucleon, and k and γ are constants, respectively. Ranges before (R_1) and after (R_2) an energy degrader whose thickness is d have the following relation:

$$R_1 = d + R_2. \tag{3.15}$$

Therefore, the energy after degrader $E_2(A, Z)$ can be expressed as

$$E_2(A, Z) = E_1(A, Z)\left(1 - \frac{d}{kE_1^\gamma}\frac{Z^2}{A}\right)^{1/\gamma}, \tag{3.16}$$

where $E_1(A, Z)$ is the energy before degrader. Since $E_1(A, Z)$ corresponds to $B\rho_1$ which is confined by Eq. (3.12), $E_1(A, Z)$ is given by

$$E_1(A, Z) \simeq \frac{1}{2}v^2 \propto \left(\frac{Z}{A}B\rho_1\right)^2. \tag{3.17}$$

Hence, the following relation between $B\rho_1$ and $B\rho_2$ can be derived as

$$B\rho_2(A, Z) \simeq B\rho_1\left\{1 - \frac{d}{k'}\frac{A^{2\gamma-1}}{Z^{2\gamma-2}}(B\rho_1)^{-2\gamma}\right\}^{1/2\gamma}. \tag{3.18}$$

In other words, $B\rho_2$ depends on $A^{2\gamma-1}/Z^{2\gamma-2}$. Therefore by selecting $B\rho_2$ with F2 slit, secondary beams can be analyzed by $A^{2\gamma-1}/Z^{2\gamma-2}$. In the present study, an aluminum (Al) wedge-shaped degrader was adopted. Taking the fact that γ is 1.75 for Al degrader into account, the $B\rho_1 - \Delta E - B\rho_2$ method can separate secondary beams depending on A/Z and $A^{2.5}/Z^{1.5}$.

When we can identify each nuclide in the following second stage in event-by-event mode, The experimental data for several nuclides can be obtained in one beam-line setting at the same time by adjusting the width of F1 and F2 slits. In the present study, we utilized such cocktail beams which contain about five nuclides with sufficient statistics. The schematic diagram of separation of secondary beams on the nuclear chart is shown with A/Z and $A^{2.5}/Z^{1.5}$ separation lines in Fig. 3-9. The red filled region in Fig. 3-9 corresponds to mixing nuclides by utilizing a cocktail beam.

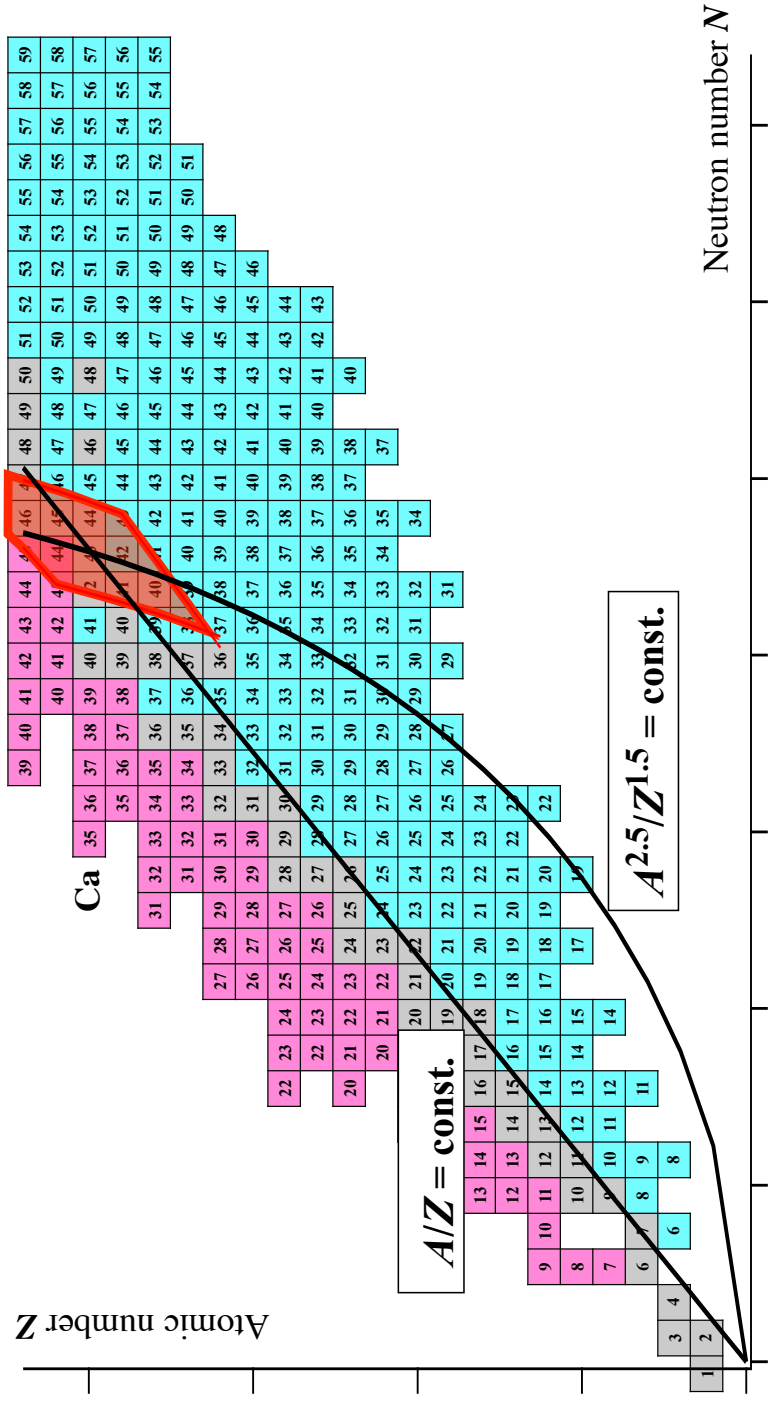

Figure 3-9: Selection lines optimized for ^{43}Ca on the nuclear chart. By adjusting the width on F1 and F2 slits, a cocktail beam which contains nuclei in the red region can be utilized.

3.4 Particle Identification at 2nd Stage of BigRIPS

After the purification of secondary beams at the first stage of BigRIPS separator, secondary beams are further identified depending on their Z and A/Q in event-by-event mode at the second stage which corresponds to the beam line between F3 and F7. Figure 3-10 shows the schematic configuration of the second stage with installed detectors and the reaction target. In the present study, the reaction target was installed at F5 which is the momentum-dispersive focal plane. Therefore, the PID was performed with detectors between F3 and F5 before the reaction target and between F5 and F7 after reaction target, respectively. The $B\rho - TOF - \Delta E$ method was adopted in both regions. Three kinds of detectors such as the Parallel Plate Avalanche Counter (PPAC), Plastic scintillation counter (PL), and Multi-Sampling ionization chamber (IC) were used in the present study. Table 3-3 shows used detectors for each PID. The information of A/Q and Z can be derived in the following way.

In order to derive $B\rho$, we measured the relative magnetic rigidity δ to that of central trajectory $B\rho_0$ defined as

$$\delta \equiv 100 \times \frac{B\rho - B\rho_0}{B\rho_0}. \tag{3.19}$$

The magnetic field of dipole magnet was measured directly with the NMR probe. With the first-order ion optical transfer matrix $\boldsymbol{M}$, δ can be derived by the following matrix equation:

$$\begin{pmatrix} X_j \\ A_j \\ \delta_{ij} \end{pmatrix} = \begin{pmatrix} M_{XX} & M_{XA} & M_{X\delta} \\ M_{AX} & M_{AA} & M_{A\delta} \\ M_{\delta X} & M_{\delta A} & M_{\delta\delta} \end{pmatrix} \begin{pmatrix} X_i \\ A_i \\ \delta_{ij} \end{pmatrix}, \tag{3.20}$$

where X and A are the position and angle on the horizontal direction, respectively. The subscripts i, j represent upstream and downstream information, respectively. From Eq. 3.20, δ_{ij} is derived as

$$\delta_{ij} = \frac{1}{M_{X\delta}} \left(X_j - M_{XX} X_i - M_{XA} A_i \right). \tag{3.21}$$

In order to determine X and A, the beam trajectory is reconstructed by position information from PPACs installed in each focal plane. We note that any PPACs were not used after the reaction target shown in Table 3-3 so as to detect particles with a 100% detection efficiency. For this reason, we determined only X by F5PL and F7PL which are position sensitive due to the readout on both sides of the horizontal direction. With ignoring the third

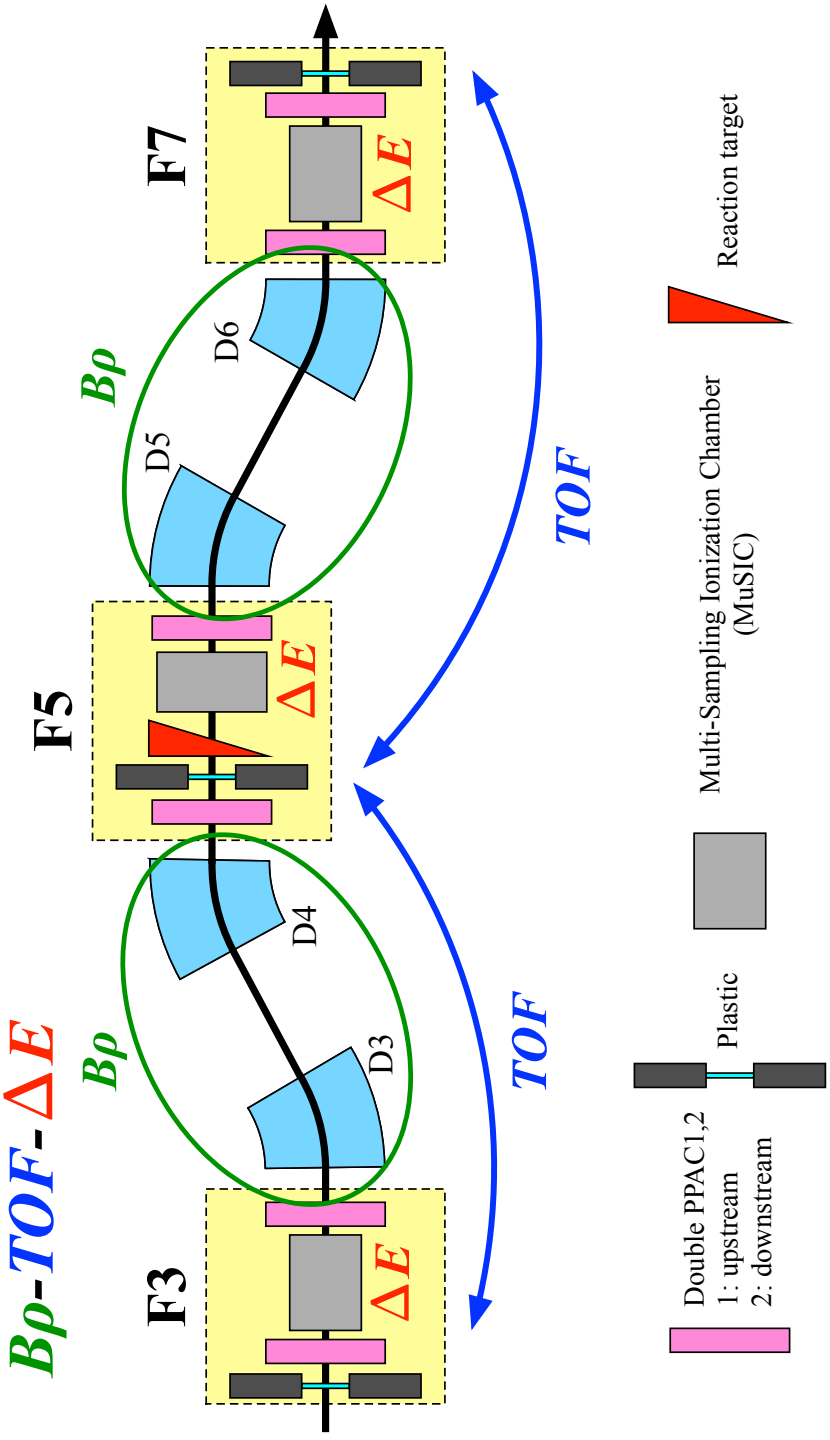

Figure 3-10: Schematic drawing of the 2nd stage of BigRIPS.

Table 3-3: Used detectors in order to reconstruct the PID information.

Physical quantity	Upstream (F3-F5)	Downstream (F5-F7)
$B\rho$	D3+D4 +F3PPAC1/2 +F5PPAC1(or F5PL)	D5+D6 +F5PPAC1(or F5PL) +F7PL
TOF	F3PL+F5PL	F5PL+F7PL
ΔE	F3IC	F5IC+F7IC

Table 3-4: First-order ion optical transfer matrix between F3 and F5 [BigRIPS4].

M_{F3F5}		X (/mm)	A (/mrad)	Y (/mm)	B (/mrad)	δ (/%)
X	(mm)	0.926591	−0.00471245	0	0	31.6690
A	(mrad)	−0.0196513	1.07932	0	0	−0.0150266
Y	(mm)	0	0	1.03406	0.0222120	0
B	(mrad)	0	0	0.291468	0.960798	0
δ	(%)	−0.0361262	1.94078	0	0	78.5482

Table 3-5: First-order ion optical transfer matrix between F5 and F7 [BigRIPS4].

M_{F5F7}		X (/mm)	A (/mrad)	Y (/mm)	B (/mrad)	δ (/%)
X	(mm)	1.08043	0.0226346	0	0	−34.1741
A	(mrad)	−0.0182343	0.925174	0	0	0.654360
Y	(mm)	0	0	0.962937	0.0269719	0
B	(mrad)	0	0	0.294048	1.03025	0
δ	(%)	−0.00476105	−1.79602	0	0	78.5442

term of Eq. (3.21) (described later), δ_{F5F7} is finally given as

$$\delta_{\mathrm{F5F7}} = \frac{1}{M_{X\delta}} \left(X_{\mathrm{F7}} - M_{XX} X_{\mathrm{F5}} \right). \tag{3.22}$$

Tables 3-4 and 3-5 show the first-order ion optical transfer matrix before and after reaction target, respectively. By using these parameters, each δ is explicitly given as

$$\delta_{\mathrm{F3F5}}[\%] = \frac{1}{31.6690}(X_{\mathrm{F5}}[\mathrm{mm}] - 0.926591 X_{\mathrm{F3}}[\mathrm{mm}] + 0.00471245 A_{\mathrm{F3}}[\mathrm{mrad}]), \tag{3.23}$$

$$\delta_{\mathrm{F5F7}}[\%] = -\frac{1}{34.1741}(X_{\mathrm{F7}}[\mathrm{mm}] - 1.08043 X_{\mathrm{F5}}[\mathrm{mm}]). \tag{3.24}$$

Considering X and A are the same order of magnitude as $\sim 10^1$, we estimate the third terms of Eq. (3.20) at 10^{-2} relative to the leading term which is small enough to be ignored. Therefore, the approximation of Eq. (3.22) do not give the fatal influence on the resolution of PID. On the other hand, since X_{F5} at the momentum-dispersive focal plane is larger than $X_{\mathrm{F3,F7}}$ at the achromatic focal plane, Eqs. (3.23) and (3.24) for non-reacting particles can be reduced to more simple expression as

$$\delta[\%] \sim \frac{X_{\mathrm{F5}}[\mathrm{mm}]}{32}. \tag{3.25}$$

The time of flight TOF is deduced as the difference of timing information between PLs installed at respective focal planes as follows,

$$TOF = T_j^{\mathrm{PL}} - T_i^{\mathrm{PL}}. \tag{3.26}$$

On the other hand, TOF is represented as

$$TOF = \frac{L}{\beta c}, \tag{3.27}$$

where L is a distance between PLs. Therefore, the velocity β is given as

$$\beta = \frac{L}{TOF \cdot c}, \tag{3.28}$$

where c is the speed of light.

The energy loss ΔE is measured by ionization chambers. The stopping power $-dE/dx$ is defined by the Bethe-Bloch formula [LE87]:

$$-\frac{dE}{dx} \simeq \frac{4\pi\alpha^2\hbar^2 c^2 N_A}{m_e c^2} \rho \frac{Z_t}{A_t} \frac{Z_p^2}{\beta^2} \left[\ln\left(\frac{2 m_e c^2 \beta^2}{I} \right) - \ln(1-\beta^2) - \beta^2 \right]. \tag{3.29}$$

Z_t	: atomic number of the target nucleus
A_t	: mass number of the target nucleus
α	: fine structure constant($\equiv 1/137$)
ρ	: target density
N_A	: Avogadro's number
m_e	: electron mass ($\equiv 0.511$ MeV/c^2)
Z_p	: atomic number of the projectile nucleus
I	: average ionization potential

When $-dE/dx$ is constant in the overall length of detector Δt, the energy loss can be expressed as $\Delta E \sim (-dE/dx)\Delta t$. In the case of $\beta \ll 1$, the energy loss depends on $\Delta E \propto Z^2/\beta^2$.

From Eqs. (3.12), (3.19), and (3.28), A/Q can be derived as

$$\begin{aligned} A/Q &= \frac{c}{u}\frac{B\rho}{\beta\gamma} \\ &= \frac{c}{u}B\rho_0\left(1+\frac{\delta}{100}\right)\frac{\sqrt{1-\beta^2}}{\beta}. \end{aligned} \tag{3.30}$$

On the other hand, the atomic number Z is given from Eq. (3.29) as

$$Z = C_1\beta\sqrt{\frac{\Delta E}{\ln\left(\frac{2m_ec^2\beta^2}{I}\right)-\ln(1-\beta^2)-\beta^2}} + C_2, \tag{3.31}$$

where C_1 and C_2 are constants. Therefore, we can derive A/Q and Z of a nuclide by the $B\rho - TOF - \Delta E$ method.

Based on Eqs. (3.30) and (3.31), A/Q and Z depend on respective measured quantities qualitatively as follows:

$$\begin{aligned} A/Q &\propto TOF \cdot B\rho, \\ Z &\propto TOF^{-1} \cdot (\Delta E)^{1/2}. \end{aligned} \tag{3.32}$$

Hence, The resolutions for A/Q and Z are approximately given as

$$\left[\frac{\delta(A/Q)}{A/Q}\right]^2 = \left[\frac{\delta(TOF)}{TOF}\right]^2 + \left[\frac{1}{2}\frac{\delta(\Delta E)}{\Delta E}\right]^2, \tag{3.33}$$

$$\left[\frac{\delta(Z)}{Z}\right]^2 = \left[\frac{\delta(TOF)}{TOF}\right]^2 + \left[\frac{\delta(B\rho)}{B\rho}\right]^2. \tag{3.34}$$

3.5 Beam Line Information

In the measurement of σ_I, all experimental data were obtained in the three kinds of beam line setting. Secondary beams were produced with the combination of 345 MeV/nucleon ^{238}U beams and several Be production targets. In Table 3-6, experimental information for respective beam line settings is summarized. Since the beam energy between F5 and F7 is different between target-in and target-out measurements due to the energy loss in the reaction target, magnetic fields of all the magnets between F5 and F7 including D5 and D6 were optimized so that non-reacted particles located almost the same position in F7 in both measurements.

Table 3-6: Beam-line parameters

Setting		#1	#2	#3
Nuclide		$^{41\text{-}43}$K $^{42\text{-}44}$Ca $^{44\text{-}46}$Sc	^{44,45}K $^{45\text{-}47}$Ca	$^{46\text{-}48}$K $^{48\text{-}51}$Ca
F0 Production target Be (mm)		1	1	10
F1 Wedge degrader Al		5 mm 5.986 mrad	6 mm 7.310 mrad	5 mm 5.986 mrad
Slit (mm)	F1	$\pm$20	$^{+21.4}_{-50.0}$	$\pm$50
	F2	$\pm$10	$\pm$10	$^{+8}_{-10}$
	F5	$\pm$110	$\pm$110	$\pm$110
$B\rho_0$ (Tm)	D1	6.3000	6.8000	7.2539
	D2	5.9571	6.3931	6.9054
	D3 & D4	5.8964	6.3344	6.8445
	[F5 target]	[In] [Out]	[In] [Out]	[In] [Out]
	D5 & D6	5.2015 5.8233	5.6525 6.2618	6.1812 6.7797

3.6 Reaction Target

We employed a wedge-shaped carbon (C) target as a reaction target. As shown in Fig. 3-11, the rectangle-shaped cross section is 310 mm (H) × 80 mm (V). The wedge angle is 9.61 mrad, which results in 8.05 mm, 9.54 mm, and 11.03 mm target thicknesses at the thinnest, central, and thickest points, respectively. The F5 focal plane where the reaction target was installed is the momentum dispersive one. When the appropriate wedge-shaped target is used, we can maintain the matching between the momentum dispersion before and after the reaction target. This means that the transmission of secondary beams to F7 is improved in comparison with using a parallel-plate target. For this reason, we employed a wedge-shaped target.

The target profile was measured by using a vernier caliper and a scale. As a result, the profile of target thickness is given by

$$t(x) = 0.00961(10)x + 8.047(20)\ [\mathrm{mm}], \tag{3.35}$$

where x [mm] is a horizontal position from the thinnest point.

The wedged-shaped target was installed on the target ladder as shown in Fig. 3-12. In addition, so as to calibrate the mount position on the ladder, we also utilized a parallel-plate C target whose thickness is well known. The profile of target thickness was measured in more detail by irradiating the beam. This procedure will be mentioned in Sec. 4.5.

Finally, we consider impurities in the natural C. The natural abundance of ^{13}C compared to ^{12}C is about 1.07%. The difference of σ_{I} for ^{12}C and ^{13}C on C target is at most a few % (σ_{I} of ^{12,13}C+^{12}C at ∼1 GeV/nucleon are 853(6) mb and 862(12) mb, respectively [OZA01]), so that the effect of the contamination of ^{13}C on σ_{I} is negligibly small as 10^{-2} %. The impurities of other elements are also sufficiently small as summarized in Table 3-7.

Table 3-7: Amounts of impurities in C target [TA05].

Element	Si	Mg	Fe
Amounts	< 5 ppm	< 1 ppm	< 1 ppm

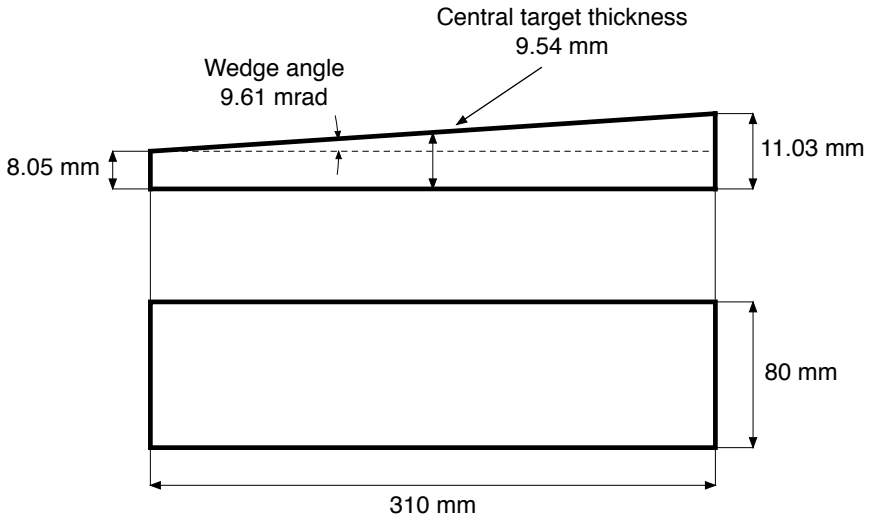

Figure 3-11: Schematic view of wedge-shaped reaction target.

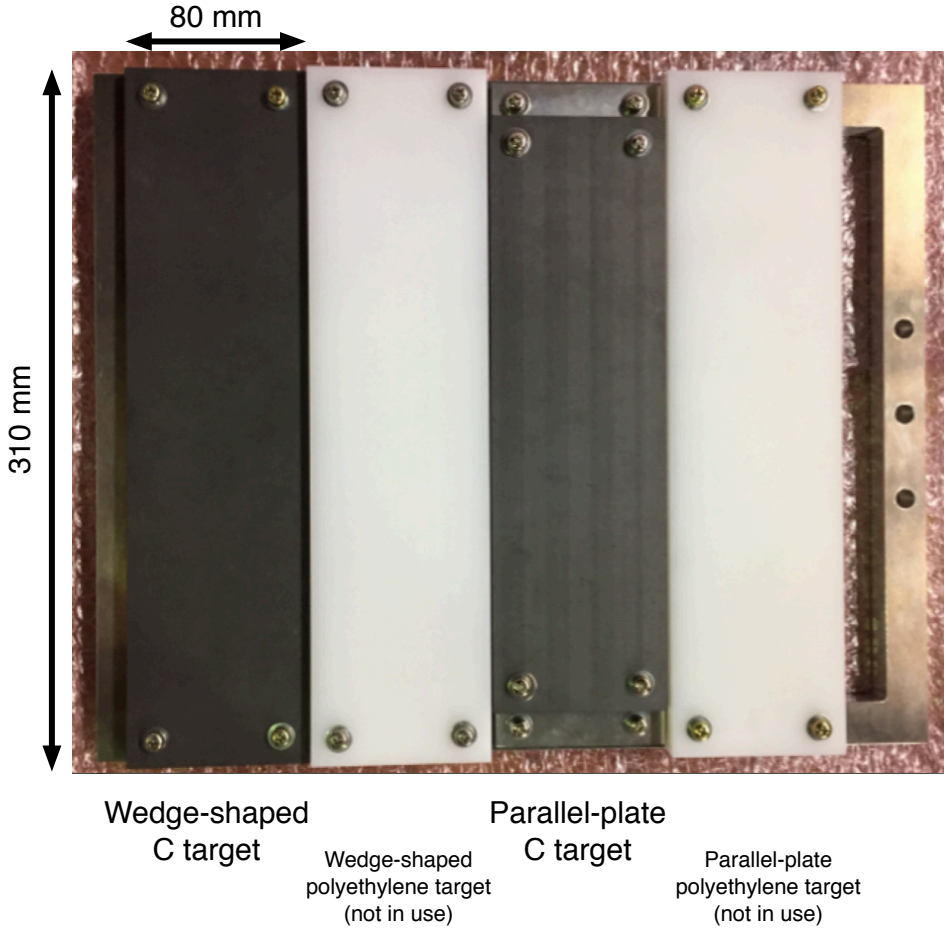

Figure 3-12: Reaction targets installed on the target ladder.

3.7 Detectors

3.7.1 Setup

Detectors were installed in vacuum chambers of F3, F5, and F7, respectively. As an example, the setup in the F5 vacuum chamber is shown in Fig. 3-13. The geometrical information for respective focal planes is also shown in Figs. 3-14, 3-15, and 3-16.

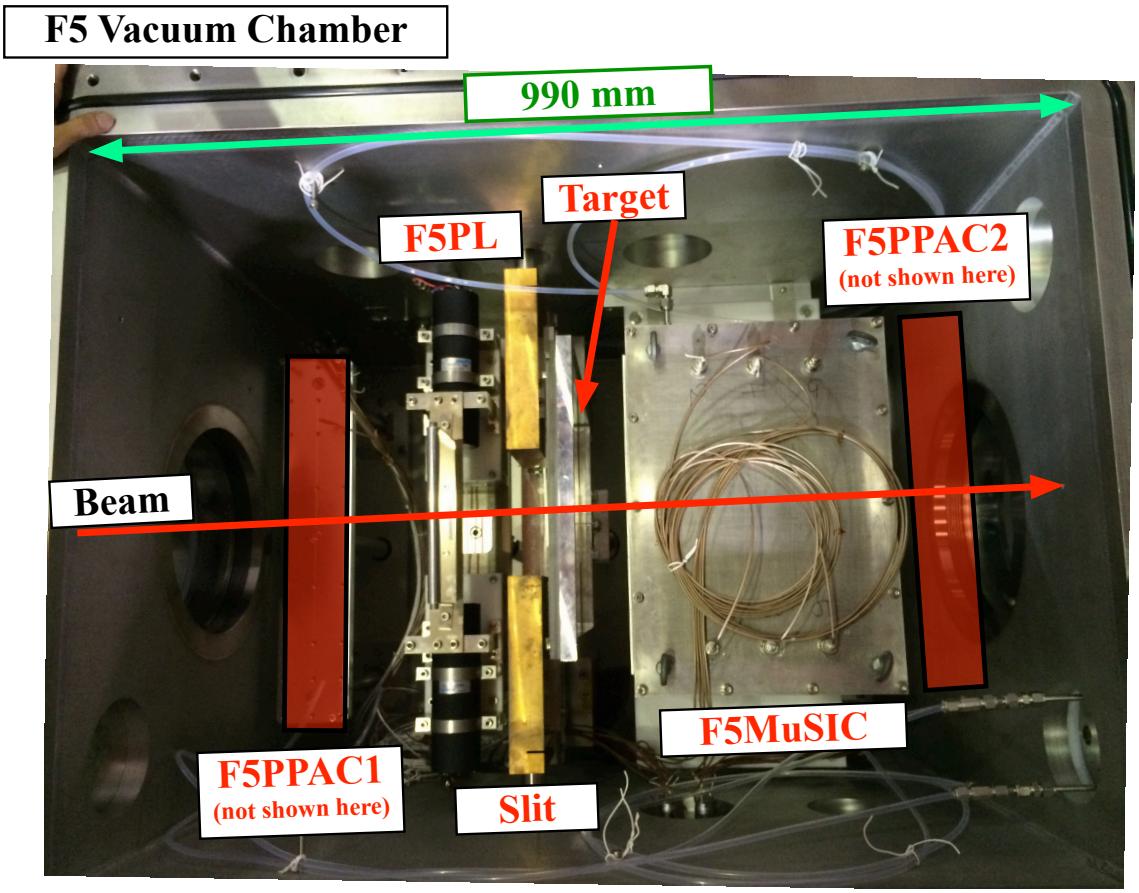

Figure 3-13: Setup in the F5 vacuum chamber.

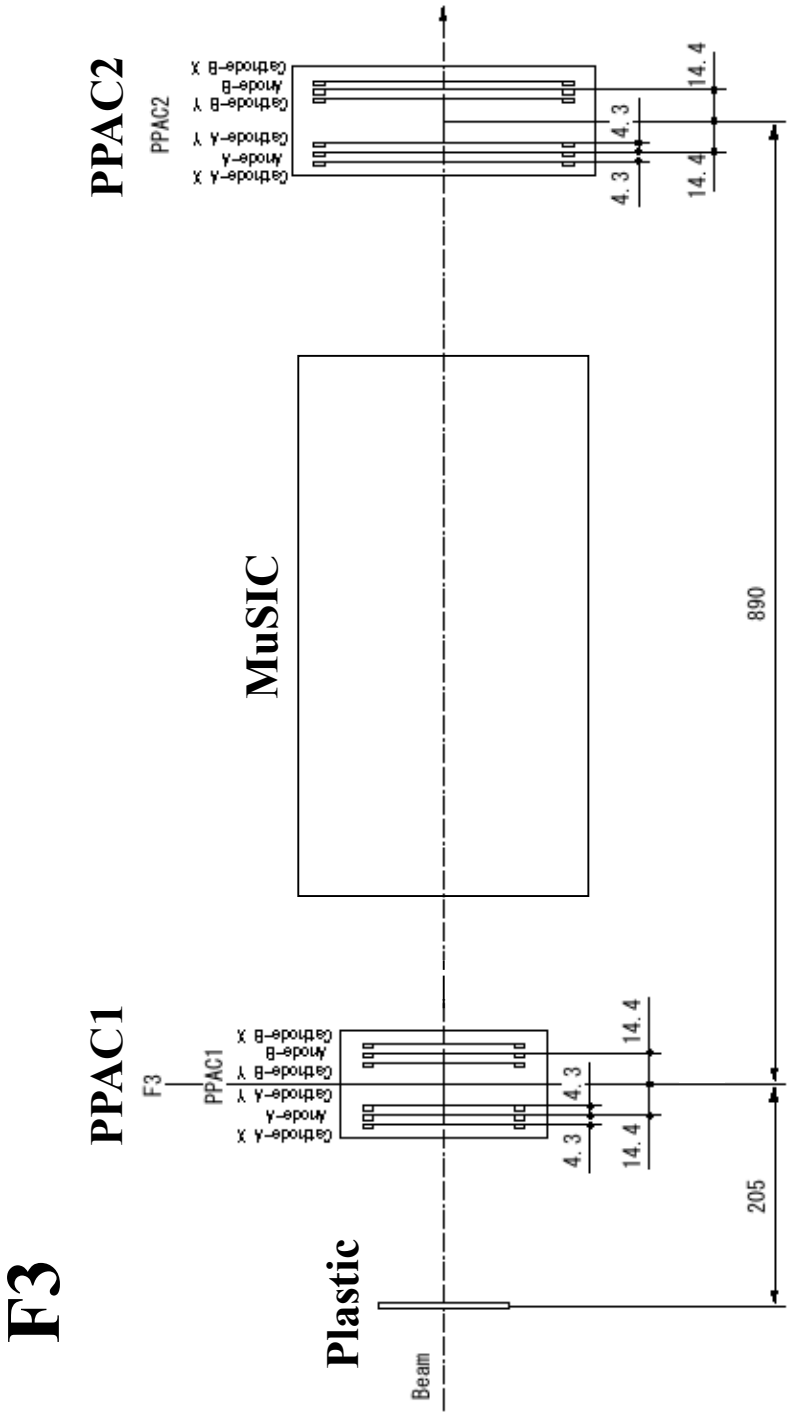

Figure 3-14: Geometrical information of detectors in the F3 vacuum chamber [BigRIPS5].

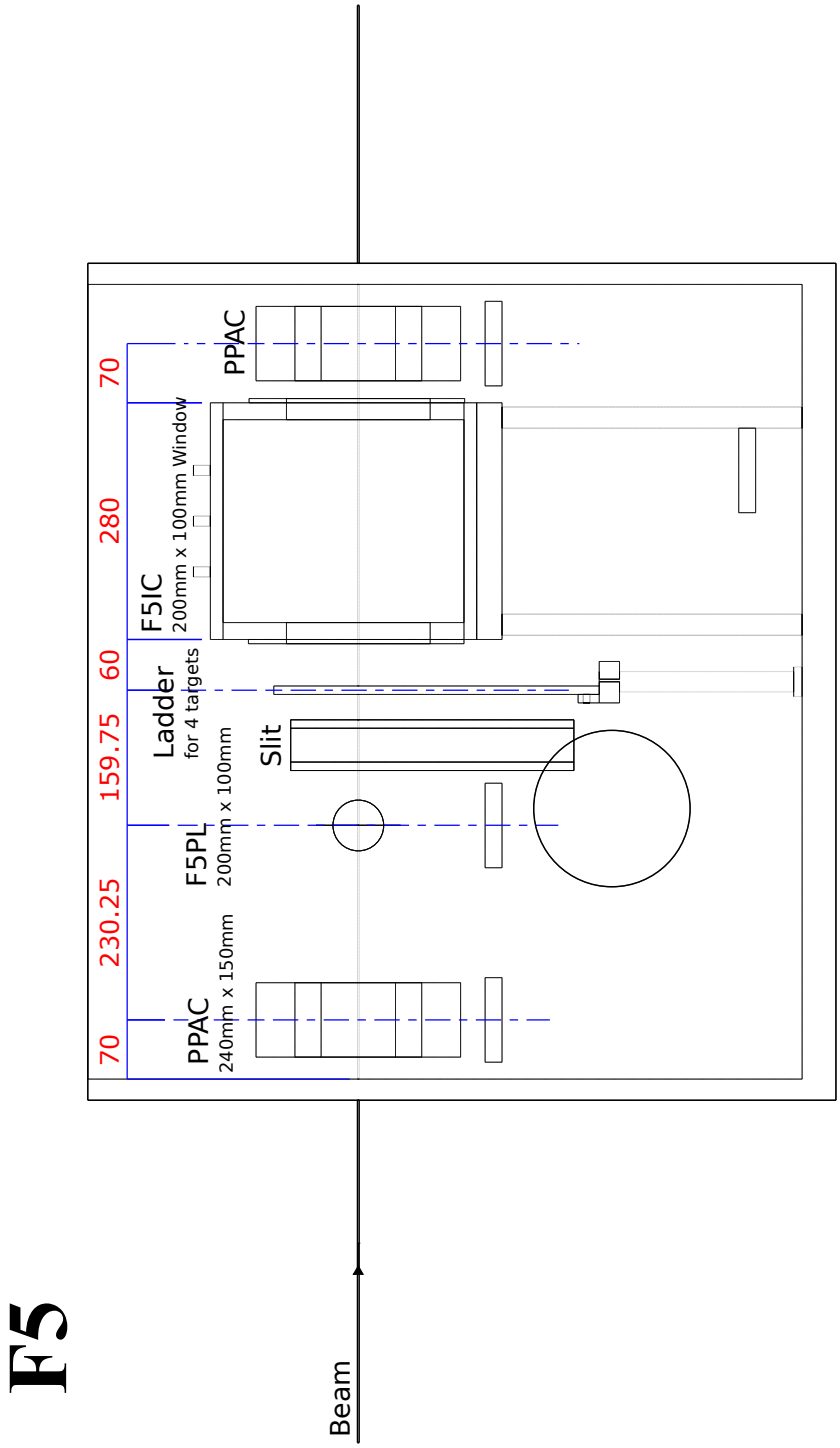

Figure 3-15: Geometrical information of detectors in the F5 vacuum chamber.

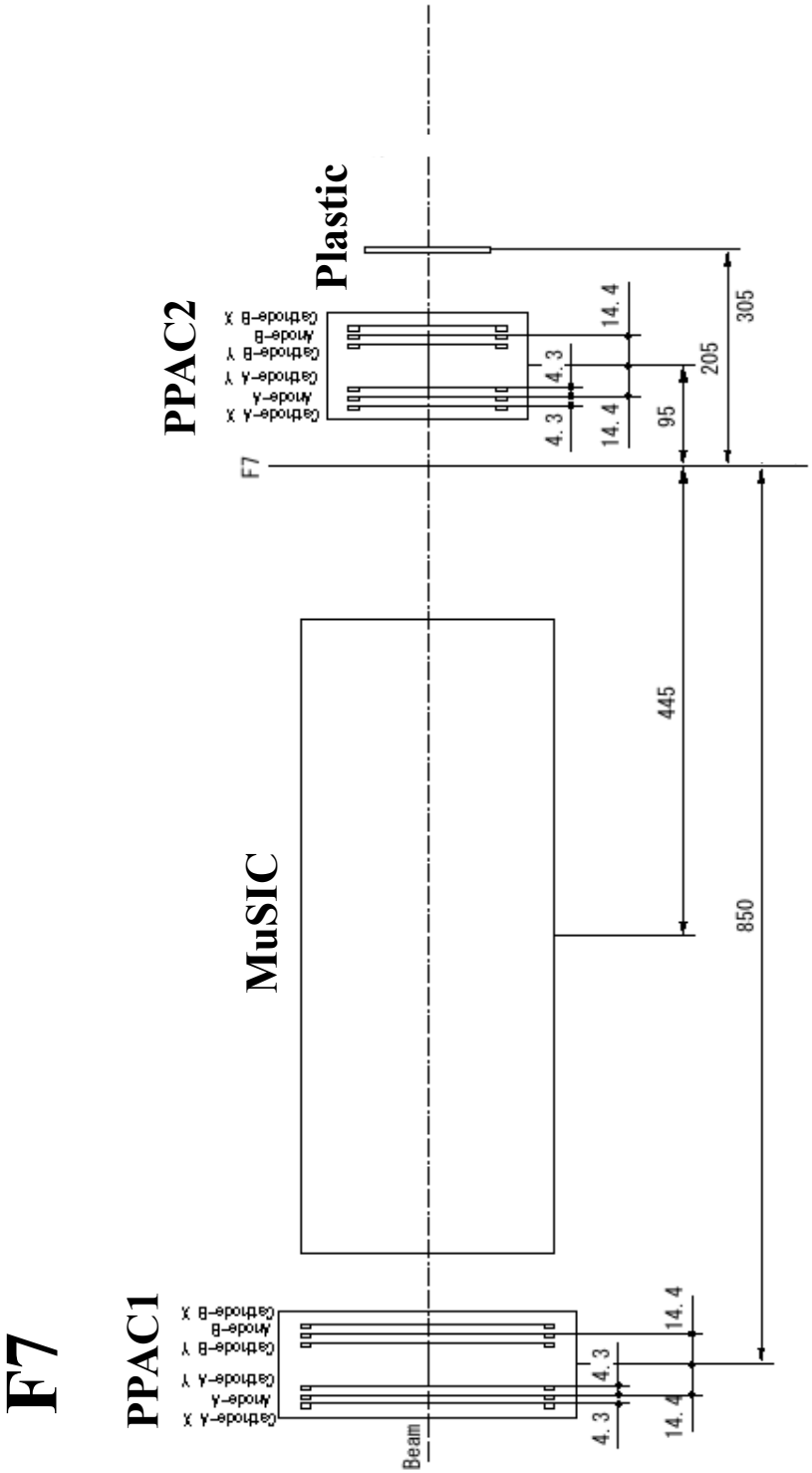

Figure 3-16: Geometrical information of detectors in the F7 vacuum chamber [BigRIPS5].

3.7.2 Plastic Scintillation Counter (PL)

Plastic scintillation counters (PL) were used in order to measure TOF. Photomultiplier tubes (PMT) were mounted on both sides of the horizontal direction with the BC-630 optical grease. The light shielding was not necessary because it was quite dark in the vacuum chamber. Since the readout was performed from both sides, we can obtain timing and energy information without depending on the beam position. In addition, the horizontal position information can be obtained from the time difference as well as the ratio of charge information obtained from both PMTs. The specifications of PMTs and scintillators are summarized in Tables 3-8 and 3-8, respectively.

Table 3-8: Specification of PMT (HAMAMATSU R2083).

R2083	
Diameter	51 mm
Photocathode material	Bialkali
Spectral response	300 to 650 nm (Peak: 420 nm)
Dynode structure	Line-focused type
Dynode stages	8
Anode to cathode voltage	< -3000 V
Gain	2.5×10^6
Rise time	0.7 ns
Transit time	16 ns
Transit time spread	0.37 ns

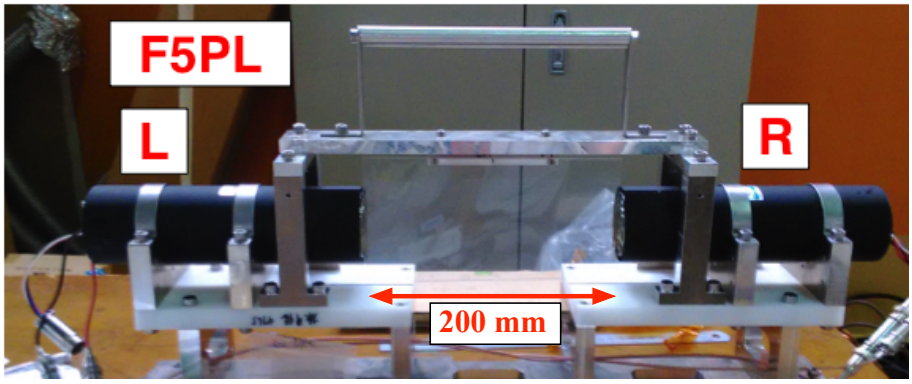

Figure 3-17: Picture of F5PL.

Table 3-9: Specification of Scintillators.

	F3PL	F5PL and F7PL
Size	100 mm (W) × 100 mm (H)	200 mm (W) × 100 mm (H)
Thickness (mm)	0.5 mm	0.5 mm
Type	EJ-230	EJ-212
Wavelength (mm)	391	423
Decay constant (ns)	1.5	2.4
Light output (% anthracene)	64	65
Attenuation length (cm)	120	250

3.7.3 Multi-Sampling Ionization Chamber (IC)

We used ionization chambers (IC) to measure ΔE for the derivation of an atomic number Z. Although a silicon (Si) detector is also one of the candidates as an energy loss detector, the analysis is complicated in terms of channeling effects [TA15]. The development of a large-size IC is not so difficult compared to a large Si detector, so that making use of IC is much better especially at F5 and F7 where the beam profile is spread. The ICs used in F5 and F7 are multi-sampling ionization chambers (MuSIC). In contrast, IC installed in F3 is a tilted electrode gas ionization chamber (TEGIC). Tilted electrodes result in different drift paths for produced electrons and ions, respectively. Consequently, the electron-ion recombination is suppressed, which contributes to the improvement of the energy resolution. The electrodes of F3IC is tilted as 30 degrees as shown in Fig. 3-18. The ICs are filled with P10 gas which consists of 90% Argon and 10% methane CH_4 and is circulated. Specifications of ICs are summarized in Table 3-10 [KA16, BigRIPS5].

Table 3-10: Specification of IC.

	F3IC	F5IC	F7IC
Effective length	480 mm	200 mm	480 mm
Sensitive area	120 mmφ	240 mm (W) $\times$150 mm (H)	240 mmφ
Number of anodes	13	5	13
Number of cathodes	12	6	12
Electrode interval	20 mm	20 mm	17 mm
Number of outputs	6	5	6
Window	Capton 125 μmt	SUS 100 μmt	Capton 125 μmt
Supplied voltage	+400 V	+400 V	+550 V

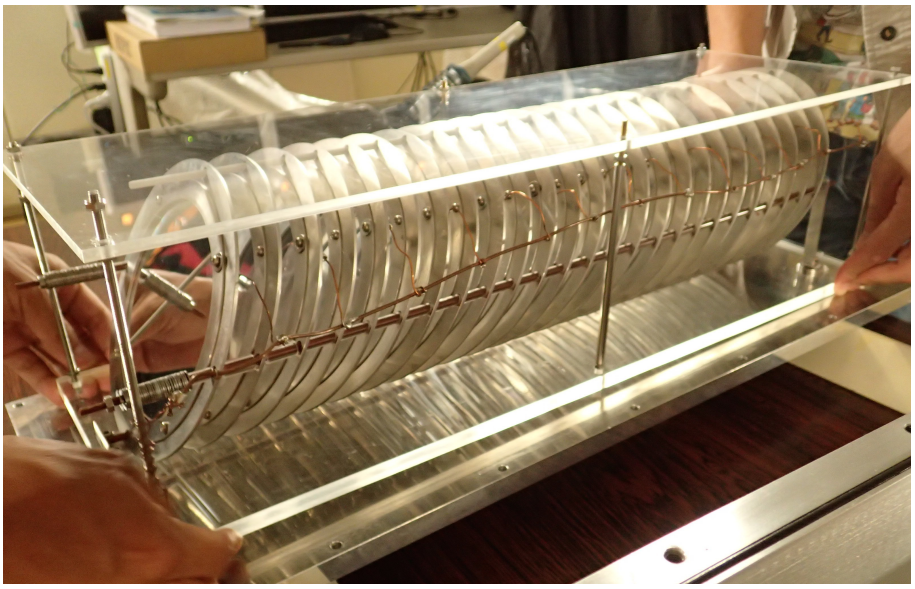

Figure 3-18: Electrode structure of F3IC (TEGIC-type IC).

Figure 3-19: Electrode structure of F5IC (MuSIC-type IC).

3.7.4 Parallel Plate Avalanche Counter (PPAC)

Two parallel plate avalanche counters (PPAC) were installed at respective focal planes in order to reconstruct the beam trajectory. In particular, the F3PPACs were also utilized in order to confine the emittance of secondary beams. Figure 3-20 shows a schematic view of PPAC [KU13]. The effective thickness of PPAC is approximately 1/10 times thinner as $\sim$ 30 mg/cm^2 than other position sensitive detectors, so that the PPAC hardly influence the transportation of RI beams.

The readout method of PPAC used in the present experiment is a delay-line type. The delay line PPAC consists of an anode electrode located between two cathode electrodes which divide into 2 mm strips along horizontal or vertical directions. The position information is obtained through the time difference between output signals from both sides of the delay line to which respective cathode strips are connected. The delay-line PPAC can be operated with high intense RI beams compared to a charge-division one. Moreover, we can remove the effects of multiple-hit events and δ rays. In order to reconstruct the beam trajectory with high detection efficiency, we used a double PPAC which has two full PPACs in a chamber of double PPAC itself. When either PPAC in a double PPAC is fired, we can obtain the position information. A perfluoropropane (C_3F_8) was adopted as a counter gas.

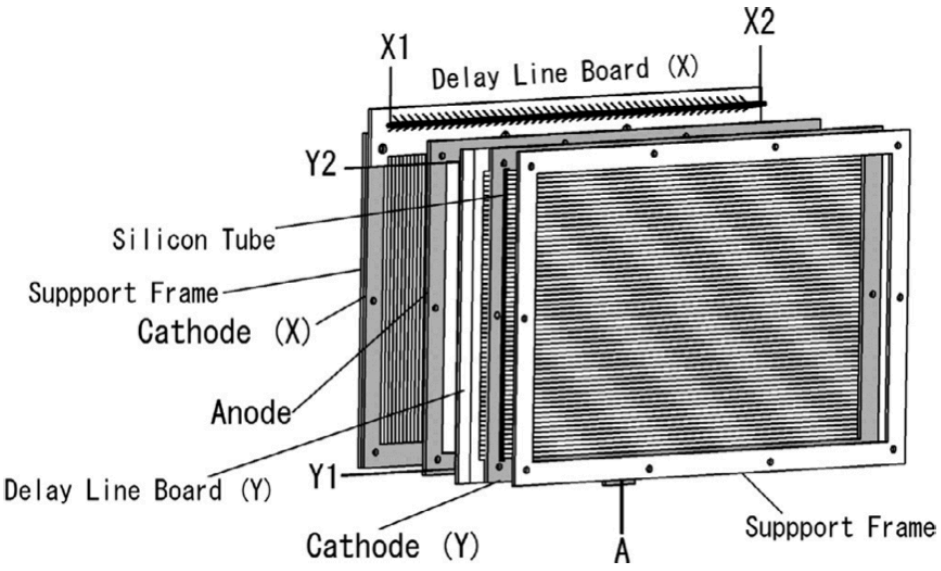

Figure 3-20: Schematic view of PPAC [KU13]. This figure is taken from Ref. [KU13].

3.8 Data Acquisition System (DAQ)

Output signals from respective detectors were processed by the NIM circuit [Circuit], then processed signals were converted to digital data by CAMAC and VME modules. The data acquisition (DAQ) was operated with the Babirl software package [RIBFDAQ]. The trigger signal is the coincidence signal between F3PL and F5PL. The coincidence timing is always determined by the output signal from left part of F3PL.

Not all events are acquired because of the dead time of DAQ. The acquired event rate n_{acq} is given by the following equation:

$$n_{\mathrm{acq}} = \frac{n_{\mathrm{beam}}}{1 + n_{\mathrm{beam}}\tau}, \tag{3.36}$$

where n_{beam} is a beam intensity and τ is a dead time per event, respectively. Figure. 3-21 shows correlations between n_{beam} and n_{acq} for respective dead times. The dead time is about 0.2 ms for the present experiment. Present experiments were performed with about 3 kcps beams in order to avoid pile-up events, which corresponds to approximately 60% DAQ efficiency.

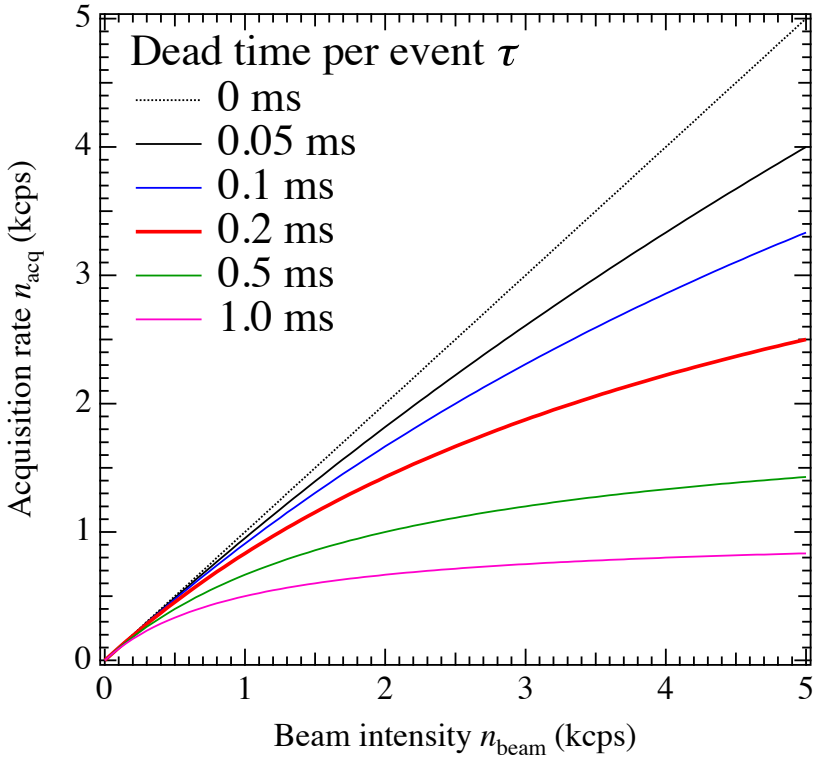

Figure 3-21: Correlation between the beam intensity n_{beam} and data acquisition rate n_{acq}.

4 Data Analysis

4.1 Analysis Before Reaction Target

For most of the Ca isotopes, the enough statistics which corresponds to the order of 10^{-3} statistical error on $\sigma_{\rm I}$ were acquired. Therefore, in the analysis before the reaction target, we aimed to achieve a relatively severe condition in terms of following points:

- Almost no contaminants ($<\sim 10^{-4}$)
- Almost no pileup events ($<\sim 10^{-4}$)

In the particle selection before reaction target, we adopted following gates.

Pileup rejection	
Gate#1	: Multiplicity = 1 or Multiplicity = 2 with $\lvert t_{\rm MHTDC}(\text{F3PL})\rvert > 14.5$ μs
Background removal	
Gate#2	: $X^Q_{\rm PL} - X^T_{\rm PL}$ of F3PL
Gate#3	: $X^Q_{\rm PL} - X^T_{\rm PL}$ of F5PL
Gate#4	: $\Delta E_{\rm F3PL}$ vs. $Z_{\rm F3IC}$
Gate#5	: $Z_{\rm F3IC}$ vs. $\Delta E_{\rm F5PL}$
Particle identification	
Gate#6	: $A/Q_{\rm F3F5}$ vs. $Z_{\rm F3IC}$
Contamination removal	
Gate#7	: $\Delta E_{\rm F3PL+F5PL}$ vs. $Z_{\rm F3IC}(A/Q_{\rm F3F5} - 2)$.

In the following subsections, we describe the above gates and conditions in detail.

4.1.1 Pileup Rejection

When incident particles contain pileup events, the result of cross section is affected directly because these events behave like other nuclides in the PID plot after reaction target. In particular, the pileup of signals from ICs are the main problem due to their own slow response. In order to discriminate pileup events, we utilized timing signals of F3PL acquired in a multi-hit time to digital Converter (MHTDC), which records timing information of plural signals per one trigger event. The MHTDC was configured to record signals within ± 20 μs relative to the trigger signal.

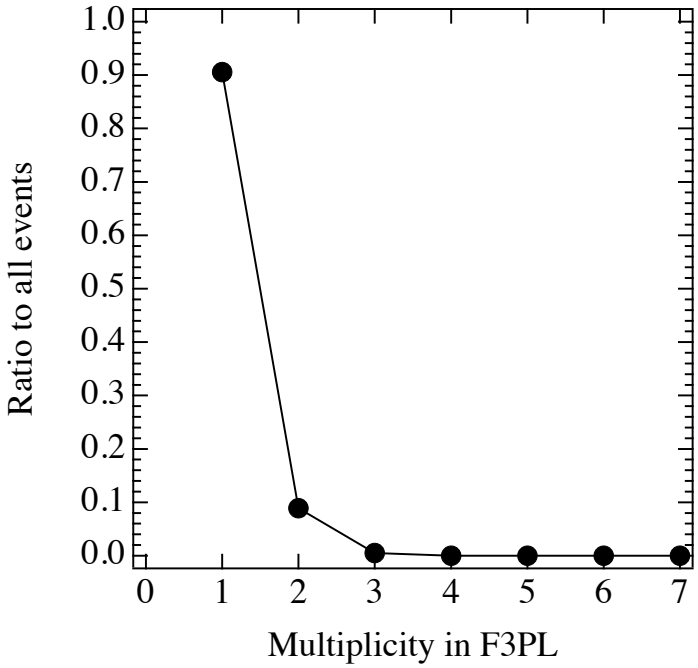

Figure 4-1: Multiplicity in F3PL.

Figure 4-1 shows the multiplicity of F3PL per one event. Single-hit events occupy the 90% of all. Then, for double-hit events (Multiplicity = 2), which corresponds to $\sim$ 10% of all events, we confirm correlations between the timing information of F3PL acquired with the MHTDC t_{MHTDC}(F3PL) and energy loss ΔE in (a) F3IC, (b) F5IC, and (c) F7IC shown in Fig. 4-2. In these figures, ΔE are plotted as functions of time t_{MTDC}(F3PL), where event corresponding to the trigger itself is located at t_{MHTDC}(F3PL) = 0 μs. The spectrum shape depends on the time constant of shaping amplifier used for ICs. Around t_{MHTDC}(F3PL) = 0, a larger ΔE which depends on t_{MHTDC}(F3PL) results from pileup of double pulses. The effect of pileup is also seen in the circle regions in Fig. 4-2.

In order to avoid these pileup events, we select events within $|t_{\mathrm{MHTDC}}(\mathrm{F3PL})| >$ 14.5 μs for Multiplicity = 2. Single-hit events (Multiplicity = 1) as shown in Fig. 4-2(d) are used without any restrictions in t_{MHTDC}(F3PL). We did not use multi-hit events more than triple particles, of which the ratio to all events is less than 0.5%.

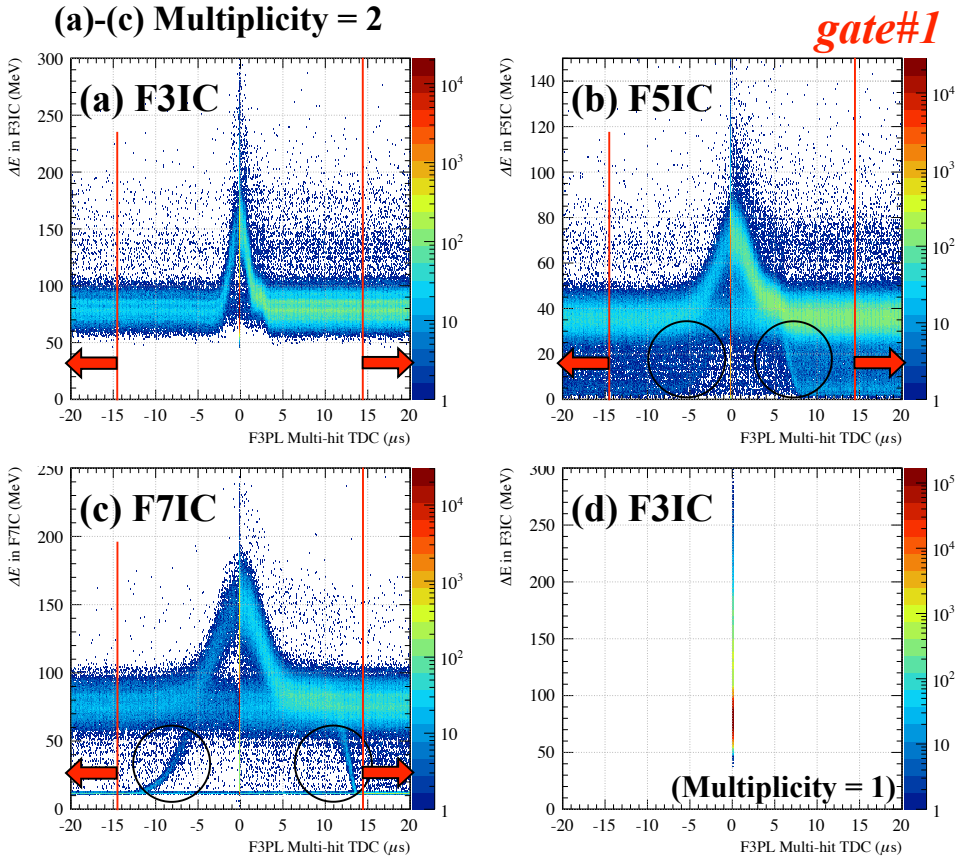

Figure 4-2: Correlations between t_{MHTDC}(F3PL) and Energy loss ΔE in (a) F3IC, (b) F5IC, and (c) F7IC, respectively. In Figs (a)-(c), events for only Multiplicity = 2 are plotted. As a comparison, correlation between t_{MHTDC}(F3PL) and Energy loss ΔE in F3IC for only Multiplicity = 1 is shown in Fig. (d). For Multiplicity = 2, The region outside red lines corresponds to non-pileup events. In the case of single-hit events (Multiplicity = 1), all events are used.

4.1.2 Background Removal

Correlation between Q and T in F3PL and F5PL

The validity of output signals for F3PL and F5PL can be distinguished from the correlation between charge and timing information. The time difference between left and right outputs of plastic scintillation counter PL $T^{\mathrm{L}}_{\mathrm{PL}} - T^{\mathrm{R}}_{\mathrm{PL}}$ enables us to derive the horizontal incident position X^{T}_{PL} as

$$X^{T}_{\mathrm{PL}} \propto \left(T^{\mathrm{L}}_{\mathrm{PL}} - T^{\mathrm{R}}_{\mathrm{PL}}\right). \tag{4.1}$$

On the other hand, emitted scintillation lights are attenuated depending on the distance between the incident horizontal position X and each PMT:

$$Q^{\mathrm{L}}_{\mathrm{PL}} \propto \exp\left(-\frac{L/2 - X}{\lambda}\right), \tag{4.2}$$

$$Q^{\mathrm{R}}_{\mathrm{PL}} \propto \exp\left(-\frac{L/2 + X}{\lambda}\right), \tag{4.3}$$

$$X^{Q}_{\mathrm{PL}} \propto \ln\left(\frac{Q^{\mathrm{L}}_{\mathrm{PL}}}{Q^{\mathrm{R}}_{\mathrm{PL}}},\right) \tag{4.4}$$

where L is a length of scintillator along the horizontal direction, λ the attenuation length, $Q^{\mathrm{L}}_{\mathrm{PL}}$ and $Q^{\mathrm{R}}_{\mathrm{PL}}$ the charge information from respective PMTs. Therefore, we can also derive the position X^{Q}_{PL} from the charge information. We selected valid outputs for F3PL and F5PL in one-dimensional $X^{Q}_{\mathrm{PL}} - X^{T}_{\mathrm{PL}}$ spectrum as shown in 4-3, which is a condition that X^{Q}_{PL} and X^{T}_{PL} are consistently in agreement with each other. Selection gates are labeled as "*gate#2*" for F3PL and "*gate#3*" for F5PL, respectively.

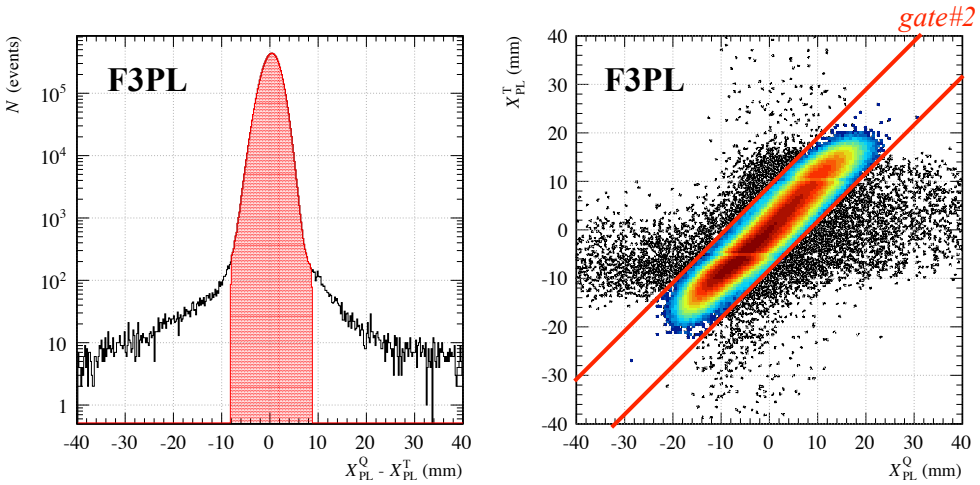

Figure 4-3: (Left): Event selection on the one-dimensional spectrum of $X^Q_{\rm PL} - X^T_{\rm PL}$ for F3PL. A black line represents a raw histogram, while the red filled region represents the selected region (*gate#2*), respectively. (Right): The two-dimensional plot of $X^Q_{\rm PL}$ and $X^T_{\rm PL}$. Black dots represent raw data, while color dots correspond to data within the red filling region in the left histogram.

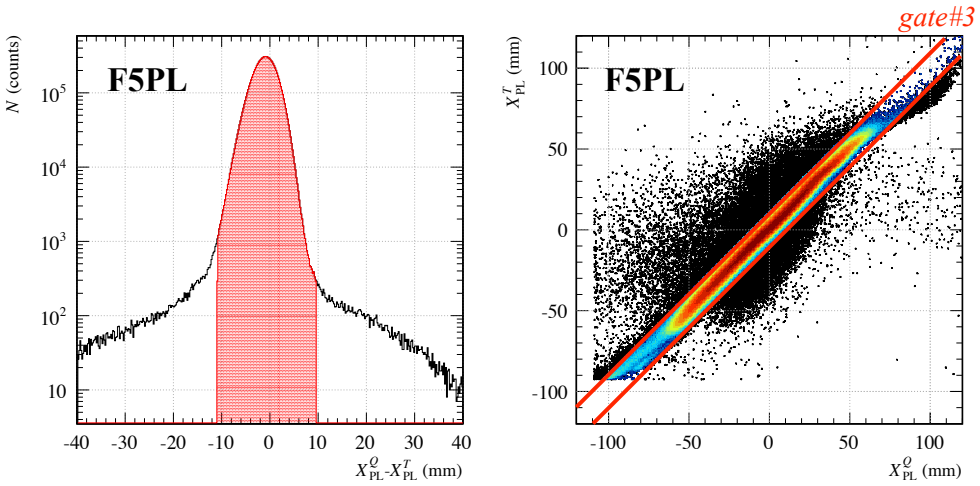

Figure 4-4: The same figures as Fig. 4-3 for F5PL. The red filled region represents the selected region (*gate#3*).

ΔE vs ΔE correlation

At upper reaches of the reaction target, particles reacting in detectors can be eliminated by the correlation of energy losses in F3PL ΔE_{F3PL}, F3IC ΔE_{F3IC}, and F5PL ΔE_{F5PL}. Non-reacted particles were selected by setting proper gates on ΔE vs. ΔE spectra. As shown in Fig. 4-5, the "*gate#4*" was set in the correlation between ΔE_{F3PL} and the atomic number Z_{F3IC} reconstructed from ΔE_{F3IC}. The set gate "*gate#5*" is shown in Fig. 4-6, which is the two-dimensional spectrum of Z_{F3IC} and ΔE_{F5PL}.

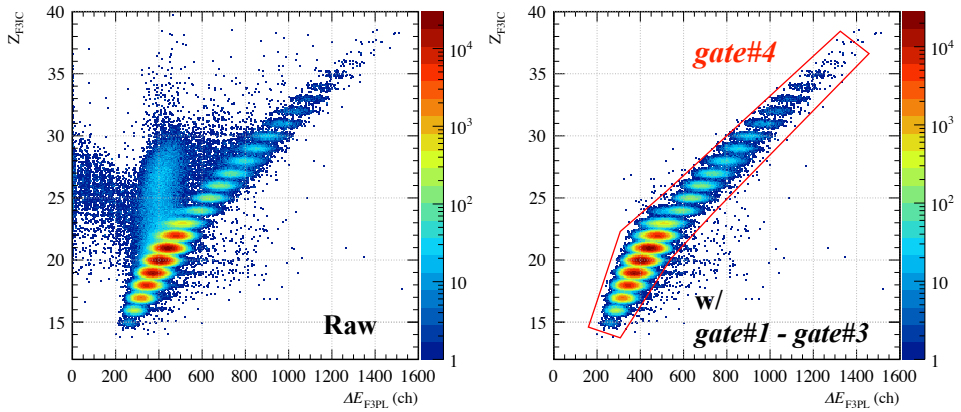

Figure 4-5: Correlation between ΔE_{F3PL} and Z_{F3IC} (left) without any gates and (right) with *gate#1*, *gate#2*, and *gate#3*.

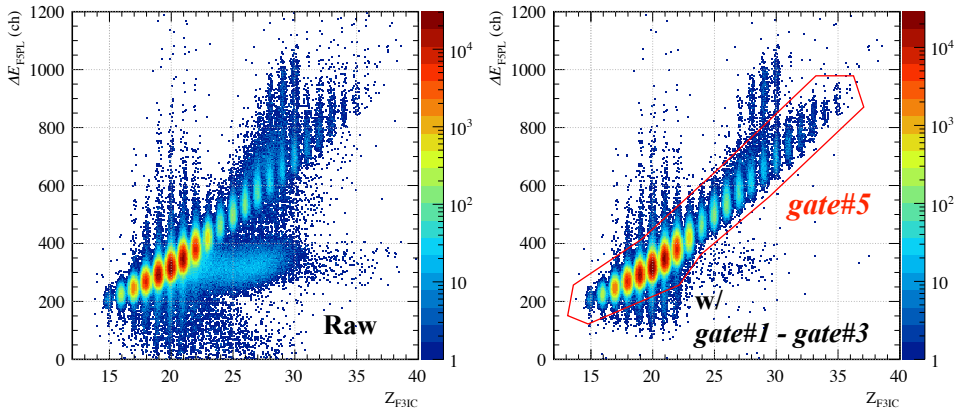

Figure 4-6: Correlation between Z_{F3IC} and ΔE_{F3PL} (left) without any gates and (right) with *gate#1*, *gate#2*, and *gate#3*.

4.1.3 Particle Selection in $A/Q_{\mathbf{F3F5}}$ vs $Z_{\mathbf{F3IC}}$ Spectrum

Set gates *gate#1* - *gate#5* purify the PID plot as shown in Fig. 4-7. Finally, we selected incoming particles in this spectrum. The analysis of each nuclide is the same manner. Hence, we explain the analysis for ^{43}Ca as an example.

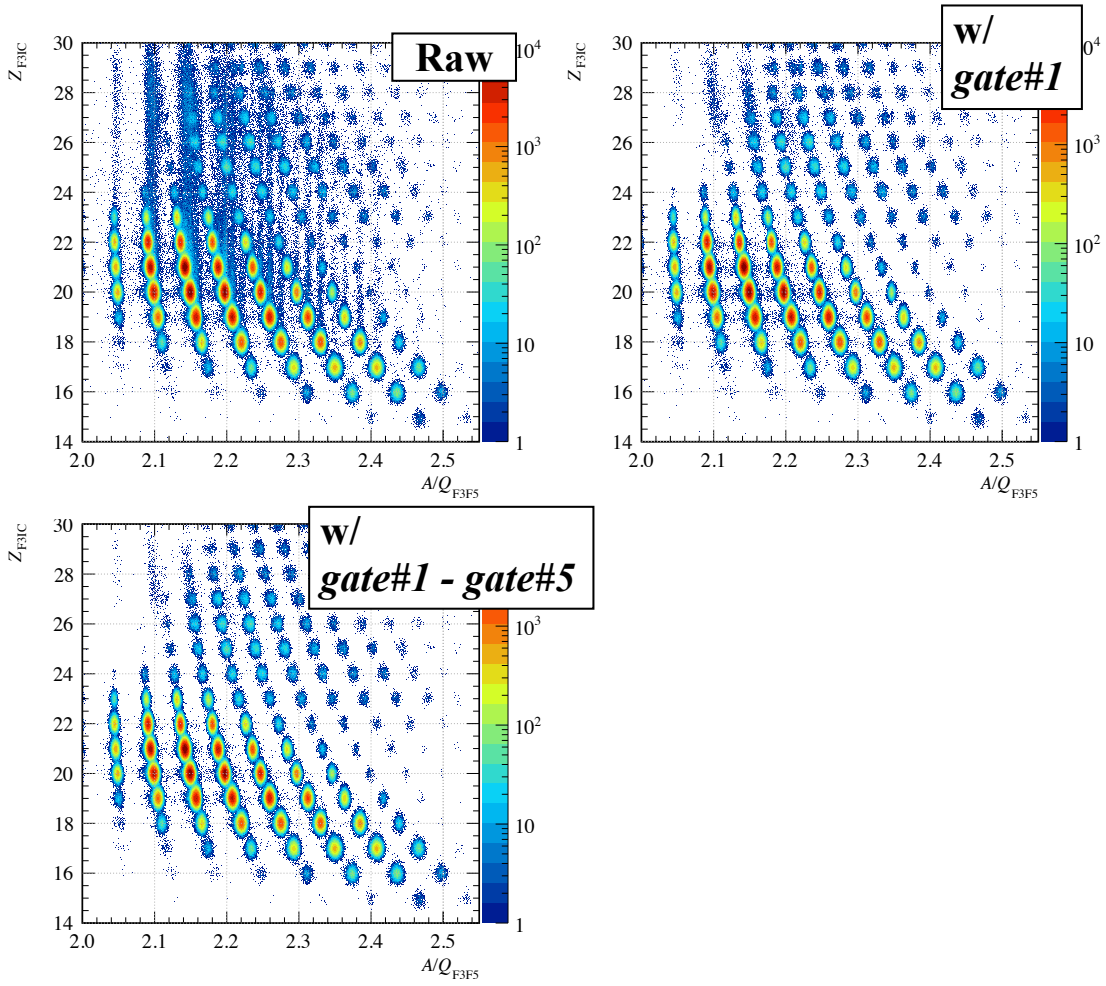

Figure 4-7: PID plots in F3-F5 (upper left) without any gates, (upper right) with only the pileup rejection *gate#1*, and (lower left) with the pileup and background rejection *gate#1* - *gate#5* .

Resolution of $A/Q_{\mathbf{F3F5}}$ and $Z_{\mathbf{F3IC}}$

In Fig. 4-8, we show the PID plot around ^{43}Ca with *gate#1* - *gate#5*. In order to confirm resolutions of A/Q_{F3F5} and Z_{F3IC}, events within red dotted lines shown in Fig. 4-8 are projected onto A/Q axis and within black dotted lines onto Z one, respectively. Nuclides are separated with excellent resolutions as 19.2σ on A/Q_{F3F5} and 6.5σ on Z_{F3IC} as shown in Fig. 4-9. Then, incident particles were selected in the PID plot with the selection gate "*gate#6*" shown by the red bold line in Fig. 4-8. We adopted an ellipse-shaped gate, which can be treated quantitatively with its central value and width in unit of the standard deviation. The width of *gate#6* is 3.5σ, which corresponds to the inclusion of 99.7% events of two-dimensional Gaussian distribution.

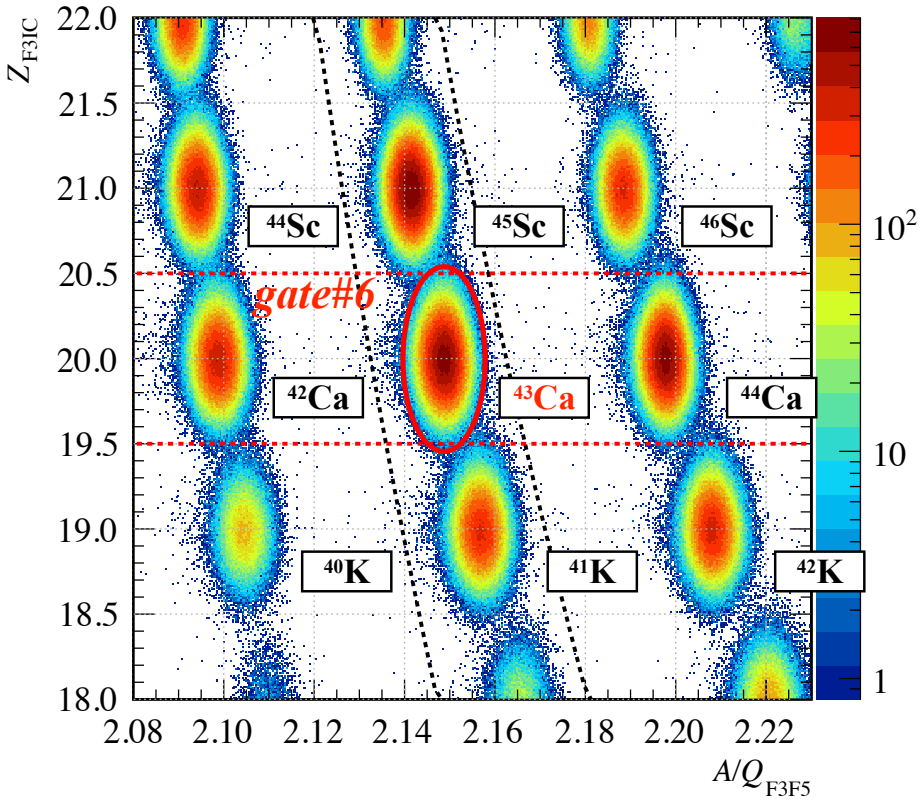

Figure 4-8: PID plots around ^{43}Ca with *gate#1* - *gate#5*.

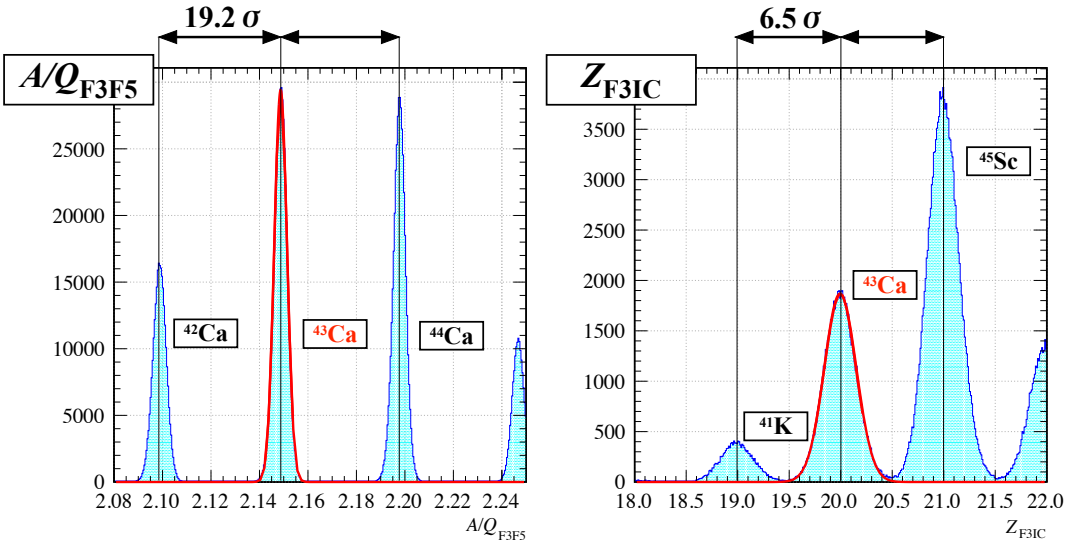

Figure 4-9: One dimensional histograms of (left) A/Q_{F3F5} and (right) Z_{F3IC} around ^{43}Ca.

In order to estimate the amount of contamination from neighboring nuclides, ^{41}K and ^{45}Sc, into the *gate#6*, we generated simulated events with the Monte Carlo method which reproduce respective positions and their widths as well as the ratio of respective events to objective nuclide ^{43}Ca. Figure 4-10 shows the simulated distributions of ^{41}K and ^{45}Sc together with the *gate#6*. The amount of these contaminants in the *gate#6* is estimated as approximately $\sim 2 \times 10^{-2}$ % relative to ^{43}Ca, which is sufficiently small. Moreover, we also reduce these contaminants by utilizing the following procedure.

Removal of Contaminations from Neighboring Nuclei

Although there is a well separation along the Z_{F3IC} axis, ^{A}Ca can be contaminated with $^{A+2}$Sc and $^{A-2}$K especially near $A/Q = 2$. Therefore, the sum of energy losses in F3PL and F5PL, $\Delta E_{\mathrm{F3PL+F5PL}}$, was utilized so as to eliminate these contaminants as much as possible. In order to confirm respective distributions of ^{41}K and ^{45}Sc in the $\Delta E_{\mathrm{F3PL+F5PL}}$ spectrum, their own atomic number was identified in more detail with the help of Z_{F7IC} shown in Fig. 4-11. We mention that this identification is not used to select incoming particles but only utilized confirming the distributions of contaminants. Figure 4-13 shows the correlation between $\Delta E_{\mathrm{F3PL+F5PL}}$ and $Z_{\mathrm{F3IC}}(-A/Q_{\mathrm{F3F5}} + 3)$, on which ^{43}Ca and its neighboring nuclides are the most separated as shown in Fig. 4-12. In Fig. 4-13, color dots represent events located within the

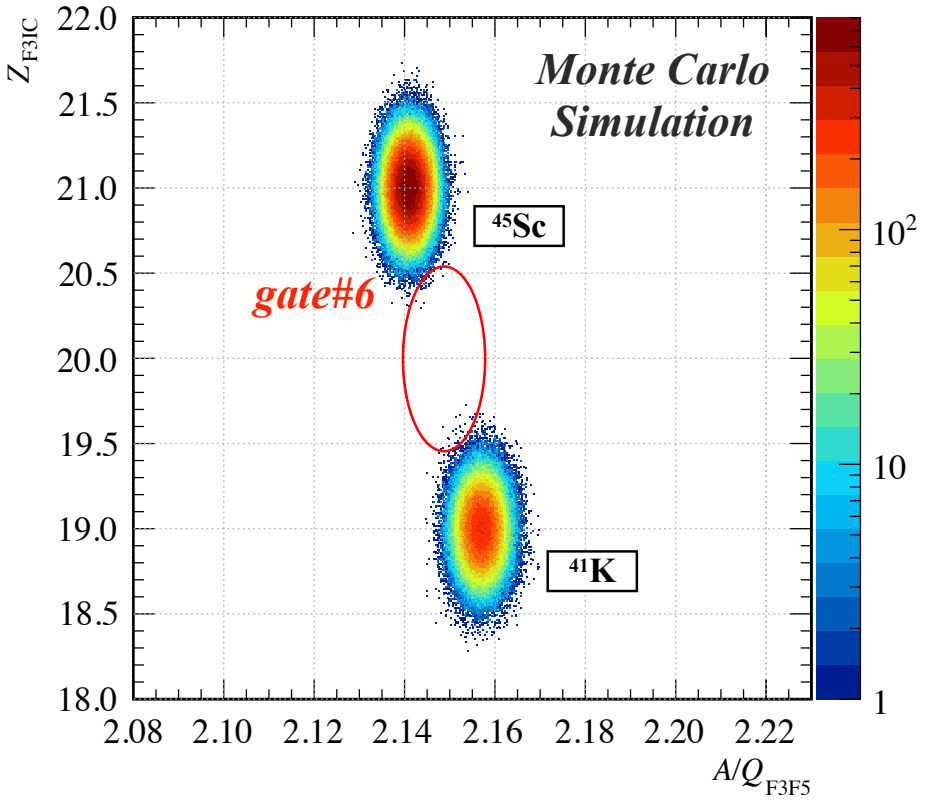

Figure 4-10: Simulated distributions of ^{41}K and ^{45}Sc.

ellipse-shaped gate shown in Fig. 4-9, while black dots are ones with additional selection shown in Fig. 4-11. Though slight contaminants exist in color dots, these can be removed by proper two-dimensional gates labeled as "$\overline{gate\#7}$" (events selected with this gate were eliminated.) without a large lack of objective nuclide. In the case of ^{43}Ca, the ratio of contaminants to objective nuclide is approximately $\sim 2 \times 10^{-2}$% without $\overline{gate\#7}$, which corresponds to $\sim 1/5$ compared to its statistical error. In addition, this effect can be reduced to less than $\sim 1/10$ with the $\overline{gate\#7}$, then this contribution can be ignored. Similarly, the effect of contamination can be canceled by the target-out measurement as far as production cross sections of objective nuclide from its contaminants are negligibly small.

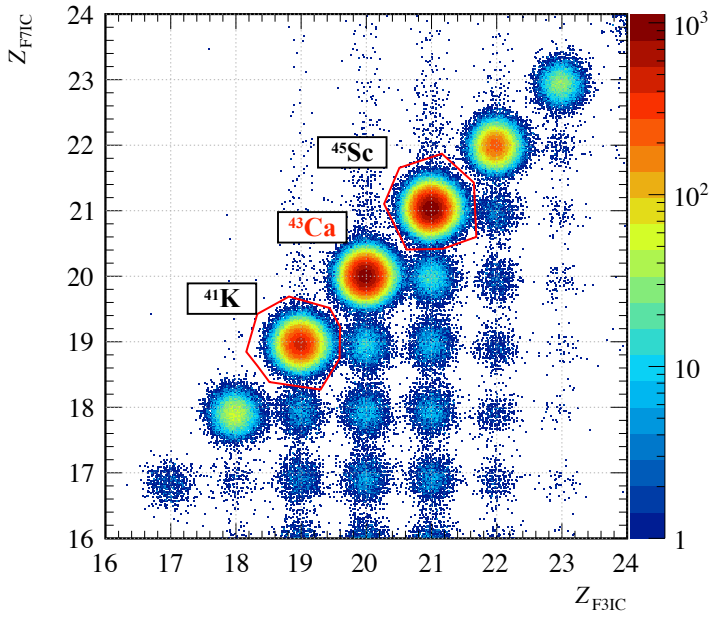

Figure 4-11: Correlation between Z_{F3IC} and Z_{F7IC}.

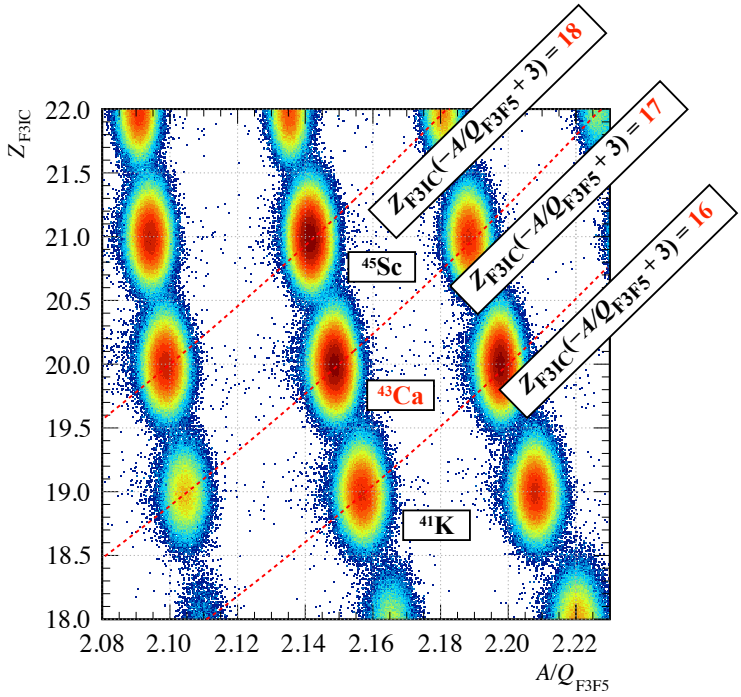

Figure 4-12: $Z_{\mathrm{F3IC}}(-A/Q_{\mathrm{F3F5}}+3) = const.$ lines on PID plots.

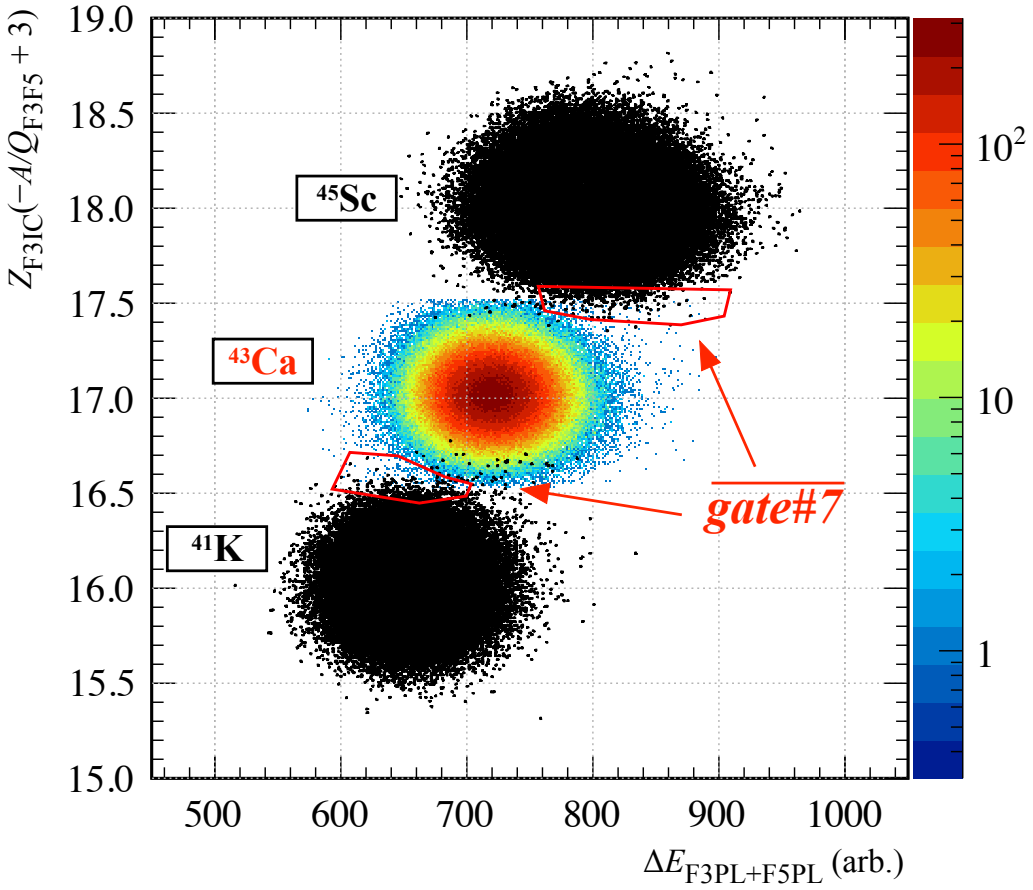

Figure 4-13: Correlation between $\Delta E_{\mathrm{F3PL+F5PL}}$ and Z_{F3IC}. Events selected with $\overline{gate\#7}$ were eliminated.

4.2 Analysis after Reaction Target

Figure 4-14 shows the PID plots between F5 and F7 with and without selecting the incident nuclide. The downstream PID has also sufficiently good separation as 16.2σ in A/Q_{F5F7} and 6.5σ in Z_{F7IC} shown in Fig. 4-15, respectively. In order to distinguish the non-nuclide-changing particles from reaction products, we performed the identification procedures described in the following subsections with adopting *DownStream* gates labeled "*#DS*".

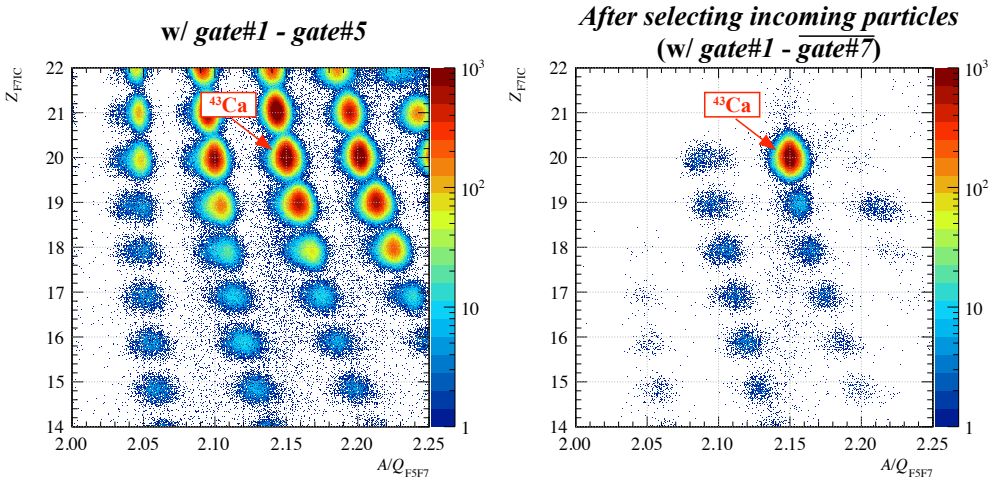

Figure 4-14: Downstream PID plots with (a) *gate#1-gate#5* and (b) *gate#1-gate#7*.

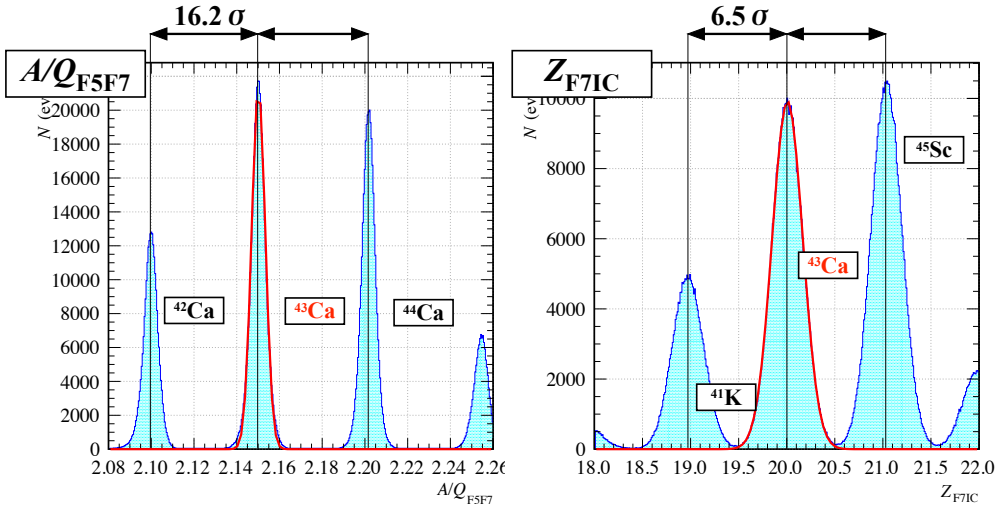

Figure 4-15: One dimensional histograms of (left) A/Q_{F5F7} and (right) Z_{F7IC} around ^{43}Ca.

4.2.1 Identification of Z

The atomic number Z after reaction target was identified from the energy losses in F5IC ΔE_{F5IC} and F7IC ΔE_{F7IC}. The correlation between Z_{F5IC} and Z_{F7IC} is shown in Fig. 4-16.

The *DS#1* events located within the red ellipse shown in Fig. 4-16 are identified as non-charge-changing particles in the target by both of F5IC and F7IC. In the analysis of σ_{I}, only *DS#1* events are treated as non-charge-changing event, which are distinguished whether their own mass A was changed or not in the following procedure mentioned in Sec. 4.2.2. The width of *DS#1* is 3.9σ of distributions on respective axes, which corresponds to the inclusion of 99.95% events of two-dimensional Gaussian distribution. The events within blue lines labeled as *DS#2* are certainly identified as non-charge-changing events in F5IC, while not in F7IC. These events correspond to reaction ones mainly in F7IC. The ratio of *DS#2* to *DS#1* is about 0.5%, which is consistent to the reaction rate in F7IC estimated by the LISE++ code.

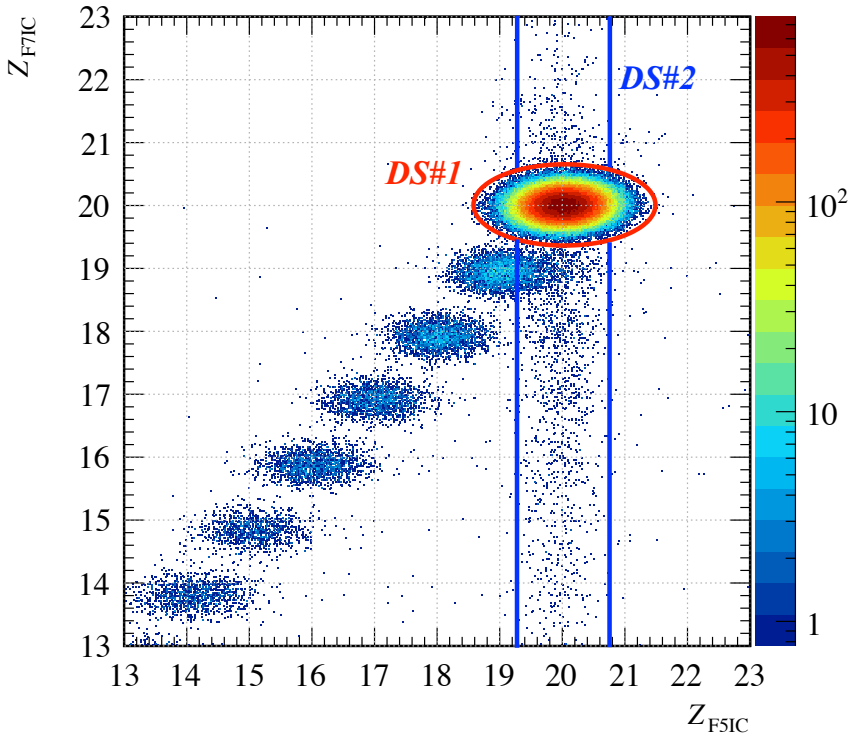

Figure 4-16: Correlation between Z_{F5IC} and Z_{F7IC}.

4.2.2 Identification of A/Q

The identifications for *DS#1* events were performed in regard not only to Z but also to A/Q. Fig. 4-17 provides the correlation between A/Q_{F5F7} and ΔE_{F7PL} for *DS#1* events. In the case of ^{43}Ca, non-nuclide-changing events are forming a peak around $A/Q_{\mathrm{F5F7}} = 2.15$. The top and bottom tails of non-nuclide-changing events corresponds to reaction ones in F7PL, where the reaction rate is about 0.4%. Events which locate around $A/Q_{\mathrm{F5F7}} = 2.15$ can be certainly identified as non-nuclide-changing ones whether particles are reacted in F7PL or not. Therefore, both of *DS#3* and *DS#4* events as shown in Fig. 4-17 were treated as non-reacted particles for the analysis of σ_{I}.

In principle, the A/Q_{F5F7} do not depend on ΔE_{F7PL}. However, in some cases, the events whose ΔE_{F7PL} are small have slightly larger A/Q_{F5F7} due to the F7PL pulse height dependence on A/Q_{F5F7}. Hence, we used a rectangle or two dimensional proper gate to count non-nuclide-changing particles depending on their ΔE_{F7PL} for less ambiguous counting. A rectangle gate whose width is about 6σ of A/Q_{F5F7} distribution was adopted for the main component of non-nuclide-changing particles labeled as "*DS#3*", while a proper two-dimensional gate for reaction events in F7PL labeled as "*DS#4*" was also added. The amount of *DS#4* is about 0.1% compared to that of *DS#3*.

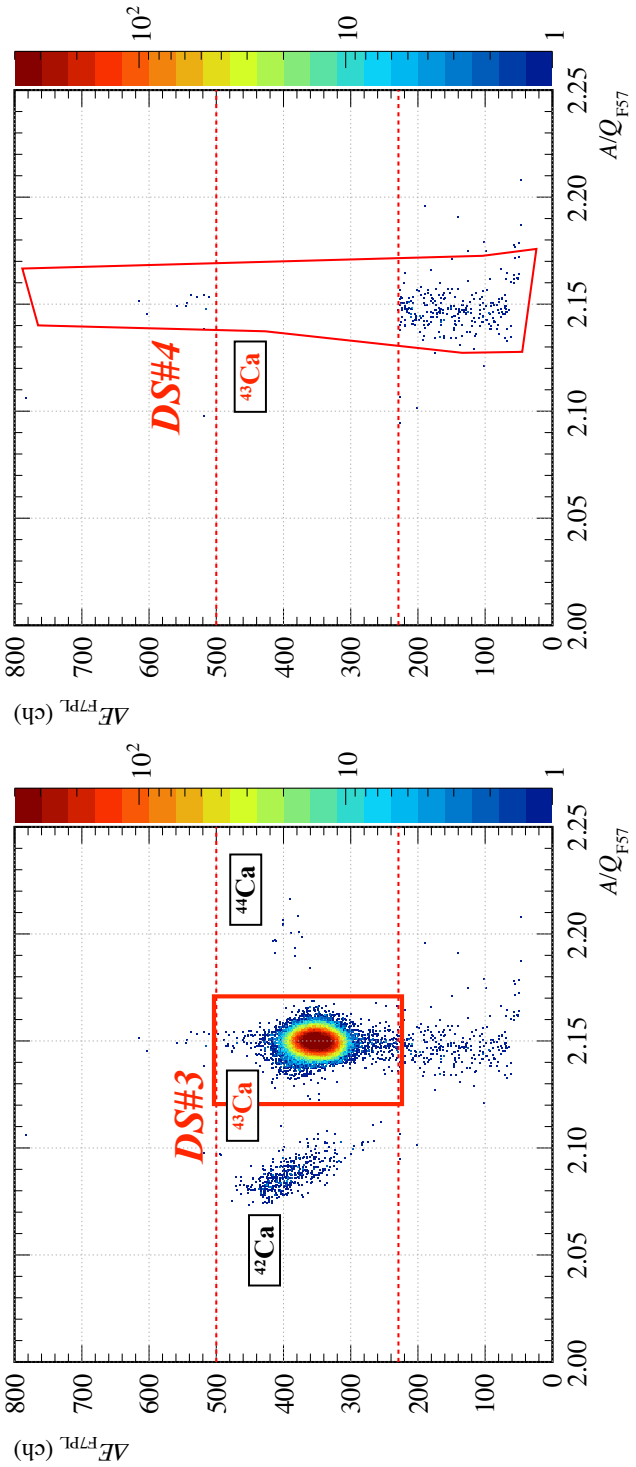

Figure 4-17: Correlation between A/Q_{F5F7} and ΔE_{F7PL} for *DS#1* events.

4.3 Target-Out Measurement

Target-out measurements were performed with the same condition as target-in ones except for the $B\rho_0$ configuration after reaction target. In the target-out measurements, downstream dipole magnets were adjusted as reproducing almost the same horizontal beam profile for non-nuclide-changing particles as the ones for target-in measurements. Hence, the incident particles were selected in exactly the same manner.

In the downstream identification, almost the same-shaped gates as target-in analysis were employed with a slight change on the width of gates. The widths of employed gates in target-out measurements are the same as those of target-in measurements in unit of σ of respective distributions, which means the absolute widths are slightly different between the target-in and -out measurements.

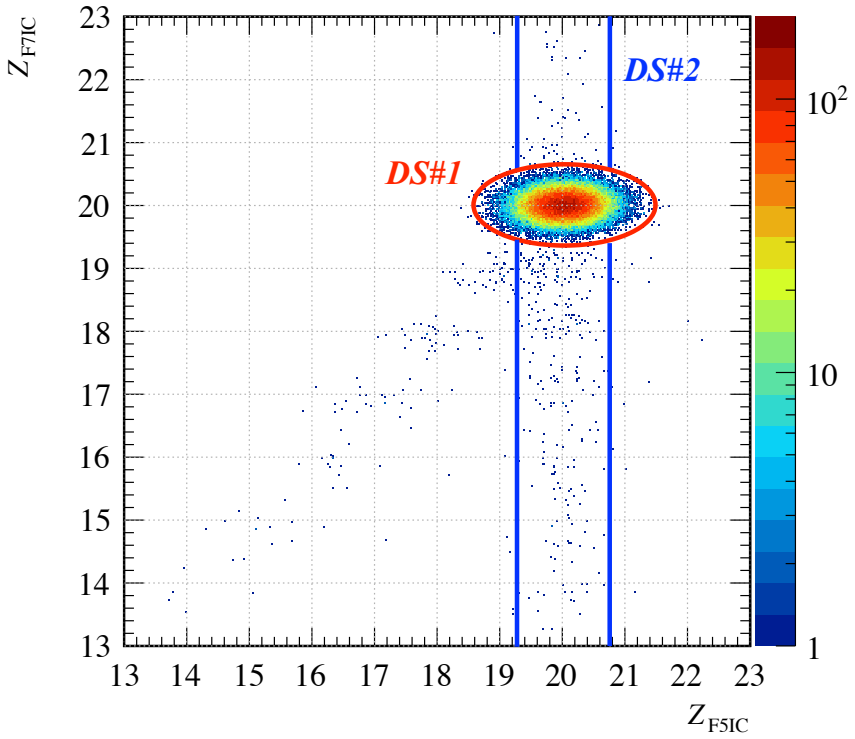

Figure 4-18: The same plot as Fig. 4-16 for the target-out measurement.

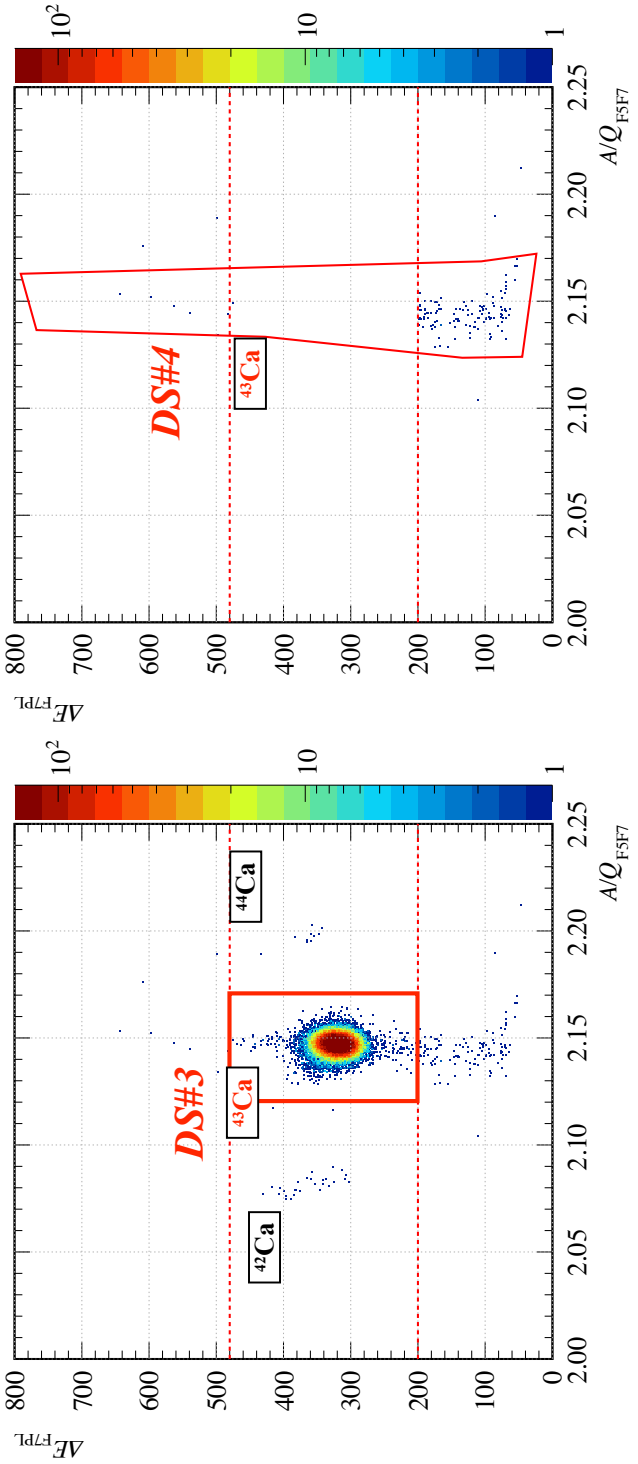

Figure 4-19: The same plot as Fig. 4-17 for the target-out measurement.

4.4 Emittance Cut

Although the BigRIPS separator has large angular and momentum acceptances, not all non-reacted-particles near the border of acceptance can be transported to F7. Therefore, in order to select fully transported particles, we confined the emittance of incident particles by using the information of position, angle, and momentum obtained from detectors before the reaction target. Specifically, the following quantities are confined from the dependence of the non-reaction rate R on them:

X_{F3} : horizontal position at F3,
Y_{F3} : vertical position at F3,
A_{F3} : horizontal angle at F3,
B_{F3} : vertical angle at F3,
X_{F5} : horizontal position at F5,
(X_{F5} corresponds to the momentum.)

$$R = \frac{N_2}{N_1}, \tag{4.5}$$

where N_1 and N_2 are the number of incident and non-reacted particles, respectively.

In Figs. 4-20, 4-21, 4-22, 4-23, and 4-24, we show the dependences of R on X_{F3}, Y_{F3}, A_{F3}, B_{F3}, and X_{F5}, respectively. The dependence of R on one quantity is examined with restrictions on the others adopted. The uniform component of non-reaction rate distribution can be considered as the fully transmitted part. In the non-reaction rate distributions on X_{F3}, Y_{F3}, A_{F3}, and B_{F3}, the constant components shown by the red circles in Figs. 4-20-4-23 were selected to analyze. On the other hand, the dependence on X_{F5} shown in 4-24 has not a constant but a slightly tilted component owing to the usage of wedge-shaped reaction target. When the thickness of reaction target is written by $t = t_0 + aX_{\mathrm{F5}}$, the non-reaction rate R can be written as

$$\begin{aligned} R &= 1 - \sigma_{\mathrm{I}}(t_0 + aX_{\mathrm{F5}}) \\ &= (1 - \sigma_{\mathrm{I}} t_0) - \sigma_{\mathrm{I}} a X_{\mathrm{F5}} \\ &= R_0 - a\left(\frac{1 - R_0}{t_0}\right) X_{\mathrm{F5}}, \end{aligned} \tag{4.6}$$

with

$$R_0 \equiv 1 - \sigma_{\mathrm{I}} t_0. \tag{4.7}$$

the slope of non-reaction rate shown in Fig. 4-24 is consistent with the angle of reaction target. Therefore, the component followed with the red line shown in Fig. 4-24 was selected as the fully transported region. The same emittance

cut determined by the above procedure was adopted both in target-in and target-out measurements.

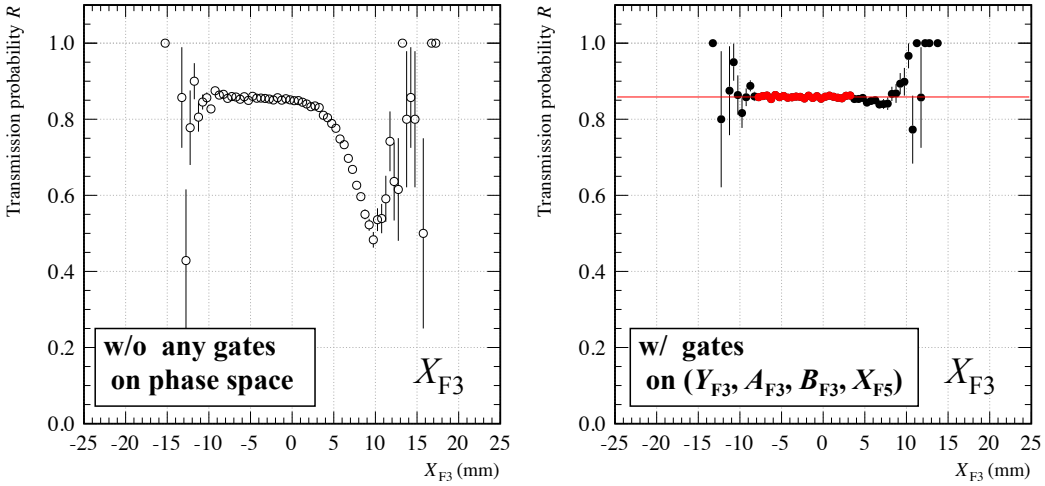

Figure 4-20: Dependence of R on X_{F3}.

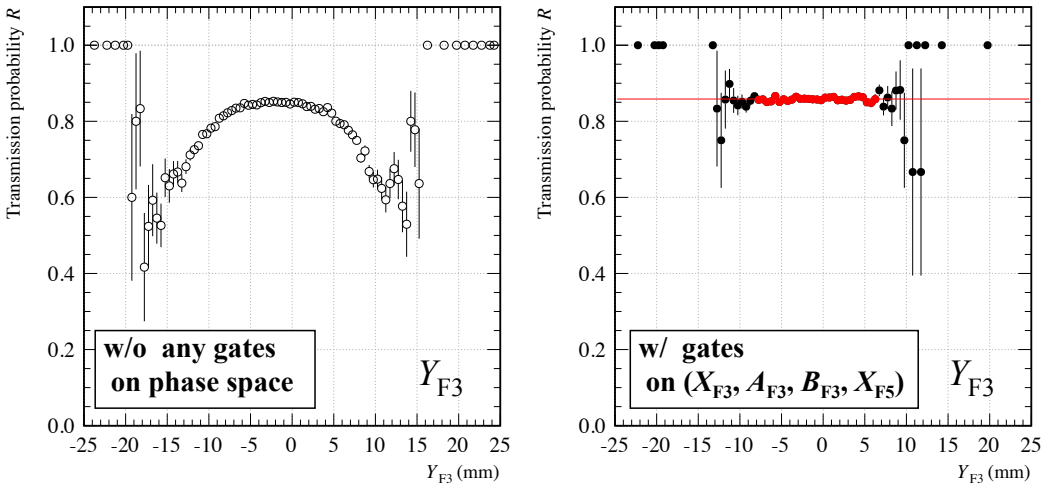

Figure 4-21: Dependence of R on Y_{F3}.

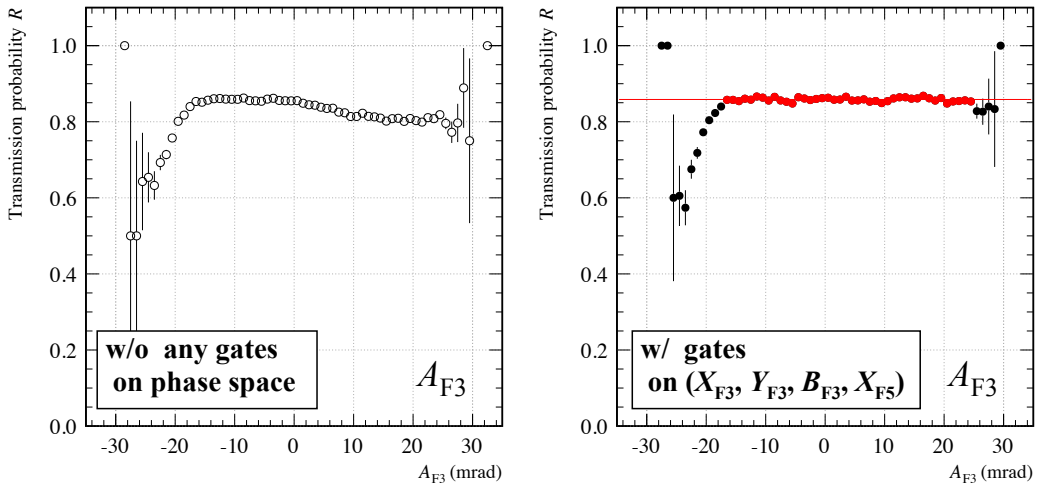

Figure 4-22: Dependence of R on A_{F3}.

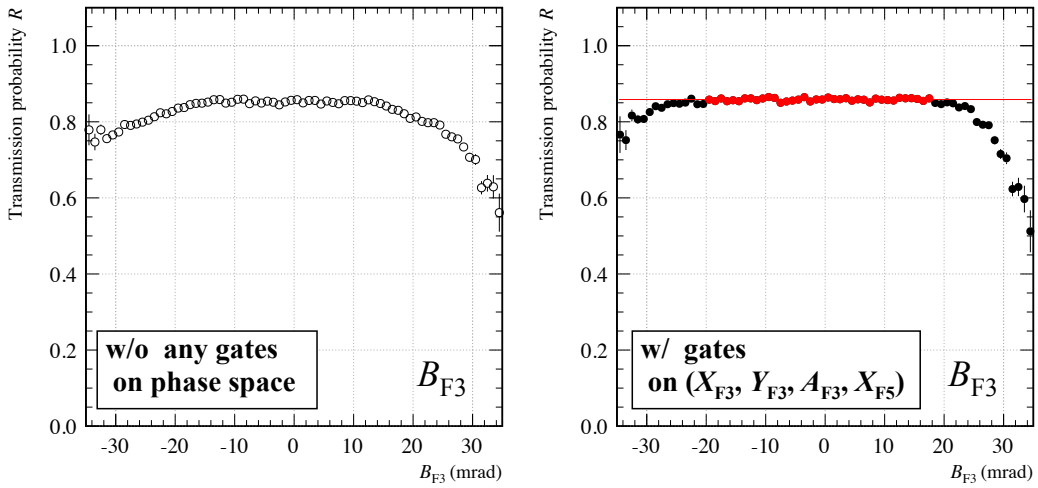

Figure 4-23: Dependence of R on B_{F3}.

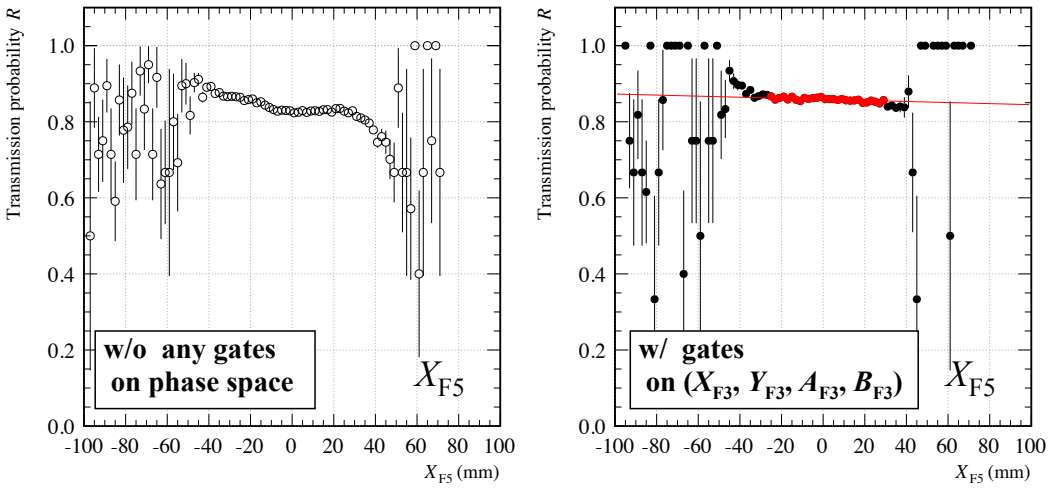

Figure 4-24: Dependence of R on X_{F5}.

4.5 Determination of Target Profile

As mentioned in 3.6, we employed a wedge-shaped C target as a reaction target installed at F5. Though the thickness of reaction target has been measured as

$$t^{\rm meas}_{\rm wedge}(x) = 1.7995(6) + 0.00181(2)x \ [{\rm g/cm^2}], \tag{4.8}$$

the actual thickness of the target as a function of horizontal position at F5 $t^{\rm meas}_{\rm wedge}(X_{\rm F5})$ also depends on the mount position onto target-ladder. Therefore, we determined $t^{\rm meas}_{\rm wedge}(X_{\rm F5})$ from the comparison with the parallel-plate C target in terms of $B\rho_{\rm F5F7}$ information. The target thickness of parallel-plate target has been also measured as

$$t^{\rm meas}_{\rm parallel} = 1.8066(6) \ [{\rm g/cm^2}]. \tag{4.9}$$

Figure 4-25 shows the measured $B\rho_{\rm F5F7}$ distribution with respective targets with the same beam condition as a function of $X_{\rm F5}$. Since the crosspoint of respective data shown in Fig. 4-25 corresponds to the point of the same target thickness, we can derive $t^{\rm wedge}_{\rm meas}(X_{\rm F5})$ from this crosspoint in harmony with Eq. 4.8 as

$$t^{\rm meas}_{\rm wedge}(X_{\rm F5}) = 1.8039(12) + 0.00181(2)X_{\rm F5} \ [{\rm g/cm^2}]. \tag{4.10}$$

On the other hand, as shown in Fig. 4-25, there is a slight nonuniformity on $B\rho_{\rm F5F7}(X_{\rm F5})$ distribution for the wedge-shaped target, which results from the nonuniformity of target thickness compared to one given by Eq. (4.10). This nonuniformity corresponds to the approximately 0.25% deviation in unit of g/cm^2 from Eq. (4.10). If we use Eq. (4.10) as a function of target thickness, this deviation have to be taken into account as a systematic error. Therefore, in order to avoid this systematic error, we utilized the distribution of target thickness, $t_{\rm wedge}(X_{\rm F5})$ directly derived from the $B\rho_{\rm F5F7}(X_{\rm F5})$ distribution in accordance with the following equation:

$$\left(\frac{t_{\rm wedge}(X_{\rm F5})}{t^{\rm meas}_{\rm wedge}(X_{\rm F5})} - 1\right) : \left(\frac{B\rho_{\rm wedge}(X_{\rm F5})}{B\rho^{\rm fit}_{\rm wedge}(X_{\rm F5})} - 1\right) = \left|\frac{t^{\rm meas}_{\rm wedge}(X_{\rm F5})}{t^{\rm meas}_{\rm parallel}} - 1\right| : -\left|\frac{B\rho^{\rm fit}_{\rm wedge}(X_{\rm F5})}{B\rho^{\rm fit}_{\rm parallel}(X_{\rm F5})} - 1\right|,$$

$$t_{\rm wedge}(X_{\rm F5}) = t^{\rm meas}_{\rm wedge}(X_{\rm F5}) \left[1 - \frac{\left|\frac{t^{\rm meas}_{\rm wedge}(X_{\rm F5})}{t^{\rm meas}_{\rm parallel}} - 1\right|}{\left|\frac{B\rho^{\rm fit}_{\rm wedge}(X_{\rm F5})}{B\rho^{\rm fit}_{\rm parallel}(X_{\rm F5})} - 1\right|} \left(\frac{B\rho_{\rm wedge}(X_{\rm F5})}{B\rho^{\rm fit}_{\rm wedge}(X_{\rm F5})} - 1\right)\right], \tag{4.11}$$

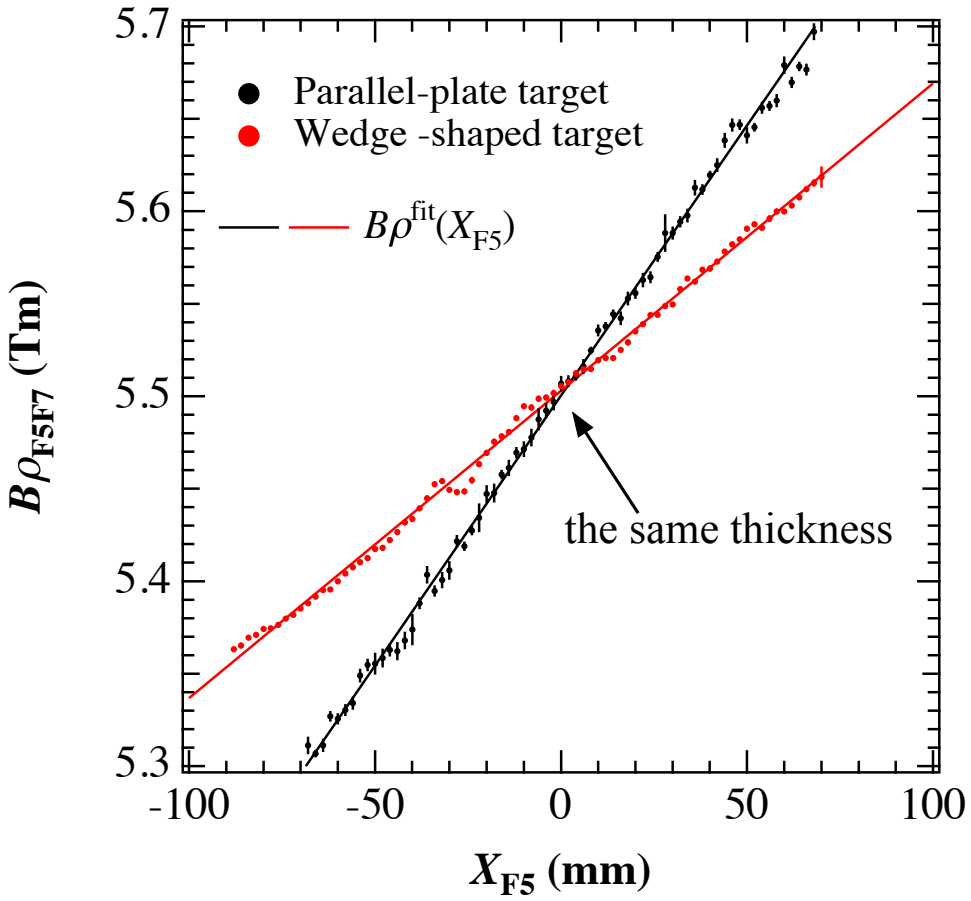

Figure 4-25: Correlations between $B\rho_{\rm F5F7}$ and $X_{\rm F5}$ for wedge-shaped (red) and parallel-plate (black) targets, respectively. The fitting lines with linear functions are also shown.

$B\rho^{\rm fit}_{\rm wedge}(X_{\rm F5})$: best-fit function to $B\rho_{\rm F5F7,wedge}(X_{\rm F5})$ shown by the red line in the left part of Fig. 4-25,

$B\rho^{\rm fit}_{\rm parallel}(X_{\rm F5})$: best-fit function to $B\rho_{\rm F5F7,parallel}(X_{\rm F5})$ shown by the black line in the left part of Fig. 4-25,

$B\rho^{\rm exp}_{\rm wedge}(X_{\rm F5})$: experimental $B\rho_{\rm F5F7}(X_{\rm F5})$ distribution shown by the red circles in the left part of Fig. 4-25.

The obtained distribution of wedge-shaped target thickness is shown in Fig. 4-26. In the present study, we employed this target thickness distribution in order to derive $\sigma_{\rm I}$. The error of target thickness in each point is at most 0.15%, which is much smaller in comparison with the most precise statistical error in the present study of approximately 0.5%.

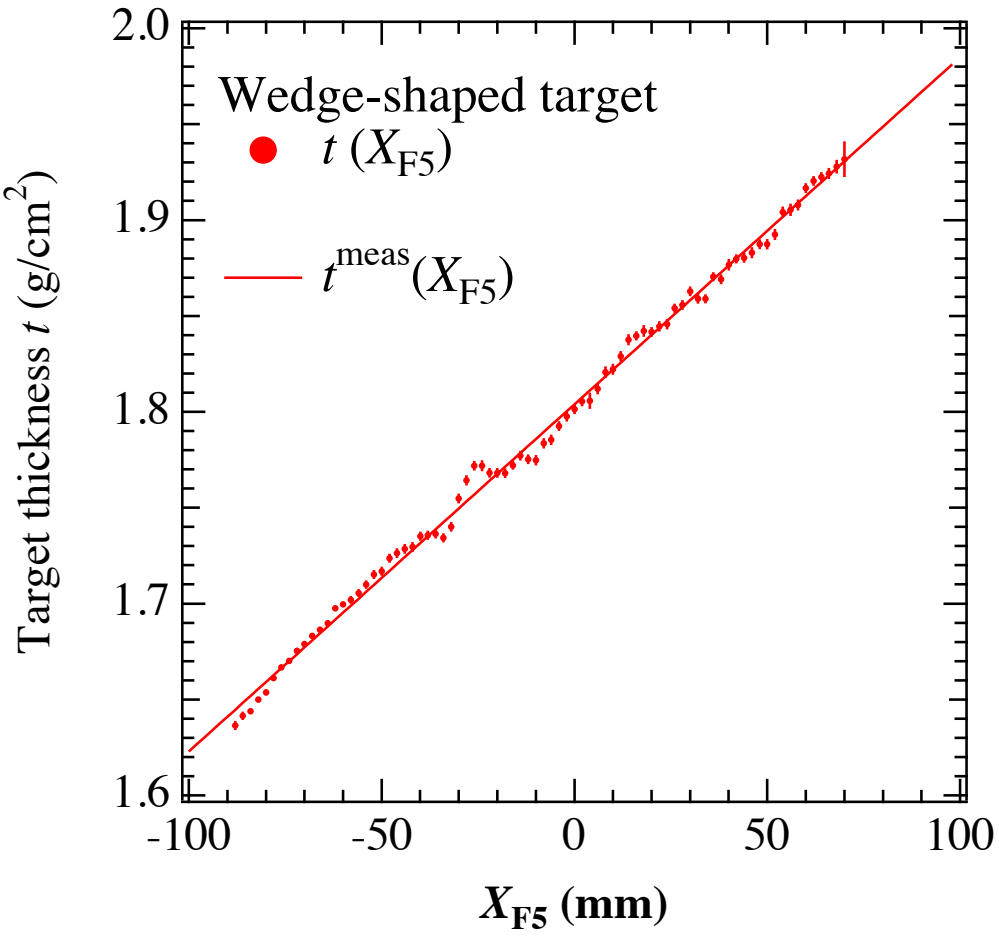

Figure 4-26: Obtained target thickness of wedge-shaped target from $B\rho(X_{\mathrm{F5}})$ in accordance with Eq. 4.11. As a comparison, $t^{\mathrm{meas}}_{\mathrm{wedge}}(X_{\mathrm{F5}})$ given by Eq. 4.10 is also shown by the red line.

4.6 Estimation of Systematic Error

In addition to the uncertainty of target thickness as mentioned in Sec. 4.5, the systematic error was considered in terms of the following points. As a result, the systematic error of 0.36% resulting from the width of the ellipse-shaped gate for *DS#1* and that of 0.15% from the target thickness were explicitly taken into account.

4.6.1 Dependence of Gate Width

As mentioned in the previous subsections, the almost all adopted gates are parametrized by the center position and the width. In order to estimate the systematic error resulting from the employed gates, we derived σ_{I} by changing the width of each set gate.

First, in order to confirm the validity of *gate#6* which is for selecting incoming particles in the upstream PID plot, we derive σ_{I} by changing the gate width. In this procedure, the gate width was changed in both target-in and target-out measurements simultaneously. Fig. 4-27 shows the gate width dependence of σ_{I} for *gate#6*. The employed gate represented by the red circle (3.5σ) is almost in the middle of constant region. The employed gate was also exactly the same between the target-in and target-out measurements, so that several contamination effects not only of neighboring nuclides but also of uniform backgrounds are canceled in principle.

Next, we confirm the gate width dependence of *DS#1* which is for selecting non-charge-changing particles in the correlation between Z_{F5IC} and Z_{F7IC}. As already mentioned in Sec. 4.3, the widths of adopted gates are the same in unit of σ in both target-in and target-out measurements (3.9σ). However, if uniform backgrounds exist, the effect of background cannot be canceled due to the different absolute widths for target-in and target-out measurements. Therefore, in order to estimate this effect, we derived σ_{I} by employing the exactly the same width in unit of absolute value for both measurements. In the present analysis, the absolute gate width for *DS#1* of the target-out measurement is larger compared to that of the target-in one. In the case of target-in measurement, the gate width which corresponds to the absolute gate width of the target-out measurement is 4.3σ in unit of σ. Figure 4-28 shows the correlation between Z_{F5IC} and Z_{F7IC} for the target-in measurement of ^{43}Ca together with the gates whose widths are 3.9σ and 4.3σ, respectively. The 4.3σ width gate results in the σ_{I} change of 7 mb, which corresponds to the relative error of 0.36%. This was regarded as an estimate of the systematic error.

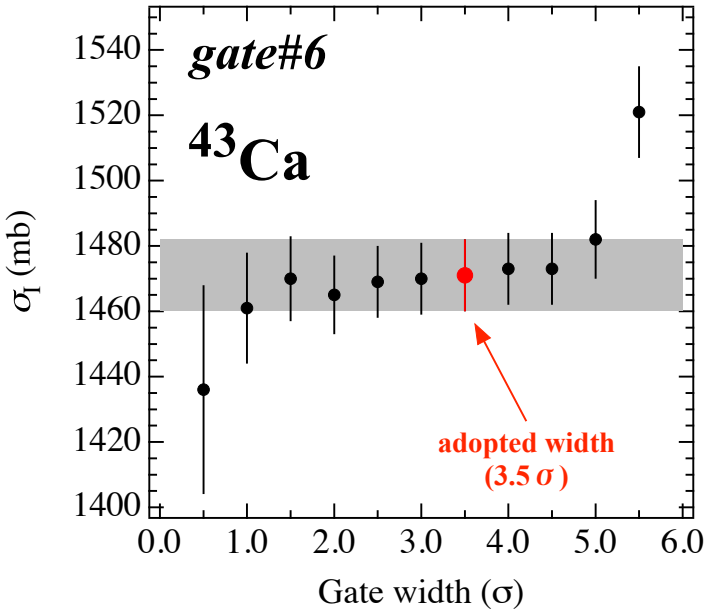

Figure 4-27: Gate width dependence of σ_{I} for *gate#6* in the case of ^{43}Ca. The red circle and gray shaded band represent the adopted gate width and the corresponding statistical error, respectively.

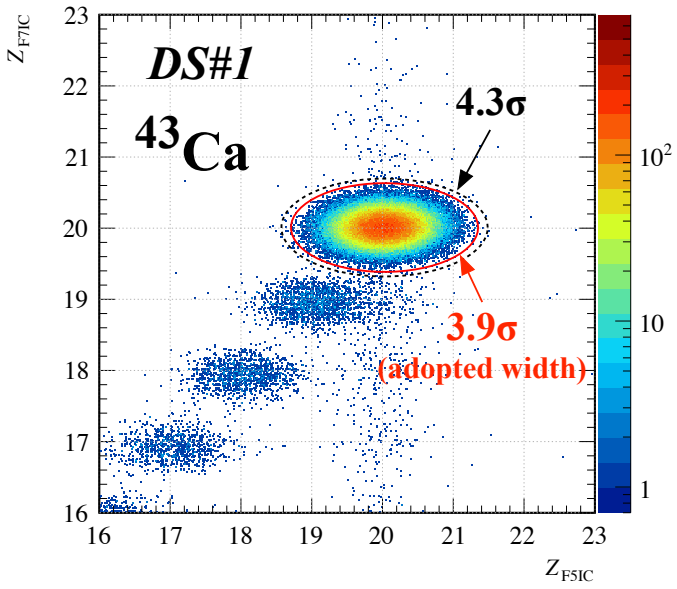

Figure 4-28: Correlation between Z_{F5IC} and Z_{F7IC} for the target-in measurement of ^{43}Ca together with the gates whose widths are 3.9σ (red solid line) and 4.3σ (black dotted line), respectively.

4.6.2 Emittance Cut Dependence

The emittance cut mentioned in Sec. 4.4 was adopted to select the constant component in the non-reaction rate R distribution. In order to consider the systematic error resulting from the condition of emittance cut, as an example, we confirmed the X_{F3} dependence of R for the target-in measurement of ^{43}Ca shown in Fig. 4-29. In Fig. 4-29, the average R and the standard deviation of selected data (red circles) around the average R are shown by the red line and the orange shaded band, respectively. We compare the standard deviation for each quantity utilized in the emittance cut procedure (X_{F3}, Y_{F3}, A_{F3}, B_{F3}, and X_{F5}) to the statistical one. As shown in Fig. 4-30, these standard deviations are consistent with the statistical error in both cases of target-in (black) and target-out (blue) measurements. Therefore, we interpreted that the systematic error resulting from the emittance cut is negligibly small compared to the statistical one. Moreover, we also derived σ_{I} with changing the widths of emittance cut, δw, in both target-in and target-out measurements simultaneously like $x_{\mathrm{min}} - \delta w < X_{\mathrm{F3}} < x_{\mathrm{max}} + \delta w$, where x_{min} and x_{max} represent the lower and upper limits of emittance cut, respectively. The σ_{I} without δw fulfills the enough severe condition not to be affected by the widths of emittance cuts. For this reason, we did not consider the systematic error resulting from the emittance cut.

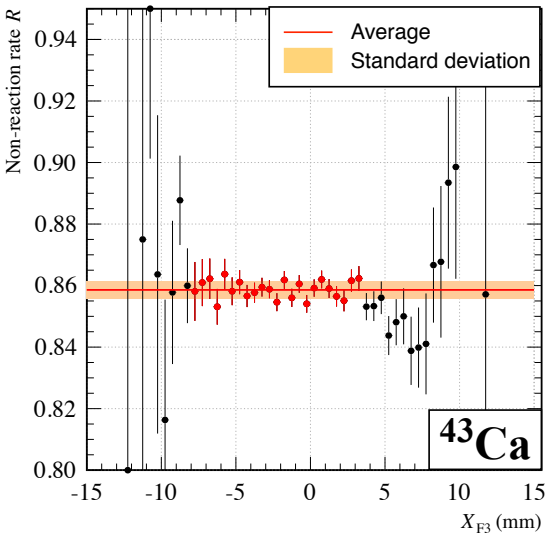

Figure 4-29: Dependence of R on X_{F3} for the target-in measurement of ^{43}Ca. Red symbols represent the selected data by the emittance cut.

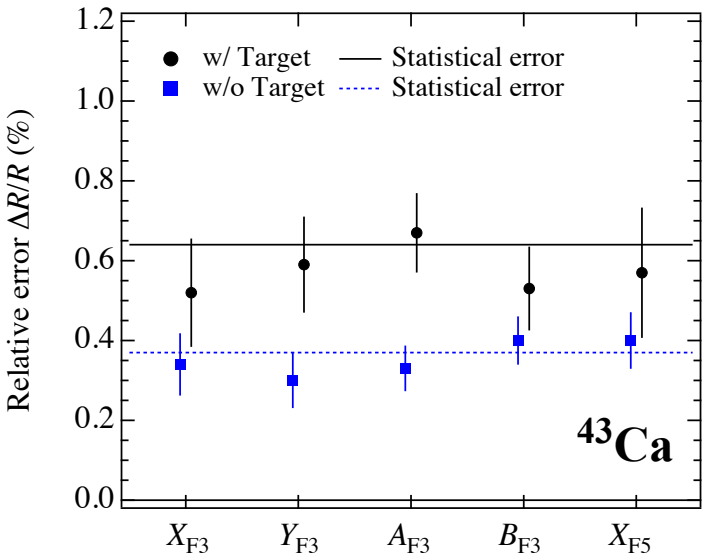

Figure 4-30: Relative errors $\Delta R/R$ of non-reaction rate distribution against X_{F3}, Y_{F3}, A_{F3}, B_{F3}, and X_{F5} for the selected region (represented by red circles in Fig. 4-29) in the case of target-in (black) and target-out (blue) measurements for ^{43}Ca. The statistical errors are also shown by the solid and dotted lines for target-in and target-out measurements, respectively.

4.6.3 Multiple Scattering

Although the condition of emittance cut for the target-in measurement is the exact same as for the target-out one, the effect of multiple scattering in the reaction target only exists in the target-in measurement. Therefore, the horizontal and vertical angular distributions after the reaction target of the target-in measurement can spread compared to those of target-out one. In the condition that the multiple scattering results from the superposition of only the small angle ($< 10°$) single Coulomb scattering, the angular distribution can be expressed by the Gaussian distribution [LE87]. The RMS scattering angle of the angular distribution due to the multiple scattering in the perpendicular plane to the beam axis σ_{mult} can be obtained by using the empirical formula [HI75]:

$$\sigma_{\mathrm{mult}}[\mathrm{rad}] = \frac{1}{\sqrt{2}} Z^{\mathrm{T}} \frac{20[\mathrm{MeV/c}]}{p\beta} \sqrt{\frac{x}{L}} \left[1 + \frac{1}{9} \log_{10} \left(\frac{x}{L} \right) \right], \tag{4.12}$$

where Z^{T} is an atomic number of target nucleus, p and β the momentum and the velocity of projectile nucleus, x the target thickness, and L the

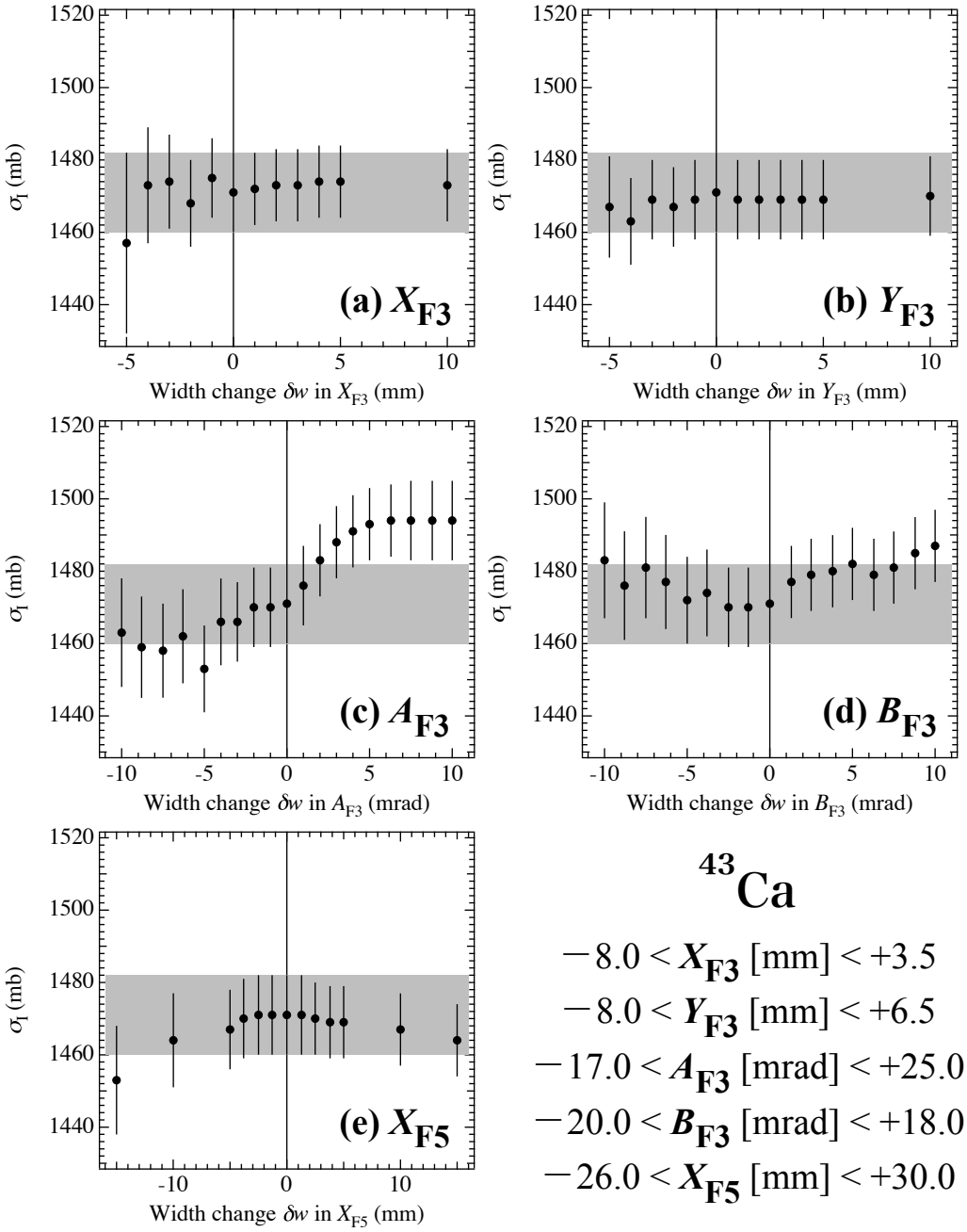

Figure 4-31: Dependences of $\sigma_{\rm I}$ for ^{43}Ca on the width change of emittance cuts, δw, like $x_{\rm min} - \delta w < X_{\rm F3} < x_{\rm max} + \delta w$, where $x_{\rm min}$ and $x_{\rm max}$ represent the lower and upper limits of emittance cut respectively. The black shaded bands represent the error of $\sigma_{\rm I}$ without δw.

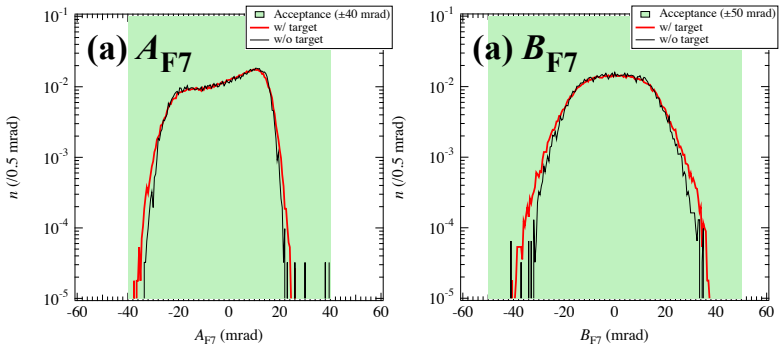

Figure 4-32: Normalized (a) horizontal and (b) vertical angular distributions in F7 whose integrations are equal to 1 for the target-in (red lines) and -out (black lines) measurements, respectively. The angular acceptances of the BigRIPS separator which are ±40 mrad (horizontal) and ±50 mrad(vertical) are also shown by shaded regions.

radiation length of target material, respectively. In the case of ^{43}Ca with the combination of 310.5 MeV/nucleon incident energy and 1.821 g/cm^2 C reaction target, $\sigma_{\rm mult}$ due to the multiple scattering in the reaction target is estimated as 2.3 mrad, which is much small compared to the angular spread of the incident beams. Figure 4-32 shows the normalized (a) horizontal and (b) vertical angular distributions at F7 whose integrations are equal to 1 for the target-in (red lines) and target-out (black lines) measurements together with the angular acceptances of the BigRIPS separator (shaded region) which are ±40 mrad (horizontal) and ±50 mrad (vertical), respectively. In these distributions, the emittance cut was adopted. Though the distributions of the target-in measurement spread slightly compared to those of the target-out one due to the multiple scattering, respective distributions fall within the angular acceptances with the order of less than 10^{-5}, which corresponds to 10^{-2} % relative error of $\sigma_{\rm I}$. Therefore, the effect of multiple scattering is also negligibly small.

4.6.4 Reproducibility of Beam Profile in F7 between Target-in and Target-out Measurements

As mentioned in Sec. 3.5, the beam energy after the reaction target is different between target-in and target-out measurements because of the energy loss in the reaction target. Though the magnetic fields of all the magnets between F5 and F7 were optimized so that the beam profile of non-nuclide-changing particles located almost the same position in F7 in both target-in and target-out measurements, the profile was not extremely the same in both

measurements. Hence, we confirm the distribution of relative momentum to that of central trajectory $B\rho_0$ between F5 and F7 δ_{F5F7}. Figure 4-33 shows the normalized δ_{F5F7} distributions of (a) ^{42}Ca, (b) ^{43}Ca, and (c) ^{44}Ca in both measurements. The experimental data for these nuclides were obtained in the same beam line setting. In this beam line setting, the magnetic fields were optimized for ^{43}Ca, that is, ^{43}Ca locates around $\delta_{\mathrm{F5F7}} \sim 0\%$ in both measurements. As can be seen in Fig. 4-33, in the case of ^{43}Ca, the relative momentum distribution of target-in measurement spreads slightly due to the energy straggling in the reaction target (this is estimated as approximately 0.04% in unit of δ_{F5F7}). However, even by taking this slight difference between both measurements into consideration, both distributions fall within the limited momentum acceptance of the BigRIPS separator (±3%) shown by shaded region. In the case of ^{42}Ca and ^{44}Ca, though the relative momentum distributions in the target-in measurement shift from the center of δ_{F5F7} due to the mass number dependence of energy loss in the reaction target, these distributions also fall with in the ±3 % acceptance. The reproducibility of the beam profile after the reaction target between target-in and target-out measurements fulfills with the quite sufficient level, so that the systematic error due to this effect can be also ignored.

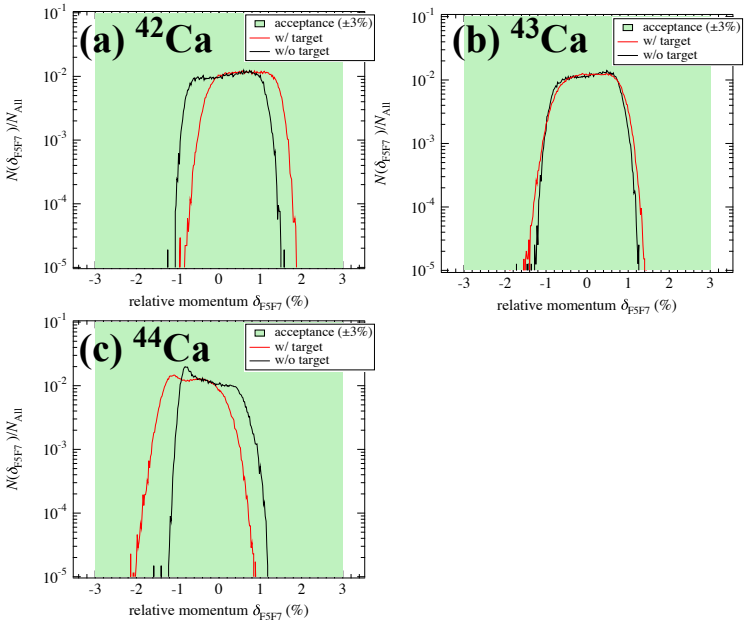

Figure 4-33: Normalized δ_{F5F7} distributions of (a) ^{42}Ca, (b) ^{43}Ca, and (c) ^{44}Ca for target-in (red lines) and target-out (black lines) measurements, respectively. The momentum acceptance of the BigRIPS separator (±3 %) is also shown by the shaded region in each figure.

4.6.5 Large-Angle Scattering via Elastic Process

If the elastic scattering with the large angle which is beyond the angular acceptance occurs in the reaction target, such events which have to be treated as non-nuclide-changing particles behave like reaction ones in the downstream PID. In the case of 310.5 MeV/nucleon ^{43}Ca beams with C target, the grazing angle $\theta_{\rm gr}$ is about $\theta_{\rm gr} \simeq 1.6$ mrad in the laboratory frame, which is much smaller than the angular acceptance. Therefore, the escaping particles from the angular acceptance of the BigRIPS separator via the elastic scattering process are due to the strong interaction. In the present study, the 40 mrad angular acceptance corresponds to the momentum transfer of $q \sim 6.8$ fm^{-1}. As an example, Fig. 4-34 shows the calculated ratio of elastic scattering cross section to Rutherford scattering one $d\sigma/d\sigma_{\rm Ruth.}$ of ^{70}Ca on ^{40}Ca target at several energies (100, 200, 300, and 400 MeV/nucleon) by T. Furumoto *et al.* [FU12] as a function of q. Though the combination of projectile and target nuclei is different from the present study, the following conclusion is not changed. From this figure, in $q > 6.8$ fm^{-1}, the order of $d\sigma/d\sigma_{\rm Ruth.}$ is approximately 10^{-6}. The integrated Rutherford scattering cross section in $q > 6.8$ fm^{-1} is estimated as ~ 4 mb, so that the corresponding integrated elastic scattering cross section is less than $\sim 10^{-6}$ mb. Therefore, this process does not influence in the present study.

4.6.6 Charge State

The different charge-state particles of the same nuclide locate different positions in the PID plot. In the following, only the hydrogen-like state is considered because the ratio of more-electron-capturing state is obviously negligibly small. In the present experiment, the magnetic field of the whole of the beam line was optimized for the fully-stripped particles ($Q = +20$ for Ca isotopes). In the case of Ca isotopes, the difference of momentum δ (magnetic rigidity) between the fully-stripped and hydrogen-like ($Q = +19$ for Ca isotopes) particles is about 5.3%, so that the hydrogen-like ones cannot transmit to F7 due to the limited momentum acceptance (± 3 %). For this reason, if the contribution of charge state distribution is different between target-in and target-out measurements, the derivation of $\sigma_{\rm I}$ can be influenced.

In the target-in measurement, the condition of the equilibrium charge-state distribution was fulfilled in F5 because the thick reaction target was installed. On the other hand, if the material thickness of detectors in F5 is quite thin, all particles have a fully-stripped charge state because only the fully-stripped particles can transmit from F3 to F5. In that case, non-fully-stripped particles cannot transmit to F7 only in the target-in measurement.

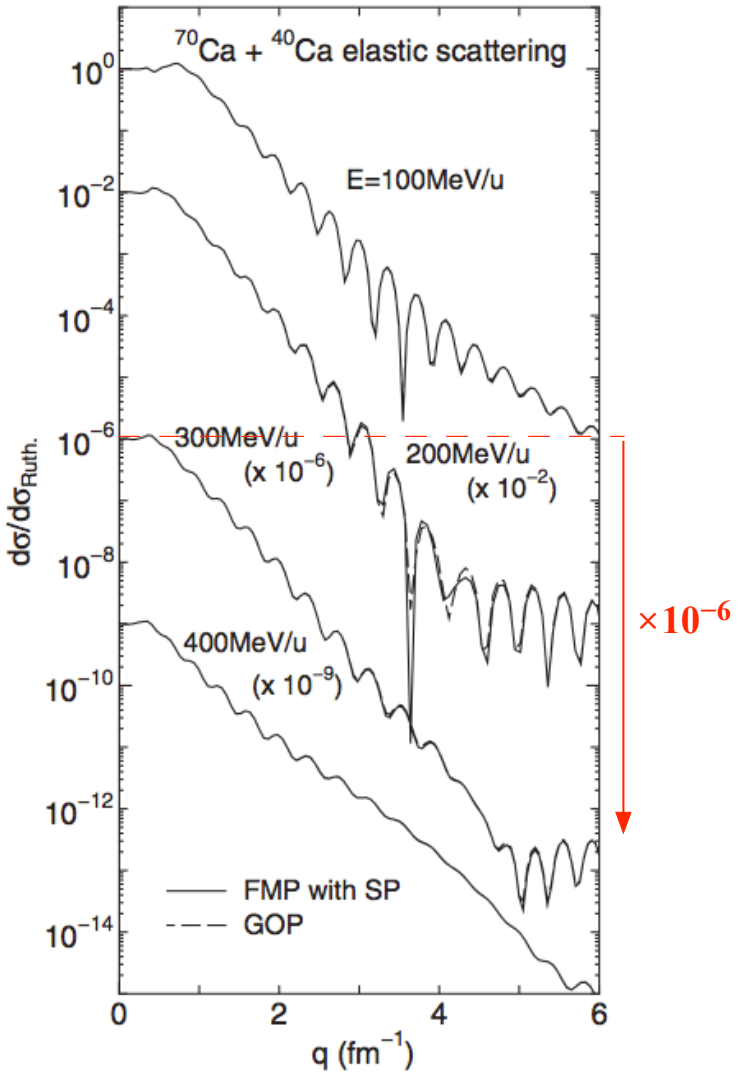

Figure 4-34: Calculated $d\sigma/d\sigma_{\mathrm{Ruth.}}$ of ^{70}Ca on ^{40}Ca target at several energies (100, 200, 300, and 400 MeV/nucleon) by using as a function of q [FU12]. In $q > 6.8$ fm^{-1}, $d\sigma/d\sigma_{\mathrm{Ruth.}}$ reduces approximately $\sim 10^{-6}$. (This figure is taken from Ref. [FU12] with the slight modification.)

However, while the target was not installed in the target-out measurement, the window of F5IC which is the thickest material besides the reaction target in F5 is also enough thick compared to the equilibrium thickness of stainless steel (material of F5IC window). Therefore, the equilibrium condition was fulfilled in both measurements.

Meanwhile, if the charge-state distribution has an energy dependence, the ratio of hydrogen-like state to fully-stripped one is different between both measurements. According to the GLOBAL [SC98] which is a simulation program for the charge-state distribution, the ratios of fully-stripped particles after the reaction target are 99.988% and 99.991% in the target-in and target-out measurements, respectively. This difference results in just $\sim$0.003% reduction of σ_{I}. As a result, the effect of non-fully-stripped particles is not influenced in the present study.

4.7 Derivation of Interaction Cross Section

In the σ_{I} measurements with a target whose thickness is not constant, σ_{I} can be strictly derived as

$$\begin{aligned}\sigma_{\mathrm{I}} &= \frac{\int N(x)\left[\frac{-1}{t(x)}\ln R(x)\right]dx}{\int N(x)dx} \\ &\equiv \langle\frac{-1}{t(x)}\ln R(x)\rangle,\end{aligned} \tag{4.13}$$

where $t(x)$ is the target profile, $R(x)$ the non-reaction rate distribution, and $N(x)$ the beam profile along the horizontal axis x, respectively. In terms of convenience, this equation can be also reduced within less than 10^{-4} discrepancy from Eq. (4.13) as (see Appendix A for details)

$$\sigma_{\mathrm{I}} = \frac{-1}{\langle t(x)\rangle}\ln\langle R(x)\rangle. \tag{4.14}$$

In the present study with $\sim$ 0.1% precisions, both equations Eqs. (4.13) and (4.14) can be employed. Therefore, we utilized Eq. (4.14) which is more easily usable form in order to derive σ_{I}. The weighted mean of target thickness $\langle t(x)\rangle$ on the horizontal beam profile at F5, $N(X_{\mathrm{F5}})$, is summarized in Fig. 4-1.

In terms of reaction energy, the beam energy is not constant due to the energy loss in the target. If we assumed the energy dependence of σ_{I} as $\sigma_{\mathrm{I}} = a_0 + a_1 E$, the weighted mean of σ_{I} on the stopping power can be written as

$$\begin{aligned}\langle\sigma_{\mathrm{I}}(E)\rangle &= \frac{\int_{E_{\mathrm{in}}}^{E_{\mathrm{out}}}\sigma_{\mathrm{I}}(E)\left(\frac{dx}{dE}\right)dE}{\int_{E_{\mathrm{in}}}^{E_{\mathrm{out}}}\left(\frac{dx}{dE}\right)dE} \\ &= a_0 + a_1\left[\frac{\int_{E_{\mathrm{in}}}^{E_{\mathrm{out}}}E(x)\left(\frac{dx}{dE}\right)dE}{\int_{E_{\mathrm{in}}}^{E_{\mathrm{out}}}\left(\frac{dx}{dE}\right)dE}\right] \\ &\equiv a_0 + a_1 E_{\mathrm{ave}} \\ &= \sigma_{\mathrm{I}}(E_{\mathrm{ave}}),\end{aligned} \tag{4.15}$$

where $E_{\rm ave}$ is a mean energy in the target. The above condition is fulfilled in the present measurement. Therefore, we adopted $E_{\rm ave}$ as a reaction energy.

4.8 Experimental Results

The target thickness and energy information are listed in Table 4-1. The experimental results of σ_{I} for $^{40-48}$K, $^{42-51}$Ca, $^{44-46}$Sc on C target are also summarized with their errors in Tables 4-1.

Table 4-1: Summary of average target thickness $\langle t(X_{\mathrm{F5}})\rangle$ and energy information. The E_{in}/A and E_{out}/A represent incident and outgoing energies per nucleon, respectively. The E_{ave}/A means an average energy per nucleon in the reaction target.

Projectile	Target thickness [g/cm^2]	E_{in}/A [MeV]	E_{out}/A [MeV]	E_{ave}/A [MeV]
^{40}K	1.848(3)	324.8	272.0	298.8
^{41}K	1.829(3)	309.6	257.1	283.7
^{42}K	1.807(3)	295.6	243.5	270.0
^{43}K	1.783(3)	281.9	244.8	256.4
^{44}K	1.852(3)	312.1	263.0	287.9
^{45}K	1.838(3)	299.2	250.3	275.1
^{46}K	1.752(3)	320.0	276.5	298.5
^{47}K	1.776(3)	311.2	267.2	289.4
^{48}K	1.788(3)	301.5	257.3	279.7
^{42}Ca	1.822(3)	324.2	269.1	297.0
^{43}Ca	1.807(3)	310.5	255.6	283.5
^{44}Ca	1.785(3)	297.0	242.5	270.2
^{45}Ca	1.841(3)	327.4	275.9	301.9
^{46}Ca	1.839(3)	315.6	264.1	290.2
^{47}Ca	1.810(3)	301.8	250.9	276.7
^{48}Ca	1.721(2)	322.1	276.8	299.7
^{49}Ca	1.742(2)	313.7	268.0	291.1
^{50}Ca	1.761(2)	305.4	259.3	282.6
^{51}Ca	1.748(2)	293.8	247.9	271.2
^{44}Sc	1.791(3)	323.6	266.3	295.4
^{45}Sc	1.780(3)	310.5	253.4	282.4
^{46}Sc	1.761(3)	297.7	240.9	269.8

Table 4-2: Summary of measured σ_{I} and their errors.

Projectile	σ_{I} [mb]	Statistic error [%]	Systematic error		Total error [%]
			Target thickness [%]	Gate width [%]	
^{40}K	1389(28)	2.0	0.15	0.4	2.0
^{41}K	1464(18)	1.2	0.15	0.4	1.3
^{42}K	1428(19)	1.2	0.15	0.4	1.3
^{43}K	1463(22)	1.5	0.15	0.4	1.5
^{44}K	1471(16)	1.0	0.15	0.4	1.1
^{45}K	1518(28)	1.8	0.15	0.4	1.9
^{46}K	1527(20)	1.2	0.15	0.4	1.3
^{47}K	1522(12)	0.7	0.15	0.4	0.8
^{48}K	1543(22)	1.4	0.15	0.4	1.4
^{42}Ca	1460(14)	0.9	0.15	0.4	1.0
^{43}Ca	1475(12)	0.7	0.15	0.4	0.8
^{44}Ca	1505(13)	0.8	0.15	0.4	0.9
^{45}Ca	1477(10)	0.5	0.15	0.4	0.7
^{46}Ca	1503(11)	0.6	0.15	0.4	0.7
^{47}Ca	1508(18)	1.1	0.15	0.4	1.2
^{48}Ca	1485(23)	1.5	0.15	0.4	1.5
^{49}Ca	1580(15)	0.8	0.15	0.4	0.9
^{50}Ca	1618(20)	1.2	0.15	0.4	1.3
^{51}Ca	1677(42)	2.4	0.15	0.4	2.5
^{44}Sc	1463(14)	0.9	0.15	0.4	1.0
^{45}Sc	1488(12)	0.7	0.15	0.4	0.8
^{46}Sc	1514(27)	1.7	0.15	0.4	1.8

5 Discussion

5.1 Deduction of RMS Matter Radii

In order to derive the RMS matter radii $\langle r^2 \rangle_{\rm m}^{1/2}$, which mean RMS ones of nucleon density distributions $\rho_{\rm N}(r)$ from experimental $\sigma_{\rm I}$, the Glauber calculation with the MOL approximation shown in Eq. (2.70) was utilized. As already shown in Sec. 2.5, we can calculate $\sigma_{\rm R}$ from projectile and target densities $\rho^{\rm P,T}(r)$. In the present study, we obtain $\langle r^2 \rangle_{\rm m}^{1/2}$ to reproduce the experimental $\sigma_{\rm I}$ with the Glauber calculation using a model function as a projectile density distribution which will be explained in Sec. 5.1.2.

5.1.1 Nucleon Density Distribution of Target Nucleus ^{12}C

The charge density distribution $\rho_{\rm ch}(r)$ of ^{12}C has been well known by the electron elastic scattering measurement [VR87]. A harmonic-oscillator-type (HO-type) function was employed as a charge density profile of ^{12}C:

$$\rho_{\rm ch}(r) = \rho_0 \left[1 + \alpha \left(\frac{r}{r_0} \right) \right] \exp \left[- \left(\frac{r}{r_0} \right)^2 \right], \tag{5.1}$$

where ρ_0 is a central density. The parameters α and r_0 were determined by the electron elastic scattering [VR87]. This function has to fulfill the following equation:

$$Ze = 4\pi \int \rho_{\rm ch}(r) r^2 dr. \tag{5.2}$$

The charge density distribution includes not only its point-proton density distribution $\rho_{\rm p}(r)$ but also a charge spread of proton itself $\rho_{\rm H}(r)$. Therefore, $\rho_{\rm p}(r)$ was extracted from $\rho_{\rm ch}(r)$ by unfolding $\rho_{\rm H}(r)$ with the following equation as

$$\rho_{\rm ch}(r) = e \int \rho_{\rm H}(r) \rho_{\rm p}(r) d^3 r. \tag{5.3}$$

Hereafter, a "proton" density distribution means a "point-proton" density distribution $\rho_{\rm p}(r)$. Moreover, so as to take the quadrupole deformation effect into account, we modified the functional shape as below:

$$\begin{aligned} \rho(r) &= \int \rho_0 \left\{ 1 + \alpha \left(\frac{r}{R(\theta)} \right) \right\} \exp \left\{ - \left(\frac{r}{R(\theta)} \right)^2 \right\} d\Omega, \\ R(\theta) &= R_0 \left\{ 1 + \beta_2 Y_{20}(\theta) \right\}, \end{aligned} \tag{5.4}$$

where $Y_{20}(\theta)$ is the spherical harmonics. Through the above procedure, $\rho_{\rm p}(r)$ was obtained. Since ^{12}C has the same number of protons and neutrons, we

Table 5-1: Parameters for the density distribution of ^{12}C.

Nuclide	Functional type	R_0	a	β_2
^{12}C	HO	1.42	1.906	−0.623

assumed that the neutron density distribution $\rho_{\rm n}(r)$ is the same as $\rho_{\rm p}(r)$. A "neutron" density distribution also represents a "point-neutron" density distribution. The parameters of ^{12}C density distribution are summarized in Table 5-1. From the previous studies, it has been shown that the energy dependence of $\sigma_{\rm R}$ for ^{12}C on ^{9}Be and ^{27}Al as well as ^{12}C can be reproduced quite well by the Glauber calculation with the MOL approximation using this density distribution [TA05].

5.1.2 Model Functions of Density Distributions of Projectile Nuclei

A two-parameter-Fermi-type (2pF-type) function was assumed as a density profile of the projectile nucleus. We note that $\rho_{\rm p}(r)$ and $\rho_{\rm n}(r)$ were treated with independent parameters. The 2pF-type function is defined as

$$\rho_{\rm p,n}(r) = \rho_{\rm p,n}(0)\frac{1+\exp\left(-\dfrac{C_{\rm p,n}}{a_{\rm p,n}}\right)}{1+\exp\left(\dfrac{r-C_{\rm p,n}}{a_{\rm p,n}}\right)}, \tag{5.5}$$

$a_{\rm p,n}$: surface diffuseness,
$C_{\rm p,n}$: half-density radius,
$\rho_{\rm p,n}(0)$: central density,

Here, subscripts "p" and "n" represent proton and neutron, respectively. In analogy with Eq. (5.2), each density distribution fulfill the following relation:

$$(\text{Number of particles}) = 4\pi\int r^2\rho_{\rm p,n}(r)dr. \tag{5.6}$$

Although a nucleon density distribution $\rho_{\rm N}(r)$ which is a sum of $\rho_{\rm p}(r)$ and $\rho_{\rm n}(r)$ has 6 parameters $a_{\rm p,n}$, $C_{\rm p,n}$, and $\rho_{\rm p,n}(0)$, there are only 4 independent constraints: (1) the present experimental $\sigma_{\rm I}$, (2) the existing charge radius

Table 5-2: Parameters of the 3pF-type functions of ^{40,42,44,48}Ca [FR68] and those of the converted 2pF-type functions through the χ^2-fitting procedure.

Nuclide	$\rho_{\rm ch}(r)$ (3pF-type)			$\rho_{\rm p}(r)$ (2pF-type)		
	C (fm)	a (fm)	w (fm)	C (fm)	a (fm)	$\rho(0)$ (fm^{-3})
^{40}Ca	3.6758	0.5851	−0.1017	3.613	0.493	0.0845
^{42}Ca	3.7278	0.5911	−0.1158	3.642	0.508	0.0824
^{44}Ca	3.7481	0.5715	−0.0948	3.629	0.590	0.0802
^{48}Ca	3.7444	0.5255	−0.03	3.711	0.532	0.0779

$\langle r^2\rangle_{\rm ch}^{1/2}$ obtained from the isotope shift, and Eq. (5.6) for (3) $\rho_{\rm p}(r)$ and (4) $\rho_{\rm n}(r)$. Therefore, we have to consider additional two constraints. In the present study, central densities of proton $\rho_{\rm p}(0)$ and nucleon $\rho_{\rm N}(0)$ were employed as additional constraints. Note that $\rho(0)$ means not only an exact density at $r = 0$ fm but a saturation density in the bulk part of density distribution.

Central Proton Density $\rho_{\rm p}(0)$

Among Ca isotopes, $\rho_{\rm ch}(r)$ of stable isotopes ^{40,42,44,48}Ca were obtained from the electron elastic scattering measurements [FR68]. The three-parameter-Fermi-type (3pF-type) function was assumed as a charge density profile in the analysis of Ref. [FR68]. Therefore, in order to study $\rho_{\rm p}(0)$ of 2pF-type function, we converted these 3pF-type functions to the 2pF-type ones with the χ^2-fitting procedure. In this analysis, $\rho_{\rm H}(r)$ was unfolded from $\rho_{\rm ch}(r)$ in order to derive $\rho_{\rm p}(r)$. Table 5-2 shows obtained parameters of converted 2pF-type functions. The obtained $\rho_{\rm p}(0)$ are plotted by red open circles as a function of $\delta = (N - Z)/A$ in Fig.5-1. In comparison, $\rho_{\rm p}(0)$ of Fe, Zn, and Sn isotopes are also shown in the same figure. Here, the 3pF-type function was also adopted to Sn isotopes, so that the same procedure as Ca isotopes was performed to Sn isotopes in order to extract $\rho_{\rm p}(0)$ of 2pF-type function. The linear decrease of $\rho_{\rm p}(0)$ along δ can be seen for all isotope chains. The possible reason is considered that the proton radius enlarges as increasing neutron excess to reduce the symmetry energy at the nuclear surface, so that this tendency may be regarded as a common feature in any isotopic chains. Furthermore, the Hartree-Fock (HF) calculations of Sn isotopes with Gogny D1S, NL3, and SLy4 interactions [WA10] also support this dependence. Therefore, the constraint on $\rho_{\rm p}(0)$ was determined

by fitting $\rho_{\rm p}(0)$ of Ca isotopes as a function of δ with a linear function:

$$\rho_{\rm p}(0) = 0.0843 - 0.0389\delta \ [\mathrm{fm}^{-3}]. \tag{5.7}$$

While the δ dependence of $\rho_{\rm p}(0)$ of K and Sc isotopes cannot be mentioned because there is little data on the charge distributions in the isotopic chain, the difference of $\rho_{\rm p}(0)$ between Ca and Fe or Zn isotopes is small. For this reason, K and Sc isotopes are treated here by the same condition as Eq. (5.7).

As a result, $\rho_{\rm p}(r)$ can be determined by the combination of the RMS proton radius $\langle r^2 \rangle_{\rm p}^{1/2}$ [AN13, KR14, GA16] and Eq. (5.7). Here, $\langle r^2 \rangle_{\rm p}^{1/2}$ can be obtained from the unfolding procedure given as

$$\langle r^2 \rangle_{\rm p} = \langle r^2 \rangle_{\rm ch} - R_{\rm p}^2 - \frac{N}{Z} R_{\rm n}^2 - \frac{3\hbar^2}{4m_{\rm p}^2 c^2}, \tag{5.8}$$

where $R_{\rm p,n}$ are respective RMS charge radii of proton and neutron themselves ($R_{\rm p} = 0.8751(61)$ fm [PA16], $R_{\rm n}^2 = -0.1149(24)$ fm [KO97]) and $3\hbar^2/(4m_{\rm p}^2c^2)$ represents the Darwin-Foldy correction term [FR97]. Parameters of each proton density profile are summarized in Table 5-3.

Table 5-3: Parameters of each proton density distribution $\rho_{\rm p}(r)$.

Nuclide	$\langle r^2\rangle_{\rm p}^{1/2}$ (fm)	$C_{\rm p}$ (fm)	$a_{\rm p}$ (fm)	$\rho_{\rm p}(0)$ (fm^{-3})
^{40}K	3.333(4)	3.595	0.4930	0.08231
^{41}K	3.349(4)	3.606	0.4971	0.08138
^{42}K	3.350(4)	3.626	0.4912	0.08050
^{43}K	3.353(5)	3.644	0.4868	0.07966
^{44}K	3.352(4)	3.663	0.4801	0.07886
^{45}K	3.358(5)	3.678	0.4783	0.07809
^{46}K	3.348(4)	3.701	0.4651	0.07736
^{47}K	3.349(4)	3.718	0.4602	0.07666
^{48}K	3.378(4)	3.718	0.4748	0.07599
^{42}Ca	3.411(3)	3.643	0.5158	0.08240
^{43}Ca	3.397(3)	3.671	0.5003	0.08152
^{44}Ca	3.424(3)	3.675	0.5117	0.08067
^{45}Ca	3.401(3)	3.708	0.4900	0.07987
^{46}Ca	3.396(3)	3.725	0.4845	0.07910
^{47}Ca	3.379(3)	3.753	0.4660	0.07836
^{48}Ca	3.380(3)	3.770	0.4604	0.07765
^{49}Ca	3.395(3)	3.778	0.4654	0.07697
^{50}Ca	3.424(3)	3.778	0.4810	0.07632
^{51}Ca	3.439(3)	3.785	0.4865	0.07569
^{44}Sc	3.442(2)	3.712	0.5114	0.08249
^{45}Sc	3.445(3)	3.730	0.5076	0.08164
^{46}Sc	3.424(9)	3.761	0.4865	0.08083

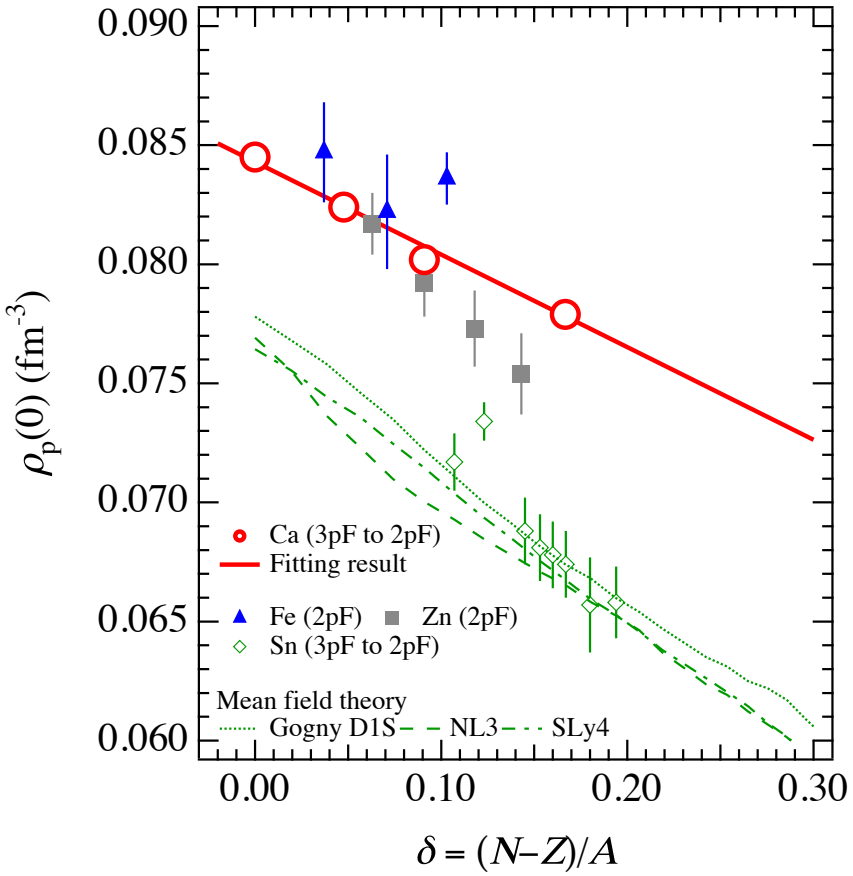

Figure 5-1: Relative neutron excess δ dependence of $\rho_p(0)$. Open circles, closed triangles, closed squares, and open diamonds represent Ca, Fe, Zn, and Sn isotopes, respectively, which were calculated with parameters of respective Fermi functions deduced by elastic electron scattering experiments [VR87]. $\rho_p(0)$ of Ca and Sn isotopes (open symbols) were deduced by converting 3pF-type functions to 2pF ones. The solid red line represents the function Eq. 5.7. The dotted, dashed, and dash-dotted lines show HF calculations for Sn isotopes with Gogny D1S, NL3, SLy4 interactions, respectively [WA10].

Central Nucleon Density $\rho_{\mathrm{N}}(0)$

As mentioned in Sec. 1.2, the elastic scattering from ^{40,42,44,48}Ca by using proton, α, and pion beams were measured so far [FR68, AL76, AL77, CH77, RA81, AL82, BO84]. In the analyses of hadron elastic scatterings, the 3pF-type function was also employed as $\rho_{\mathrm{N}}(r)$. Therefore, we convert these 3pF-type functions to 2pF-type ones in the same manner as $\rho_{\mathrm{ch}}(r)$. Fig. 5-2 shows the central density of nucleon density distribution $\rho_{\mathrm{N}}(0)$ as a function of δ. While there are large discrepancies between the data one another for each isotope, $\rho_{\mathrm{N}}(0)$ seems to be independent on δ, which are different from the case of $\rho_{\mathrm{p}}(0)$. This property may be considered as a saturation property of nuclear matter.

Figure 5-3 shows theoretical central densities of proton, neutron, and nucleon density distributions $\rho_{\mathrm{p,n,N}}(0)$ of Sn and Pb isotopes obtained from the conversion of the HF densities with Gogny D1S, NL3, and SLy4 interactions to the 2pF-type functions [WA10]. Any interactions support the constant saturation property of $\rho_{\mathrm{N}}(0)$ for both isotopes. Furthermore, we show respective parameters of 2pF-type function for Sn and Pb isotopes obtained from the same manner as $\rho_{\mathrm{p,n,N}}(0)$ with HF calculations using Gogny D1S interaction [WA10] in Fig. 5-4. Though a and C are influenced by a shell effect which can be seen as a dip or a kink in Fig. 5-4. For this reason, constraints on $\rho_{\mathrm{p}}(0)$ and $\rho_{\mathrm{N}}(0)$ may be the most preferable.

Hence, we assumed that $\rho_{\mathrm{N}}(0)$ has a constant value for any isotopes. The constant $\rho_{\mathrm{N}}(0)$ was obtained by the weighted mean of experimental $\rho_{\mathrm{N}}(0)$ whose own error was mentioned in respective references (shown by closed symbols in Fig. 5-2) as

$$\rho_{\mathrm{N}}(0) = 0.176 \ [\mathrm{fm}^{-3}]. \tag{5.9}$$

The standard deviation $\Delta\rho_{\mathrm{N}}(0)$ around the weighted mean value shown by the red shaded band in Fig. 5-2 was taken into consideration as a systematic error when we deduce a matter radius (mentioned in detail in Fig. 5-5) :

$$\Delta\rho_{\mathrm{N}}(0) = 0.011 \ [\mathrm{fm}^{-3}]. \tag{5.10}$$

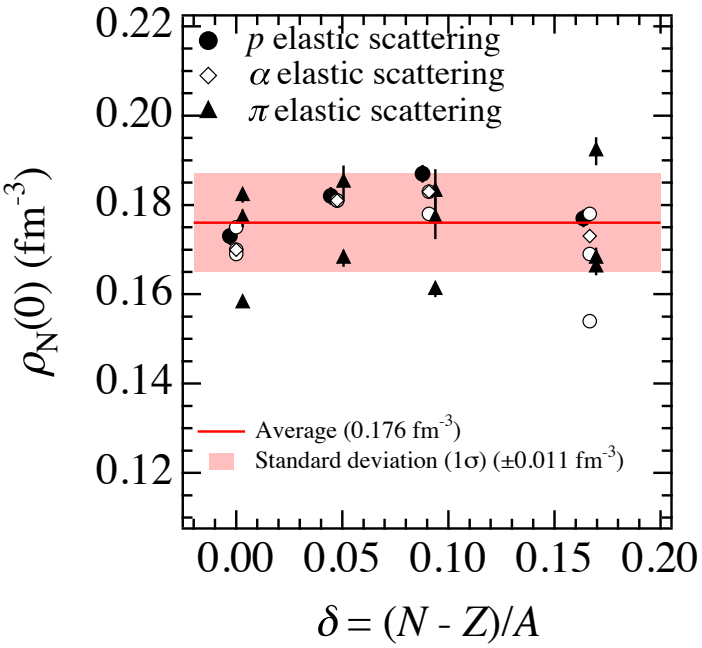

Figure 5-2: Relative neutron excess δ dependence of $\rho_N(0)$ of ^{40,42,44,48}Ca deduced by proton (circle), α (diamond), and pion (triangle) elastic scatterings, respectively [FR68, AL76, AL77, CH77, RA81, AL82, BO84]. Closed (Open) symbols mean data with (without) error information. The solid line represents the weighted-mean value Eq. 5.9 for all closed symbols. The standard deviation around the weighted-mean value is also shown by the red shaded band.

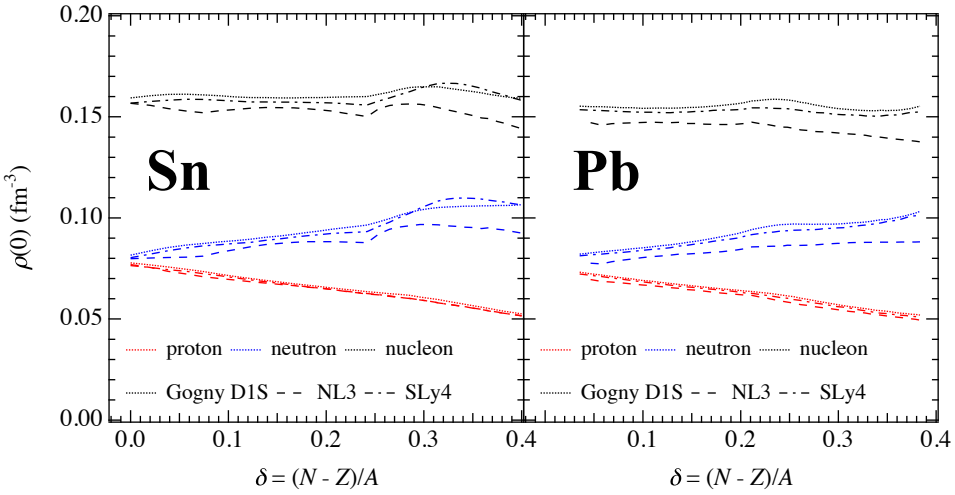

Figure 5-3: Relative neutron excess δ dependence of $\rho_{p,n,m}(0)$ (red, blue, black) of Sn and Pb isotopes obtained from the conversion of the HF densities with Gogny D1S (dotted lines), NL3 (dashed lines), and SLy4 (dash-dotted lines) interactions to the 2pF-type functions [WA10].

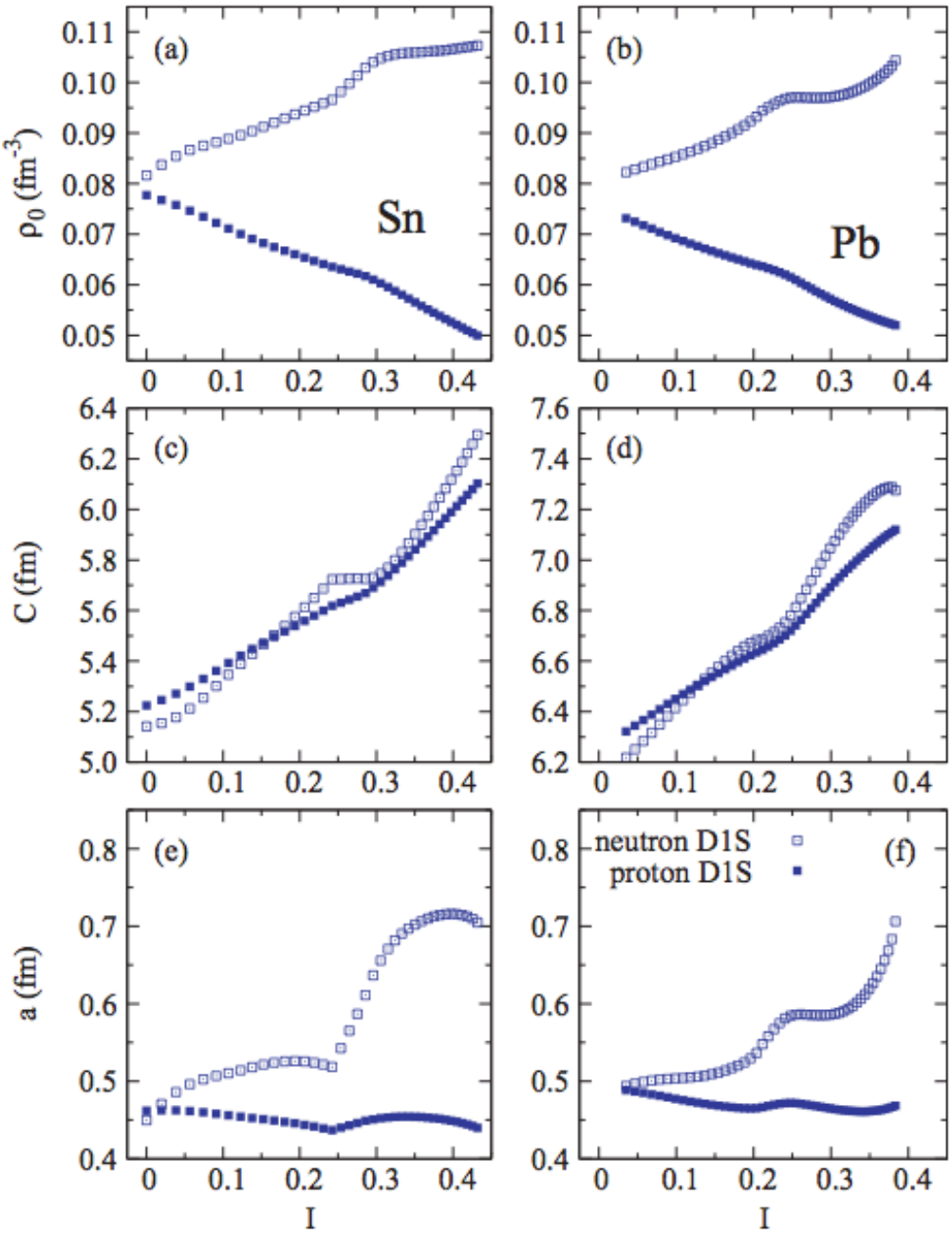

Figure 5-4: Relative neutron excess δ (written by "I") dependence of $\rho_{\mathrm{p,n}}(0)$ (written by "ρ_0"), $C_{\mathrm{p,n}}$, and $a_{\mathrm{p,n}}$ of Sn and Pb isotopes obtained from the conversion of the HF densities with Gogny D1S interaction to the 2pF-type functions. This figure is taken from Ref. [WA10].

5.1.3 Deduced RMS Radii $\langle r^2 \rangle^{1/2}$ and Neutron Skin Thickness r_{np}

In consequence, with assumptions on the projectile density distribution mentioned in Sec. 5.1.2, we can deduce the RMS neutron and matter radii $\langle r^2 \rangle^{1/2}_{\rm n,m}$ defined as

$$\langle r^2 \rangle^{1/2}_{\rm n} = \sqrt{\frac{4\pi}{N} \int r^4 \rho_{\rm n}(r) dr}, \tag{5.11}$$

$$\langle r^2 \rangle^{1/2}_{\rm m} = \sqrt{\frac{4\pi}{A} \int r^4 \rho_{\rm N}(r) dr}. \tag{5.12}$$

These respective RMS radii are related to each other by the following equation:

$$A\langle r^2 \rangle_{\rm m} = Z\langle r^2 \rangle_{\rm p} + N\langle r^2 \rangle_{\rm n}. \tag{5.13}$$

Fig. 5-5 is the contour plot of $\sigma_{\rm I}$ in relation to $\rho_{\rm N}(0)$ and $\langle r^2 \rangle^{1/2}_{\rm m}$ for ^{42}Ca together with the experimental $\sigma_{\rm I}$ (red solid line) and its corresponding error (shaded band). The correlation between $\langle r^2 \rangle^{1/2}_{\rm m}$ and $\sigma_{\rm I}$ has a gentle dependence on $\rho_{\rm N}(0)$. Therefore, a change of $\langle r^2 \rangle^{1/2}_{\rm m}$ within the uncertainty of central nucleon density $\Delta\rho_{\rm N}(0)$ shown by the blue dotted lines was estimated as a systematic error of $\langle r^2 \rangle^{1/2}_{\rm m}$. This systematic error is about 0.02 fm, which is comparable to the most precise statistical error in the present study.

As an example, $\rho_{\rm p}(r)$ and the deduced $\rho_{\rm n}(r)$ of ^{49}Ca are shown in Fig. 5-6. The neutron skin structure emerges at the nuclear surface. From the difference of RMS radii of these density distributions, we can obtain the neutron skin thickness $r_{\rm np}$. The deduced $\langle r^2 \rangle^{1/2}_{\rm n,m}$ and $r_{\rm np}$ are summarized together with $\langle r^2 \rangle^{1/2}_{\rm p}$ [AN13, KR14, GA16] in Table 5-4.

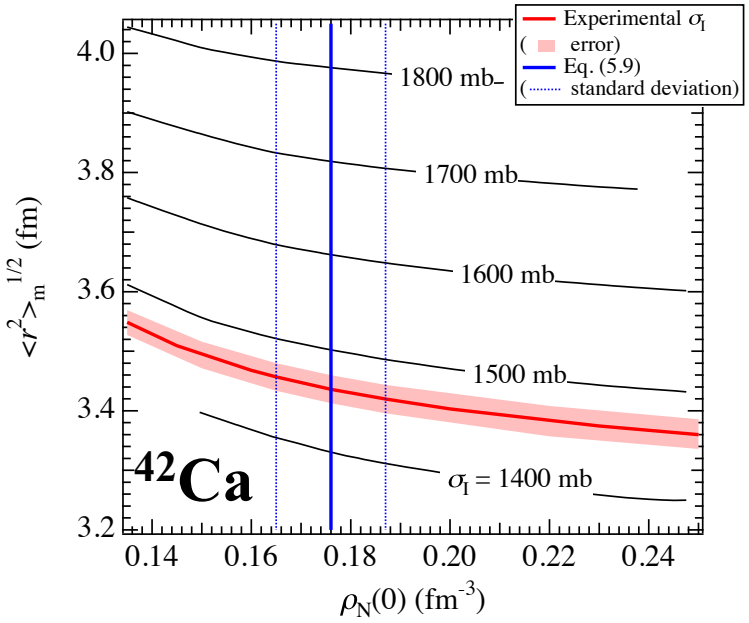

Figure 5-5: Contour plot of $\sigma_{\rm I}$ of $\rho_{\rm N}(0)$ with $\langle r^2 \rangle_{\rm m}^{1/2}$ for ^{42}Ca. The red line and shaded band represent the experimental $\sigma_{\rm I}$ and its corresponding error, respectively. The blue solid and dotted lines show the constraint on $\rho_{\rm N}(0)$ and its standard deviation $\Delta\rho_{\rm N}(0)$ defined by Eqs. (5.9) and (5.10).

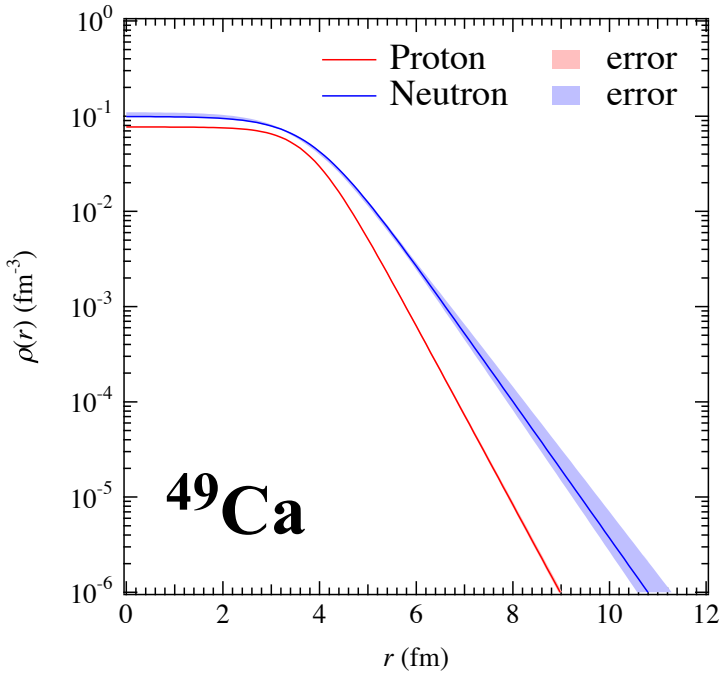

Figure 5-6: Summary of deduced $\rho_{\rm p}(r)$ (red) and $\rho_{\rm n}(r)$ (blue) of ^{49}Ca. The shaded band represents an error region.

Table 5-4: Deduced $\langle r^2 \rangle_{\rm n,m}^{1/2}$ and $r_{\rm np}$ together with $\langle r^2 \rangle_{\rm p}^{1/2}$ [AN13, KR14, GA16]. Round and square brackets show statistical error and systematic one resulting from $\Delta\rho_{\rm N}(0)$, respectively.

Nuclide	$\langle r^2 \rangle_{\rm p}^{1/2}$ (fm)	$\langle r^2 \rangle_{\rm n}^{1/2}$ (fm)	$\langle r^2 \rangle_{\rm m}^{1/2}$ (fm)	$r_{\rm np}$ (fm)
^{40}K	3.328(6)	3.32(9)[3]	3.32(5)[2]	−0.01(9)[3]
^{41}K	3.344(6)	3.53(6)[3]	3.43(3)[2]	0.18(6)[3]
^{42}K	3.344(6)	3.39(6)[3]	3.37(3)[2]	0.05(6)[3]
^{43}K	3.348(6)	3.47(6)[3]	3.42(4)[2]	0.13(6)[3]
^{44}K	3.347(6)	3.51(4)[3]	3.44(3)[2]	0.16(4)[3]
^{45}K	3.353(7)	3.61(7)[3]	3.51(4)[2]	0.26(7)[3]
^{46}K	3.343(6)	3.64(5)[3]	3.52(3)[2]	0.30(5)[3]
^{47}K	3.344(6)	3.62(3)[3]	3.509(18)[21]	0.27(3)[3]
^{48}K	3.372(6)	3.64(5)[3]	3.54(3)[2]	0.27(5)[3]
^{42}Ca	3.406(5)	3.46(4)[3]	3.44(2)[2]	0.06(4)[3]
^{43}Ca	3.392(5)	3.50(4)[3]	3.45(2)[2]	0.11(4)[3]
^{44}Ca	3.418(5)	3.55(4)[3]	3.49(2)[2]	0.13(4)[3]
^{45}Ca	3.395(5)	3.50(3)[3]	3.451(16)[19]	0.10(3)[3]
^{46}Ca	3.396(5)	3.55(3)[3]	3.486(17)[20]	0.16(3)[3]
^{47}Ca	3.379(5)	3.56(5)[3]	3.49(3)[2]	0.18(5)[3]
^{48}Ca	3.380(5)	3.51(6)[4]	3.45(3)[2]	0.13(6)[4]
^{49}Ca	3.395(5)	3.72(4)[3]	3.59(2)[2]	0.33(4)[3]
^{50}Ca	3.424(5)	3.78(4)[3]	3.64(3)[2]	0.36(4)[3]
^{51}Ca	3.439(5)	3.89(9)[3]	3.72(6)[2]	0.45(9)[3]
^{44}Sc	3.442(5)	3.42(4)[3]	3.43(2)[2]	−0.02(4)[3]
^{45}Sc	3.445(5)	3.48(4)[3]	3.465(19)[18]	0.04(4)[3]
^{46}Sc	3.424(10)	3.56(7)[3]	3.50(4)[2]	0.13(8)[3]

5.2 Evolution of Nuclear Radii

5.2.1 Comparison to Results of Hadron Elastic Scattering

First of all, we compare the present $\langle r^2 \rangle_{\rm m}^{1/2}$ of the Ca isotopic chain to the previous values deduced from hadron elastic scattering measurements [AL77, CH77, AL82, BO84, MC86, GI92] in Fig. 5-7. Although the absolute values of $\langle r^2 \rangle_{\rm m}^{1/2}$ have large discrepancies between the data one another in respective stable isotopes, the relative values of $\langle r^2 \rangle_{\rm m}^{1/2}$ from the one of ^{48}Ca are relatively consistent with each other, including present results as shown in Fig. 5-8. Moreover, present results can be obtained systematically along the long chain with better precisions. Especially, there are first experimental results of matter and neutron radii beyond the neutron magic number $N = 28$. Therefore, the present results make us to discuss the evolution of matter and neutron radii in Ca isotopes.

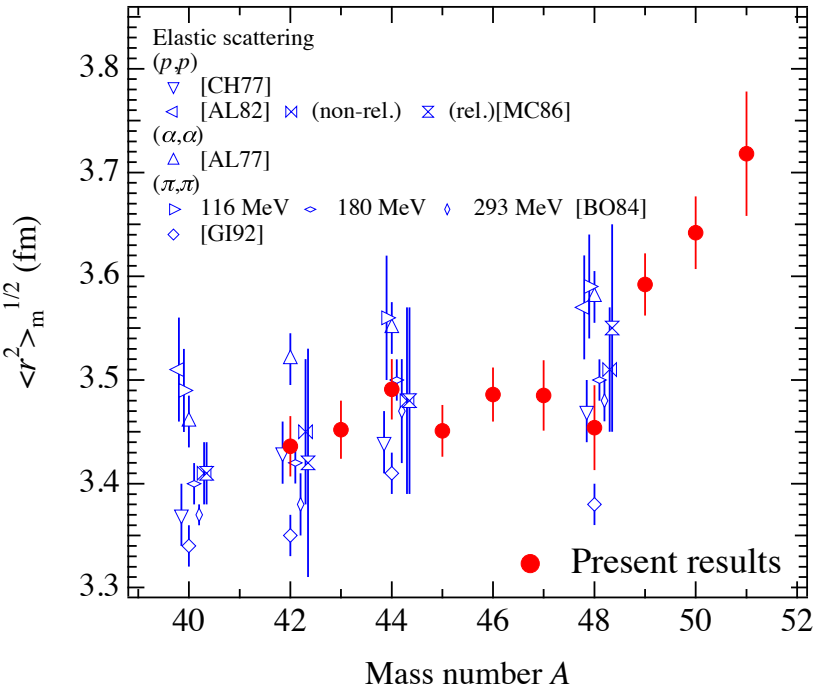

Figure 5-7: Deduced $\langle r^2 \rangle_{\rm m}^{1/2}$ of Ca isotopes in comparison with previous experimental results deduced by hadron elastic scattering measurements [AL77, CH77, AL82, BO84, MC86, GI92]. In Ref. [MC86], $\langle r^2 \rangle_{\rm m}^{1/2}$ were derived with both of a non-relativistic (non-rel.) and a relativistic (rel.) analyses. The pion elastic scattering of Ref. [BO84] with different bombarding energies 116, 180, and 293 MeV are also shown, respectively.

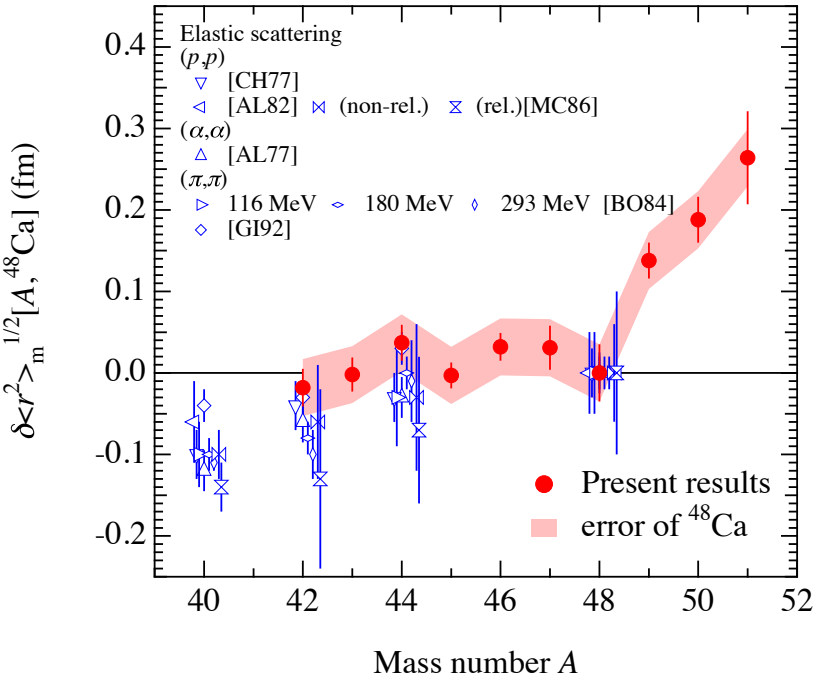

Figure 5-8: Relative value of $\langle r^2 \rangle_{\rm m}^{1/2}$ to the one of ^{48}Ca, $\delta\langle r^2 \rangle_{\rm m}^{1/2}[A, 48]$, as a function of mass number A. The red filled band represents the error of present $\langle r^2 \rangle_{\rm m}^{1/2}$ of ^{48}Ca. Other definitions are the same as for Fig. 5-7.

5.2.2 Mass Number Dependence

Figures 5-9 and 5-10 show $\langle r^2 \rangle_{\rm m}^{1/2}$ of Ca, K, and Sc isotopes together with the systematic A dependence of stable nuclei (black solid line) and its standard deviation (gray shaded band). This systematics was obtained by fitting $\langle r^2 \rangle_{\rm p}^{1/2}$ of stable nuclei with a $A^{1/3}$ function (the detailed information is mentioned in Appendix B). Stable nuclei located near the beta-stability line have similar proton and neutron radii ($\langle r^2 \rangle_{\rm p}^{1/2} \simeq \langle r^2 \rangle_{\rm n}^{1/2} \simeq \langle r^2 \rangle_{\rm m}^{1/2}$). For most of Ca isotopes whose valence neutrons are sitting in $1f_{7/2}$ orbital, their $\langle r^2 \rangle_{\rm m}^{1/2}$ are roughly consistent with the systematics of stable nuclei. On the other hand, $\langle r^2 \rangle_{\rm m}^{1/2}$ of Ca isotopes beyond $N = 28$ increase rapidly apart from the systematics of stable nuclei. The point where the slope of A dependence change corresponds to the magic number $N = 28$. Across this magic number, the configuration of valence neutron orbital changes from the $1f_{7/2}$ to the $2p_{3/2}$. Such a shell closure effect also can be seen in $\langle r^2 \rangle_{\rm m,n}^{1/2}$ as well as $\langle r^2 \rangle_{\rm ch}^{1/2}$ (mentioned in Sec. 1.2).

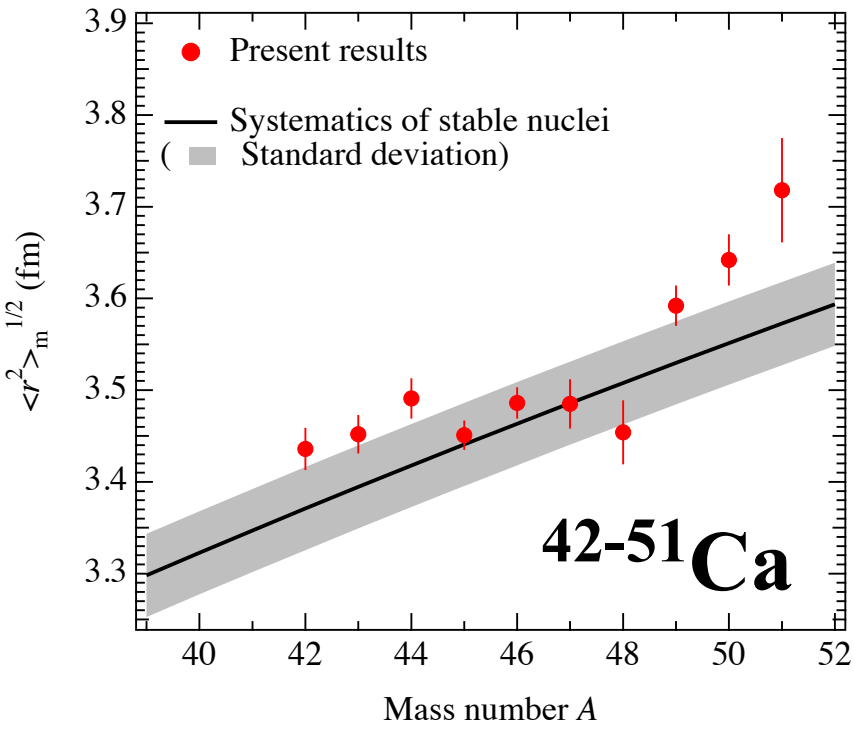

Figure 5-9: Mass number dependence of $\langle r^2 \rangle_{\rm m}^{1/2}$ of $^{42-51}$Ca. The black solid line and shaded band represent systematics of stable nuclei and their standard deviation, respectively.

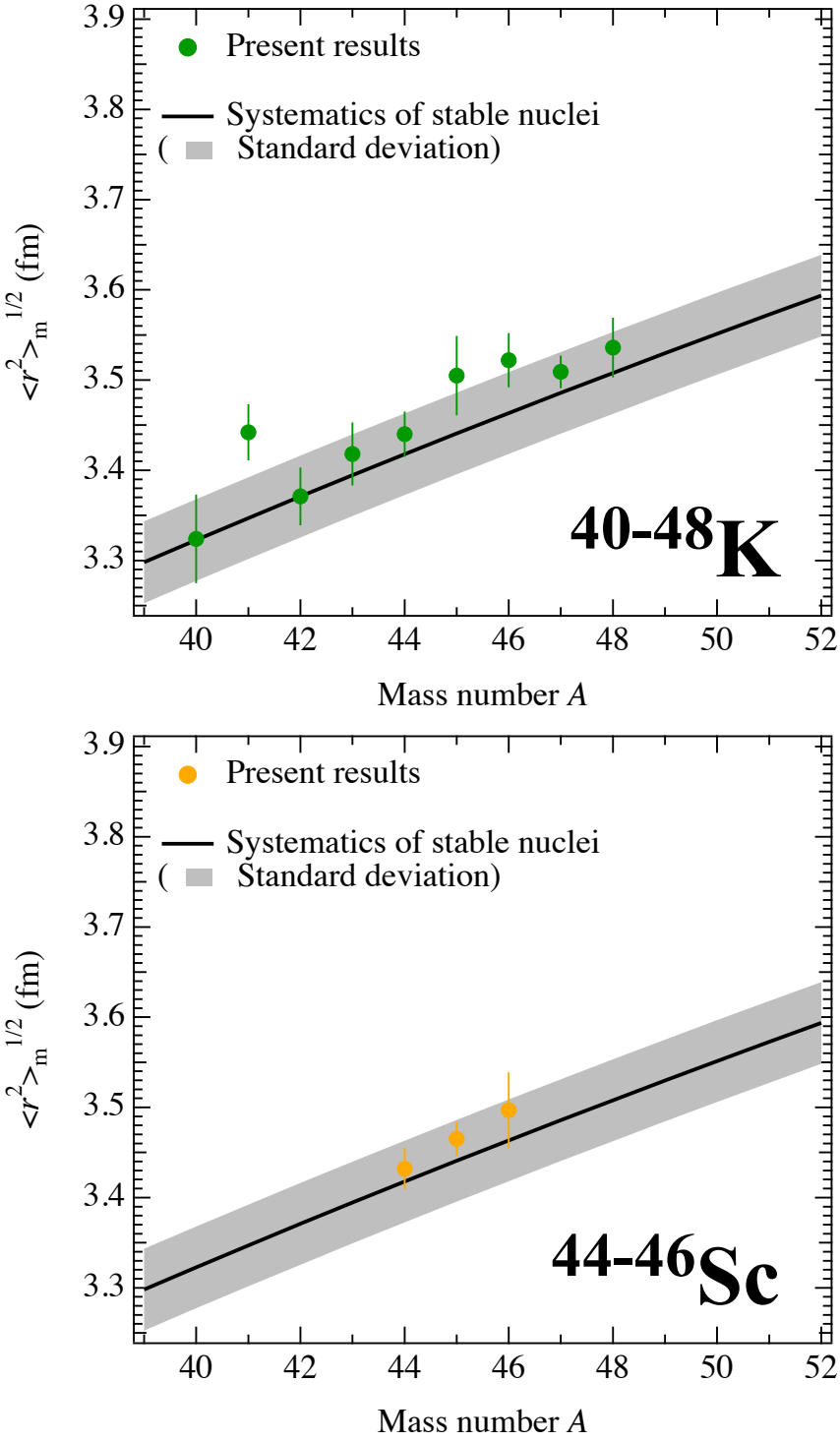

Figure 5-10: The same figures as Fig. 5-9 of $^{40-48}$K and $^{44-46}$Sc.

5.2.3 Contribution of Quadrupole Deformation

Nuclear radii are also influenced by a nuclear deformation. Especially, the systematics of $\sigma_{\rm I}$ for neutron-rich Ne and Mg isotopes which include nuclei located in the island of inversion around $N = 20$ can be reproduced by taking the quadrupole deformation into account [TA12, SU13, TA14]. Thereby, we also consider the effect of quadrupole deformation in the Ca region so as to confirm whether the large enhancement of $\langle r^2 \rangle_{\rm m}^{1/2}$ beyond $N = 28$ can be explained by nuclear deformation or not.

The RMS radius of a deformed nucleus $\langle r^2 \rangle_{\rm def}^{1/2}$ can be obtained with that of a spherical nucleus $\langle r^2 \rangle_{\rm sph}^{1/2}$ [SC14] as

$$\langle r^2 \rangle_{\rm def}^{1/2} = \langle r^2 \rangle_{\rm sph}^{1/2} \sqrt{1 + \frac{5}{4\pi}\beta_2^2}, \tag{5.14}$$

where the β_2 is a quadrupole deformation parameter. Under the assumption of the rotation of a uniformly charged quadrupolar deformed nucleus, the β_2 can be derived with a $0_1^+ \rightarrow 2_1^+$ reduced transition probability $B(E2)\uparrow$ [PR16] as

$$B(E2)\uparrow = e^2 \left(\frac{3Zr_0^2}{4\pi} \right) \beta_2^2. \tag{5.15}$$

We can also obtain β_2 from an electric quadrupole moment as

$$Q_0 = \sqrt{\frac{3}{5\pi}} (Zr_0^2)\beta_2, \tag{5.16}$$

where Q_0 is the intrinsic electric quadrupole moment. The Q_0 is related with the spectroscopic electric quadrupole moment Q which is an observable in an measurement as

$$Q = \frac{I(2I-1)}{(I+1)(2I+3)} Q_0. \tag{5.17}$$

We summarize β_2 of K, Ca, and Sc isotopes derived from the experimental $B(E2)\uparrow$ and Q in Table 5-5 [CO66, AV11, GA15, TE15, PR16]. Note that the β_2 of $^{42-48}$K cannot refer because these have not been measured yet. In the Ca region, the absolute value of quadrupole deformation parameter $|\beta_2|$ as shown in Fig. 5-11 is at most about 0.25, which is not so large compared to nuclei in the island of inversion as $|\beta_2| = 0.3 \sim 0.6$. The moderate deformation around the midpoint of $1f_{7/2}$ shell such as ^{42}Ca and ^{44}Ca was described qualitatively by taking the effect of nucleon excitations across the *sd* shell into account within the framework of large-scale shell model calculation [CA01]. The importance of cross-shell excitation was also pointed out

from the point of view of the experimental charge radii [CA01] and magnetic moments [GA15, SC03, TAY05].

In Figs. 5-12 and 5-13, the present results are compared to the values taking into account the deformation effect (open squares) based on Eq. (5.14), where the systematics of stable nuclei was adopted as $\langle r^2 \rangle_{\rm sph}^{1/2}$. From this comparison, the gentle enhancements on $\sigma_{\rm I}$ around the midpoint of $1f_{7/2}$ shell (^{41}K and ^{42,44}Ca) are regarded as a consequence of nuclear deformation. On the other hand, the trend of $\langle r^2 \rangle_{\rm m}^{1/2}$ beyond $N = 28$ cannot be explained at all.

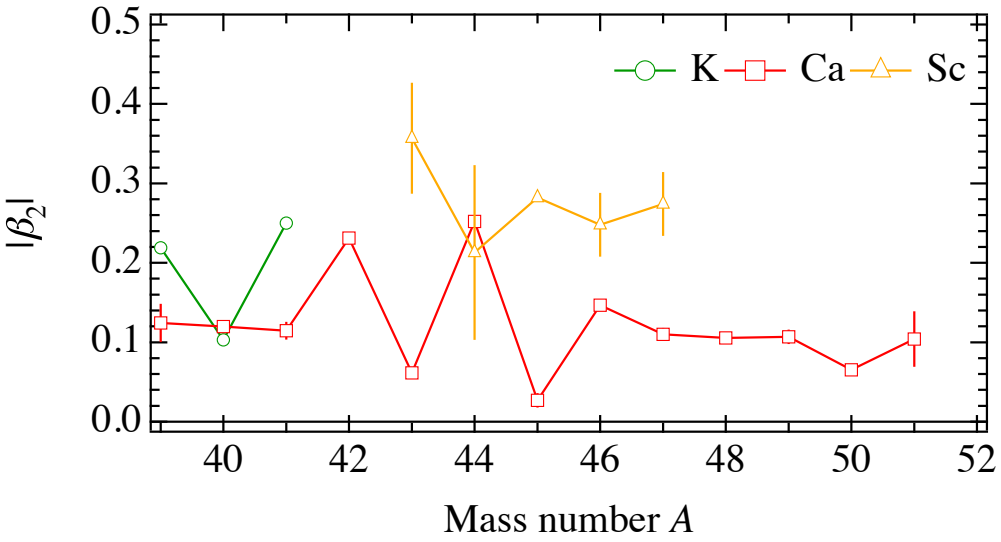

Figure 5-11: Absolute values of quadrupole deformation parameter $|\beta_2|$ as a function of Mass number A.

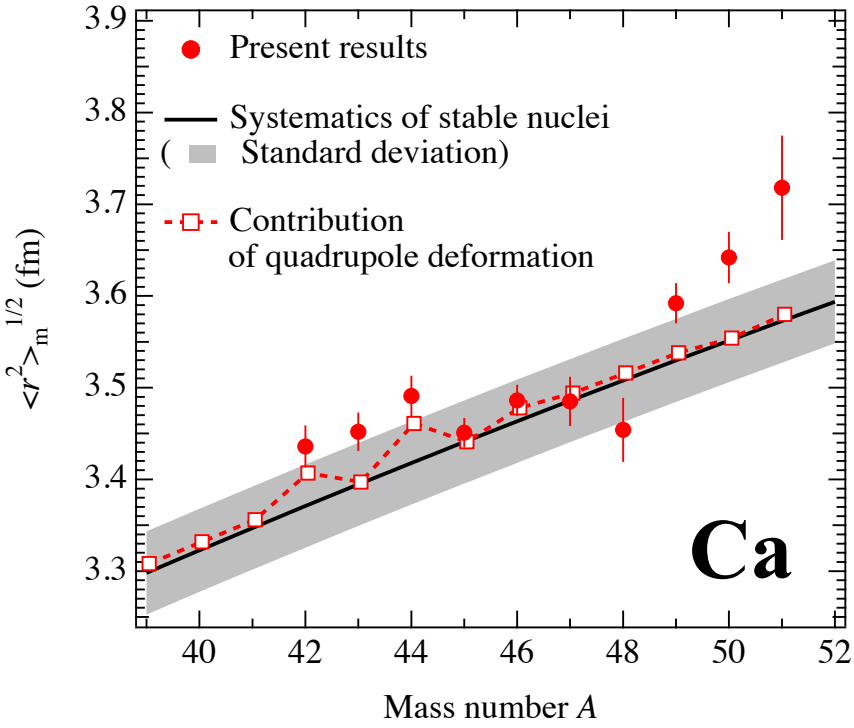

Figure 5-12: Comparison of experimental $\langle r^2 \rangle_{\rm m}^{1/2}$ with RMS radii including the contribution of quadrupole deformation shown (open squares) in Ca isotopes. Other definitions are the same as Fig. 5-9.

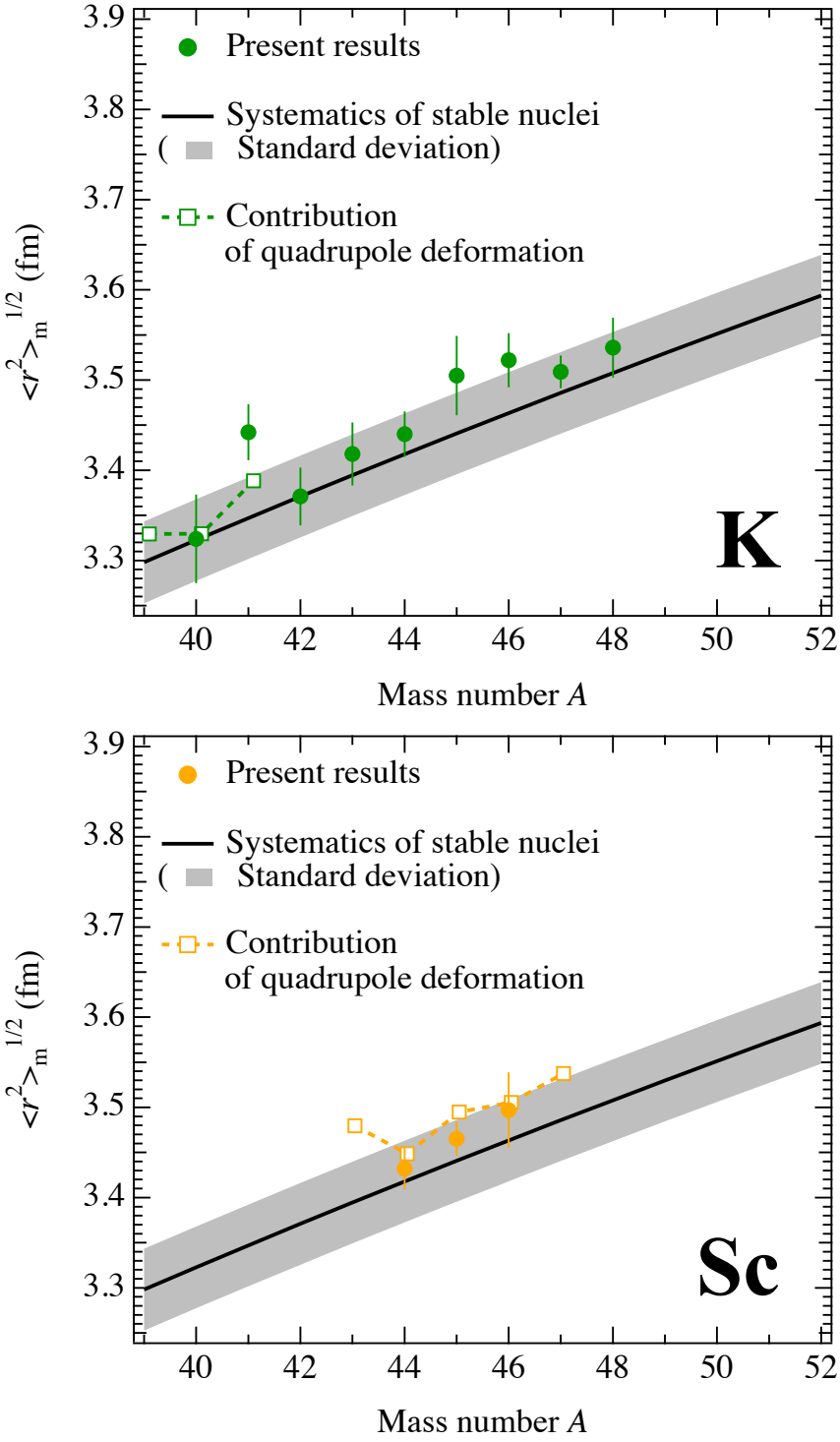

Figure 5-13: The same figures as Fig. 5-12 of $^{40-48}$K and $^{44-46}$Sc.

Table 5-5: Summary of experimental Q, $B(E2)\uparrow$, and β_2 [CO66, AV11, GA15, TE15, PR16].

Nuclide	I	Q $(e\cdot\mathrm{fm}^2)$	$B(E2)\uparrow$ $(e^2\cdot\mathrm{fm}^4)$	β_2 (fm)
^{39}K	3/2	6.03(6)		0.219(2)
^{40}K	4	−7.51(8)		−0.1055(11)
^{41}K	3/2	7.34(7)		0.258(3)
^{39}Ca	3/2	3.6(7)		0.12(2)
^{40}Ca	0		92(70)	0.120(4)
^{41}Ca	7/2	−8.0(8)		−0.115(11)
^{42}Ca	0		369(20)	0.231(6)
^{43}Ca	7/2	−4.44(6)		−0.0616(8)
^{44}Ca	0		467(21)	0.252(6)
^{45}Ca	7/2	2.0(7)		0.027(9)
^{46}Ca	0		168(13)	0.147(6)
^{47}Ca	7/2	8.4(6)		0.110(8)
^{48}Ca	0		$92(^{+12}_{-5})$	$0.105(^{+7}_{-3})$
^{49}Ca	3/2	−3.6(3)		−0.107(9)
^{50}Ca	0		$37.3(^{+20}_{-18})$	$0.0654(^{+18}_{-16})$
^{51}Ca	3/2	3.6(12)		0.10(4)
^{43}Sc	7/2	−27(5)		−0.36(7)
^{44}Sc	2	10(5)		0.21(11)
^{45}Sc	7/2	−22.0(2)		−0.282(3)
^{46}Sc	2	12(2)		0.25(4)
^{47}Sc	7/2	−22(3)		−0.27(4)

5.2.4 Enhancement Mechanism of Nuclear Radii beyond $N = 28$

The trend of $\langle r^2 \rangle_{\rm m}^{1/2}$ beyond $N = 28$ cannot be interpreted by taking the deformation effect into consideration. We investigate this mechanism further in the following.

Examination by Single Particle Model

The nuclear radius is enhanced when the valence nucleon has a small orbital angular momentum such as s or p waves and is bound loosely. Beyond $N = 28$, the configuration of valence neutron is changed from $1f_{7/2}$ to $2p_{3/2}$ orbitals, so that the wave function of valence neutron can spread spatially. Therefore, in the case of ^{49}Ca, we considered a single particle model (SPM) with the combination of ^{48}Ca core and a $2p_{3/2}$ valence neutron $(\nu 2p_{3/2})^1$.

The wave function of valence neutron was calculated by solving a Schrödinger equation using a Woods-Saxon potential $V_{\rm WS}$ plus centrifugal $V_{\rm CF}$ as well as plus spin-orbit $V_{\rm LS}$ ones:

$$\begin{aligned} V(r) &= V_{\rm WS} + V_{\rm CF} + V_{\rm LS} \\ &= \frac{V_0}{1+\exp\left(\frac{r-r_0}{a}\right)} + \frac{l(l+1)\hbar^2}{2\mu r^2} - 0.44 V_0 (\vec{l}\cdot\vec{s}) r_0^2 \frac{1}{r^2}\frac{d}{dr}\left[\frac{1}{1+\exp\left(\frac{r-r_0}{a}\right)}\right] \end{aligned} \tag{5.18}$$

with

$$\begin{aligned} r_0 &\equiv 1.2 A^{1/3} \text{ fm} \\ a &\equiv 0.6 \text{ fm}, \end{aligned} \tag{5.19}$$

where V_0, μ, l, and s represent the potential depth, the reduced mass, the orbital angular momentum, and the intrinsic spin of valence nucleon, respectively. The mass number of core nucleus was adopted to obtain r_0. The potential depth V_0 was tuned to reproduce the one-neutron separation energy $S_{\rm n}$ of ^{49}Ca (Table 5-6). We assumed the bare ^{48}Ca nucleus as a core, which means the RMS radius of core density distribution is determined to reproduce the $\sigma_{\rm I}$ of ^{48}Ca. The obtained core and valence neutron densities are also shown in Fig. 5-14.

In Figure 5-15, the calculated $\langle r^2 \rangle_{\rm m}^{1/2}$ of the SPM with the combination of ^{48}Ca and $2p_{3/2}$ valence neutron is shown by the blue open square and line together with the present results. This simple model can not explain the enhancement of ^{49}Ca at all. This may be because the valence neutron of nuclei beyond $N = 28$ is bound so strong compared to a halo nucleus (separation energy is below 1 MeV) that an independent picture between a core and a valence neutron is not so good in this case.

The correlation between the core and the valence neutron is strong, so that the ^{48}Ca core may be excited. This may also result in a complicated configuration mixing. As a very simple example, we show the SPM with the combination of ^{46}Ca core and three $2p_{3/2}$ valence neutrons $(\nu 2p_{3/2})^3$ by the purple open triangle in Fig. 5-15. The bare ^{46}Ca is assumed as a core and the wave function of valence neutron is calculated in the same manner as $(\nu 2p_{3/2})^1$ to reproduce the one-third of three neutron separation energy $S_{3n}/3 \simeq 7.46$ MeV. While $\langle r^2 \rangle_{\rm m}^{1/2}$ of $^{46}\mathrm{Ca} + (\nu 2p_{3/2})^3$ is larger than that of $^{48}\mathrm{Ca} + (\nu 2p_{3/2})^1$ as shown in Fig. 5-15, this calculation cannot also reproduce the experimental $\langle r^2 \rangle_{\rm m}^{1/2}$.

Table 5-6: Experimental one neutron separation energy $S_{\rm n}$ of ^{49,50,51}Ca [WA17].

	^{49}Ca	^{50}Ca	^{51}Ca
S_n (MeV)	5.14645(18)	6.3608(16)	4.8144(17)

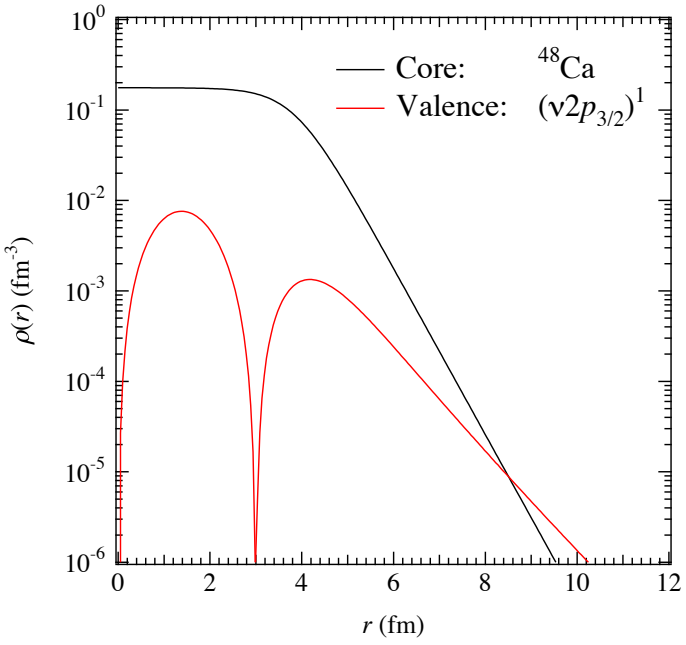

Figure 5-14: Density distribution of ^{49}Ca with the single particle model of core(^{48}Ca)+$(\nu 2p_{3/2})^1$ valence neutron.

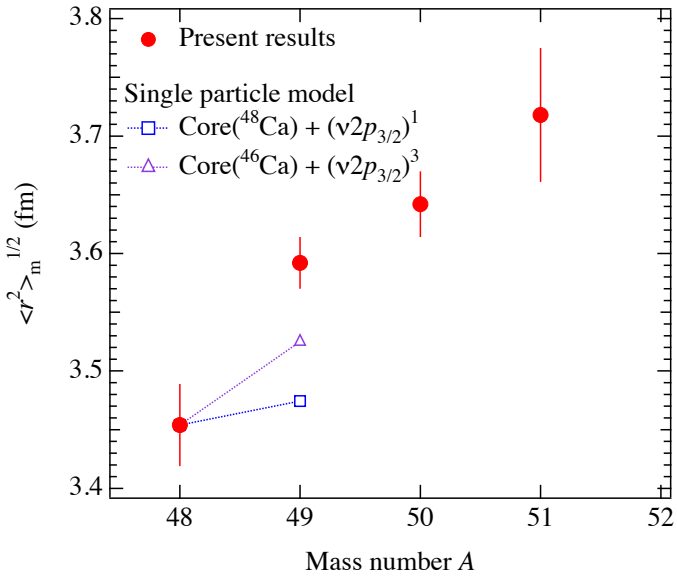

Figure 5-15: Experimental $\langle r^2 \rangle_{\rm m}^{1/2}$ of Ca isotopes in comparison with $\langle r^2 \rangle_{\rm m}^{1/2}$ calculated by the single particle model.

Finally, we estimate the effect of core enlargement for ^{49,50,51}Ca within the SPM. The RMS radius of the system which consists of core and valence neutrons $\langle r^2 \rangle_{\rm c+v}^{1/2}$ is related to respective RMS radii by the following equation:

$$\langle r^2 \rangle_{\rm c+v}^{1/2} = \sqrt{\frac{A_{\rm c}\langle r^2 \rangle_{\rm c} + A_{\rm v}\langle r^2 \rangle_{\rm v}}{A_{\rm c} + A_{\rm v}}}. \tag{5.20}$$

$\langle r^2 \rangle_{\rm c}^{1/2}$	: RMS radius of core nucleus
$\langle r^2 \rangle_{\rm v}^{1/2}$	: RMS radius of valence neutrons
$A_{\rm c}$	: The number of nucleons in the core nucleus
$A_{\rm v}$	: The number of valence neutrons

It was assumed that the mass number of core is $A_{\rm c} = 48$. Here, we note that the assumed core is not necessarily the same as the bare ^{48}Ca. The single particle density distributions were calculated in the same manner as the above discussion to reproduce $S_{\rm n}$, $S_{\rm 2n}/2$, and $S_{\rm 3n}/3$ in the case of ^{49}Ca, ^{50}Ca, and ^{51}Ca, respectively. Actually, when the core is excited, the valence neutrons are more bound in order to reproduce the separation energy. As an example, in the case of ^{48}Ca+$(\nu 2p_{3/2})^1$, the binding energy dependence of the core enlargement relative to $\langle r^2 \rangle_{\rm m}^{1/2}$ of the bare ^{48}Ca, $\langle r^2 \rangle_{\rm c}^{1/2} - \langle r^2 \rangle_{\rm m}^{1/2}(^{48}{\rm Ca})$, is shown in Fig. 5-16. If the binding energy is larger than the experimental S_n,

the value of estimated core enlargement is not influenced beyond the error. We summarize the deduced $\langle r^2\rangle_{\rm c}^{1/2}$ and $\langle r^2\rangle_{\rm c}^{1/2} - \langle r^2\rangle_{\rm m}^{1/2}(^{48}{\rm Ca})$ in Table 5-7. In order to explain the large enhancement of matter radius beyond $N = 28$, the core has to be enlarged at least about 0.1-0.2 fm.

Table 5-7: Summary of deduced $\langle r^2\rangle_{\rm c}^{1/2}$ together with $\langle r^2\rangle_{\rm v}^{1/2}$ and the experimental $\langle r^2\rangle_{\rm m}^{1/2}$. The core enlargement relative to $\langle r^2\rangle_{\rm m}^{1/2}$ of ^{48}Ca, $\langle r^2\rangle_{\rm c}^{1/2} - \langle r^2\rangle_{\rm m}^{1/2}(^{48}{\rm Ca})$, is also summarized.

Nuclide	$\langle r^2\rangle_{\rm m}^{1/2}$ (fm)	$\langle r^2\rangle_{\rm v}^{1/2}$ (fm)	$\langle r^2\rangle_{\rm c}^{1/2}$ (fm)	$\langle r^2\rangle_{\rm c}^{1/2} - \langle r^2\rangle_{\rm m}^{1/2}(^{48}{\rm Ca})$ (fm)
^{49}Ca	3.59(2)	4.34	3.57(2)	0.12(4)
^{50}Ca	3.64(3)	4.27	3.61(3)	0.16(5)
^{51}Ca	3.72(6)	4.30	3.68(6)	0.22(7)

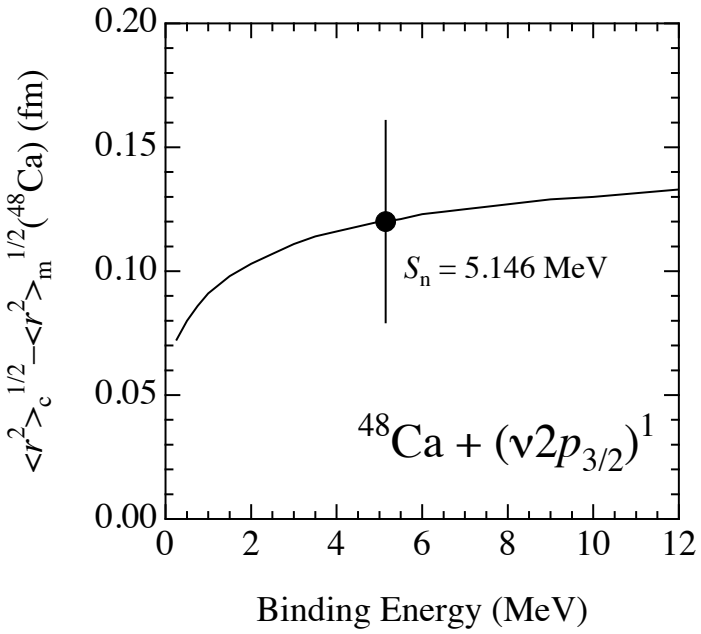

Figure 5-16: Binding energy dependence of $\langle r^2\rangle_{\rm c}^{1/2} - \langle r^2\rangle_{\rm m}^{1/2}(^{48}{\rm Ca})$ in the case of $^{48}{\rm Ca} + (\nu 2p_{3/2})^1$. The core enlargement with the experimental $S_{\rm n}$ is also shown by the closed circle.

Comparison to Theoretical Calculations

Next, in order to discuss the mechanism of the evolution of nuclear radii beyond $N = 28$ in more detail, we compared experimental nuclear radii to theoretical ones. The $\langle r^2 \rangle^{1/2}_{\rm p,m}$ of Ca isotopes were calculated with the Hartree Fock (HF) + BCS [HOR17] and the Relativistic Mean Field (RMF) [PI17] theories. In the case of HF+BCS calculations, KDEv1 [AG05], LNS [GA06], SkI3 [RE95], SkM* [BA82], SkT1, SkT2, SkT3 [TO84], SLy4,[CH97] and SV-sym32 [KL09] Skyrme interactions were adopted. On the other hand, NL3 [LA97, LA99], FSUGold [TO05], and FSUGarnet [CH15] relativistic interactions were employed in the RMF calculations. Figure 5-17 represents the present experimental $\langle r^2 \rangle^{1/2}_{\rm m}$ and $\langle r^2 \rangle^{1/2}_{\rm p}$ obtained from isotope shifts [GA16] as a function of neutron number N together with respective theoretical calculations. Though almost all calculations exhibit a kink structure at the neutron magic number $N = 28$ not only in the case of $\langle r^2 \rangle^{1/2}_{\rm m}$ but also in that of $\langle r^2 \rangle^{1/2}_{\rm p}$, any calculations cannot be reproduced experimental $\langle r^2 \rangle^{1/2}_{\rm m}$ and $\langle r^2 \rangle^{1/2}_{\rm p}$ simultaneously in the wide range of N.

On the other hand, as mentioned in Sec. 1.2, the *ab initio* coupled-cluster calculations of $\langle r^2 \rangle^{1/2}_{\rm p}$ with the NNLO$_{\rm sat}$ chiral effective field theory (χEFT) interaction which includes the contribution of three-body force microscopically were also performed for neutron-rich Ca isotopes [GA16]. As shown in Fig. 5-18, the *ab initio* calculations (black bold line) reproduce relatively better than the mean field (HF+BCS and RMF) ones. However, the unexpectedly large enhancements of $\langle r^2 \rangle^{1/2}_{\rm p}$ beyond $N = 28$ cannot be explained quantitatively even by using such a sophisticated theory [GA16].

In order to estimate these enhancements beyond $N = 28$ in more detail, we introduced a slope parameter of RMS radii against neutron number N, $SL_{\rm m,p}$, defined by the following equation:

$$SL_{\rm m,p} = \frac{d\langle r^2 \rangle^{1/2}_{\rm m,p}}{dN}. \tag{5.21}$$

The $SL_{\rm m,p}$ were obtained by fitting available data in $N \geq 28$ to a linear function. We show the correlation between SL and the RMS radii of ^{48}Ca, $\langle r^2 \rangle^{1/2}[^{48}{\rm Ca}]$, for proton and matter radii, respectively, in Fig. 5-19. Here, $\langle r^2 \rangle^{1/2}[^{48}{\rm Ca}]$ was utilized as a barometer to estimate whether the theoretical calculations reproduce the absolute values of experimental ones or not. In this figure, the experimental $SL_{\rm m,p}$ and $\langle r^2 \rangle^{1/2}_{\rm m,p}[^{48}{\rm Ca}]$ are represented by the horizontal and vertical red solid lines, respectively, with their corresponding errors shown by dotted lines. From the comparison between $SL_{\rm m}$ and $SL_{\rm p}$, the evolution of $\langle r^2 \rangle^{1/2}_{\rm m}$ by increasing N is more drastic than that of $\langle r^2 \rangle^{1/2}_{\rm p}$, which is also followed by the theoretical $SL_{\rm m,p}$. Moreover, surprisingly, the

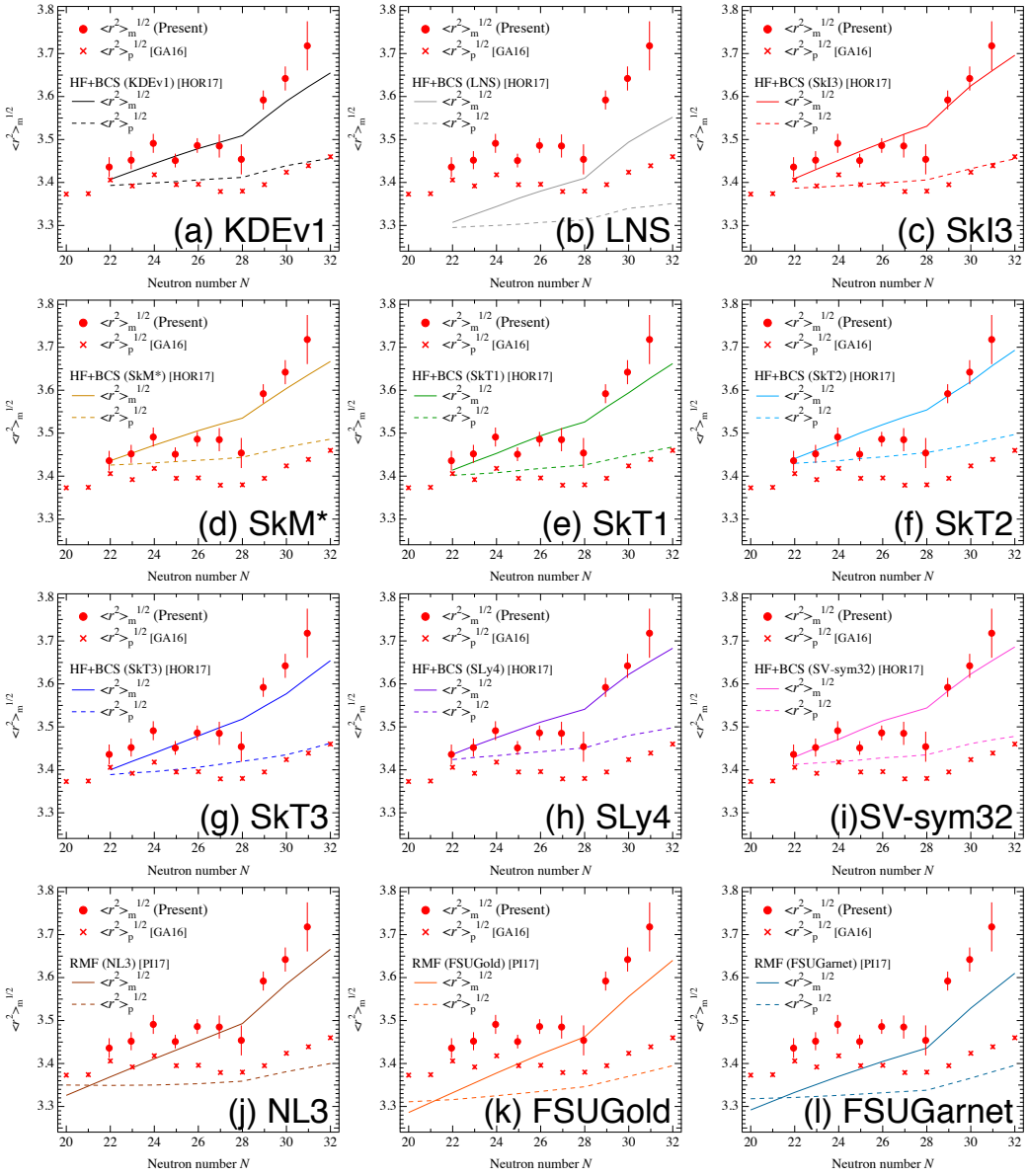

Figure 5-17: Present experimental $\langle r^2 \rangle_{\rm m}^{1/2}$ (closed circles) and previously measured $\langle r^2 \rangle_{\rm p}^{1/2}$ (crosses) by isotope shifts [GA16] of Ca isotopes as a function of neutron number N together with the theoretical values not only with HF+BCS [HOR17] using (a) KDEv1, (b) LNS, (c) SkI3, (d) SkM*, (e) SkT1, (f) SkT2, (g) SkT3, (h) SLy4, and (i) SV-sym32 Skyrme interactions but also with RMF [PI17] using (j) NL3, (k) FSUGold, and (l) GSUGarnet relativistic interactions, respectively.

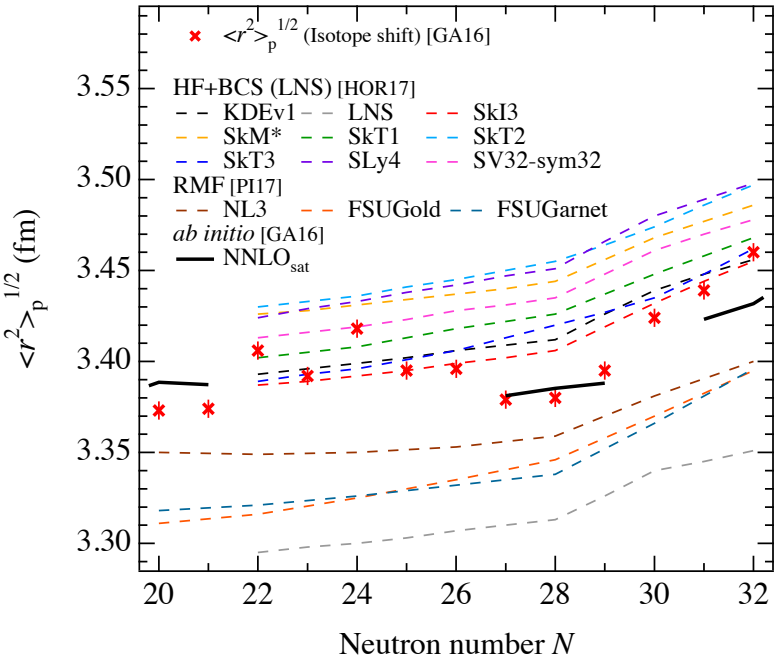

Figure 5-18: Experimental $\langle r^2 \rangle_{\rm p}^{1/2}$ (crosses) [GA16] of Ca isotopes as a function of neutron number N together with the theoretical calculations with HF+BCS [HOR17], RMF [PI17], and *ab initio* using $\rm NNLO_{sat}$ (black bold line) [GA16].

experimental SL is about twice larger than any calculated ones in both cases ($SL_{\rm m}$ and $SL_{\rm p}$), which infers that the reason why almost all theoretical RMS radii underestimate the experimental ones beyond $N = 28$ in both cases may have a common problem. In terms of the theoretical study of $\langle r^2 \rangle_{\rm ch}^{1/2}$ for Pb isotopes across $N = 126$ with the Skyrme-HF and RMF calculations [BE03], it was pointed out that the spin-orbit force is one of the candidates for the origin of the kink property. Anyway, more theoretical studies are required for the quantitative and comprehensive description of both matter and proton radii across the neutron magic number $N = 28$. Here, we emphasize that the common property of the ratio of experimental $SL_{\rm m,p}$ to theoretical ones is found for the first time.

We also consider this enhancement property within the framework of 2pF-type function. As already mentioned in Sec. 5.1.2, The 2pF-type function is characterized by only 3 parameters, a half-density radius C, surface diffuseness a, and central density $\rho(0)$. In order to access the information of these parameters in regard to theoretical results, we converted the theoretical density distributions calculated with the HF+BCS theory (private commu-

nication by W. Horiuchi and S. Ebata) to the 2pF-type functions by the χ^2 fitting procedure. To obtain the information of C and a, the fitting procedure has to be done with a good accuracy especially at the nuclear surface rather than the central part of density distribution. Therefore, the fitting was done to reproduce the $r^2\rho(r)$ distribution. Figure 5-20 shows obtained (a) C and (b) a of proton (solid lines) and neutron (dashed lines) density distributions as a function of N, respectively. Kink structures are clearly seen at $N = 28$ in Fig. 5-20(b). Therefore, it seems that the drastic enhancement of nuclear radii beyond $N = 28$ results from a large contribution of the sudden increase of surface diffuseness. This may be related to the fact that the configuration of valence neutrons is changed from $1f_{7/2}$ orbital to $2p_{3/2}$ one which can further spread spatially. In order to achieve the more quantitative description of the evolution of nuclear radii beyond $N = 28$, the reproduction of surface structure is extremely important. Also, from this point of view, the precise description of spin-orbit force seems to be significant because this force contributes to the shape of potential surface.

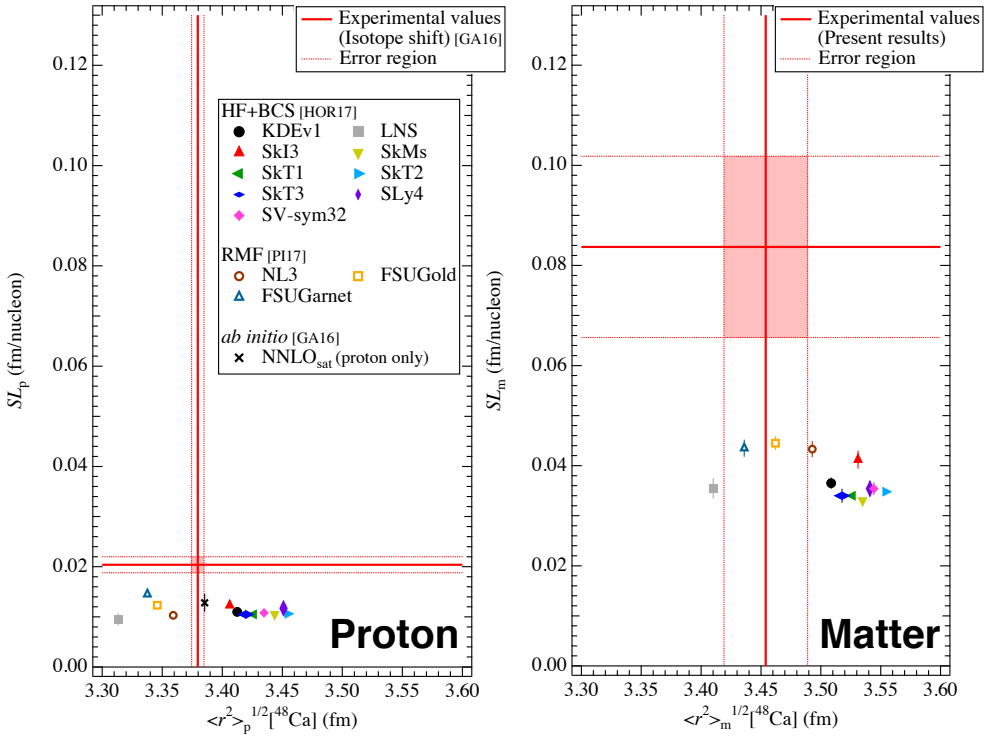

Figure 5-19: Two-dimensional plots of $SL_{\rm p,m}$ as a function of $\langle r^2\rangle_{\rm p,m}^{1/2}$. The experimental values and corresponding errors are represented by the red solid and dotted lines, respectively. Each color definition means the same as in Figs. 5-17 and 5-18.

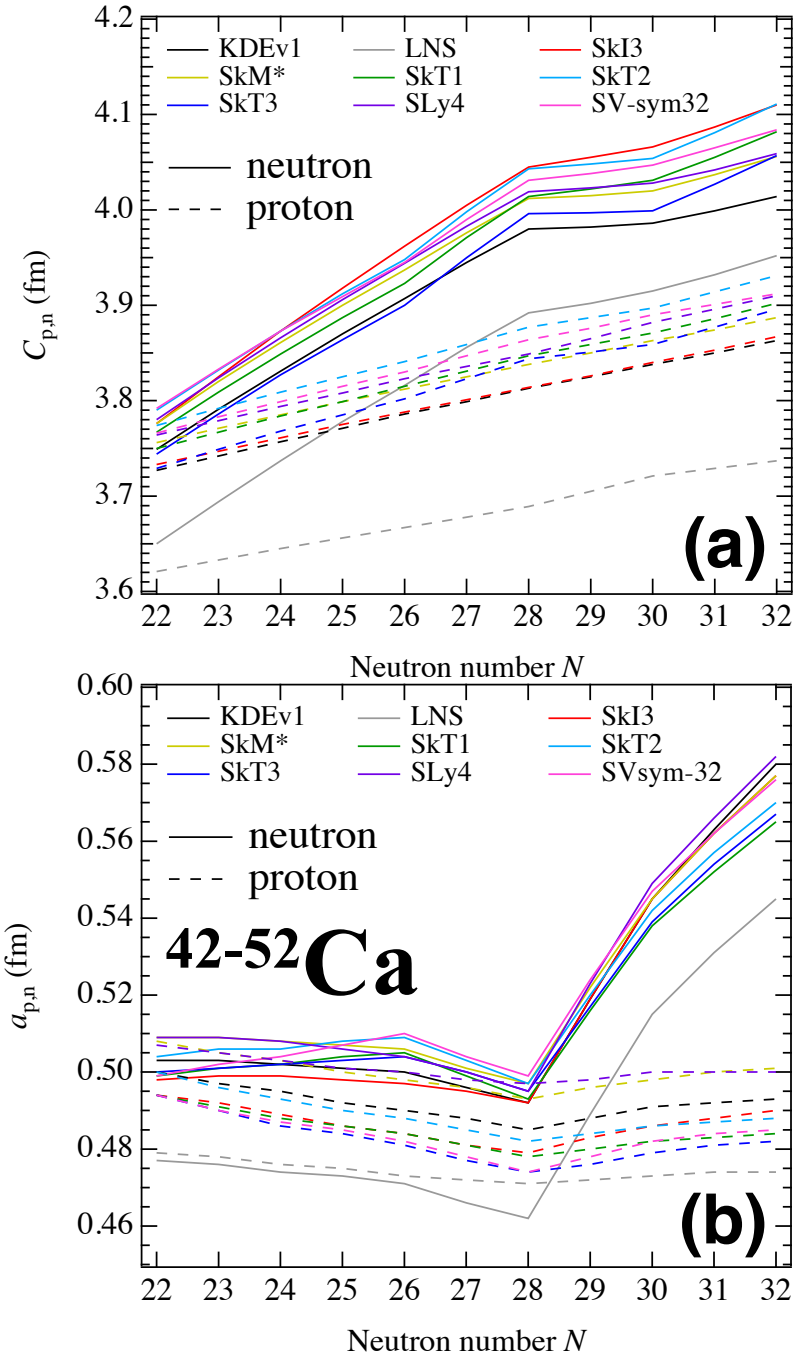

Figure 5-20: Obtained information of (a) half-density radius C and (b) surface diffuseness a of 2pF-type function from the realistic density distributions calculated with HF+BCS theory as a function of N

Contribution of Spin-Orbit Force

We mention such a drastic change of the trend of nuclear radii in other regions. The $\sigma_{\rm I}$ for N, O, F, Ne, Na, and Mg isotopes located in the vicinity of $N = 14$ [SU95, SU98, OZ01, KA11, TA12, SU13, TA14, HO17, OH18] show a similar behavior (Fig. 5-21). A kink structure can be seen even in the well-bound nucleus ($S_{\rm n} = 4.25(14)$ MeV at ^{25}Ne) as well as in the loosely-bound one ($S_{\rm n} = 1.54(25)$ MeV at ^{22}N). Especially, the enhancements of $\sigma_{\rm I}$ at ^{22}N, ^{23}O, and ^{24}F which cannot be explained with the single particle model are put in the spotlight as an anomaly in neutron-rich nuclei [KA01, TA01]. The elucidation of kink mechanism emerged at the magic number may result in a comprehensive understanding of the $N = 14$ anomaly. In terms of the experiment, $\sigma_{\rm I}$ measurements for nuclides across the magic number can provide important information to study the nuclear magicity. On the other hand, the charge radii have been already measured systematically for many isotopic chains. I. Angeli *et al.* pointed out that a neutron number dependence of charge radii exhibits a similar kink not only in the traditional magic numbers $N = 2, 28, 50, 82$, and 126 but also in $N = 6$ and 14 as shown in Fig. 5-22 [AN13]. These kink structures can be also seen in the isotonic chains. In particular, very recently, the magicity of $Z = 6$ for several isotonic chains was discussed [TR18]. However, the kink structure cannot be found at magic numbers of 8 and 20 in either isotopic or isotonic chains.

Based on the shell model proposed by Mayer and Jensen, the magic numbers can be classified into two cases as shown in Fig. 5-23. Ones of 2, 8, and 20 emerge even with the harmonic-oscillator as well as the Woods-Saxon potentials. In contrast, the others of 28, 50, 82, and 126 can occur owing to the introduction of spin-orbit potential. Furthermore, the numbers of 6 and 14 also correspond to the sub-shell closures of $j_> = l + 1/2$ orbitals. Therefore, it seems that the kink structure of the trend of nuclear radii can be seen only at shell closures which emerge due to the spin-orbit splitting. From this point of view, the kink structure may be deeply related to the spin-orbit force. In the following, we show the speculation of the relation between the kink structure and the spin-orbit force.

Within the framework of mean field theory with the Skyrme interaction, the spin-orbit potential $V^{\rm n}_{\rm SO}(r)$ for neutrons is represented as [SA14]

$$\begin{aligned} V^{\rm n}_{\rm SO}(r) &\equiv U^{\rm n}_{\rm SO}(r)(\boldsymbol{l}\cdot\boldsymbol{s}) \\ &= \left[\frac{1}{r}\left(b_4\frac{d\rho_{\rm N}(r)}{dr} + b'_4\frac{d\rho_{\rm n}(r)}{dr}\right) + \left(\alpha\frac{J_{\rm n}(r)}{r} + \beta\frac{J_{\rm p}(r)}{r}\right)\right](\boldsymbol{l}\cdot\boldsymbol{s}), \end{aligned} \tag{5.22}$$

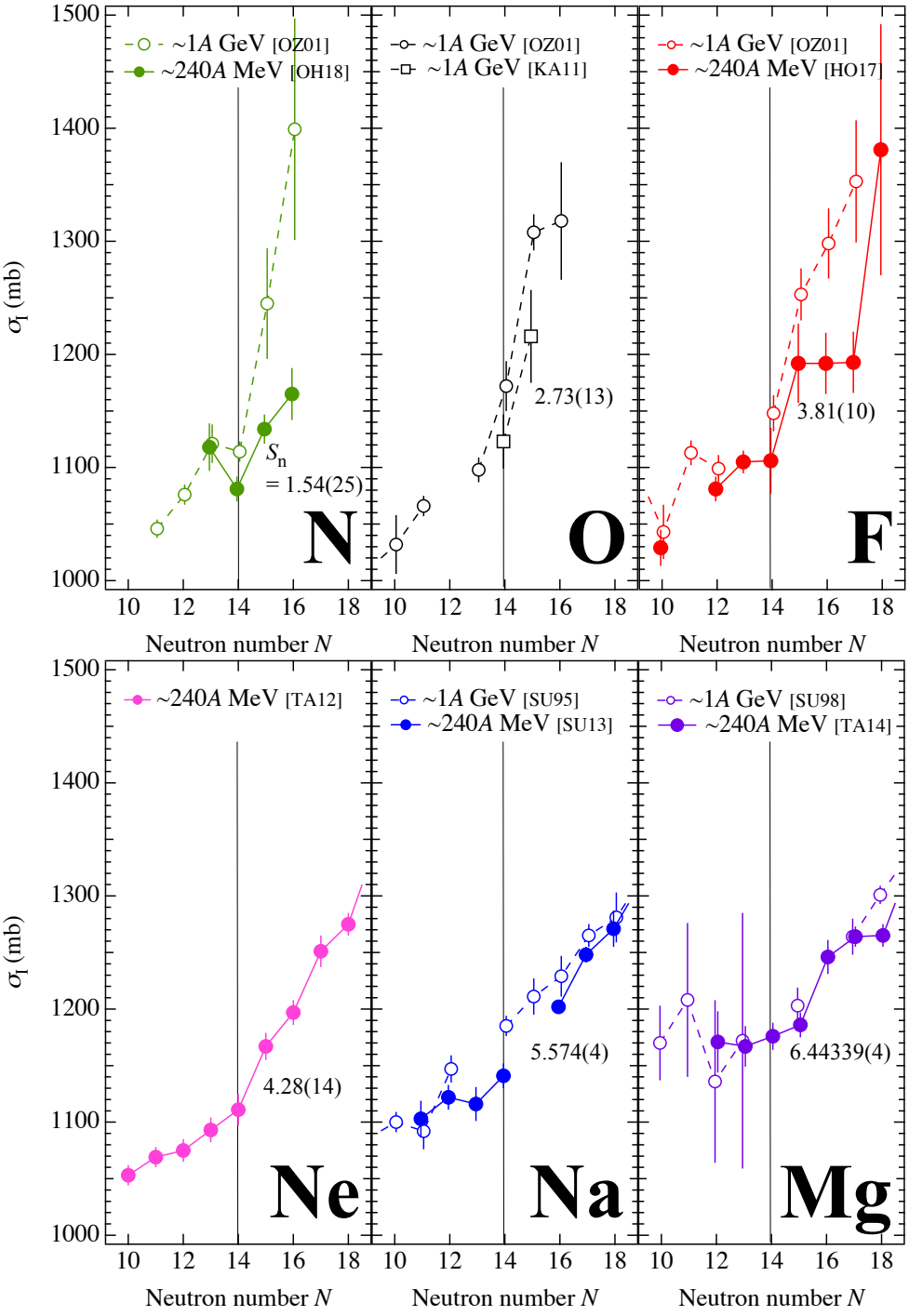

Figure 5-21: Neutron number dependence of σ_{I} of N, O, F, Ne, Na, and Mg isotopes on C target at around 240A MeV (closed symbols) or 1A GeV (open symbols) [SU95, SU98, OZ01, KA11, TA12, SU13, TA14, HO17, OH18]. S_{n} of nuclei whose $N = 15$ are also shown in MeV.

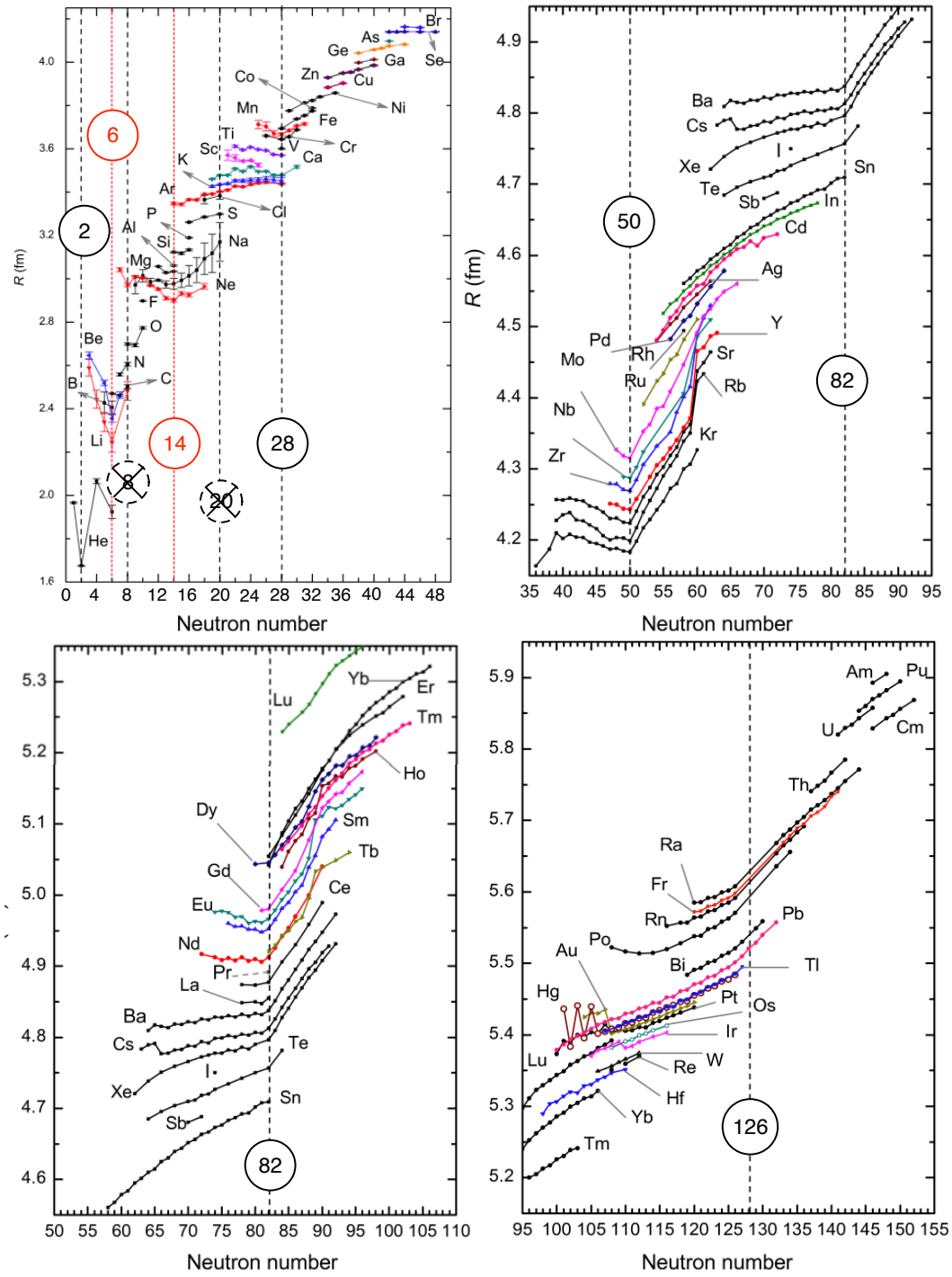

Figure 5-22: Neutron number dependence of charge radii $\langle r^2 \rangle_{ch}^{1/2}$ [AN13]. These figures are taken from Ref. [AN13] with slight modifications.

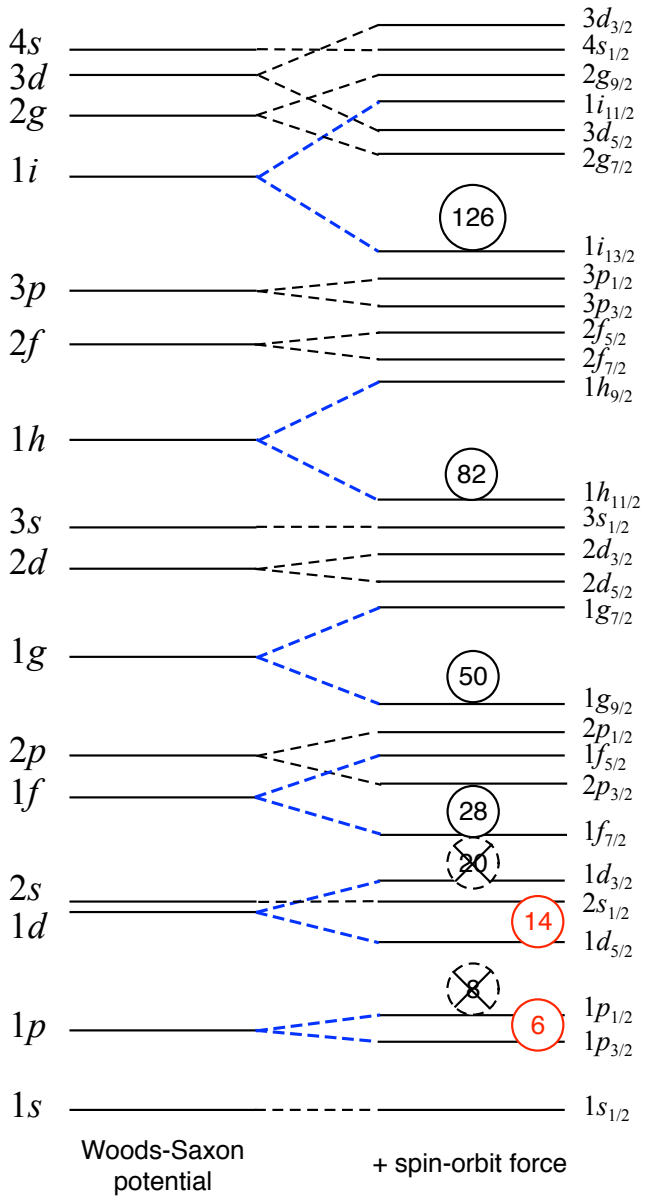

Figure 5-23: Schematic view of the emergence of magic numbers based on the shell model with the Woods-Saxon potential (left) and the Woods-Saxon plus spin-orbit ones (right). The kink structure of the trend of nuclear radii can be observed only at magic numbers occurred by the spin-orbit splitting (blue dashed lines) represented by the black solid circles. The kink structure is also exhibited at sub-shell closures of 6 and 14 (red circles) which are also emerged by the spin-orbit force.

$$\alpha = \frac{1}{8}(t_1 - t_2) - \frac{1}{8}(t_1 x_1 - t_2 x_2),$$
$$\beta = -\frac{1}{8}(t_1 x_1 - t_2 x_2), \tag{5.23}$$

where $(t_1, t_2, x_1, x_2, b_4, b'_4)$ is a set of Skyrme parameters of effective 2-body interaction. The $J_{\rm p}(r)$ and $J_{\rm n}(r)$ are proton and neutron spin-orbit densities defined as

$$J_{\rm q}(r) = \frac{1}{4\pi r^3} \sum_i v_i^2 (2j_i + 1) \left[j_i(j_i+1) - l_i(l_i+1) - \frac{3}{4} \right] R_{\rm i}^2(r), \tag{5.24}$$

where $v_{\rm i}$ is the occupation probability, $j_{\rm i}$ the total spin, $l_{\rm i}$ the orbital angular momentum, and $R_{\rm i}$ the radial part of the single particle wave function, respectively. The subscript "q" means proton "p" or neutron "n".

The change of density profile can affect the strength of spin-orbit potential $U_{\rm SO}^{\rm n}(r)$ due to the $\rho(r)$ dependence of the first term of Eq. (5.22). Figure 5-24 shows the ratio of the first term of $U_{\rm SO}^{\rm n}(r)$ to the central potential by the HF+BCS calculation with SLy4 interaction. Here, the Woods-Saxon potential $V_{\rm WS}(r)$ was adopted as the central potential. The contribution of spin-orbit potential becomes relatively large in the potential surface beyond $N = 28$ due to the sudden increase of surface diffuseness. Although the origin of increase of surface diffuseness itself cannot be mentioned, the spin-orbit force can be related to the kink structure of the trend of nuclear radii.

The Skyrme parameters b_4 and b'_4 which represent the strength of 2 body spin-orbit interaction may also contribute to the strength of kink structure. For general Skyrme forces, the value of b'_4 is assumed to be the same as that of b_4. On the other hand, within the framework of RMF theory, the spin-orbit interaction depends only on the derivative of nucleon density distribution $d\rho_{\rm N}(r)/dr$, which corresponds to $b'_4 = 0$ MeV $\cdot$ fm^5. It was pointed out that this difference between the HF with general Skyrme forces and RMF theories plays a crucial role in order to explain the kink at $N = 128$ magic number of charge radii of Pb isotopes [RE95, SH95, SA01, GO13]. The SkI3 Skyrme interaction was constructed with $b'_4 = 0$ MeV $\cdot$ fm^5 in order to reproduce the difference of charge radii between ^{208}Pb and ^{214}Pb as well as the ground state properties of some magic nuclei. In the case of Ca isotopes, as shown in Fig. 5-19, HF+BCS calculation with SkI3 interaction and RMF calculations have relatively large values of $SL_{\rm m}$ in comparison to HF+BCS ones with other Skyrme interactions of $b_4 = b'_4$.

The second term of $U_{\rm SO}^{\rm n}(r)$ represents the contribution of the spin-orbit densities $J_q(r)$. Since the value of $j_i(j_i+1) - l_i(l_i+1) - 3/4$ in Eq. (5.24) has opposite sign between the pair of spin-orbit splitting orbitals, $j_> = l + 1/2$ and $j_< = l - 1/2$, the effect of $J_q(r)$ for the pair of fully-occupied spin-orbit

orbitals is negligibly small. Therefore, $J_q(r)$ represents the effect of non-fully occupied spin-orbit splitting orbitals. For example, in the case of $^{42-51}$Ca, neutron $1f$ orbitals only contribute to $U^{\rm n}_{\rm SO}(r)$ via $J_{\rm n}(r)$. According to [ST77], $\alpha < 0$ in Eq. (5.22) may be preferable [SA14]. In this condition, the effect of $J_{\rm n}(r)$ expands the shell gap between orbitals of $j_>$ and $j_<$ as adding more neutron in the orbital of $j_>$. On the other hand, the neutron shell gap at $N = 28$ becomes narrower with filling neutrons in the $f_{5/2}$ ($j_<$) orbital, so that ^{48}Ca may not be a good core for Ca isotopes beyond $N = 28$ due to the smaller shell gap. From this point of view, the occupation of orbitals of spin-orbit partners is important to discuss the strength of spin-orbit splitting. Furthermore, the tensor force may be also related to the spin-orbit splitting because of the same functional shape of the term from the tensor force as the second term of $U^{\rm n}_{\rm SO}(r)$ [ST77, SA14]. In addition, several possibilities on contributions from the spin-orbit potential were discussed in relation to the points such as the development of neutron-skin [FU93, OT07] and the 3-body spin-orbit interaction [NA15a, NA15b].

However, the above descriptions are just speculations, that is, the mechanism of kink structure at the magic number in the trend of nuclear radii has not been understood yet in the microscopic level. Therefore, the further theoretical studies are desired to explain the emergence of kink structure in more detail. The present results which are the first systematic ones of experimental matter radii across the neutron magic number are so valuable for the detailed theoretical studies together with previously measured charge radii. Therefore, further experimental investigations on systematic matter radii like the present one can also contribute to solving the problem.

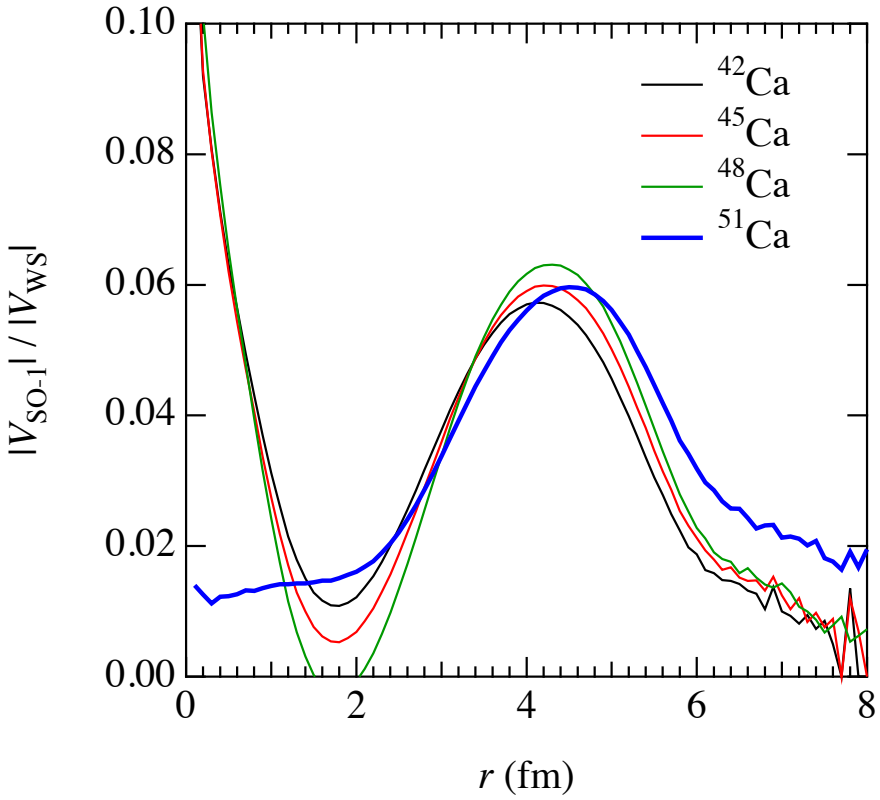

Figure 5-24: Ratio of the first term of Eq. (5.22), $U^{\text{n}}_{\text{SO-1}}$, to V_{WS} by the HF+BCS calculation with SLy4 interaction against the distance from the center of nucleus r. The black, red, green, and blue lines represent ^{42}Ca, ^{45}Ca, ^{48}Ca, and ^{51}Ca, respectively.

5.3 Derivation of L

Figure 5-25 shows the present experimental $r_{\rm np}$ of K, Ca, and Sc isotopes as a function of δ. Thus, we successfully obtained $r_{\rm np}$ from the direct extraction with $r_{\rm m}$ and $r_{\rm p}$ in a wide range of δ, as $0.05 < \delta < 0.22$. These data show the gradual development of neutron skin structure with increasing neutron excess. The present result of ^{48}Ca is consistent with the recent experimental one by the dipole polarizability $\alpha_{\rm D}$ ($r_{\rm np}$ = 0.14-0.20 fm) [BI17] shown by the red bar in Fig. 5-25. We try to derive the EOS parameter L from the present $r_{\rm np}$. In order to derive L from $r_{\rm np}$, there are mainly two different methods as

- Analysis based on the droplet model [CE09, WA09]
- Analysis based on the effective interaction [CH10, RO15]

M. Centelles and M. Warda *et al.* analyzed 26 $r_{\rm np}$ data (from ^{40}Ca to ^{238}U) obtained from antiprotonic atoms [JA04] based on the droplet model with Eqs. (1.7)-(1.9) [CE09, WA09]. However, very recently, W. Horiuchi *et al.* showed a crucial underestimation of $r_{\rm np}$ calculated by the droplet model as increasing neutron excess as shown in Fig. 5-26 [HOR17]. This discrepancy results from reducing a higher-order term in deriving Eq. (1.7) [MY74].

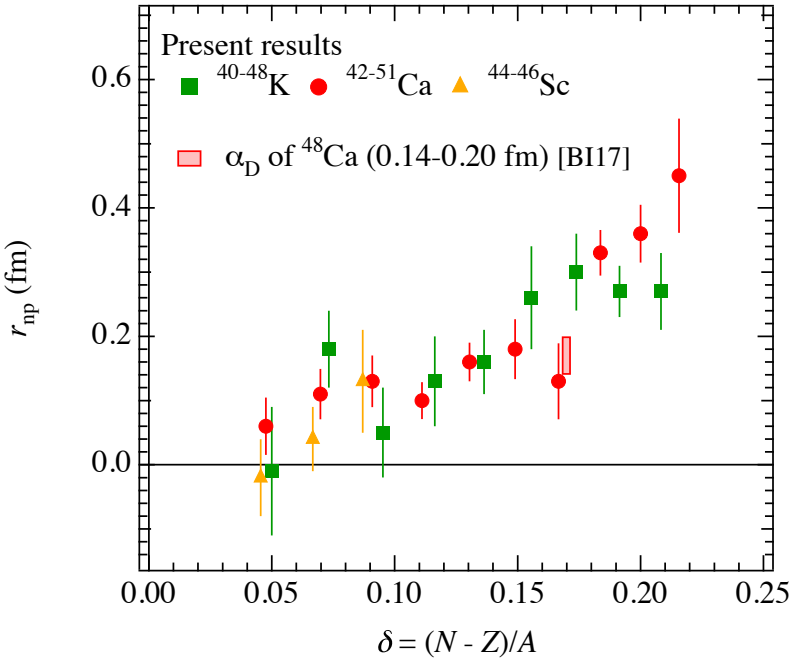

Figure 5-25: Neutron-skin thickness $r_{\rm np}$ of K (green squares), Ca (red circles), and Sc (orange triangles) isotopes as a function of δ.

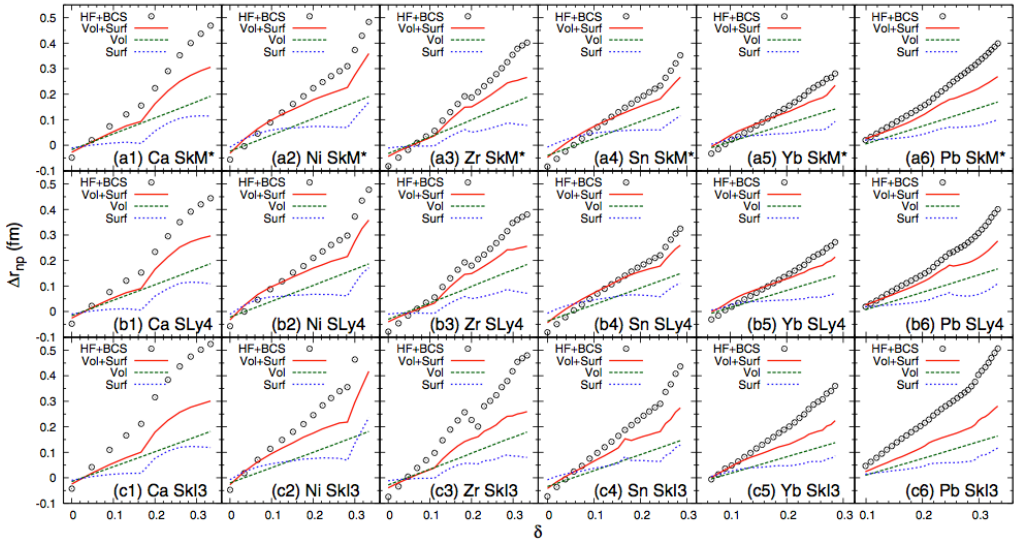

Figure 5-26: Calculated neutron-skin thickness (written by "$\Delta r_{\rm np}$") of even-even Ca, Ni, Zr, Sn, Yb, and Pb isotopes as a function of δ. Open circles show the HF calculations including the BCS effect (HF+BCS) using SkM*, SLy4, and SkI3 interactions. The red solid, green dashed, and blue dotted lines represent neutron-skin thicknesses and their bulk and surface terms (defined in Ref. [HOR17]) calculated by the droplet model with 2pF-type functions to which were obtained by converting the exact HF+BCS density distributions, respectively. This figure is taken from Ref. [HOR17].

On the other hand, in the derivation method by utilizing the effective interactions, nuclear density distributions and a corresponding $r_{\rm np}$ can be obtained with the mean field theory using Skyrme, Gogny, and relativistic forces. An energy density can also be calculated (Eq. (1) in Ref. [DU12], for example), so that each effective interaction corresponds to respective EOS parameters including L. Owing to the theoretical study with several effective interactions, the linear correlation between L and $r_{\rm np}$ was suggested [BE03]. As mentioned in Sec. 1.3, for example, L.-W. Chen *et al.* deduced L as 58 ± 18 MeV from $r_{\rm np}$ of Sn isotopes with Skyrme Hartree Fock calculations using MSL0 interactions which have different L values [CH10]. It seems that this is the main method to deduce L from $r_{\rm np}$ as well as a dipole polarizability $\alpha_{\rm D}$ [CH10, TA11, RO15].

In the present study, we also employed the latter method. However, the theoretical calculations cannot explain the enhancement of nuclear radii for Ca isotopes beyond $N > 28$ as mentioned in Sec. 5.2.4. Therefore, in the following discussion, we just examine the sensitivity of the present $r_{\rm np}$ to L.

5.3.1 Correlation between $r_{\rm np}$ and L

For even-even Ca isotopes, in order to derive the correlation between $r_{\rm np}$ and L, we utilized the HF+BCS calculations by W. Horiuchi and S. Ebata (private communications) [HOR17] as well as the relativistic mean field (RMF) calculations by J. Piekarewicz [PI17]. Moreover, $r_{\rm np}$ of the doubly-magic nucleus ^{48}Ca is calculated with the density functional theories (DFTs) with non-relativistic and relativistic interactions [ZH16], so that these calculations were also employed. In Table 5-8, we summarize $r_{\rm np}$ and L of respective interactions which were used to construct the correlation between $r_{\rm np}$ and L. Figure 5-27 represents calculated $r_{\rm np}$ of ^{48}Ca as a function of L as an example. These mean field results show that $r_{\rm np}$ depends on L linearly with the correlation coefficient $r = 0.955$. Therefore, we obtained the correlation function by fitting over all mean field calculations (HF+BCS, RMF, and DFT) as shown by the red bold line in Fig. 5.25. The slope $A(\delta)$ and intercept $B(\delta)$ were derived from the linear fit to the correlation between $r_{\rm np}$ and L for each Ca isotope, so that the calculated neutron-skin thickness $r_{\rm np}^{\rm func}$ was obtained from the following equation:

$$r_{\rm np}^{\rm func}(\delta, L) \equiv A(\delta)L + B(\delta). \tag{5.25}$$

Although only the HF+BCS and RMF calculations were performed for the other even-even Ca isotopes, the result of linear fit to the HF+BCS and RMF calculations of ^{48}Ca shown by the blue thin line in Fig. 5.25 is consistent well within a 1σ confidence level of the fitting result over all mean field calculations. Therefore, it was considered that smaller references in even-even Ca isotopes excluding ^{48}Ca do not have a special influence in deducing L from $r_{\rm np}$. The L dependences of $r_{\rm np}^{\rm func}(\delta, L)$ for ^{42,44,46,48,50,52}Ca are shown in Fig. 5-28 together with that of ^{208}Pb which were obtained from the same manner with the DFTs [WA09, CE10, RO11]. A heavier (more neutron-rich) Ca isotope have a larger slope, which corresponds to a high sensitivity of $r_{\rm np}$ to deduce L. From this point of view, ^{50}Ca and ^{52}Ca have a similar sensitivity as ^{208}Pb. By using $r_{\rm np}^{\rm func}(\delta, L)$, we attempted to deduce L from the present data. Though the exact calculations can not be referred in the even-odd Ca isotopes, the HF+BCS calculations were obtained by taking the average of neighboring nuclei [HOR17]. The parameters $A(\delta)$ and $B(\delta)$ for respective Ca isotopes used in the present study are summarized in Table 5-9.

Very recently, the *ab initio* calculations of $r_{\rm np}$ of ^{48}Ca with the chiral effective field theory (χEFT) interactions which include the contribution of $3N$ force microscopically were also performed [HA16] (shown by green symbols in Fig. 5.25). The *ab initio* results are relatively small in comparison to the mean field ones beyond the standard deviation of them (red shaded

band). Especially, the *ab initio* calculation with the $\mathrm{NNLO_{sat}}$ χEFT interaction which perfectly reproduces the charge radius [GA16] of ^{48}Ca shows a quite small value. However, the *ab initio* calculations of r_{np} for other Ca nuclides besides ^{48}Ca have not been performed yet. Although the origin of this discrepancy between the mean field and the *ab initio* calculations is not well known, we assumed the correlation function constructed from the mean field calculations in the analysis here.

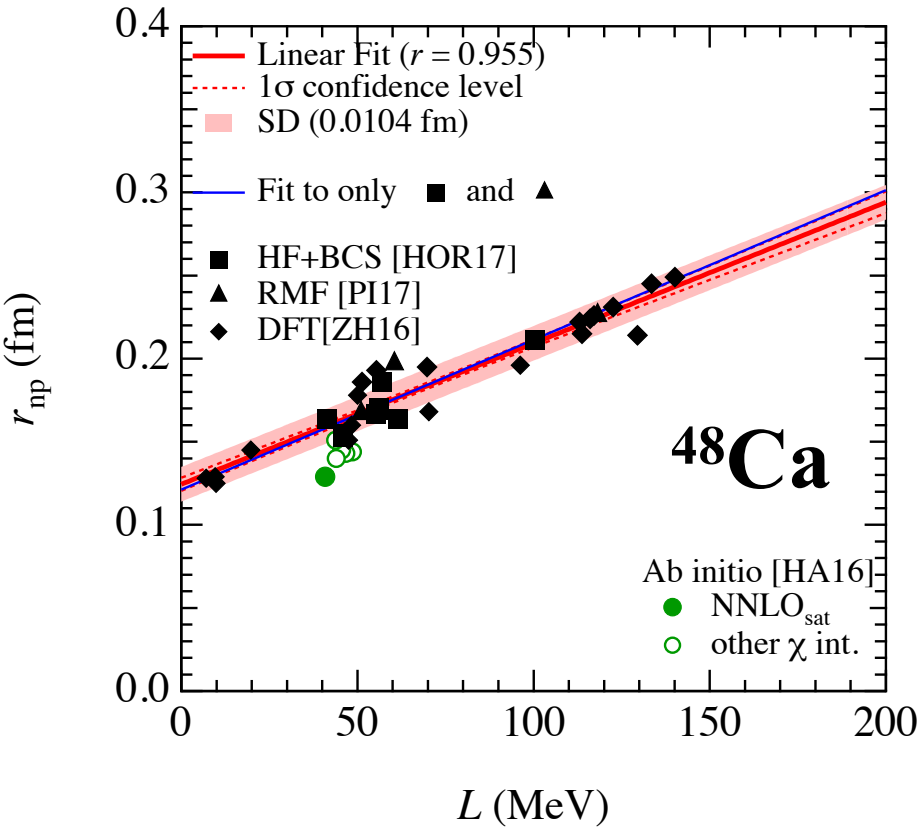

Figure 5-27: Calculated r_{np} of ^{48}Ca with the HF+BCS [HOR17] (squares), RMF [PI17] (triangles), and DFT [ZH16] (diamonds) as a function of L. The red bold line shows a linear function obtained by fitting over mean field calculations (black symbols). The red dotted line is a 1σ confidence level of the red line. The standard deviation of mean field calculations around the red line is represented by the red shaded band. The blue thin line exhibits the fitting result to the HF+BCS and the RMF data. As a comparison, the *ab initio* calculations with $\mathrm{NNLO_{sat}}$ and other several χEFT interactions are also plotted by the green closed and open circles, respectively.

Table 5-8: The mean field calculations (HF+BCS [HOR17], RMF [PI17], and DFT [ZH16]) of $r_{\rm np}$ with several interactions and the corresponding L.

Method	Interaction	L [MeV]	$r_{\rm np}$[fm]					
			^{42}Ca	^{44}Ca	^{46}Ca	^{48}Ca	^{50}Ca	^{52}Ca
HF+BCS	KDE0v1	41.4	0.026	0.083	0.129	0.164	0.246	0.317
	SkM*	45.8	0.019	0.075	0.121	0.155	0.223	0.289
	SLy4	45.9	0.022	0.077	0.121	0.153	0.234	0.294
	SkT3	55.3	0.022	0.078	0.128	0.167	0.234	0.307
	SkT2	56.2	0.021	0.080	0.131	0.169	0.241	0.309
	SkT1	56.2	0.023	0.082	0.134	0.170	0.242	0.313
	SV-sym32	57.1	0.032	0.095	0.150	0.186	0.266	0.332
	LNS	61.5	0.023	0.081	0.129	0.164	0.253	0.320
	SkI3	100.5	0.041	0.110	0.166	0.211	0.315	0.384
RMF	FSUGarnet	51.0	0.022	0.081	0.128	0.167	0.267	0.343
	FSUGold	60.5	0.030	0.097	0.152	0.197	0.305	0.391
	NL3	118.2	0.038	0.111	0.172	0.226	0.334	0.423
DFT	MSk3	7.0				0.128		
	MSk6	9.6				0.129		
	SIII	9.9				0.125		
	SKP	19.7				0.145		
	SLy6	47.5				0.151		
	SLy5	48.3				0.160		
	SII	50.0				0.178		
	DD-ME2	51.3				0.186		
	DD-ME1	55.4				0.193		
	DD-PC1	69.8				0.195		
	SKMP	70.3				0.168		
	SV	96.2				0.196		
	PC-PK1	113.1				0.222		
	NL-SH	113.7				0.215		
	PK1	116.0				0.224		
	PCF1	117.1				0.226		
	NL3	118.5				0.226		
	NL3*	122.6				0.231		
	SkI5	129.5				0.214		
	NL1	140.1				0.249		
	NL2	133.5				0.245		

Table 5-9: Parameters of $r_{\rm np}^{\rm func}(\delta, L)$.

Nuclide	δ	Slope $A(\delta)$ [fm/MeV]	Intercept $B(\delta)$ [fm]
^{42}Ca	0.048	0.00026(5)	0.010(4)
^{43}Ca	0.070	0.00044(11)	0.031(7)
^{44}Ca	0.091	0.00048(8)	0.057(5)
^{45}Ca	0.111	0.00064(14)	0.074(9)
^{46}Ca	0.130	0.00067(11)	0.097(7)
^{47}Ca	0.149	0.00082(17)	0.106(10)
^{48}Ca	0.167	0.00085(5)	0.124(4)
^{49}Ca	0.184	0.00119(20)	0.144(12)
^{50}Ca	0.200	0.00133(25)	0.180(17)
^{51}Ca	0.216	0.00144(24)	0.203(14)

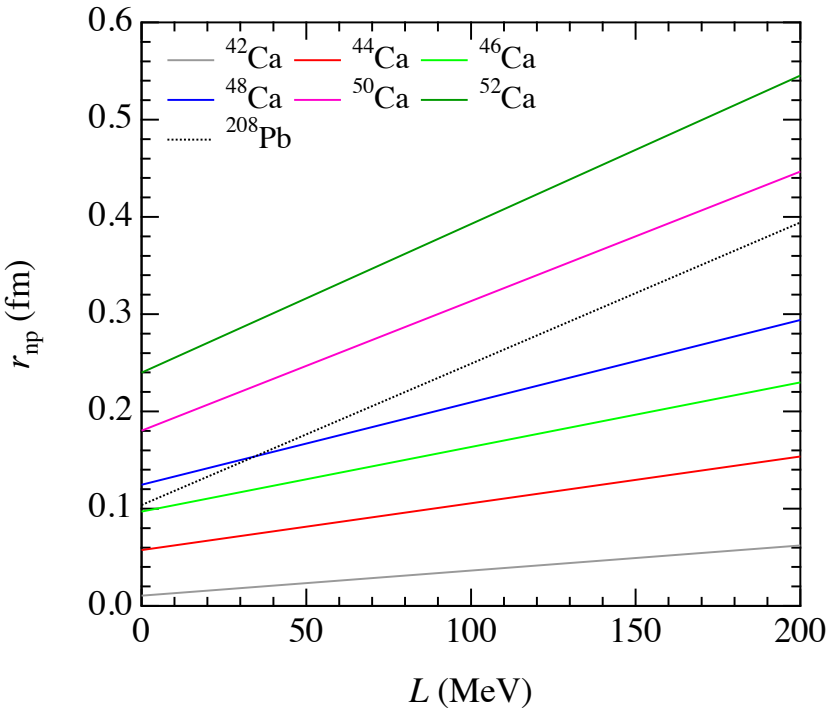

Figure 5-28: Dependence of $r_{\rm np}^{\rm func}(\delta, L)$ on L for ^{42,44,46,48,50,52}Ca together with the one for ^{208}Pb.

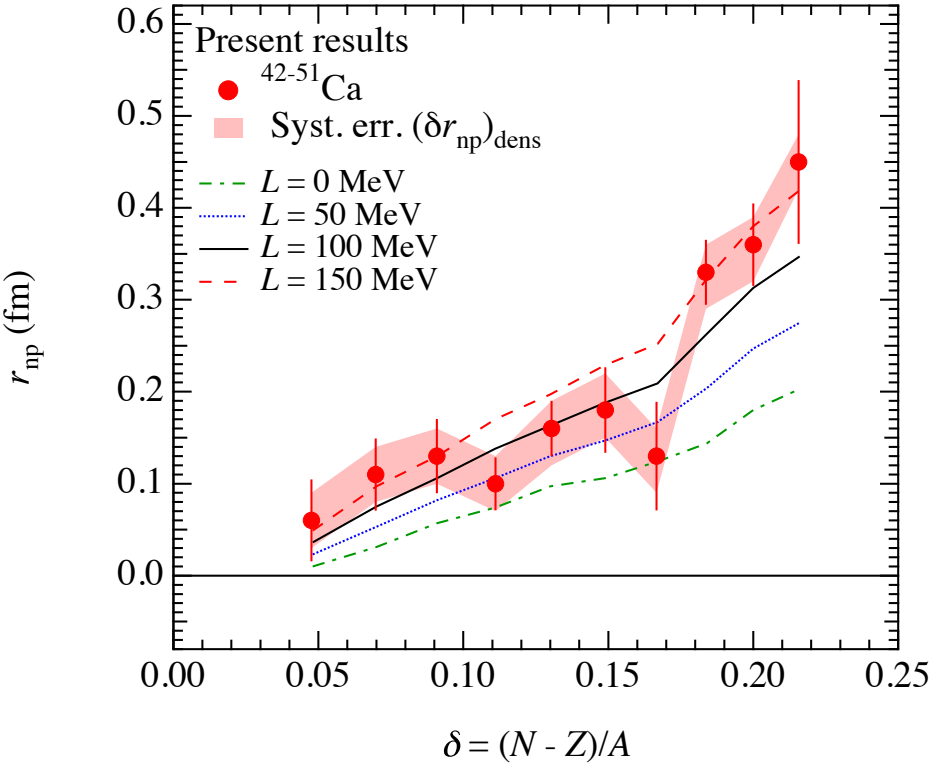

Figure 5-29: Present $r_{\rm np}$ of Ca isotopes together with their systematic errors (shaded band) results from Eq. (5.10) as a function of δ. As a comparison, $r_{\rm np}^{\rm func}(\delta, L)$ with $L = 0$ (green dash-dotted), 50(blue dotted),100 (black solid), and 150 (red dashed) MeV are also shown.

5.3.2 Sensitivity of $r_{\rm np}$ to L

Figure 5-29 shows $r_{\rm np}$ as a function of δ together with $r_{\rm np}^{\rm func}(\delta, L)$ with $L = 0, 50, 100,$ and 150 MeV, respectively. Present results are distributed within $0 < L < 150$ MeV. In order to deduce L quantitatively, we utilized the χ^2 fitting procedure with the correlation function $r_{\rm np}^{\rm func}(\delta, L)$. As shown in Sec. 5.2.4, the mean field calculations cannot quantitatively reproduce the mass dependence of the present $\langle r^2 \rangle_{\rm m}^{1/2}$ as well as that of $\langle r^2 \rangle_{\rm ch}^{1/2}$. [GA16]. Hence, by taking this fact into account, the fitting procedures were performed to the following data set:

(i) $^{42-48}$Ca

(ii) $^{42-51}$Ca

Table 5-10: Summary of deduced L through the χ^2 fitting procedures.

Data set	L [MeV] (a) $\rho_{\rm N}(0) = 0.176$ fm^{-3}	(b) $\rho_{\rm N}(0) = 0.165$ fm^{-3}	(c) $\rho_{\rm N}(0) = 0.187$ fm^{-3}
(i) $^{42-48}$Ca	80(37)	134(24)	27(45)
(ii) $^{42-51}$Ca	118(16)	156(21)	79(16)

Also, the present result of $r_{\rm np}$ has a systematic error $(\delta r_{\rm np})_{\rm dens}$ resulting from the uncertainty of central matter density $\Delta\rho_{\rm N}(0) = 0.011$ fm^{-3} (Eq. (5.10)) relative to $\rho_{\rm N}(0) = 0.176$ fm^{-3} (Eq. (5.9)) as shown in Fig. 5-29 by the shaded band. Therefore, in order to treat this systematic error appropriately, we also performed the fitting procedure with the following cases:

(a) $r_{\rm np}$ $[\rho_{\rm N}(0) = 0.176$ fm$^{-3}]$,

(b) $r_{\rm np} + (\delta r_{\rm np})_{\rm dens}$ $[\rho_{\rm N}(0) = 0.165$ fm$^{-3}]$,

(c) $r_{\rm np} - (\delta r_{\rm np})_{\rm dens}$ $[\rho_{\rm N}(0) = 0.187$ fm$^{-3}]$.

Figure 5-30 shows χ^2 distributions as a function of L The deduced results are also summarized in Table 5-10. In the case (i-a; $^{42-48}$Ca with $\rho_m(0) = 0.176$ fm^{-3}), L is deduced as $L = 80(37)_{\rm stat}$ MeV (the subscript means statistical error), which is consistent with the average of previous results $L = 58.9 \pm 16.5$ MeV [LI13]. Though the fitting result to data including nuclei beyond $N > 28$ (ii-a) is relatively large (this may be because the theoretical nuclear radii of $^{49-51}$Ca are underestimated.), this data set has a possibility to determine L with a good statistical error as $\delta L_{\rm stat} = 16$ MeV. On the other hand, the deduction of L also depends on $\rho_{\rm N}(0)$ as shown in Fig. 5-30. When we assumed the uncertainty $\Delta\rho_{\rm N}(0) = 0.011$ fm, the systematic error of L is estimated as about $(\delta L)_{\rm syst} = 40$-$50$ MeV. Therefore, the precision for the determination of L is governed by this systematic error.

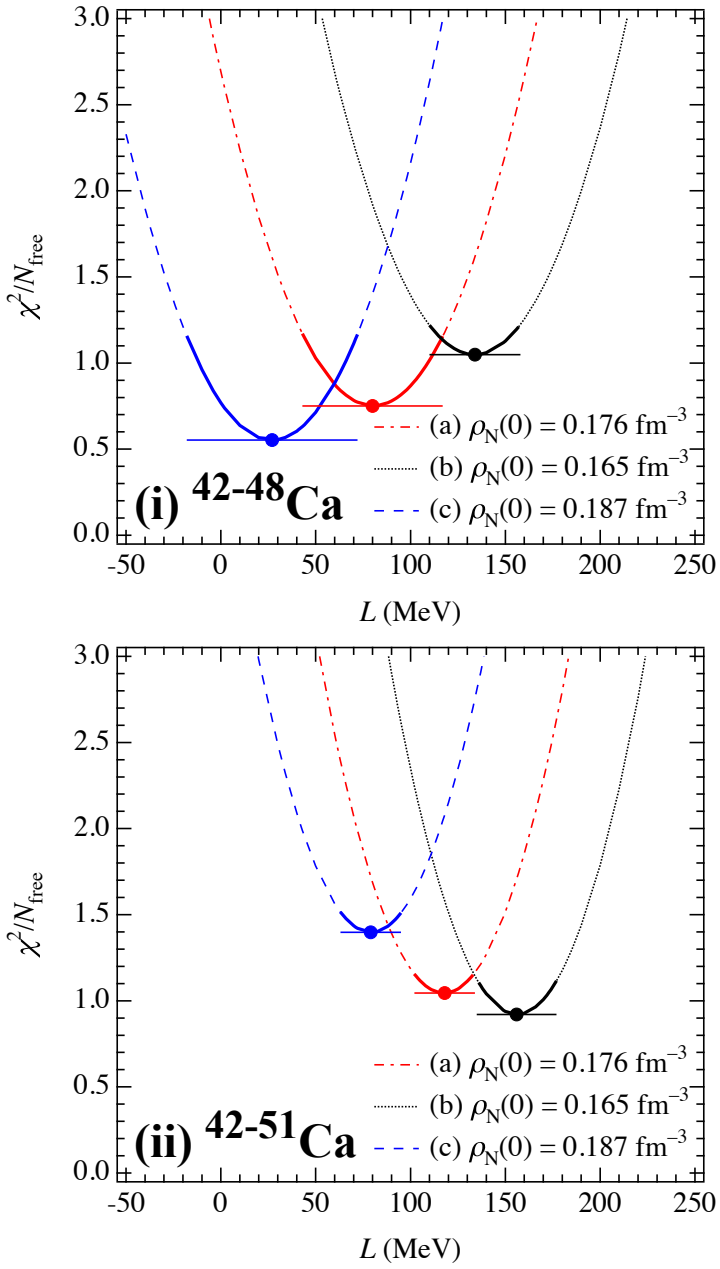

Figure 5-30: The χ^2 distribution of the fitting to (i) $^{42-48}$Ca and (ii) $^{42-51}$Ca with several assumptions of central nucleon density $\rho_{\rm N}(0)$. Each solid line represents the error region.

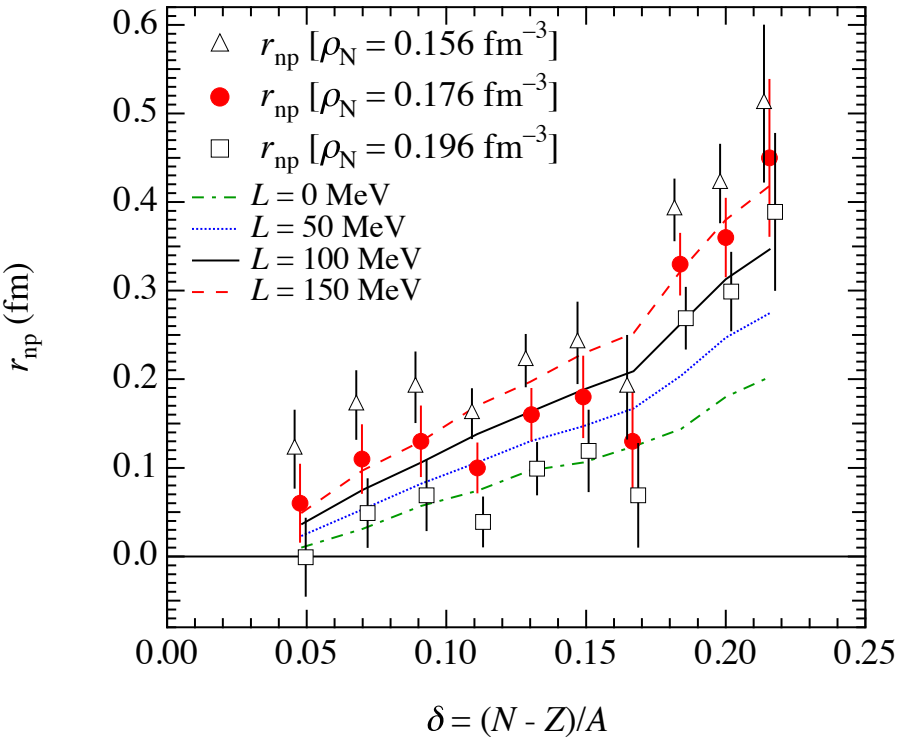

Figure 5-31: Dependence of r_{np} with $\rho_N(0) = 0.156$ (open triangles), 0.176 (red closed circles), and (open squares) against δ. Other definitions are the same as Fig. 5-29.

In order to recognize the effect of $\rho_N(0)$ on r_{np} explicitly, as an example, we show the δ dependence of r_{np} with $\rho_N(0) = 0.156$ (open triangles), 0.176 (red closed circles), and 0.196 (open squares) fm^{-3} in Fig. 5-31. Although the absolute values of r_{np} are changed in accordance with $\rho_N(0)$, the relative ones (which means the shift of r_{np} from ^{42}Ca to ^{A}Ca) are independent on $\rho_N(0)$. Since the slope of calculated lines shown in Fig. 5-31 strongly depends on L, the relative r_{np} may also have a sensitivity to L. Therefore, we attempted to deduce L from the χ^2 fit with L and $\rho_N(0)$ as free parameters. The fitting procedure was performed only to the data set (ii) $^{42-51}$Ca. We show the contour plot of χ^2/N_{free} in relation to L and $\rho_N(0)$ for this fitting procedure in Fig. 5-32. Here, N_{free} means a degree of freedom ($N_{free} = 8$ in the present case). From this fit, we can extract the information of L as summarized in Table 5-11. This shows that the simultaneous determination of L and $\rho_N(0)$ can be also accomplished from the systematic data set of σ_I along the isotopic chain, if the structure is well solved.

Table 5-11: Deduced L and corresponding $\rho_{\rm N}(0)$ from the contour plot shown in Fig. 5-32.

L (MeV)	$\rho_{\rm N}(0)$ (fm^{-3})
140^{+44}_{-30}	$0.169^{+0.008}_{-0.010}$

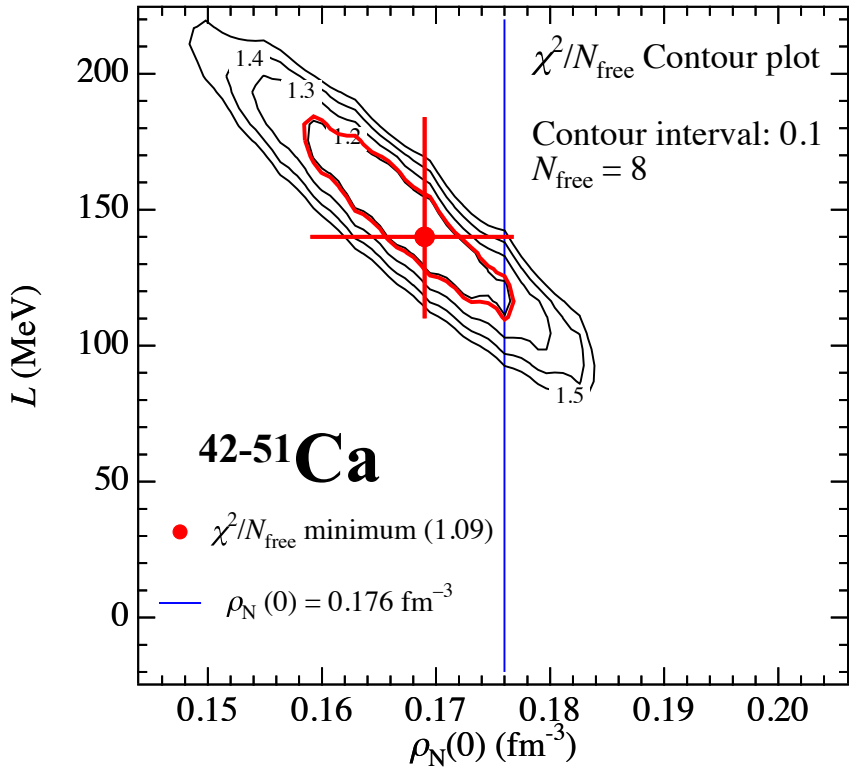

Figure 5-32: Contour plot of $\chi^2/N_{\rm free}$ in relation to L and $\rho_{\rm N}(0)$ for the fitting to the data set (ii) $^{42-51}$Ca. The red circle shows the deduced value and the red contour represents the error region which corresponds to the value of minimum $\chi^2/N_{\rm free} + 1/N_{\rm free}$. As a comparison, $\rho_{\rm N} = 0.176$ fm^{-3} (Eq. (5.9)) is also shown by the blue line.

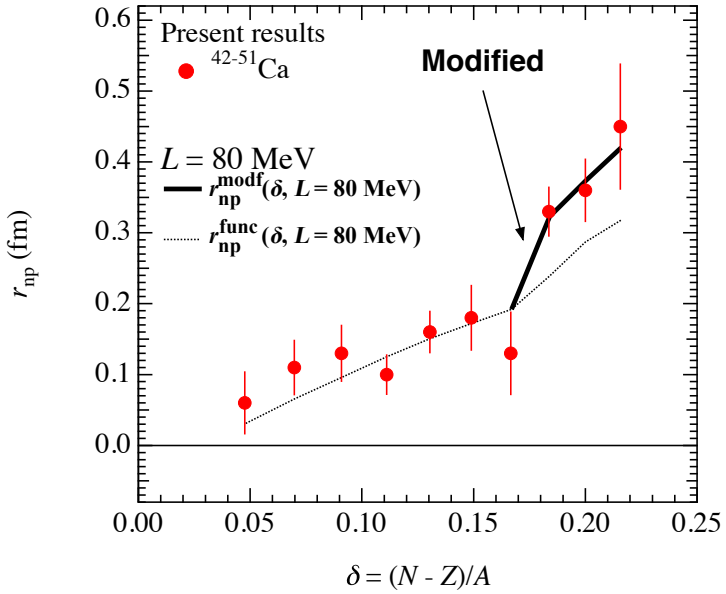

Figure 5-33: Comparison of present results with $\rho_{\rm N}(0) = 0.176$ fm^{-3} (closed circles) to $r_{\rm np}^{\rm func}(\delta, L = 80$ MeV) (dotted line) and $r_{\rm np}^{\rm modf}(\delta, L = 80$ MeV) (bold solid line).

Finally, we examine the sensitivity of the whole of the present $r_{\rm np}$ to L in more detail by the following way. As shown in Fig. 5-29, in spite of the fact that $r_{\rm np}$ of $^{42-48}$Ca with $\rho_{\rm N}(0) = 0.176$ fm^{-3} results in $L = 80(37)$ MeV, the ones of $^{49-51}$Ca prefer much larger L as approximately $L = 150$ MeV. This can be attributed to the fact that the theoretical calculations underestimate the nuclear radii for Ca isotopes beyond $N = 28$ significantly. For this reason, in order to avoid this effect on the examination of sensitivity, we modified $r_{\rm np}^{\rm func}(\delta, L)$ only for $^{49-51}$Ca by introducing a scale factor α to reproduce the systematics of experimental $r_{\rm np}$ with $L = 80$ MeV as follows:

$$r_{\rm np}^{\rm modf}(\delta, L) \equiv \alpha \times r_{\rm np}^{\rm func}(\delta, L), \tag{5.26}$$

where $r_{\rm np}^{\rm modf}(\delta, L)$ is the modified function. Here, the scale factor was determined as about $\alpha \sim 1.3$. The modified function $r_{\rm np}^{\rm modf}(\delta, L = 80$ MeV) is shown in Fig. 5-33 by the bold line together with $r_{\rm np}^{\rm func}(\delta, L = 80$ MeV) (dotted line). The fitting result with $r_{\rm np}^{\rm modf}(\delta, L)$ is summarized in Table 5-12 and also shown in Fig. 5-34 as a contour plot of $\chi^2/N_{\rm free}$ in relation to L and $\rho_{\rm N}(0)$. This examination shows the present data set have a sensitivity as 30 MeV precision to determine L, which is comparable to the previous experimental studies ($L = 58.9 \pm 16.5$ MeV [LI13]). Therefore, From the point of view

not only of the determination of L but also of the evolution of nuclear radii across the neutron magic number $N = 28$, the future progress in theoretical studies in Ca isotopes to explain proton and neutron radii simultaneously is strongly desired.

Table 5-12: Deduced L and corresponding $\rho_{\rm N}(0)$ from the contour plot shown in Fig. 5-34.

L (MeV)	$\rho_{\rm N}(0)$ (fm^{-3})
66(30)	0.183(9)

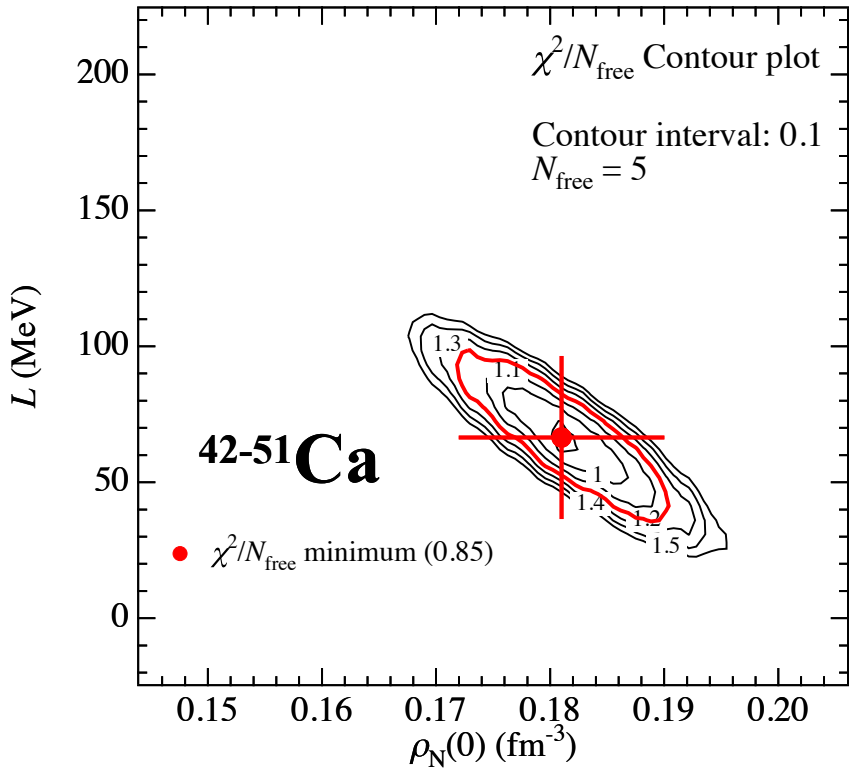

Figure 5-34: Contour plot of $\chi^2/N_{\rm free}$ in relation to L and $\rho_{\rm N}(0)$ for the fitting to the data set (ii) $^{42-51}$Ca. This fitting was performed with the modified correlation functions. Since the minimum $\chi^2/N_{\rm free}$ is less than 1, we employed the error region upto the value of $1 + 1/N_{\rm free} = 1.2$. Other definitions mean the same as Fig. 5-32.

6 Summary

6.1 Summary

In this study, we measured the interaction cross sections $\sigma_{\rm I}$ for $^{42-51}$Ca and their neighboring nuclides $^{40-48}$K and $^{44-46}$Sc on a natural C target at around 270 MeV/nucleon with the transmission method. The experiment was performed at the RIBF facility at RIKEN by using the BigRIPS fragment separator. The present $\sigma_{\rm I}$ data are the first systematic ones along the isotopic chain in Ca mass region. The root-mean-square (RMS) matter radii $\langle r^2\rangle_{\rm m}^{1/2}$ were successfully deduced based on the Glauber-type calculation with the modified optical limit approximation. The present results of $\langle r^2\rangle_{\rm m}^{1/2}$ are more precise than the previously measured ones which are for only stable Ca isotopes ^{40,42,44,48}Ca. We also determined the neutron radii and therefore the neutron-skin thicknesses $r_{\rm np}$ from the deduced $\langle r^2\rangle_{\rm m}^{1/2}$ in combination with the RMS proton radii $\langle r^2\rangle_{\rm p}^{1/2}$, which were derived from the previously measured charge radii by isotope shifts. These results represent the first precise and systematic data for the neutron distributions of Ca isotopes across the $N = 28$ magic number. From the obtained $\langle r^2\rangle_{\rm m}^{1/2}$ and $r_{\rm np}$, the following results and conclusions have been presented.

- For nuclides below $N = 28$, the trend of $\langle r^2\rangle_{\rm m}^{1/2}$ follows the systematics of spherical stable nuclei. Moreover, the mild enhancement of $\langle r^2\rangle_{\rm m}^{1/2}$ around the midpoint of $1f_{7/2}$ shell can be explained by taking the effect of quadrupole deformation into account.

- The $\langle r^2\rangle_{\rm m}^{1/2}$ of Ca isotopes beyond $N = 28$ are significantly enhanced compared to the systematics of spherical stable nuclei, This is consistent with the trend of previously measured charge radii. These enhancements of $\langle r^2\rangle_{\rm m}^{1/2}$ cannot be explained by the effect of quadrupole deformation.

- In the case of ^{49}Ca, we also examined the enhancement of $\langle r^2\rangle_{\rm m}^{1/2}$ within the framework of the single particle model (SPM) with the combination of ^{48}Ca core + $2p_{3/2}$ valence neutron. However, this model also cannot reproduce the experimental result, which may indicate the need to consider the core excitation in ^{49}Ca. This may also indicate a complicated configuration mixing. To explain the experimental $\langle r^2\rangle_{\rm m}^{1/2}$ of ^{49,50,51}Ca within the SPM, the core has to be enlarged by at least about 0.1-0.2 fm.

- The present experimental $\langle r^2 \rangle_{\rm m}^{1/2}$ and the previously measured $\langle r^2 \rangle_{\rm p}^{1/2}$ were compared to several theoretical calculations using the Hartree Fock (HF) and relativistic mean field (RMF) theories. Although the theoretical calculations also show the slope change of the trend of nuclear radii beyond $N = 28$, the slope of experimental results about two times as large as those of theoretical calculations for both $\langle r^2 \rangle_{\rm m}^{1/2}$ and $\langle r^2 \rangle_{\rm p}^{1/2}$. The theoretical calculations also show that the enhancement of nuclear radius may result from the sudden increase of surface diffuseness.

- The $r_{\rm np}$ were directly determined from $r_{\rm m}$ by adopting the known $r_{\rm p}$. The present $r_{\rm np}$ of ^{48}Ca is consistent with the recent experimental result by the dipole polarizability $\alpha_{\rm D}$.

- The sensitivity of the present $r_{\rm np}$ to the EOS parameter L was examined. The correlation between $r_{\rm np}$ and L was studied with the help of the mean field calculations. Although the present experimental $r_{\rm np}$ have a possibility to deduce L with 16 MeV statistical error, the precision for the determination of L is dictated by the large systematic error which results from the uncertainty of nucleon density distribution $\Delta\rho_{\rm N}(0)$.

- It was shown that the above systematic error can be avoided by utilizing the relative values of $r_{\rm np}$. Taking such approach, the present data including ^{49,50,51}Ca are expected to have a sensitivity of 30 MeV to determine L.

6.2 Future Prospect

6.2.1 Nuclear Structure

In the present study, the evolution of nuclear radii beyond $N = 28$ was discussed from several aspects. Within the framework of the HF theory, for example, the kink structure at the neutron magic number $N = 28$ may be related to the strength of spin-orbit force. However, this mechanism cannot be understood well in the microscopic level at present. Therefore, further progress of theoretical study to explain this mechanism simultaneously for both proton and matter radii is strongly desired. The experimental matter radii across the neutron magic number has been determined for the first time. It will be interesting to understand theoretically the evolution of the matter radii.

It was also pointed out $\sigma_{\rm I}$ measurements may provide a useful means to identify the emergence/disappearance of a neutron magic number. Such

indication has been suggested from the systematics of charge radii. However, in order to establish this method, further studies are required. Therefore, $\sigma_{\rm I}$ for other nuclides across the well known magic numbers should be measured in order to verify whether the kink structure is commonly found or not.

In terms of the shell evolution in the Ca isotopic chain, ^{52}Ca and ^{54}Ca were reported as newly established doubly-magic nuclei. Hence, it will be of interest to measure $\sigma_{\rm I}$ for more neutron-rich Ca isotopes.

6.2.2 Equation of State

Due to the underestimation of presently available theoretical calculations for nuclear radii of Ca isotopes beyond $N = 28$ compared to experimental results, we could not deduce a precise value of L from the present data. Therefore, the future progress in the theoretical framework which can explain the evolution of nuclear radii for Ca isotopes including $^{49-51}$Ca in the microscopic level is anticipated. It will be interesting to know if the *ab initio* calculations using the NNLO$_{\rm sat}$, which can reproduce the experimental charge radii relatively well, can reproduce the experimental matter radii, and hence provide a more reliable means to extract L from the present directly-determined $r_{\rm np}$.

In deducing L from the absolute value of $r_{\rm np}$, $\Delta\rho_{\rm N}(0)$ which was determined from several hadron elastic scattering data results in a large systematic error. This may be improved in several ways. The hadron elastic scattering data have large discrepancies between different measurements beyond the quoted errors. Since the 1980s when the latest results of those data were reported, theoretical physics has achieved steady progress. For this reason, the reanalysis of hadron elastic scattering data with the more sophisticated theory may reduce this systematic error. Further experimental studies for deducing nucleon density distributions of Ca isotopes such as additional hadron elastic scattering experiments and the measurement of the energy dependence of reaction cross sections can also help to reduce the uncertainties of central nucleon density.

The present $r_{\rm np}$'s of Ca isotopes were obtained in the range of $0.05 < \delta < 0.22$, where δ is a relative neutron excess $\delta = (N - Z)/A$. In order to improve the sensitivity to L, measurements of $r_{\rm np}$ in a wider range are required. For example, Ni isotopic chain is one of the next objectives. We have measured $\sigma_{\rm I}$ for $^{58-78}$Ni ($0.03 < \delta < 0.28$) in the same experiment as for nuclides reported in this thesis. Besides, we have also measured the charge-changing-cross sections $\sigma_{\rm CC}$, which is being developed as a probe for proton radii. By the combination of $\sigma_{\rm I}$ and $\sigma_{\rm CC}$, $r_{\rm np}$ for Ni isotopes will be extracted and discussed in the near future.

References

[AB12] S. Abrahamyan *et al.*, Phys. Rev. Lett. **108**, 112502 (2012).

[AG05] B. K. Agrawal *et al.*, Phys. Rev. C **72**, 014310 (2005).

[AL76] G. D. Alkhazov *et al.*, Nucl. Phys. A **274**, 443-462 (1976).

[AL77] G. D. Alkhazov *et al.*, Nucl. Phys. A **280**, 365-376 (1977).

[AL82] G. D. Alkhazov *et al.*, Nucl. Phys. A **381**, 430-444 (1982).

[AN09] I. Angeli *et al.*, J. Phys. F: Nucl. Part. Phys. **36**, 085102 (2009).

[AN13] I. Angeli and K.P. Marinova, Atom. Data and Nucl. Data Tabl. **99**, 69-95 (2013).

[AV11] M. Avgoulea *et al.*, J. Phys. G: Nucl. Part. Phys. **38**, 025104 (2011).

[BA82] J. Bartel *et al.*, Nucl. Phys. A **386**, 79 (1982).

[BA86] G. Baur *et. al.*, Nucl. Phys. A **458**, 188 (1986).

[BA16] M. Baido and G.F. Burgio, Prog. in Part. and Nucl. Phys. **91**, 203-258 (2016).

[BE03] M. Bender *et al.*, Rev. Mod. Phys. **75**, 121 (2003).

[BI17] J. Birkhan, Phys. Rev. Lett. **118**, 252501 (2017).

[BigRIPS1] Facility of RIBF at the RIKEN Nishina Center.
http://www.nishina.riken.jp/facility/RIBFfacility.html

[BigRIPS2] Information of accelerator at RIBF.
http://www.nishina.riken.jp/RIBF/accelerator/concept.html

[BigRIPS3] Information of BigRIPS fragment separator.
http://www.nishina.riken.jp/RIBF/BigRIPS/config.html

[BigRIPS4] Information of optics of the BigRIPS.
http://ribf.riken.jp/BigRIPSInfo/optics/optics.html

[BigRIPS5] Detailed information of the BigRIPS.
http://ribf.riken.jp/BigRIPSInfo/

[BL16] B. Blank *et al.*, Phys. Rev. C **93**, 061301 (2016).

[BO84] K. G. Boyer *et al.*, Phys. Rev. C **29**, 182-194 (1984).

[BU05] A. Bürger *et al.*, Phys. Lett. B **622**, 29-34 (1984).

[CA01] E. Caurier *et al.*, Phys. Lett. B **522**, 240-244 (2001).

[CE09] M. Centelles *et al.*, Phys. Rev. Lett. **102**, 122502 (2009).

[CE10] M. Centelles *et al.*, Phys. Rev. C **82**, 054314 (2010).

[CE16] I. Čeliković *et al.*, Phys. Rev. Lett. **116**, 162501 (2016).

[CH68] R. Chapman *et al.*, Nucl. Phys. A **119**, 305-324 (1968).

[CH77] A. Chaumeaux *et al.*, Phys. Lett. B **72**, 33-36 (1977).

[CH97] E. Chabanat *et al.*, Nucl. Phys. A **627**, 79 (1997).

[CH10] L.-W. Chen et al., Phys. Rev. C **82**, 024321 (2010).

[CH15] W.-C. Chen and J. Piekarewicz, Phys. Lett. B **748**, 284 (2015).

[Circuit] Electrical circuit used in the BigRIPS experiment.
http://ribf.riken.jp/BigRIPSInfo/daq/circuit.html

[CO66] R. G. Cornwell *et al.*, Phys. Rev. **141**, 1106-1111 (1966).

[DI05] D.-C. Dinca *et al.*, Phys. Rev. C **71**, 041302(R) (2005).

[DU12] M. Dutra *et al.*, Phys. Rev. C **85**, 035201 (2012).

[EK15] A. Ekström *et al.*, Phys. Rev. C **91**, 051301(R) (2015).

[FR68] R. F. Frosch *et al.*, Phys. Rev. **174**, 1380-1399 (1968).

[FR97] J.L. Friar *et al.*, Phys. Rev. A **56**, 4579 (1997).

[FU93] N. Fukunishi *et al.*, Phys. Rev. C **48**, 1648 (1993).

[FU12] T. Furumoto *et al.*, Phys. Rev. C **85**, 044607 (2012).

[GA06] L. G. Gao *et al.*, Phys. Rev. C **73**, 014313 (2006).

[GA15] R. F. Garcia Ruiz *et al.*, Phys. Rev. C **91**, 041304(R) (2015).

[GA16] R. F. Garcia Ruiz *et al.*, Nature Phys. **12**, 594-599 (2016).

[GI92] W. R. Gibbs and J.-P. Dedonder, Phys. Rev. C **46**, 1825 (1992).

[GO74] A. S. Goldhaber, Phys. Lett. B **53**, 306 (1974).

[GO13] P.M. Goddard *et al.*, Phys. Rev. Lett. **110**, 032503 (2013).

[HA15] T. Hashimoto *et al.*, Phys. Rev. C **92**, 031305(R) (2015).

[HA16] G. Hagen *et al.*, Nature Phys. **12**, 186-190 (2016).

[HE13] W. He *et al.*, Chin. Phys. Lett. **30**, 042501 (2013).

[HI75] V. L. Highland, Nucl. Instr. and Meth. **129**, 497-499 (1975).

[HO12] J.D. Holt *et al.*, J. Phys. G: Nucl. Part. Phys. **39**, 085111 (2012).

[HO16] W. Horiuchi *et al.*, Phys. Rev. C **93**, 044611 (2016).

[HO17] A. Homma *et al.*, JPS Conf. Proc. **14**, 021010 (2017).

[HOR17] W. Horiuchi, S. Ebata, and K. Iida, Phys. Rev. C **96**, 035804 (2017), and private communication.

[II04] K. Iida and K. Oyamatsu, Phys. Rev. C **69**, 037301 (2004).

[IM16] H. Imao *et al.*, Proc. of the 13th Ann. Meeting of Particle Acc. Soc. of Japan, 56-60 (2016).

[JA02] R.V.F. Jannnssens *et al.*, Phys. Lett. B **546**, 55-62 (2002).

[JA04] J. Jastrzebski *et al.*, Int. Jour. of Mod. Phys. E **13**, 343-351 (2004).

[KA01] R. Kanungo *et al.*, Phys. Lett. B **512**, 261-267 (2001).

[KA09] D. Kaji *et al.*, Journal of Physical Society of Japan **78**, 035003 (2009).

[KA11] R. Kanungo *et al.*, Phys. Rev. C **84**, 061304 (2011).

[KA16] Y. Kanke, Master thesis, Tokyo University of Science (2016).

[KI05] K. Kimura *et al.*, Nucl. Instr. and Meth. in Phys. Research A **538**, 608-614 (2005).

[KL07] A. Klimikiewicz *et al.*, Phys. Rev. C **76**, 051603(R) (2007).

[KL09] P. KLúpfel *et al.*, Phys. Rev. C **79**, 034310 (2009).

[KO84] S. Kox *et al.*, Nucl. Phys. A **420**, 162 (1984).

[KO87] S. Kox *et al.*, Phys. Rev. C **35**, 1678 (1987).

[KO97] S. Kopecky *et al.*, Phys. Rev. C **56**, 2229 (1997).

[KR94] A. Krasznahorkay *et al.*, Nucl. Phys. A **567**, 521-540 (1994).

[KR99] A. Krasznahorkay *et al.*, Phys. Rev. Lett. **82**, 3216-3219 (1999).

[KR04] A. Krasznahorkay *et al.*, Nucl. Phys. A **731**, 224-234 (2004).

[KR14] K. Kreim *et al.*, Phys. Lett. B **731**, 97-102 (2014).

[KU12] T. Kubo *et al.*, Prog. Theor. Exp. Phys. **2012**, 03C003 (2012).

[KU13] H. Kumagai *et al.*, Nucl. Instr. and Meth. in Phys. Research B **317**, 717-727 (2013).

[LA97] G. A. Lalazissis *et al.*, Phys. Rev. C **55**, 540 (1997).

[LA99] G. A. Lalazissis *et al.*, Atom. Data Nucl. Data Tables **71**, 1 (1999).

[LE87] W. R. Leo, Springer-Verlag, (1987).
Techniques for Nuclear and Particle Physics Experiments. - A How-to Approach -

[LI04] S. Liddick *et al.*, Phys. Rev. Lett. **92**, 072502 (2004).

[LI07] T. Li *et al.*, Phys. Rev. Lett. **99**, 162503 (2007).

[LI11] Bao-An Li *et al.*, Journal of Phys.: Conference Series **312**, 042006 (2011).

[LI13] Bao-An Li and Xiao Han, Phys. Lett. B **727**, 276-281 (2013).

[LISE] Simulation code "LISE++" for the secondary beam production.
http://lise.nscl.msu.edu/lise.html

[LO15] G. Lorrusso *et al.*, Phys. Rev. Lett. **114**, 192501 (2015).

[MC86] R. H. McCamis *et al.*, Phys. Rev. C **33**, 1624-1633 (1986).

[MI98] M. Mihara, Doctoral thesis, Osaka University (1998).

[MI12] K. Minomo *et al.*, Phys. Rev. Lett. **108**, 052303 (2012).

[MY69] W. D. Myers and W. J. Swiatecki, Ann. of Phys. **55**, 395-505 (1969).

[MY74] W. D. Myers and W. J. Swiatecki, Ann. of Phys. **84**, 186-210 (1974).

[MY80] W. D. Myers and W. J. Swiatecki, Nucl. Phys. A **336**, 267-278 (1980).

[NA10] Database of the nucleon-nucleon total cross section. http://pdg.lbl.gov/2010/hadronic-xsections/hadron.html

[NA15a] H. Nakada and T. Inakura, Phys. Rev. C **91**, 021302 (2015).

[NA15b] H. Nakada, Phys. Rev. C **92**, 044307 (2015).

[NI11] D. Nishimura, Doctoral thesis, Osaka University (2011).

[OG92] Y. Ogawa, K. Yabana and Y. Suzuki, Nucl. Phys. A **543**, 722 (1992).

[OH05] T. Otsuka *et al.*, Phys. Rev. Lett. **95**, 232502 (2005).

[OT07] T. Otsuka *et al.*, Prog. in Part. and Nucl. Phys. **59**, 425-431 (2007).

[OH08] T. Ohnishi *et al.*, Journal of the Phys. Society of Japan **77**, 083201 (2008).

[OH10] T. Ohnishi *et al.*, Journal of Physical Society of Japan **79**, 073201 (2010).

[OH18] K. Ohnishi, Master thesis, Osaka University (2018).

[OZ01] A. Ozawa *et al.*, Nucl. Phys. A **691**, 599-617 (2001).

[OZA01] A. Ozawa *et al.*, Nucl. Phys. A **693**, 32-62 (2001).

[PA84] C. Palmer *et al.*, J. Phys. B **17**, 2197-2211 (1984).

[PA16] C. Patrignani *et al.*, Chin. Phys. C **40**, 100001 (2016).

[PI09] J. Piekarewicz and M. Centelles, Phys. Rev. C **79**, 054311 (2009).

[PI17] J. Piekarewicz, Phys. Rev. C **96**, 044314 (2017).

[PR01] J.I. Prisciandaro *et al.*, Phys. Lett. B **510**, 17-23 (2001).

[PR16] B. Pritychenko *et al.*, Atomic Data and Nuclear Data Tables **107**, 1-139 (2016).

[RA81] L. Ray *et al.*, Phys. Rev. C **23**, 828-837 (1981).

[RE95] P.-G. Reinhard and H. Flocard, Nucl. Phys. A **584**, 467 (1995).

[RIBFDAQ] Information of data acquisition system of the RIBF experiment. https://ribf.riken.jp/RIBFDAQ/index.php?DAQ%2FInformation

[RO11] X. Roca-Maza *et al.*, Phys. Rev. Lett. **106**, 252501 (2011).

[RO13] D.M. Rossi *et al.*, Phys. Rev. Lett. **111**, 242503 (2013).

[RO15] X. Roca-Maza *et al.*, Phys. Rev. C **92**, 064304 (2015).

[SA89] M.G. Saint-Laurent *et al.*, Z. Phys. A **332**, 457-465 (1989).

[SA01] H. Sagawa *et al.*, Nucl. Phys. A **688**, 755-764 (2001).

[SA14] H. Sagawa and G. Coló, Prog. in Part. and Nucl. Phys. **76**, 76-115 (2014).

[SC98] C. Scheidenberger *et al.*, Nucl. Instr. and Meth. in Phys. Res. B **142**, 441-462 (1998).

[SC03] S. Schielke *et al.*, Phys. Lett. B **571**, 29 (2003).

[SC14] C. Scheidenberger, Lecture Notes in Physics 879, (2014).

[SH95] M. M. Sharma *et al.*, Phys. Rev. Lett. **74**, 3744 (1995).

[SI03] I. Sick, Phys. Lett. B **576**, 62 (2003).

[ST77] F. Stancu *et al.*, Phys. Lett. B **68**, 108-112 (1977).

[ST13] D. Steppenbeck *et al.*, Nature **502**, 207-210 (2013).

[SU75] G. Sussmann, Z. Phys. A **204**, 145 (1975).

[SU95] T. Suzuki *et al.*, Phys. Rev. Lett. **75**, 3241 (1995).

[SU98] T. Suzuki *et al.*, Nucl. Phys. A **630**, 661-677 (1998).

[SU03] Y. Suzuki *et al.*, "Structure and Reactions of Light Exotic Nuclei" published in the USA and Canada by Talyor and Francis Inc. (2003).

[SU08] Y. Suzuki, 日本物理学会誌 Vol. **63**, No. 6 419-426 (2008).

[SU12] K. Sümmer, Phys. Rev. C **86**, 014601 (2012).

[SU13] H. Suzuki *et al.*, Nucl. Intr. and Methods in Physics Research B **317**, 756-768 (2013).

[SU13] S. Suzuki, Doctoral thesis, Niigata University (2013).

[SUM17] T. Sumikama *et al.*, Phys. Rev. C **95**, 051601(R) (2017).

[SUZ17] H. Suzuki *et al.*, Phys. Rev. Lett. **119**, 192503 (2017).

[TA85a] I. Tanihata *et al.*, Phys. Rev. Lett. **55**, 2676 (1985).

[TA85b] I. Tanihata *et al.*, Phys. Lett. B **160**, 380 (1985).

[TA89] I. Tanihata *et al.*, Proc. for Conf. "Radioactive Nuclear Beams", p.429 (World Scientific Berkely, California, USA, 1989).

[TA92] I. Tanihata *et al.*, Phys. Lett. B **289**, 261-266 (1992).

[TA01] I. Tanihata, Nucl. Phys. A **682**, 114c-123c (2001).

[TA05] M. Takechi, Doctoral thesis, Osaka University (2005).

[TAY05] M. J. Taylor *et al.*, Phys. Lett. B **605**, 265 (2005).

[TA11] A. Tamii *et al.*, Phys. Rev. Lett. 107, 062502 (2011).

[TA12] M. Takechi *et al.*, Phys. Lett. B **707**, 357-361 (2012).

[TA14] M. Takechi *et al.*, Phys. Rev. C **90**, 061305(R) (2014).

[TAR14] C.M. Tarbert *et al.*, Phys. Rev. Lett. **112**, 242502 (2014).

[TA15] M. Tanaka, Master thesis, Osaka University (2015).

[TE08] S. Terashima *et al.*, Phys. Rev. C **77**, 024317 (2014).

[TE15] T. Q. Teodoro *et al.*, Phys. Rev. A **91**, 032516 (2015).

[TO84] F. Tondeur *et al.*, Nucl. Phys. A **420**, 297 (1984).

[TO05] B. G. Todd-Rutel and J. Piekarewicz , Phys. Rev. Lett. **95**, 122501 (2005).

[TR01] A. Trzcińska *et al.*, Phys. Rev. Lett. **87**, 082501 (2001).

[TR18] D. T. Tran *et al.*, Nature Communications **9**, 1594 (2018).

[VA02] K. Varga *et al.*, Phys. Rev. C **66**, 0034611 (2002).

[VR87] H. De Vries *et al.*, Atom. Data and Nucl. Data Tables **36**, 495-536 (1987).

[WA09] M. Warda *et al.*, Phys. Rev. C **80**, 024316 (2009).

[WA10] M. Warda *et al.*, Phys. Rev. C **81**, 054309 (2010).

[WA14] M. Warda *et al.*, Phys. Rev. C **89**, 064302 (2014).

[WAT14] S. Watanabe *et al.*, Phys. Rev. C **89**, 044610 (2014).

[WA17] M. Wang *et al.*, Chin. Phys. C **41** 030003 (2017).

[WI11] O. Wieland and A. Bracco, Prog. in Part. and Nucl. Phys. **66**, 374-378 (2011).

[WI13] F. Wienholtz *et al.*, Nature **498**, 346-349 (2013).

[YO99] D. H. Youngblood *et al.*, Phys. Rev. Lett. **82**, 691-694 (1999).

[YA12] K. Yamada *et al.*, Proc. of IPAC12, TUOBA02 (2012).

[ZE10] J. Zenihiro *et al.*, Phys. Rev. C **82**, 0444611 (2010).

[ZH16] P.W. Zhao and S. Gandolfi, Phys. Rev. C **94**, 041302(R) (2016).

A Derivation Formula of Interaction Cross Section

In the σ_{I} measurements with a target whose thickness is not constant, σ_{I} can be strictly derived as

$$\begin{aligned}\sigma_{\mathrm{I}} &= \frac{\int N(x)\left[\frac{-1}{t(x)}\ln R(x)\right]dx}{\int N(x)dx} \\ &\equiv \langle\frac{-1}{t(x)}\ln R(x)\rangle,\end{aligned} \tag{A.1}$$

where $t(x)$ is the target profile, $R(x)$ the non-reaction rate distribution, and $N(x)$ the beam profile along the horizontal axis x, respectively. In the following, we show the validity of the following equation within less than 10^{-4} descripancy:

$$\langle\frac{-1}{t(x)}\ln R(x)\rangle \simeq \frac{-1}{\langle t(x)\rangle}\ln\langle R(x)\rangle. \tag{A.2}$$

When the wedge-shaped target is employed, $t(x)$ can be defined as

$$t(x) = \langle t\rangle + a\left(x - \langle x\rangle\right), \tag{A.3}$$

where $\langle t\rangle$ is a weighted-mean thickness, a a slope of the target thickness, and $\langle x\rangle$ a weighted-mean position of the beam profile, respectively. By using Eq. (A.3), the left-hand side of Eq. (A.2) can be converted to:

$$\begin{aligned}\langle\frac{-1}{t(x)}\ln R(x)\rangle &= -\int\left[\frac{1}{t(x)}\ln R(x)f(x)\right]dx \\ &= -\int\left[\frac{1}{\langle t\rangle + a\left(x-\langle x\rangle\right)}\ln R(x)f(x)\right]dx \\ &= -\frac{1}{\langle t\rangle}\int\left[\left\{\sum_{n=0}\left(\frac{a\left(x-\langle x\rangle\right)}{\langle t\rangle}\right)^n\right\}\ln R(x)f(x)\right]dx \\ &= -\frac{1}{\langle t\rangle}\int\left[1\cdot\ln R(x)f(x)\right]dx \\ &\quad -\frac{1}{\langle t\rangle}\int\left[\left(-\frac{a\left(x-\langle x\rangle\right)}{\langle t\rangle}\right)\cdot\ln R(x)f(x)\right]dx \\ &\quad -\frac{1}{\langle t\rangle}\int\left[\left(-\frac{a\left(x-\langle x\rangle\right)}{\langle t\rangle}\right)^2\cdot\ln R(x)f(x)\right]dx \\ &\quad \vdots,\end{aligned} \tag{A.4}$$

where $f(x)$ is a probability function of beam profile defined as

$$f(x) \equiv \frac{N(x)}{\int N(x)dx}. \tag{A.5}$$

In the present work, $a\left(x - \langle x \rangle\right)/\langle t \rangle$ is estimated as

$$\begin{aligned} \langle t \rangle &= 1.81 \text{ [g/cm}^2\text{]} \\ a &= 1.87 \times 10^{-3} \text{ [g/cm}^2\text{/mm]} \\ x - \langle x \rangle &= 10 \text{ [mm]} \\ \frac{a\left(x - \langle x \rangle\right)}{\langle t \rangle} &\sim 10^{-2}. \end{aligned} \tag{A.6}$$

Therefore, we can ignore the terms after the third one in Eq. (A.4) within less than 10^{-4} accuracy:

$$\langle \frac{-1}{t(x)} \ln R(x) \rangle = -\frac{1}{\langle t \rangle} \left[\langle \ln R \rangle - \int \frac{a\left(x - \langle x \rangle\right)}{\langle t \rangle} \cdot \ln R(x) f(x) dx \right]. \tag{A.7}$$

From the Cumulant expansion, $\ln\langle R \rangle$ can be reduced as

$$\begin{aligned} \langle R \rangle &= \langle e^{\ln R} \rangle \\ &= e^{\langle \ln R \rangle} \langle e^{(\ln R - \langle \ln R \rangle)} \rangle \end{aligned} \tag{A.8}$$

$$\begin{aligned} \ln\langle R \rangle &= \langle \ln R \rangle + \ln\left(1 + \frac{1}{2}\langle (\ln R - \langle \ln R \rangle) \rangle + \cdots\right) \\ &\sim \langle \ln R \rangle + \frac{1}{2}\langle (\ln R - \langle \ln R \rangle)^2 \rangle \end{aligned} \tag{A.9}$$

By substituting Eq. (A.9) into Eq. (A.7), the following equation can be derived:

$$\begin{aligned} &\langle \frac{-1}{t(x)} \ln R(x) \rangle \\ &= -\frac{1}{\langle t \rangle} \ln\langle R \rangle + \frac{1}{\langle t \rangle}\frac{1}{2}\langle (\ln R - \langle \ln R \rangle)^2 \rangle + \frac{1}{\langle t \rangle} \left\langle \frac{a\left(x - \langle x \rangle\right)}{\langle t \rangle} \cdot \ln R(x) \right\rangle. \\ &= -\frac{1}{\langle t \rangle} \ln\langle R \rangle \left[1 - \frac{1}{2}\frac{\langle (\ln R - \langle \ln R \rangle)^2 \rangle}{\ln\langle R \rangle} - \frac{\left\langle \frac{a\left(x - \langle x \rangle\right)}{\langle t \rangle} \cdot \ln R(x) \right\rangle}{\ln\langle R \rangle} \right] \end{aligned} \tag{A.10}$$

On the other hand, $\ln R$ also can be represented as

$$\ln R = -\sigma_{\rm I}\langle t\rangle \left\{1 + \frac{a}{\langle t\rangle}(x - \langle x\rangle)\right\}. \tag{A.11}$$

Therefore, the dispersion of $\ln R$ is converted to:

$$\begin{aligned}\langle(\ln R - \langle \ln R\rangle)^2\rangle &= \langle(\ln R)^2\rangle - \langle \ln R\rangle^2 \\ &= \sigma_{\rm I}^2\langle t\rangle^2 \cdot \frac{a^2}{\langle t\rangle^2}\langle(x - \langle x\rangle)^2\rangle \\ &= \left(\sigma_{\rm I}\langle t\rangle \cdot \frac{\langle x - \langle x\rangle\rangle}{\langle t\rangle}\right)^2\end{aligned} \tag{A.12}$$

From Eq. (A.12), the effect of the second term in Eq. (A.10) is negligibly small as

$$\begin{aligned}\frac{1}{2}\cdot\frac{\langle(\ln R - \langle \ln R\rangle)^2\rangle}{\ln\langle R\rangle} &= \frac{1}{2}\cdot\frac{1}{\ln\langle R\rangle}\cdot\left(\sigma_{\rm I}\langle t\rangle \cdot \frac{\langle x - \langle x\rangle\rangle}{\langle t\rangle}\right)^2 \\ &= \frac{1}{2}\left(\frac{\sigma_{\rm I}\langle t\rangle}{\ln\langle R\rangle}\right)(\sigma_{\rm I}\langle t\rangle)\left(\frac{\langle x - \langle x\rangle\rangle}{\langle t\rangle}\right)^2 \\ &\sim \frac{1}{2}\cdot 1\cdot 10^{-1}\cdot 10^{-4} \sim 10^{-5}\end{aligned} \tag{A.13}$$

The third term in Eq. (A.10) also can be ignored as

$$\begin{aligned}\frac{\left\langle \dfrac{a\,(x - \langle x\rangle)}{\langle t\rangle}\cdot \ln R(x)\right\rangle}{\ln\langle R\rangle} &= \frac{1}{\ln\langle R\rangle}\left\langle \frac{a\,(x - \langle x\rangle)}{\langle t\rangle}(-\sigma_{\rm I}\langle t\rangle)\left\{1 + \frac{a}{\langle t\rangle}(x - \langle x\rangle)\right\}\right\rangle \\ &= \left(-\frac{\sigma_{\rm I}\langle t\rangle}{\ln\langle R\rangle}\right)\cdot\left(\frac{a^2\langle(x - \langle x\rangle)^2\rangle}{\langle t\rangle^2}\right) \\ &\sim 1\cdot 10^{-4} \sim 10^{-4}\end{aligned} \tag{A.14}$$

Therefore, Eq. (A.10) can be reduced to Eq. (A.2) within less than 10^{-4} discrepancy.

B Mass number dependence of matter radii for stable nuclei

In the case of stable nuclei, the RMS charge radii $\langle r^2 \rangle_{\rm ch}^{1/2}$ have been systematically measured via the electron elastic scattering, the isotope shift, and the transition energy of muonic atom [AN13]. In Fig. B.1, previously measured RMS proton radii $\langle r^2 \rangle_{\rm p}^{1/2}$ of stable nuclei which were derived from $\langle r^2 \rangle_{\rm ch}^{1/2}$ in accordance with Eq. (5.8) are shown by open or closed circles. Based on the fact that the stable nuclei have the almost same RMS matter radii $\langle r^2 \rangle_{\rm m}^{1/2}$ as the RMS proton ones $\langle r^2 \rangle_{\rm p}^{1/2}$, we can regard the mass number A dependence of $\langle r^2 \rangle_{\rm p}^{1/2}$ as that of $\langle r^2 \rangle_{\rm m}^{1/2}$. The A dependence of $\langle r^2 \rangle_{\rm m}^{1/2}$ was obtained through the fitting for the experimental $\langle r^2 \rangle_{\rm p}^{1/2}$ between $35 \leq A \leq 48$ shown by closed circles in Fig. B.1 to the function of $A^{1/3}$ as

$$0.9324(A + 5.232)^{1/3} \pm 0.0453(\text{S.D.})[\text{fm}], \tag{B.1}$$

where "S.D." means the standard deviation. In Fig. B.1, the fitting result and the corresponding standard deviation are represented by the solid line and the gray band, respectively.

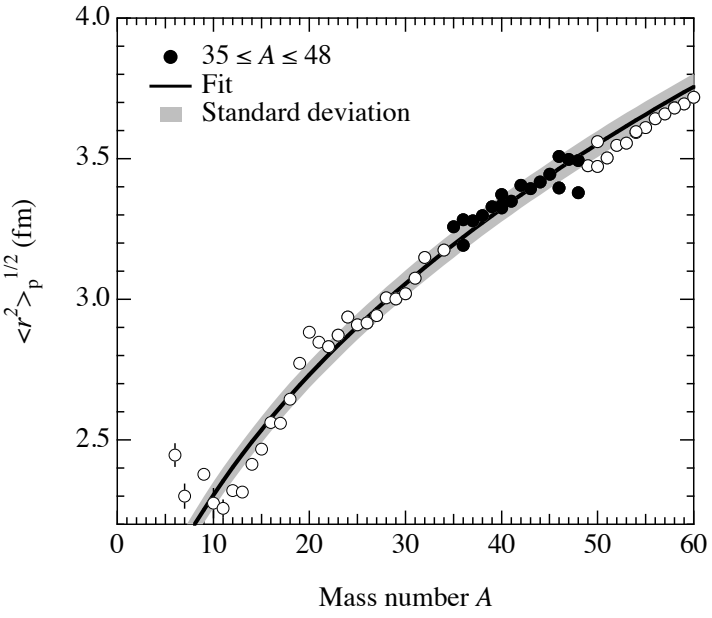

Figure B.1: Mass number A dependence of $\langle r^2 \rangle_{\rm p}^{1/2}$ of stable nuclei [AN13]. The fitting result for the nuclei between $35 \leq A \leq 48$ (closed circles) and the corresponding standard deviation are represented by the solid line and the gray band, respectively.

C PID Spectra

In Sec. 4.1, we explained the procedure of data analysis in the case of ^{43}Ca as an example. In this section, we show the spectra of particle identification before and after the reaction target in the case of the other nuclides:

(a) A/Q_{F3F5} vs. Z_{F3IC} with *gate#6*.

(b) Z_{F5IC} vs. Z_{F7IC} with *DS#1* and *DS#2*.
(When there is a tail at large Z_{F5IC}, these events were counted as non-charge-changing particles. These counting gates are shown by horizontal red solid lines in the following figures.)

(c) A/Q_{F5F7} vs. ΔE_{F7PL} with *DS#3*.

(d) A/Q_{F5F7} vs. ΔE_{F7PL} with *DS#4*.

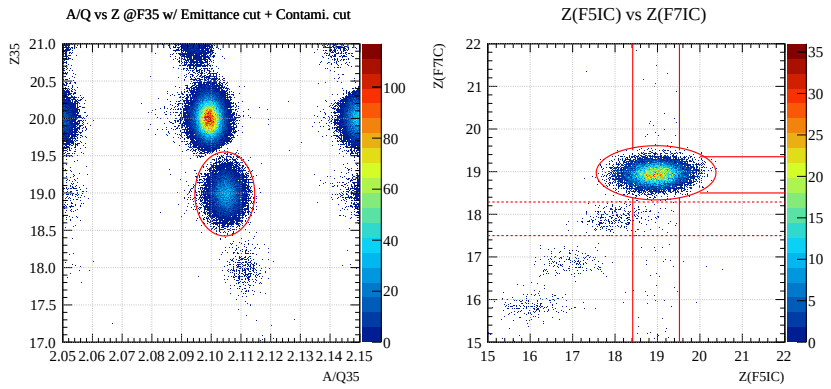

(a) A/Q_{F3F5} vs. Z_{F3IC}. (b) Z_{F5IC} vs. Z_{F7IC}.

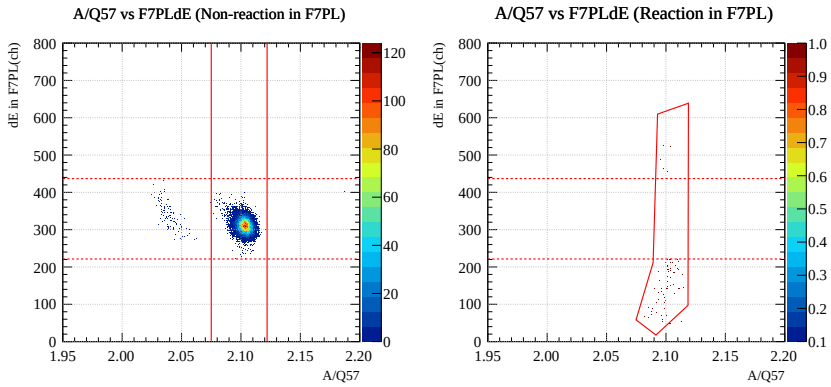

(c) A/Q_{F5F7} vs. ΔE_{F7PL}. (d) A/Q_{F5F7} vs. ΔE_{F7PL}.

Figure C.1: PID information of ^{40}K with the Reaction target.

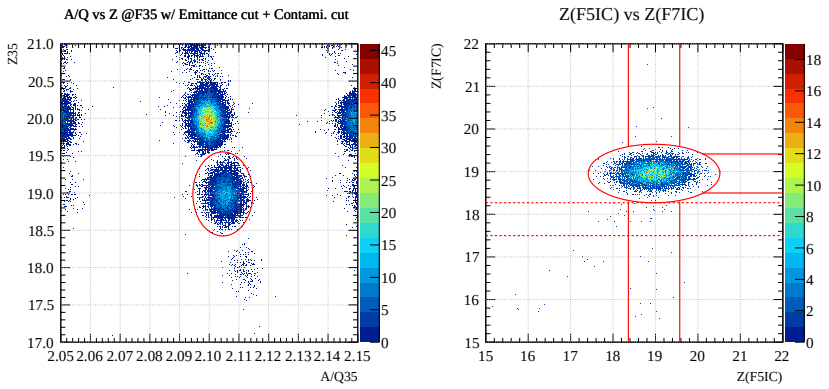

(a) A/Q_{F3F5} vs. Z_{F3IC}. (b) Z_{F5IC} vs. Z_{F7IC}.

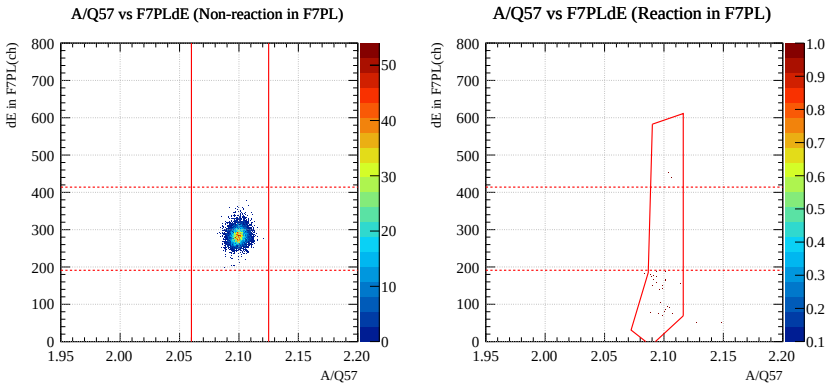

(c) A/Q_{F5F7} vs. ΔE_{F7PL}. (d) A/Q_{F5F7} vs. ΔE_{F7PL}.

Figure C.2: PID information of ^{40}K without the Reaction target.

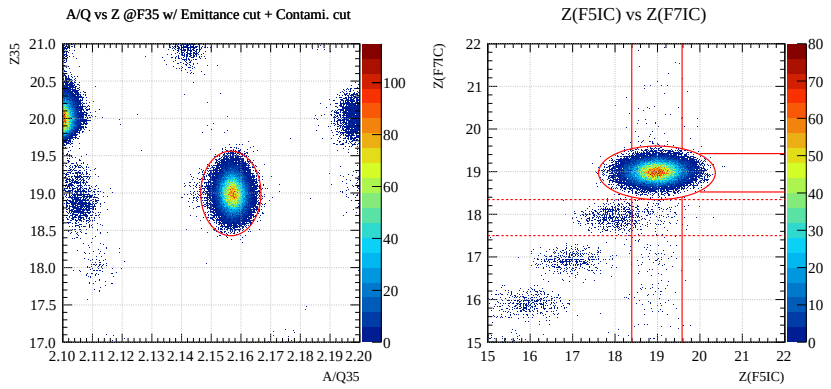

(a) A/Q_{F3F5} vs. Z_{F3IC}. (b) Z_{F5IC} vs. Z_{F7IC}.

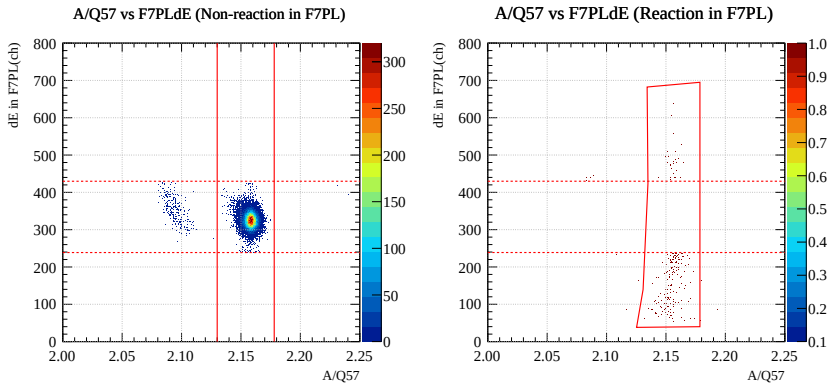

(c) A/Q_{F5F7} vs. ΔE_{F7PL}. (d) A/Q_{F5F7} vs. ΔE_{F7PL}.

Figure C.3: PID information of ^{41}K with the Reaction target.

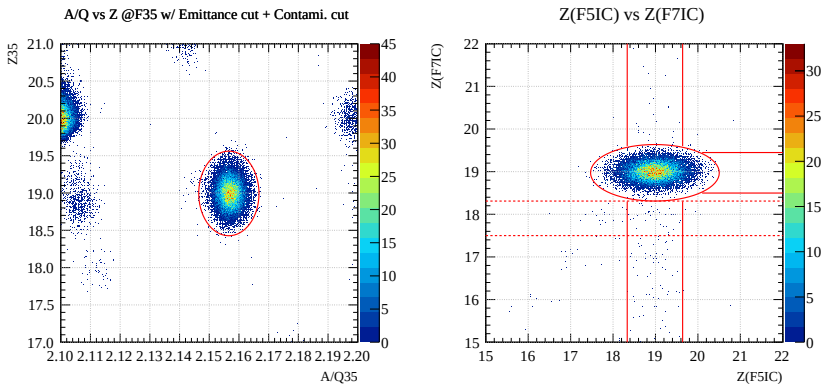

(a) A/Q_{F3F5} vs. Z_{F3IC}. (b) Z_{F5IC} vs. Z_{F7IC}.

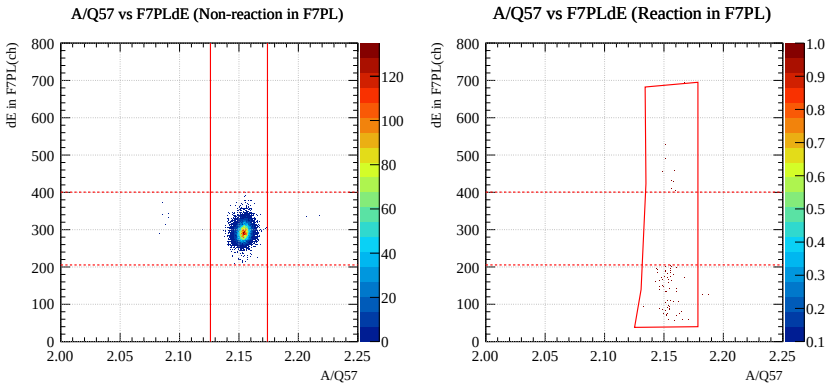

(c) A/Q_{F5F7} vs. ΔE_{F7PL}. (d) A/Q_{F5F7} vs. ΔE_{F7PL}.

Figure C.4: PID information of ^{41}K without the Reaction target.

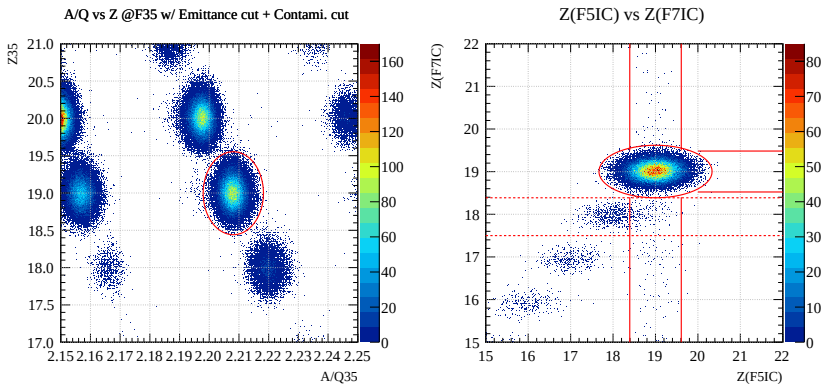

(a) A/Q_{F3F5} vs. Z_{F3IC}. (b) Z_{F5IC} vs. Z_{F7IC}.

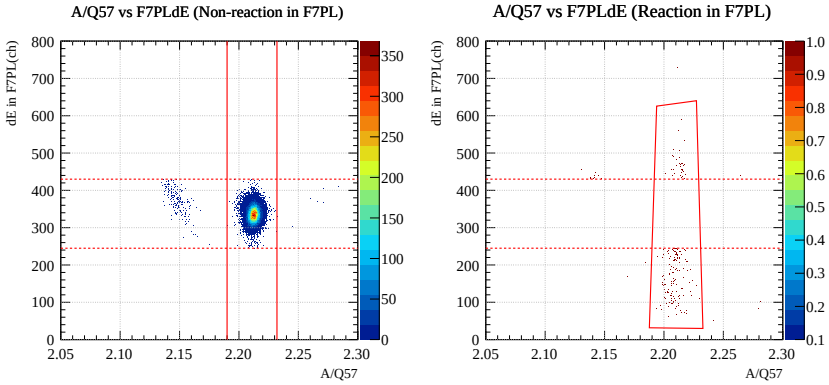

(c) A/Q_{F5F7} vs. ΔE_{F7PL}. (d) A/Q_{F5F7} vs. ΔE_{F7PL}.

Figure C.5: PID information of ^{42}K with the Reaction target.

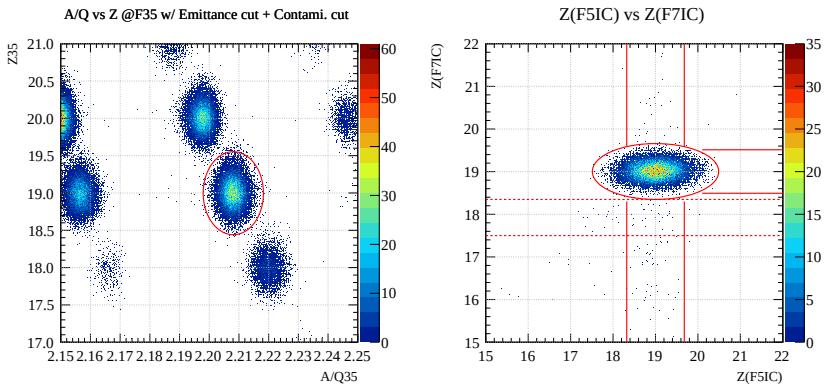

(a) A/Q_{F3F5} vs. Z_{F3IC}. (b) Z_{F5IC} vs. Z_{F7IC}.

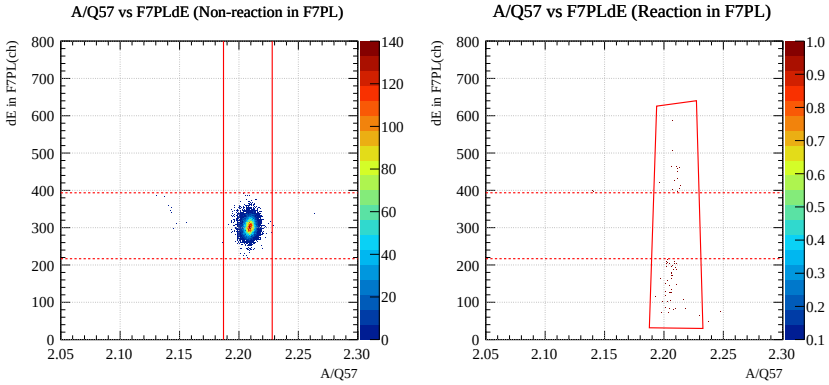

(c) A/Q_{F5F7} vs. ΔE_{F7PL}. (d) A/Q_{F5F7} vs. ΔE_{F7PL}.

Figure C.6: PID information of ^{42}K without the Reaction target.

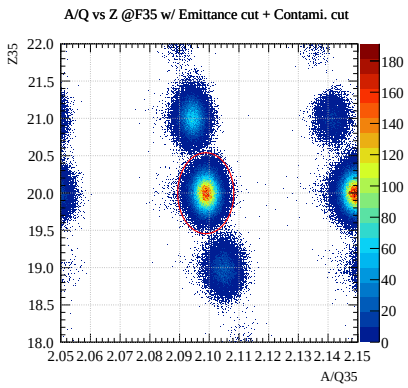

(a) A/Q_{F3F5} vs. Z_{F3IC}.

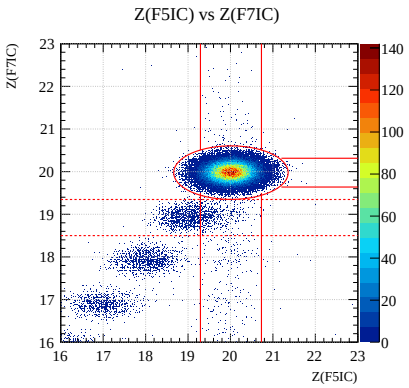

(b) Z_{F5IC} vs. Z_{F7IC}.

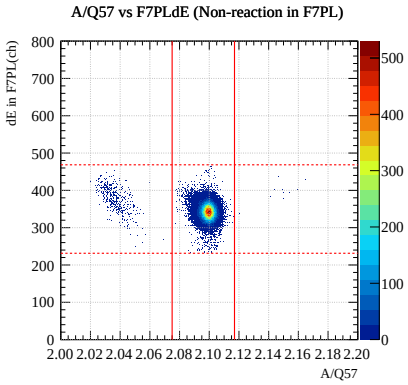

(c) A/Q_{F5F7} vs. ΔE_{F7PL}.

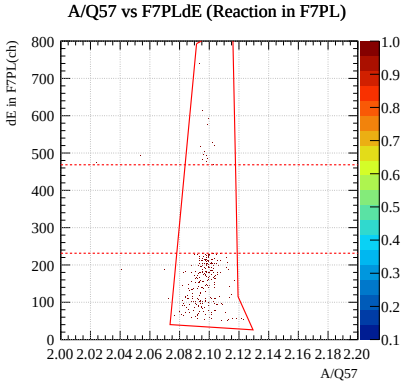

(d) A/Q_{F5F7} vs. ΔE_{F7PL}.

Figure C.7: PID information of ^{42}Ca with the Reaction target.

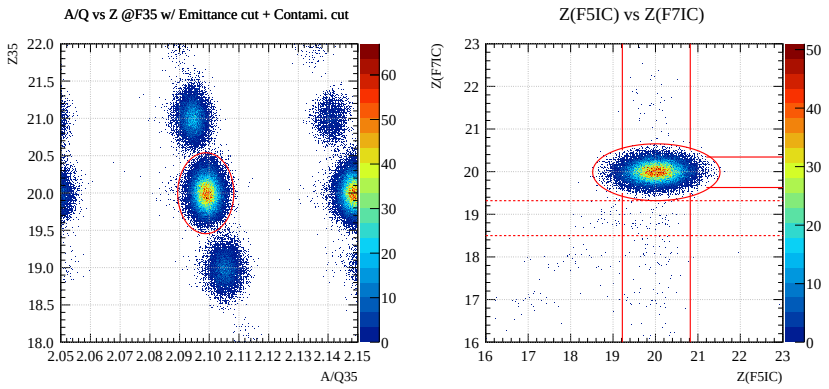

(a) A/Q_{F3F5} vs. Z_{F3IC}. (b) Z_{F5IC} vs. Z_{F7IC}.

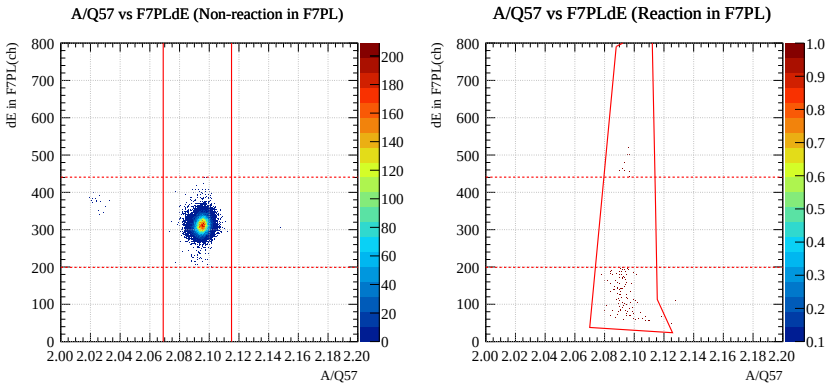

(c) A/Q_{F5F7} vs. ΔE_{F7PL}. (d) A/Q_{F5F7} vs. ΔE_{F7PL}.

Figure C.8: PID information of ^{42}Ca without the Reaction target.

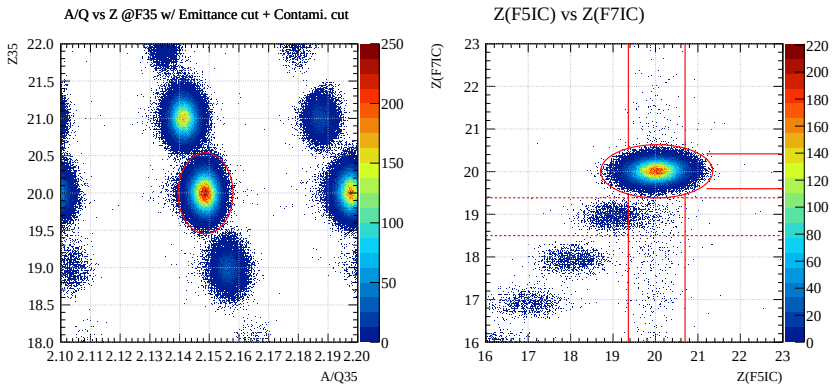

(a) A/Q_{F3F5} vs. Z_{F3IC}. (b) Z_{F5IC} vs. Z_{F7IC}.

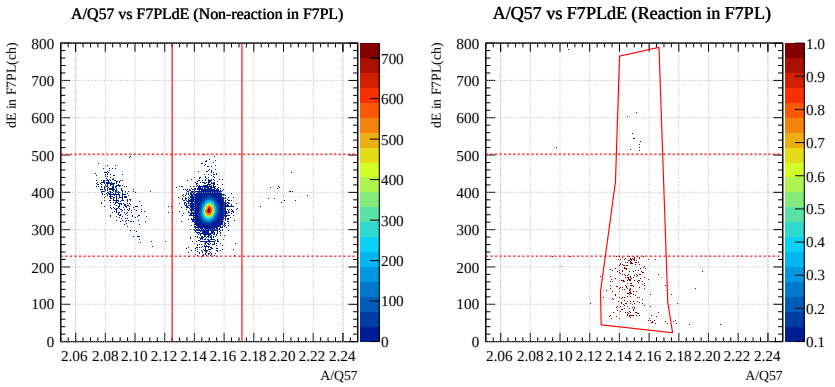

(c) A/Q_{F5F7} vs. ΔE_{F7PL}. (d) A/Q_{F5F7} vs. ΔE_{F7PL}.

Figure C.9: PID information of ^{43}Ca with the Reaction target.

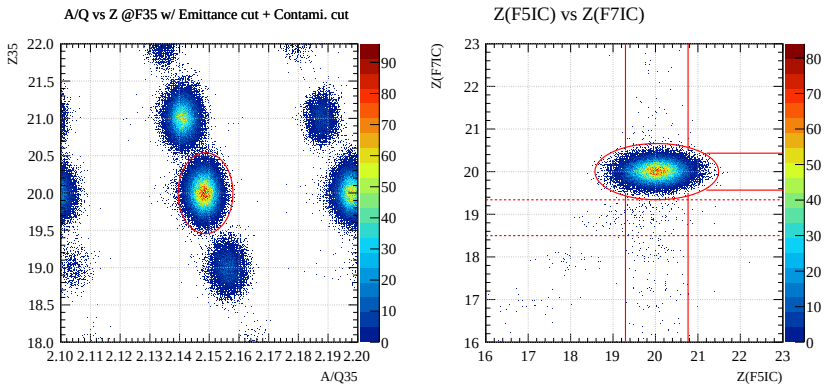

(a) A/Q_{F3F5} vs. Z_{F3IC}. (b) Z_{F5IC} vs. Z_{F7IC}.

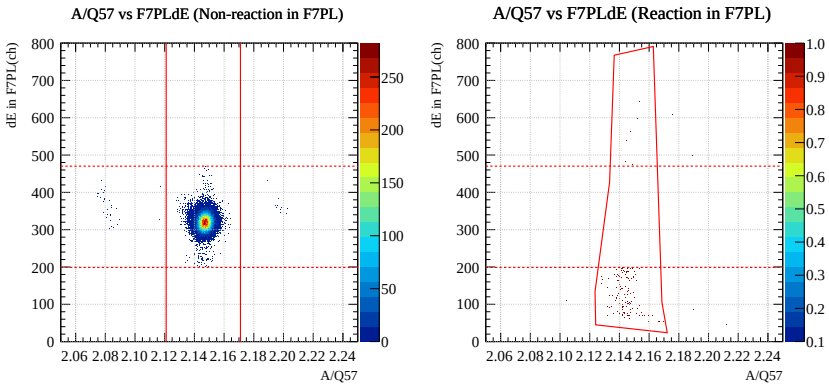

(c) A/Q_{F5F7} vs. ΔE_{F7PL}. (d) A/Q_{F5F7} vs. ΔE_{F7PL}.

Figure C.10: PID information of ^{43}Ca without the Reaction target.

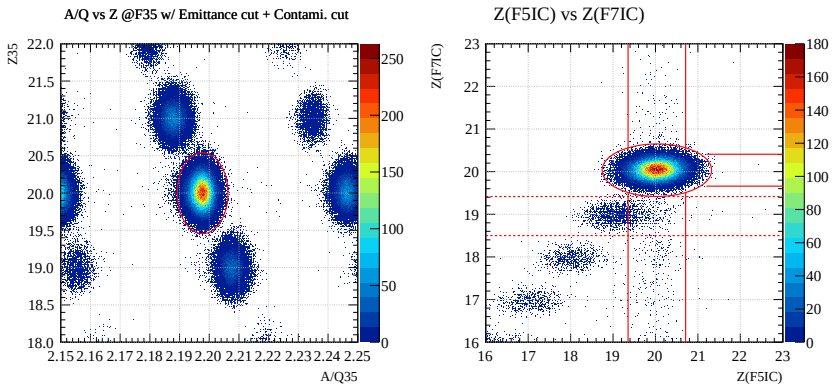

(a) A/Q_{F3F5} vs. Z_{F3IC}. (b) Z_{F5IC} vs. Z_{F7IC}.

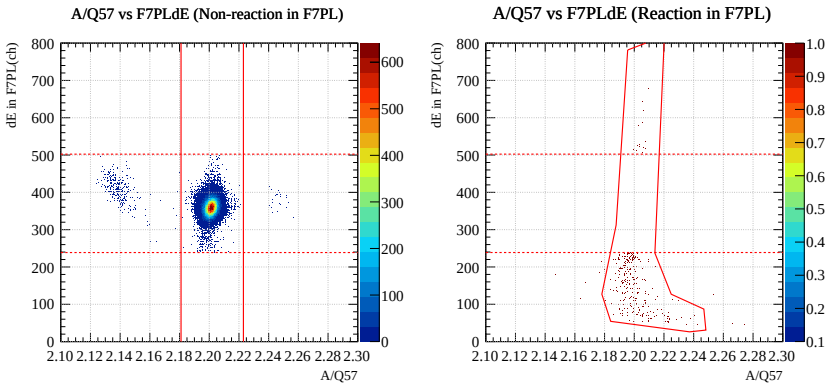

(c) A/Q_{F5F7} vs. ΔE_{F7PL}. (d) A/Q_{F5F7} vs. ΔE_{F7PL}.

Figure C.11: PID information of ^{44}Ca with the Reaction target.

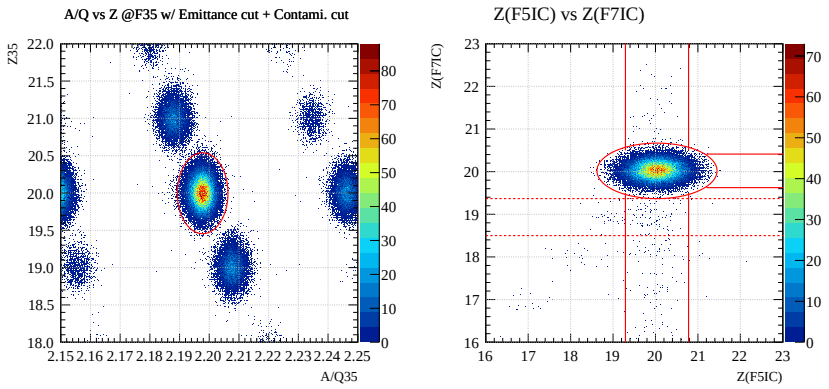

(a) A/Q_{F3F5} vs. Z_{F3IC}. (b) Z_{F5IC} vs. Z_{F7IC}.

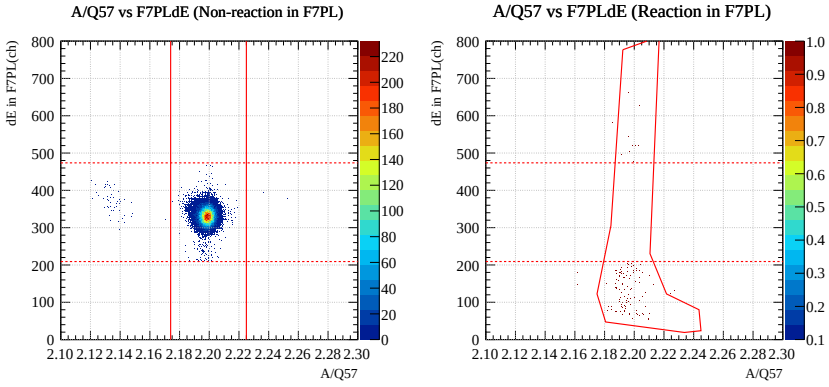

(c) A/Q_{F5F7} vs. ΔE_{F7PL}. (d) A/Q_{F5F7} vs. ΔE_{F7PL}.

Figure C.12: PID information of ^{44}Ca without the Reaction target.

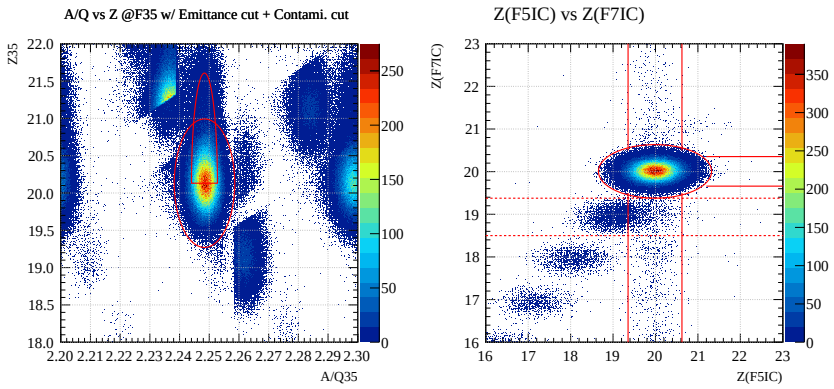

(a) A/Q_{F3F5} vs. Z_{F3IC}. (b) Z_{F5IC} vs. Z_{F7IC}.

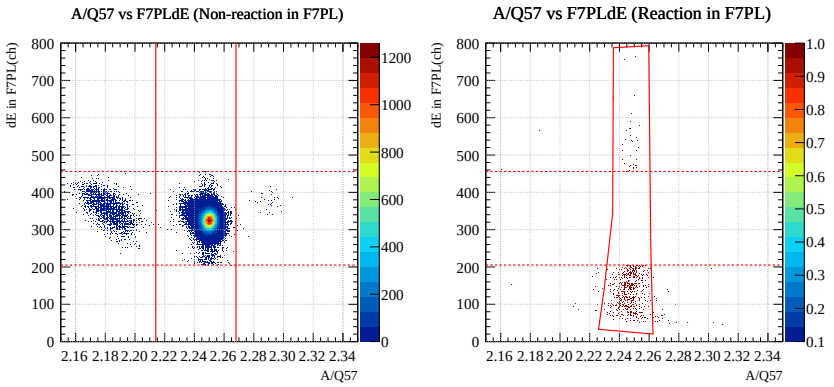

(c) A/Q_{F5F7} vs. ΔE_{F7PL}. (d) A/Q_{F5F7} vs. ΔE_{F7PL}.

Figure C.13: PID information of ^{45}Ca with the Reaction target.

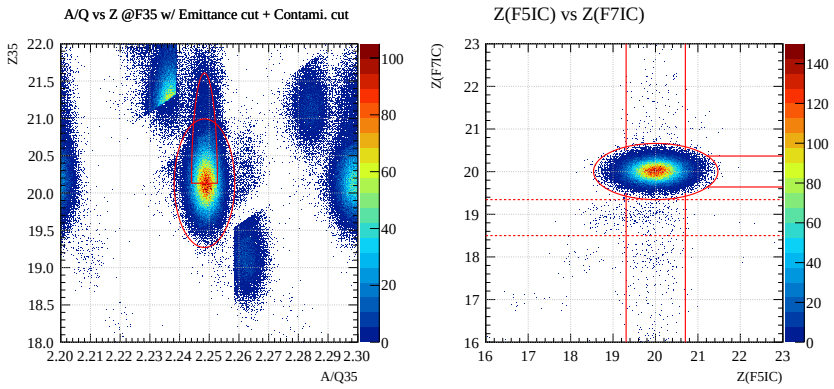

(a) A/Q_{F3F5} vs. Z_{F3IC}. (b) Z_{F5IC} vs. Z_{F7IC}.

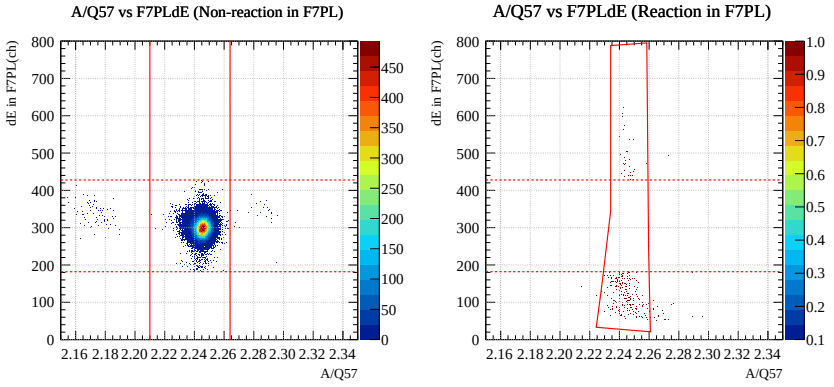

(c) A/Q_{F5F7} vs. ΔE_{F7PL}. (d) A/Q_{F5F7} vs. ΔE_{F7PL}.

Figure C.14: PID information of ^{45}Ca without the Reaction target.

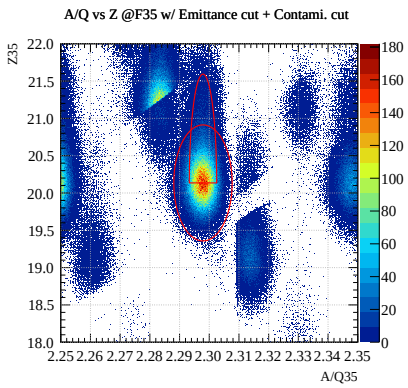

(a) A/Q_{F3F5} vs. Z_{F3IC}.

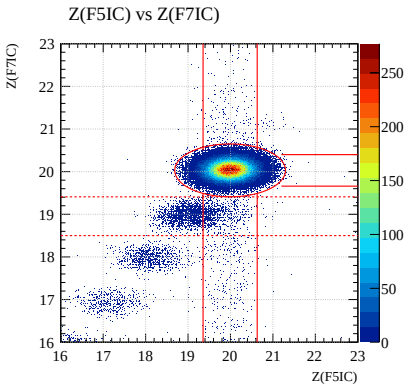

(b) Z_{F5IC} vs. Z_{F7IC}.

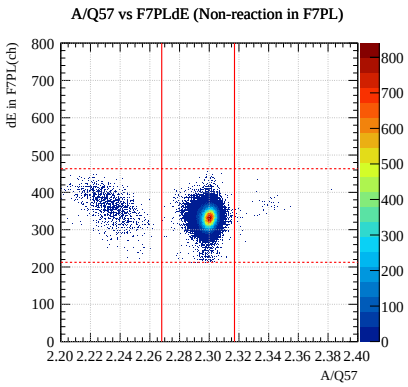

(c) A/Q_{F5F7} vs. ΔE_{F7PL}.

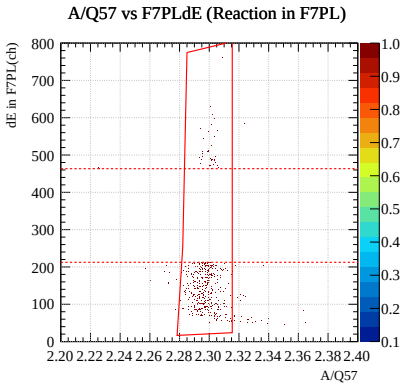

(d) A/Q_{F5F7} vs. ΔE_{F7PL}.

Figure C.15: PID information of ^{46}Ca with the Reaction target.

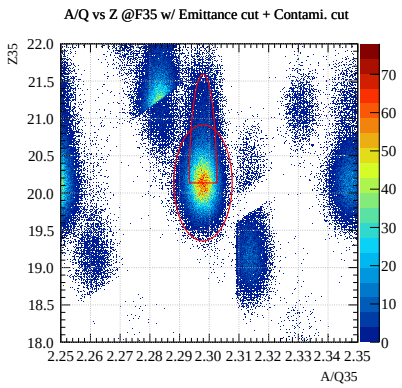

(a) A/Q_{F3F5} vs. Z_{F3IC}.

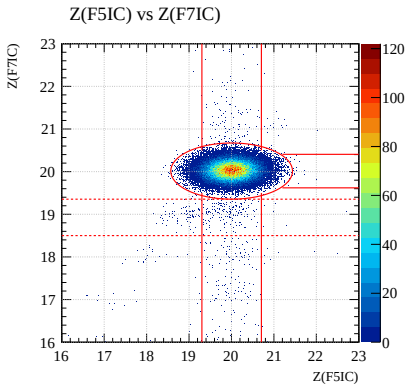

(b) Z_{F5IC} vs. Z_{F7IC}.

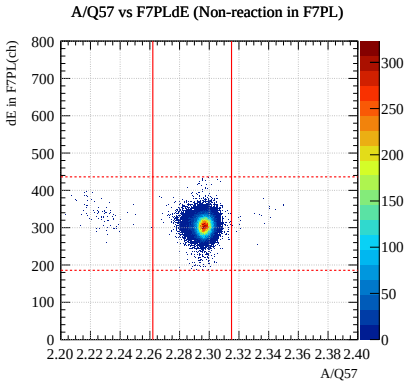

(c) A/Q_{F5F7} vs. ΔE_{F7PL}.

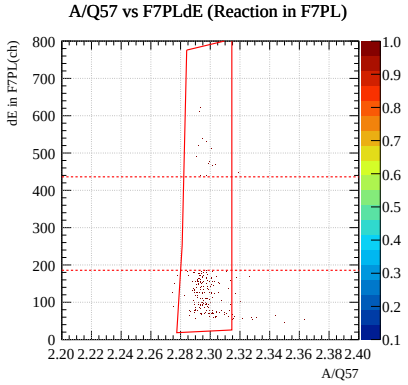

(d) A/Q_{F5F7} vs. ΔE_{F7PL}.

Figure C.16: PID information of ^{46}Ca without the Reaction target.

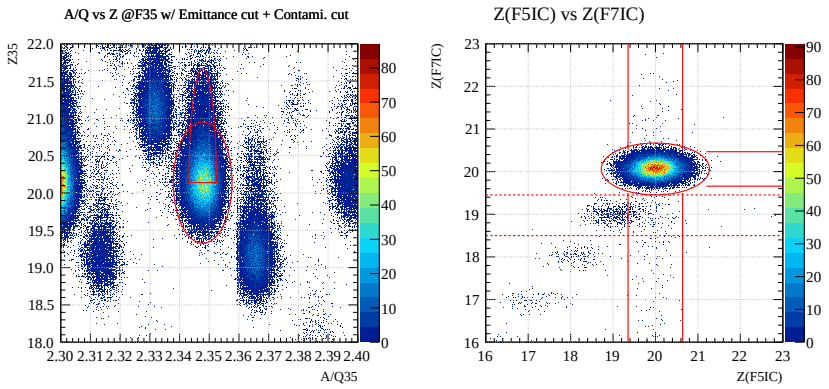

(a) A/Q_{F3F5} vs. Z_{F3IC}. (b) Z_{F5IC} vs. Z_{F7IC}.

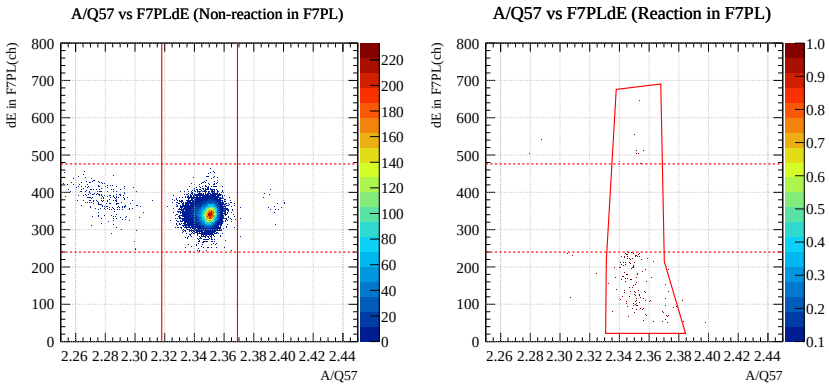

(c) A/Q_{F5F7} vs. ΔE_{F7PL}. (d) A/Q_{F5F7} vs. ΔE_{F7PL}.

Figure C.17: PID information of ^{47}Ca with the Reaction target.

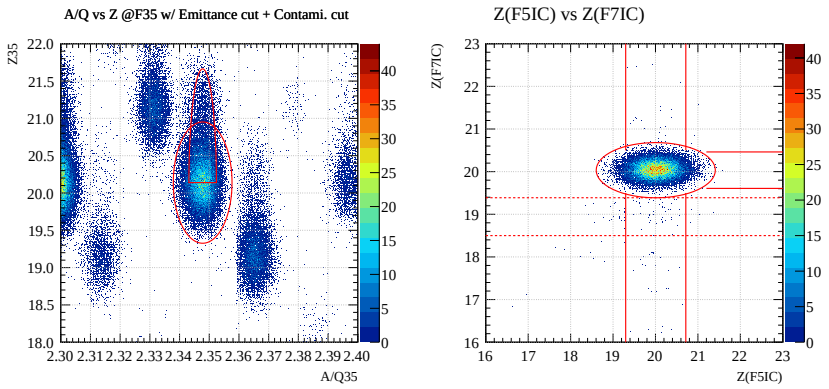

(a) A/Q_{F3F5} vs. Z_{F3IC}. (b) Z_{F5IC} vs. Z_{F7IC}.

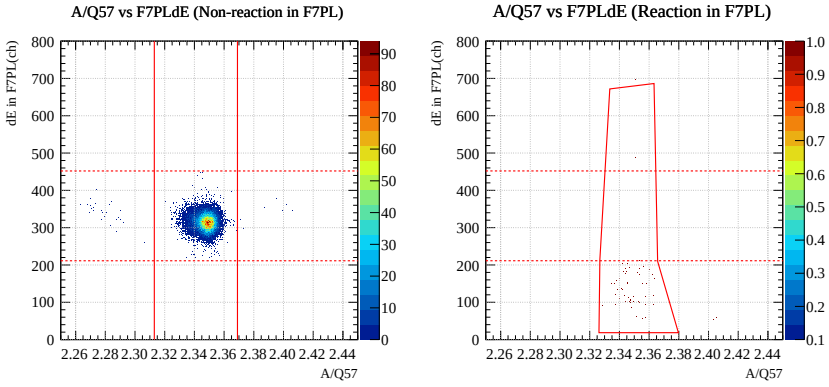

(c) A/Q_{F5F7} vs. ΔE_{F7PL}. (d) A/Q_{F5F7} vs. ΔE_{F7PL}.

Figure C.18: PID information of ^{47}Ca without the Reaction target.

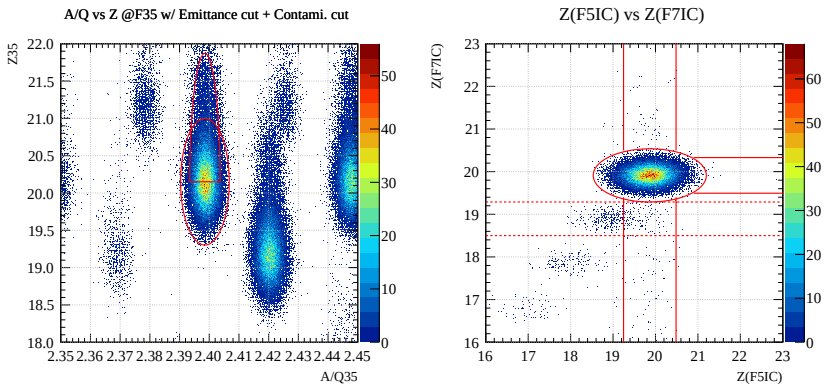

(a) A/Q_{F3F5} vs. Z_{F3IC}.

(b) Z_{F5IC} vs. Z_{F7IC}.

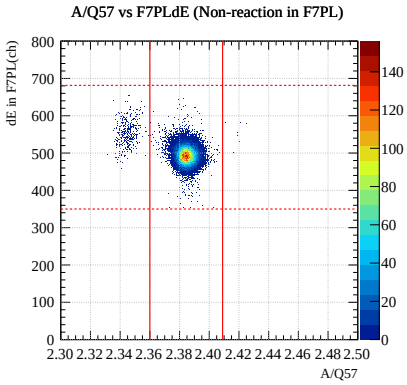

(c) A/Q_{F5F7} vs. ΔE_{F7PL}.

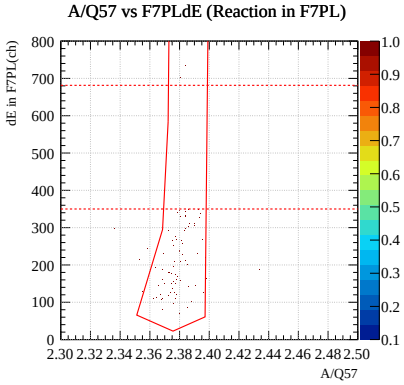

(d) A/Q_{F5F7} vs. ΔE_{F7PL}.

Figure C.19: PID information of ^{48}Ca with the Reaction target.

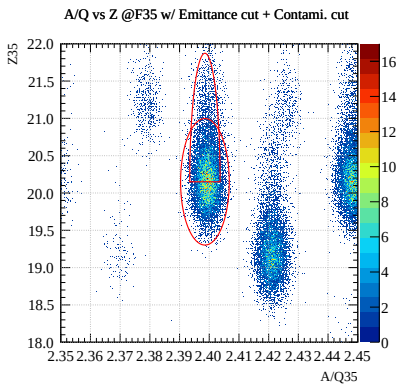

(a) A/Q_{F3F5} vs. Z_{F3IC}.

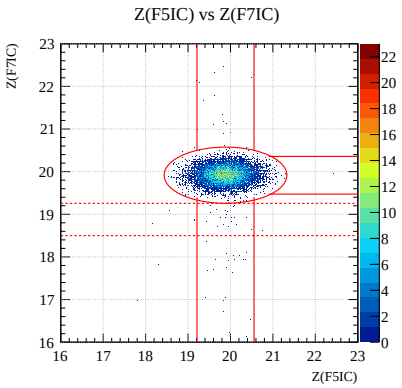

(b) Z_{F5IC} vs. Z_{F7IC}.

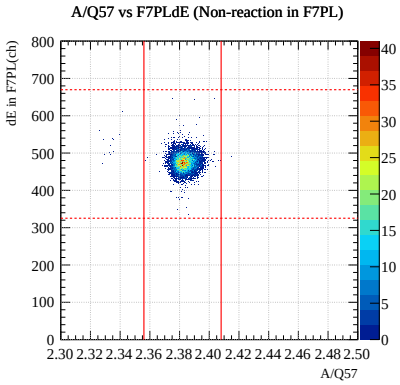

(c) A/Q_{F5F7} vs. ΔE_{F7PL}.

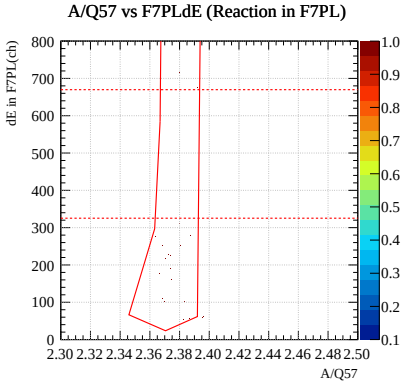

(d) A/Q_{F5F7} vs. ΔE_{F7PL}.

Figure C.20: PID information of ^{48}Ca without the Reaction target.

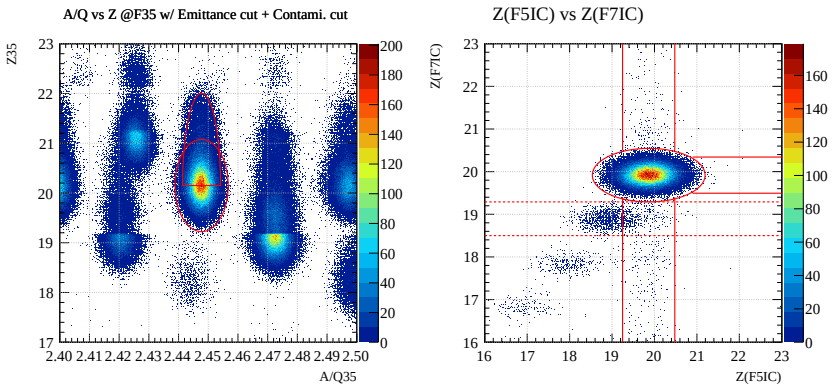

(a) A/Q_{F3F5} vs. Z_{F3IC}. (b) Z_{F5IC} vs. Z_{F7IC}.

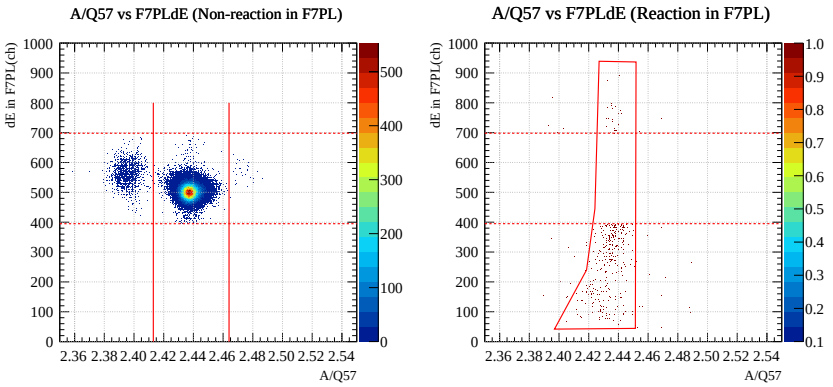

(c) A/Q_{F5F7} vs. ΔE_{F7PL}. (d) A/Q_{F5F7} vs. ΔE_{F7PL}.

Figure C.21: PID information of ^{49}Ca with the Reaction target.

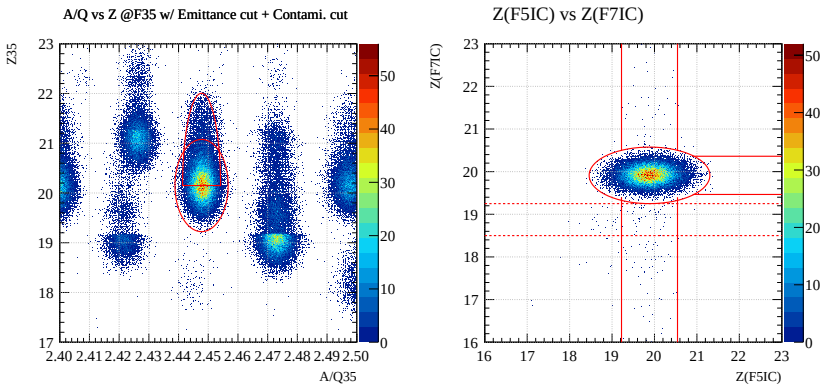

(a) A/Q_{F3F5} vs. Z_{F3IC}. (b) Z_{F5IC} vs. Z_{F7IC}.

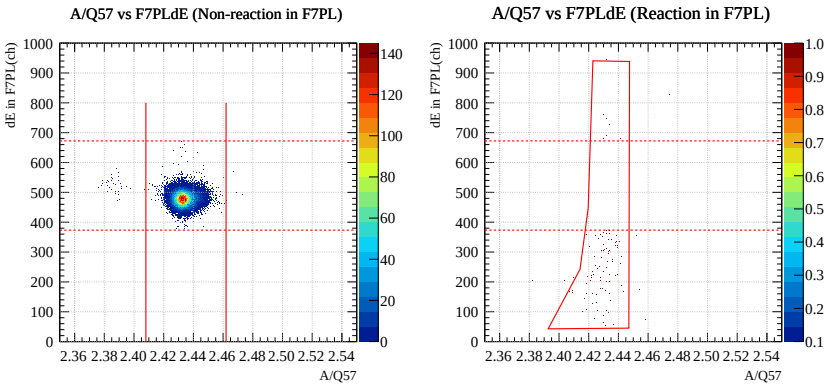

(c) A/Q_{F5F7} vs. ΔE_{F7PL}. (d) A/Q_{F5F7} vs. ΔE_{F7PL}.

Figure C.22: PID information of ^{49}Ca without the Reaction target.

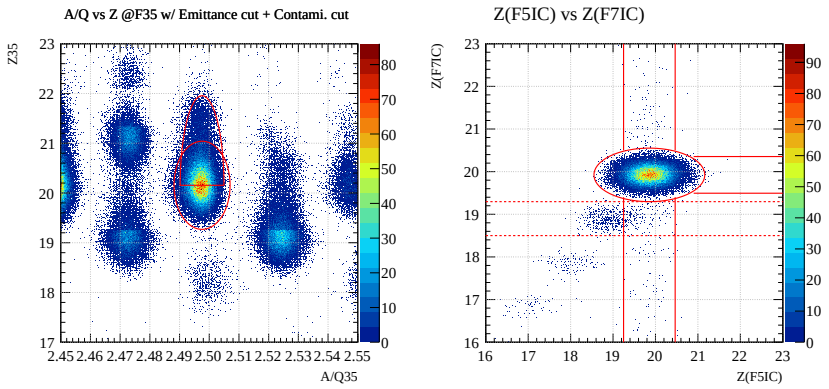

(a) A/Q_{F3F5} vs. Z_{F3IC}. (b) Z_{F5IC} vs. Z_{F7IC}.

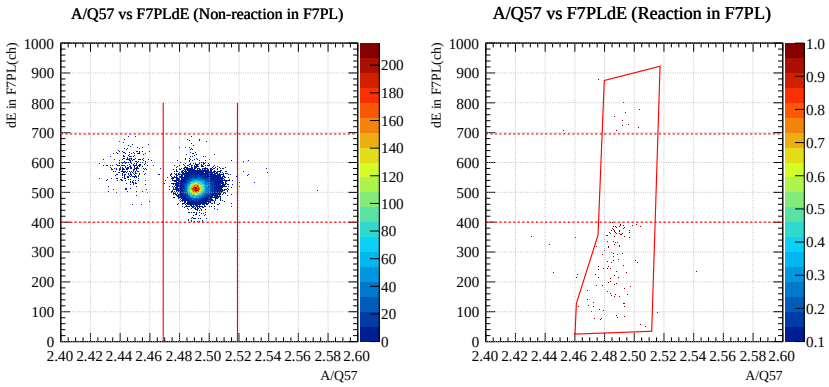

(c) A/Q_{F5F7} vs. ΔE_{F7PL}. (d) A/Q_{F5F7} vs. ΔE_{F7PL}.

Figure C.23: PID information of ^{50}Ca with the Reaction target.

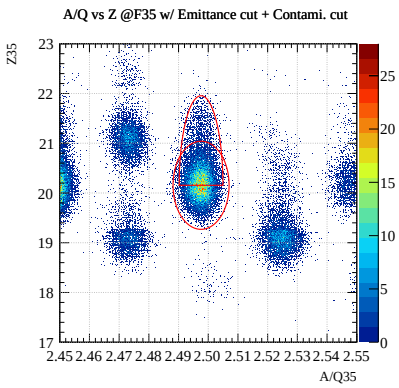

(a) A/Q_{F3F5} vs. Z_{F3IC}.

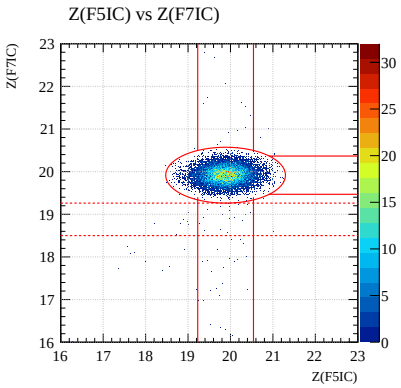

(b) Z_{F5IC} vs. Z_{F7IC}.

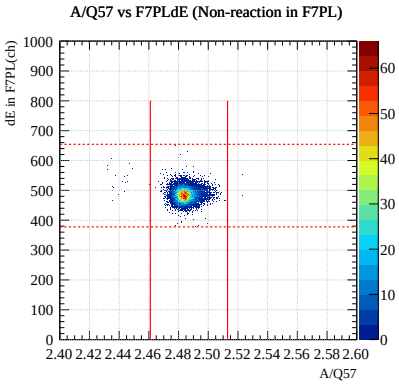

(c) A/Q_{F5F7} vs. ΔE_{F7PL}.

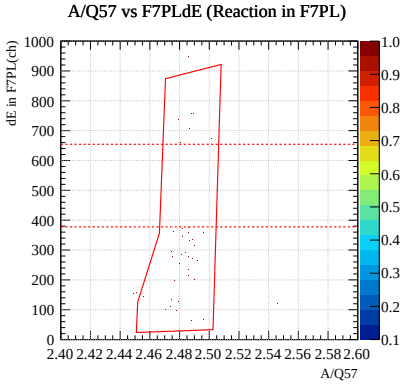

(d) A/Q_{F5F7} vs. ΔE_{F7PL}.

Figure C.24: PID information of ^{50}Ca without the Reaction target.

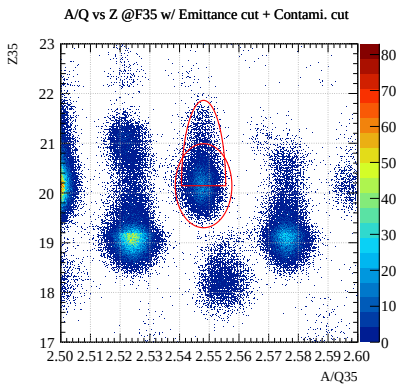

(a) A/Q_{F3F5} vs. Z_{F3IC}.

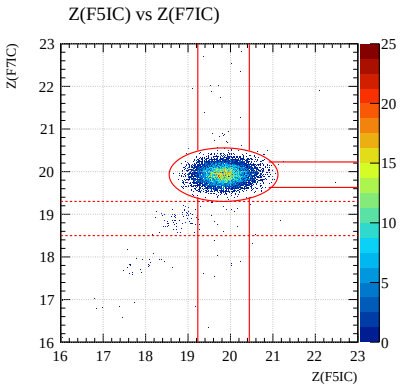

(b) Z_{F5IC} vs. Z_{F7IC}.

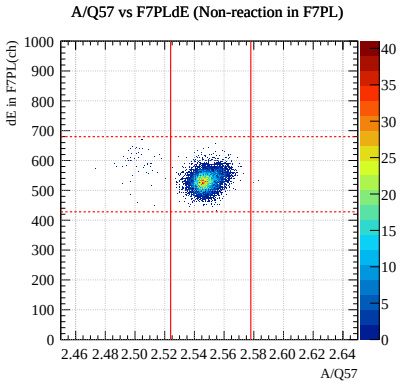

(c) A/Q_{F5F7} vs. ΔE_{F7PL}.

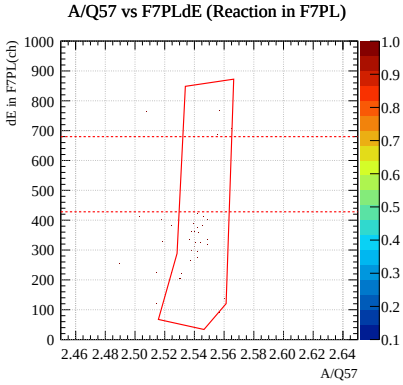

(d) A/Q_{F5F7} vs. ΔE_{F7PL}.

Figure C.25: PID information of ^{51}Ca with the Reaction target.

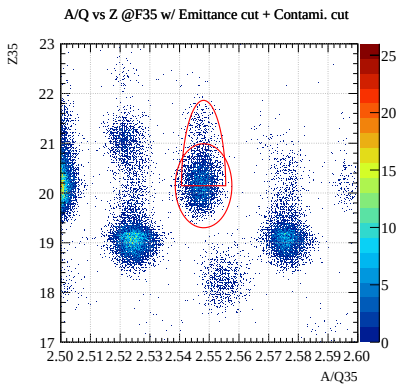

(a) A/Q_{F3F5} vs. Z_{F3IC}.

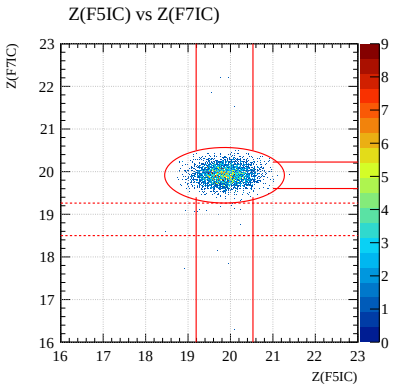

(b) Z_{F5IC} vs. Z_{F7IC}.

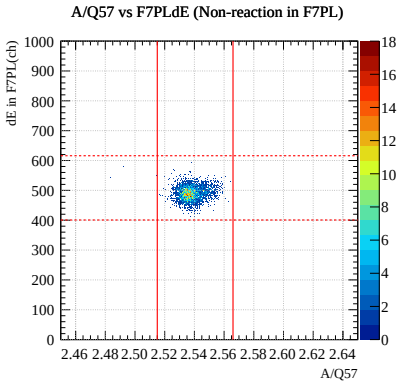

(c) A/Q_{F5F7} vs. ΔE_{F7PL}.

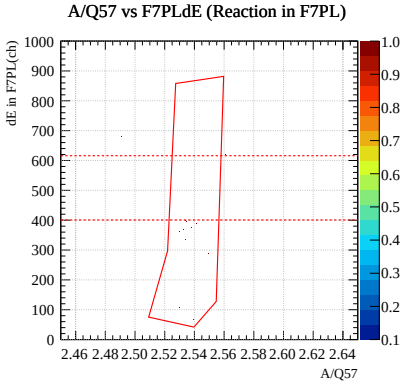

(d) A/Q_{F5F7} vs. ΔE_{F7PL}.

Figure C.26: PID information of ^{51}Ca without the Reaction target.

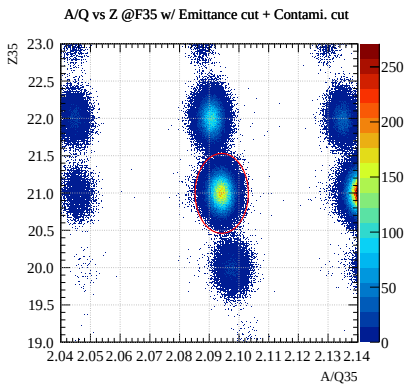

(a) A/Q_{F3F5} vs. Z_{F3IC}.

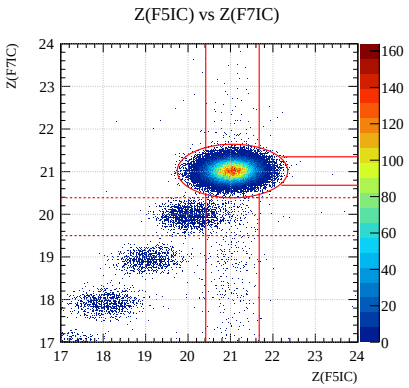

(b) Z_{F5IC} vs. Z_{F7IC}.

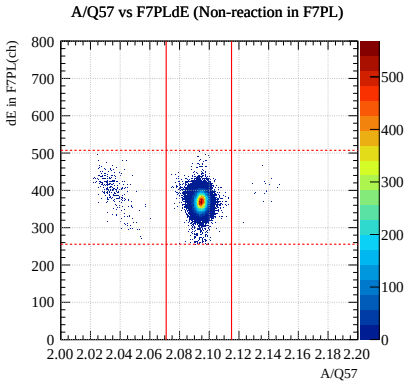

(c) A/Q_{F5F7} vs. ΔE_{F7PL}.

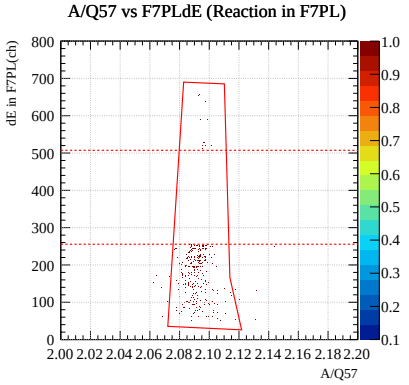

(d) A/Q_{F5F7} vs. ΔE_{F7PL}.

Figure C.27: PID information of ^{44}Sc with the Reaction target.

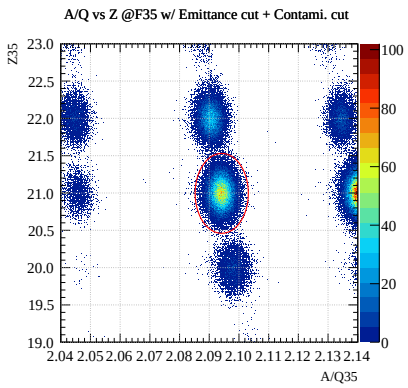

(a) A/Q_{F3F5} vs. Z_{F3IC}.

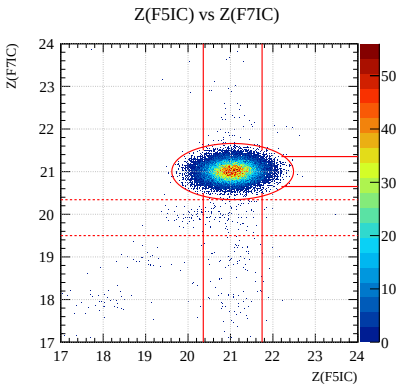

(b) Z_{F5IC} vs. Z_{F7IC}.

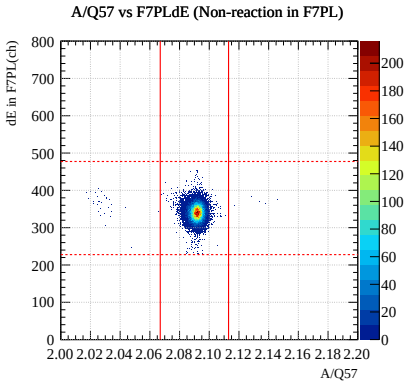

(c) A/Q_{F5F7} vs. ΔE_{F7PL}.

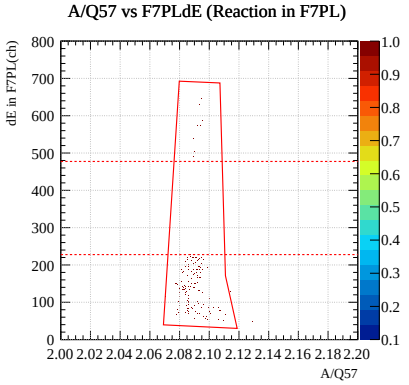

(d) A/Q_{F5F7} vs. ΔE_{F7PL}.

Figure C.28: PID information of ^{44}Sc without the Reaction target.

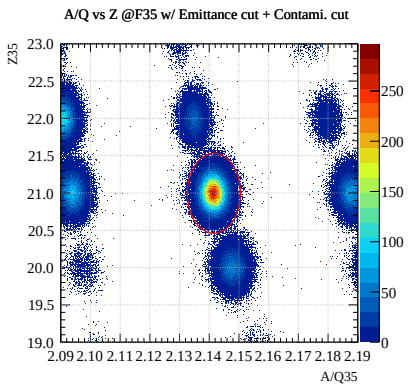

(a) A/Q_{F3F5} vs. Z_{F3IC}.

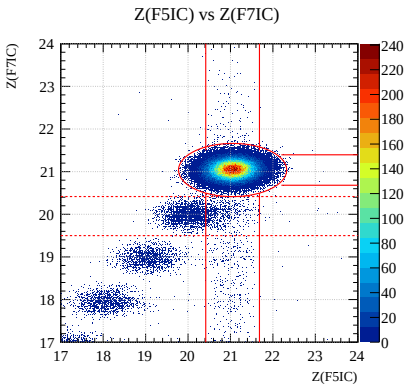

(b) Z_{F5IC} vs. Z_{F7IC}.

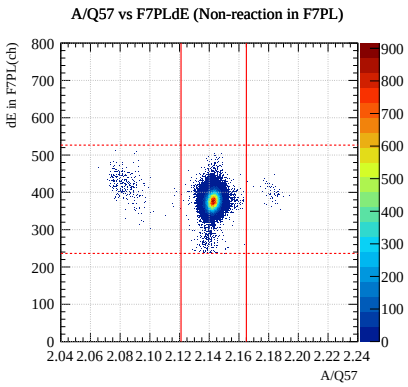

(c) A/Q_{F5F7} vs. ΔE_{F7PL}.

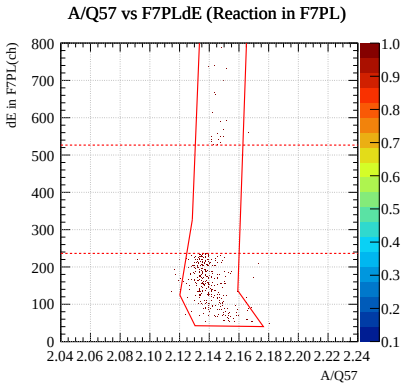

(d) A/Q_{F5F7} vs. ΔE_{F7PL}.

Figure C.29: PID information of ^{45}Sc with the Reaction target.

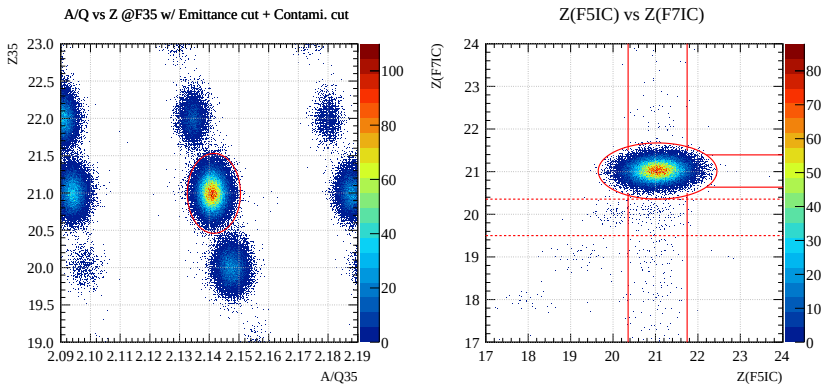

(a) A/Q_{F3F5} vs. Z_{F3IC}. (b) Z_{F5IC} vs. Z_{F7IC}.

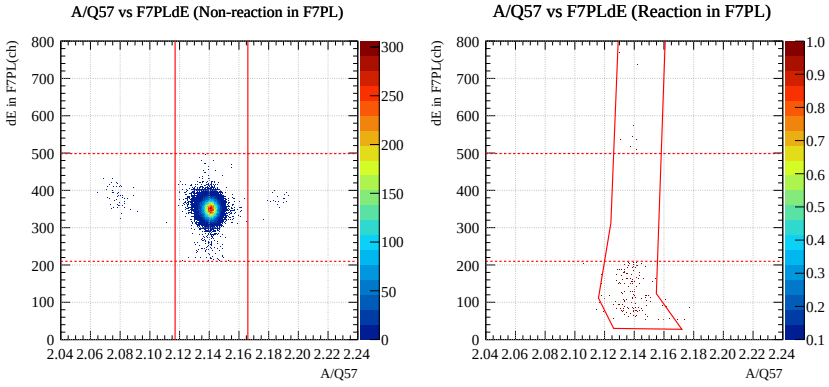

(c) A/Q_{F5F7} vs. ΔE_{F7PL}. (d) A/Q_{F5F7} vs. ΔE_{F7PL}.

Figure C.30: PID information of ^{45}Sc without the Reaction target.

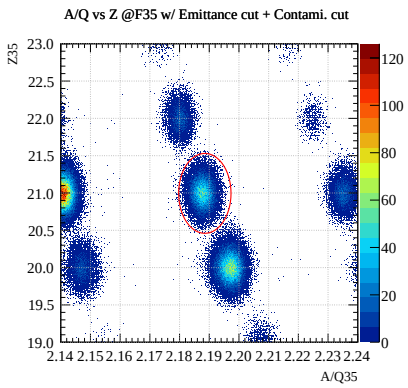

(a) A/Q_{F3F5} vs. Z_{F3IC}.

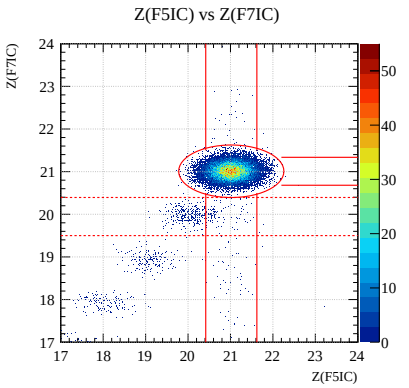

(b) Z_{F5IC} vs. Z_{F7IC}.

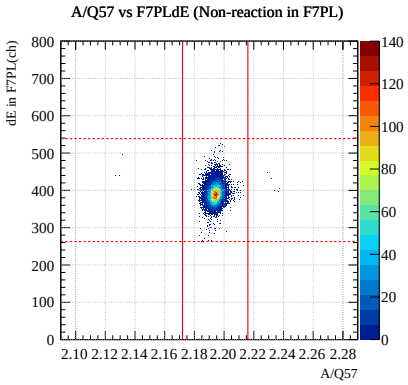

(c) A/Q_{F5F7} vs. ΔE_{F7PL}.

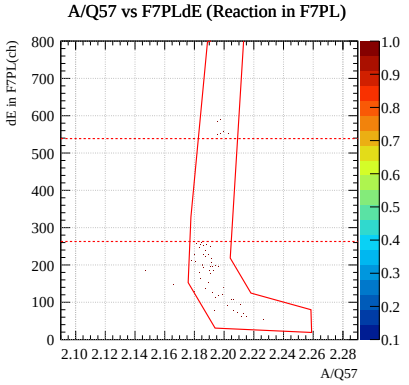

(d) A/Q_{F5F7} vs. ΔE_{F7PL}.

Figure C.31: PID information of ^{46}Sc with the Reaction target.

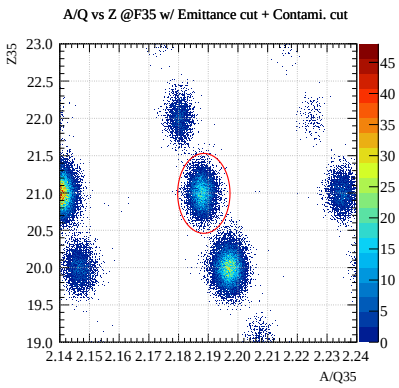

(a) A/Q_{F3F5} vs. Z_{F3IC}.

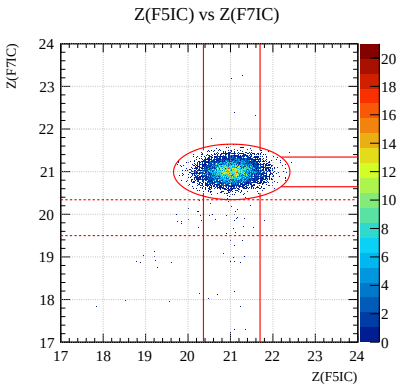

(b) Z_{F5IC} vs. Z_{F7IC}.

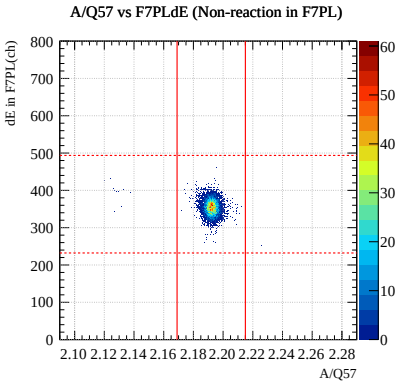

(c) A/Q_{F5F7} vs. ΔE_{F7PL}.

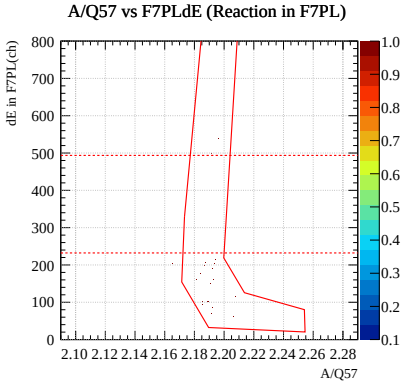

(d) A/Q_{F5F7} vs. ΔE_{F7PL}.

Figure C.32: PID information of ^{46}Sc without the Reaction target.

D Transmission Distribution

Transmission distributions along X_{F3}, Y_{F3}, A_{F3}, B_{F3}, and X_{F5} axes for each nuclide are shown in the same manner as Figs. 4-20 - 4-24.

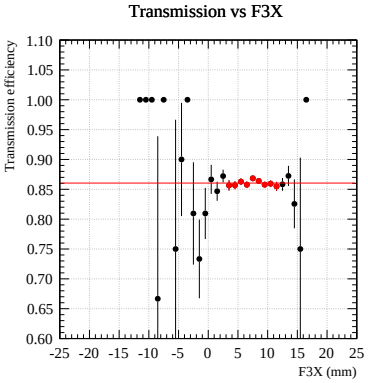

(a) F3X dependence.

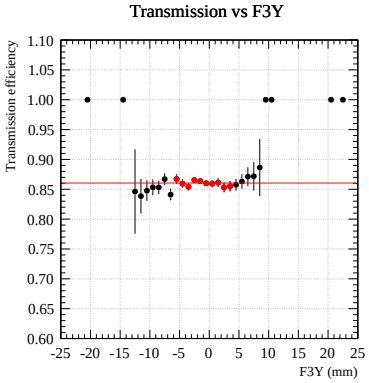

(b) F3Y dependence.

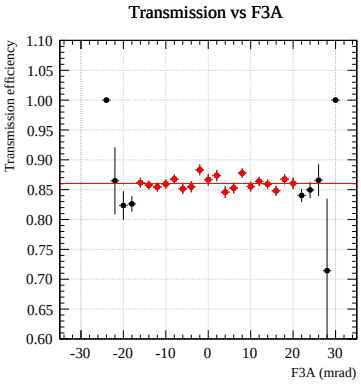

(c) F3A dependence.

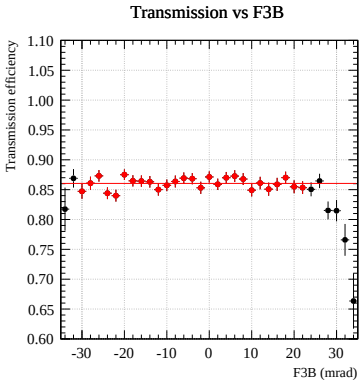

(d) F3B dependence.

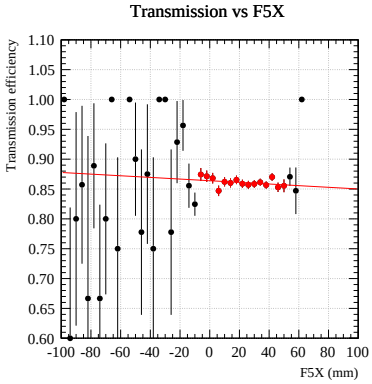

(e) F5X dependence.

Figure D.1: Transmission distributions of ^{40}K with the reaction target.

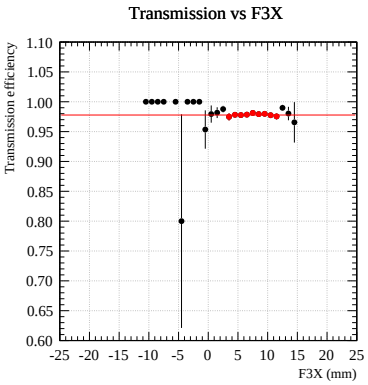

(a) F3X dependence.

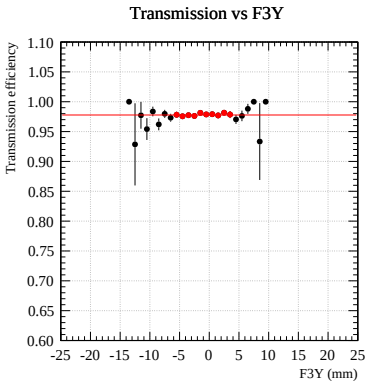

(b) F3Y dependence.

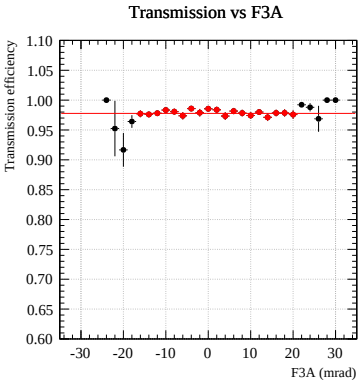

(c) F3A dependence.

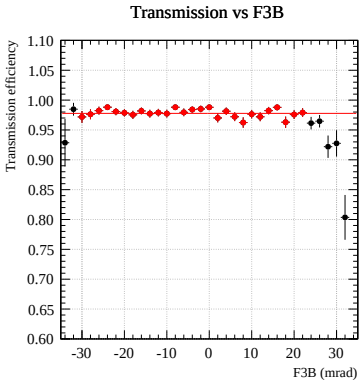

(d) F3B dependence.

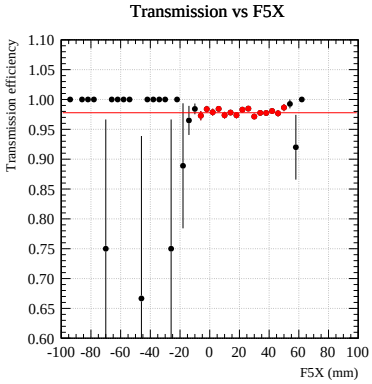

(e) F5X dependence.

Figure D.2: Transmission distributions of ^{40}K without the reaction target.

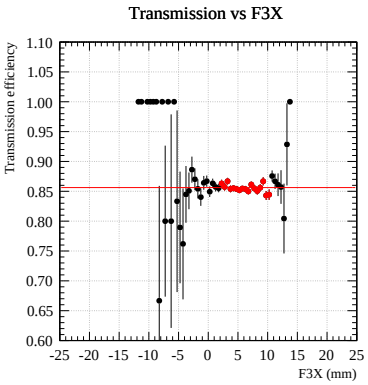

(a) F3X dependence.

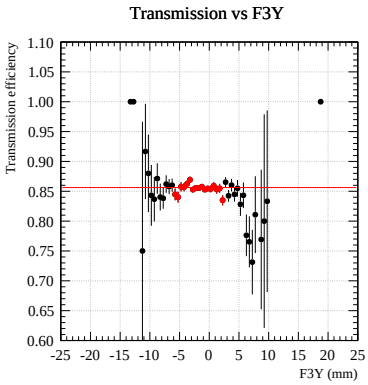

(b) F3Y dependence.

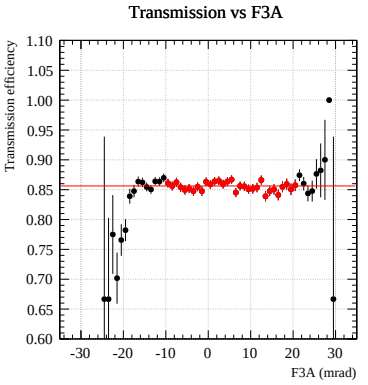

(c) F3A dependence.

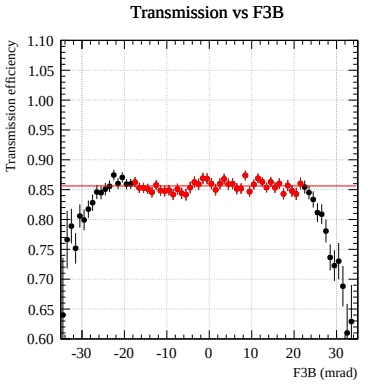

(d) F3B dependence.

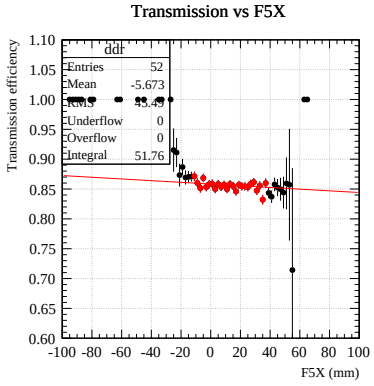

(e) F5X dependence.

Figure D.3: Transmission distributions of ^{41}K with the reaction target.

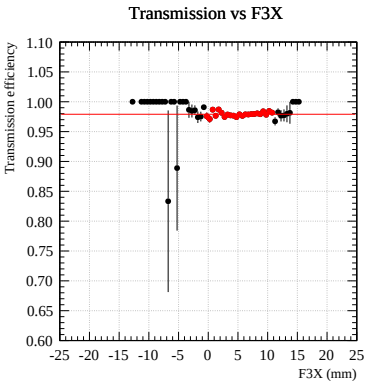

(a) F3X dependence.

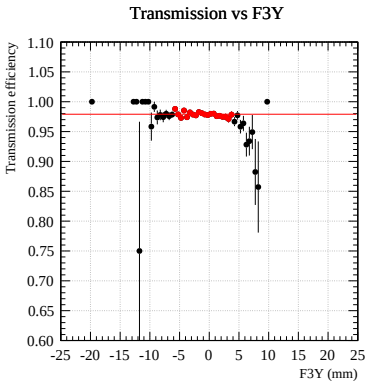

(b) F3Y dependence.

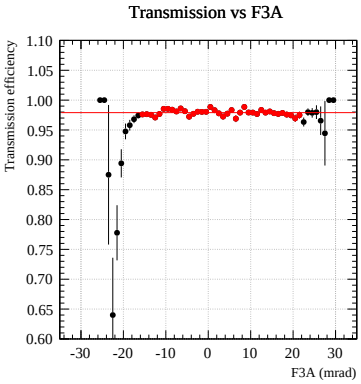

(c) F3A dependence.

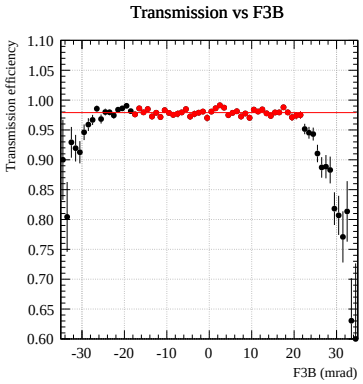

(d) F3B dependence.

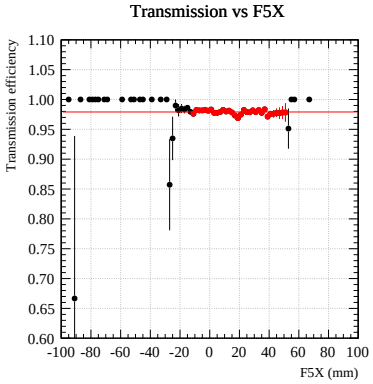

(e) F5X dependence.

Figure D.4: Transmission distributions of ^{41}K without the reaction target.

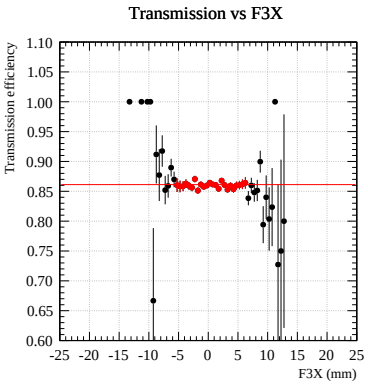

(a) F3X dependence.

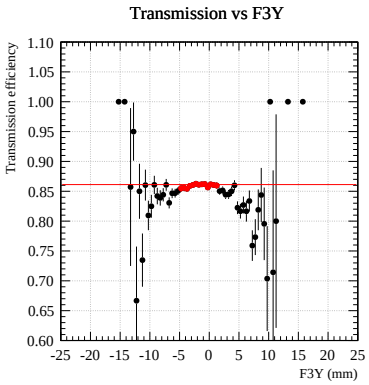

(b) F3Y dependence.

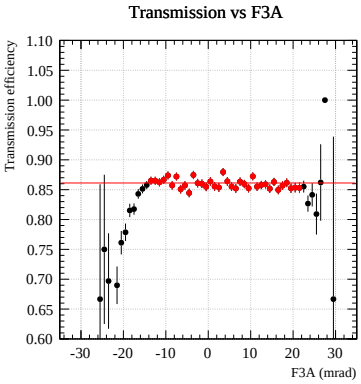

(c) F3A dependence.

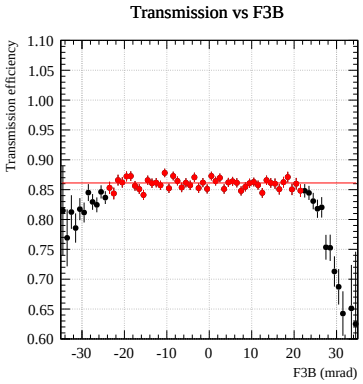

(d) F3B dependence.

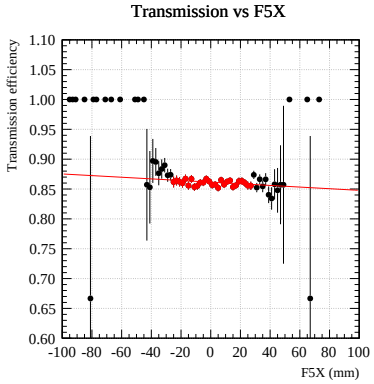

(e) F5X dependence.

Figure D.5: Transmission distributions of ^{42}K with the reaction target.

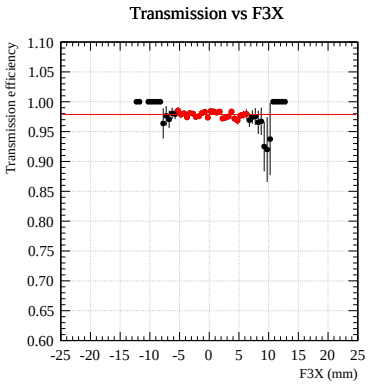

(a) F3X dependence.

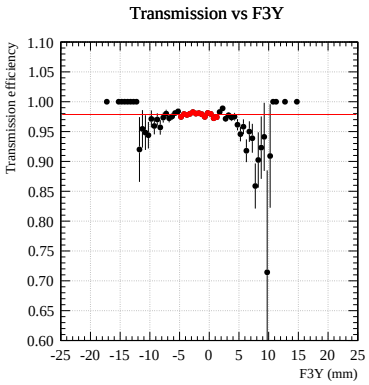

(b) F3Y dependence.

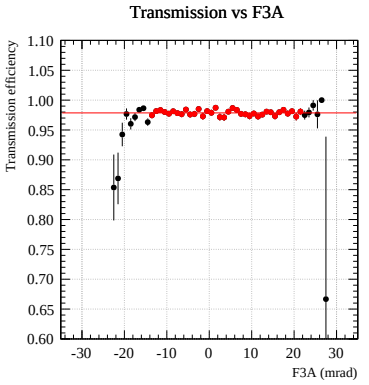

(c) F3A dependence.

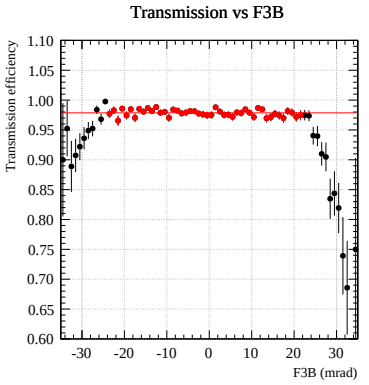

(d) F3B dependence.

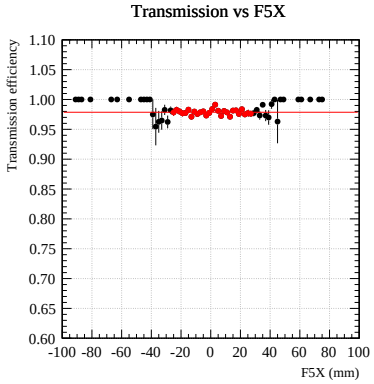

(e) F5X dependence.

Figure D.6: Transmission distributions of ^{42}K without the reaction target.

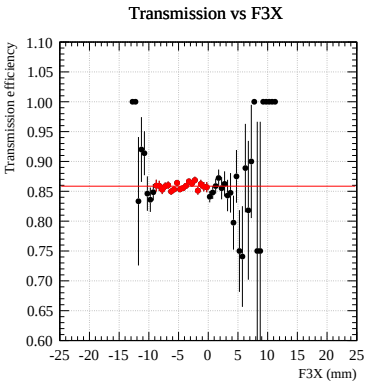

(a) F3X dependence.

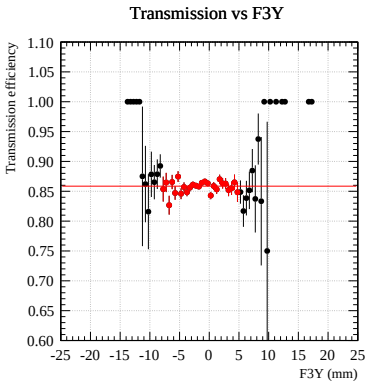

(b) F3Y dependence.

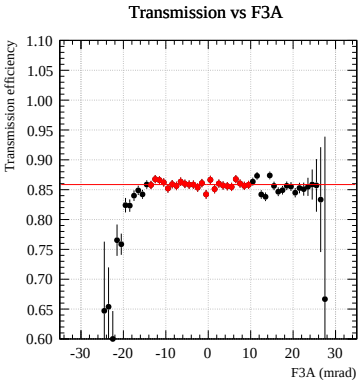

(c) F3A dependence.

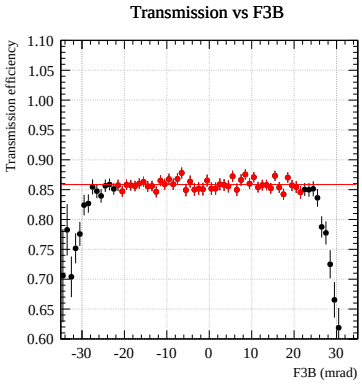

(d) F3B dependence.

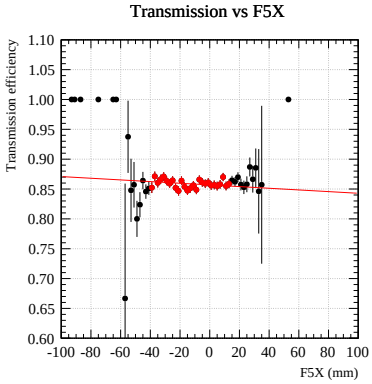

(e) F5X dependence.

Figure D.7: Transmission distributions of ^{43}K with the reaction target.

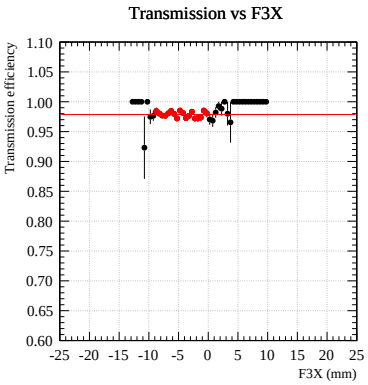

(a) F3X dependence.

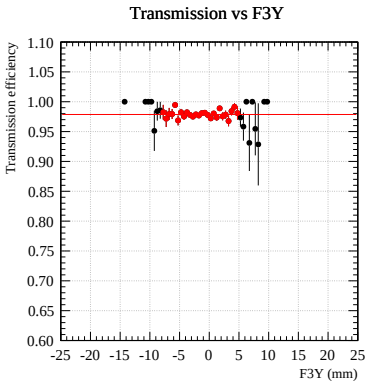

(b) F3Y dependence.

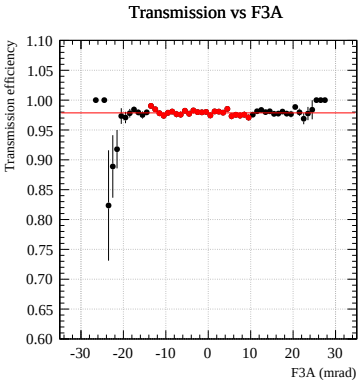

(c) F3A dependence.

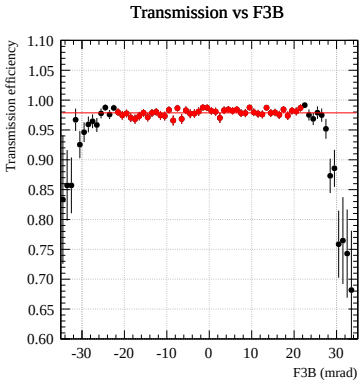

(d) F3B dependence.

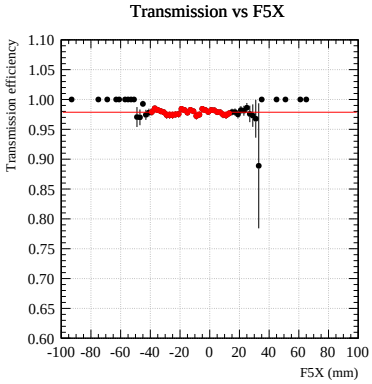

(e) F5X dependence.

Figure D.8: Transmission distributions of ^{43}K without the reaction target.

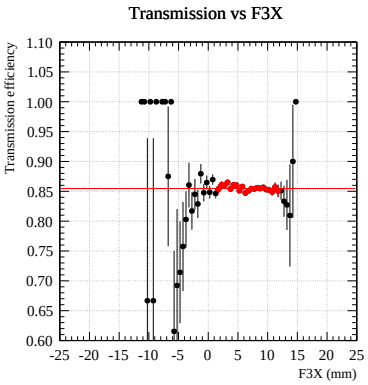

(a) F3X dependence.

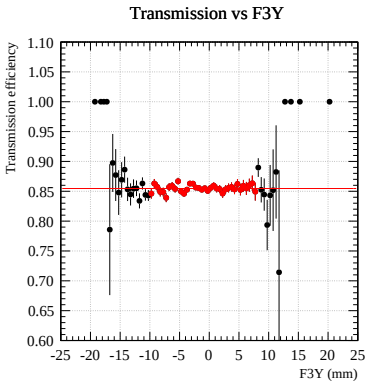

(b) F3Y dependence.

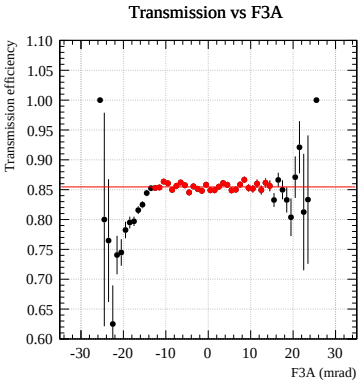

(c) F3A dependence.

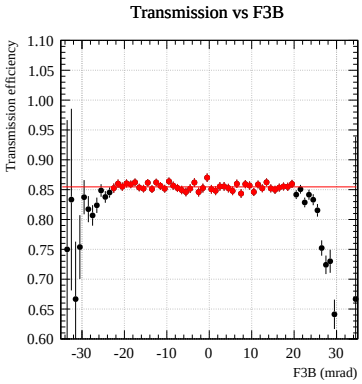

(d) F3B dependence.

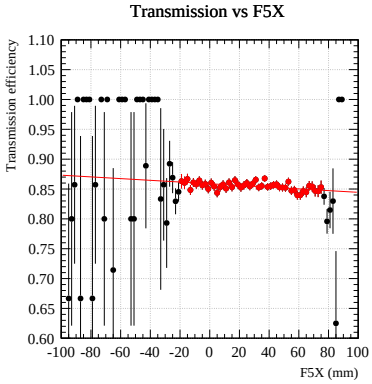

(e) F5X dependence.

Figure D.9: Transmission distributions of ^{44}K with the reaction target.

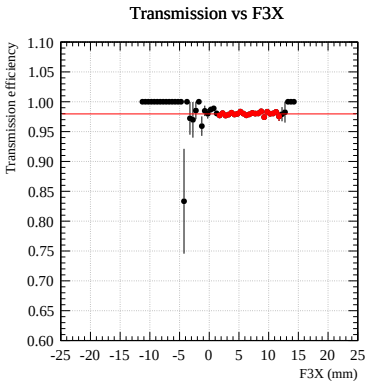

(a) F3X dependence.

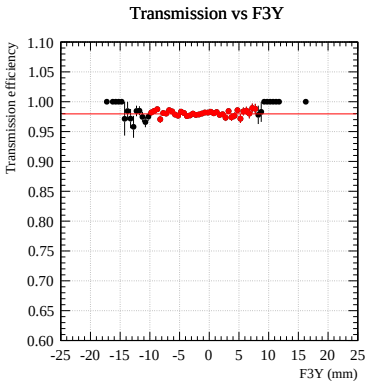

(b) F3Y dependence.

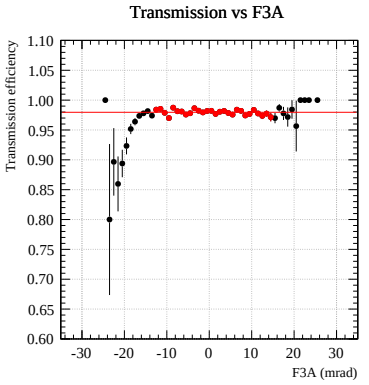

(c) F3A dependence.

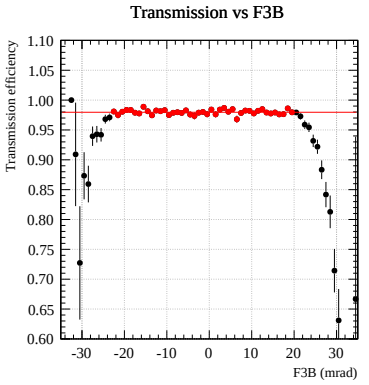

(d) F3B dependence.

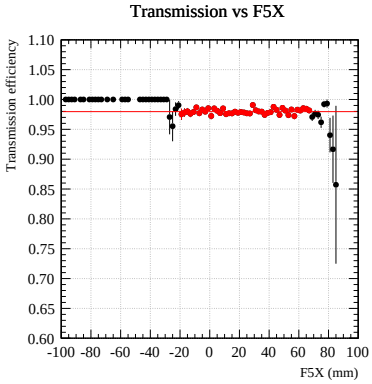

(e) F5X dependence.

Figure D.10: Transmission distributions of ^{44}K without the reaction target.

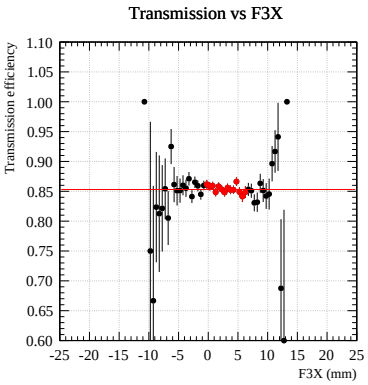

(a) F3X dependence.

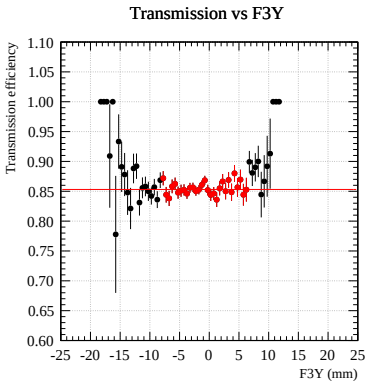

(b) F3Y dependence.

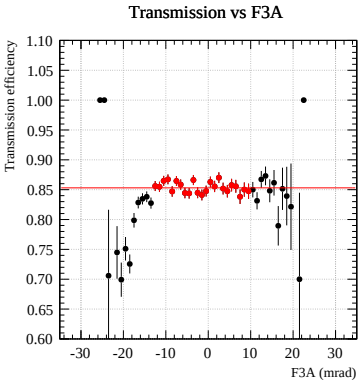

(c) F3A dependence.

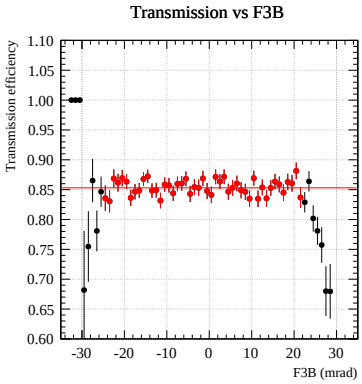

(d) F3B dependence.

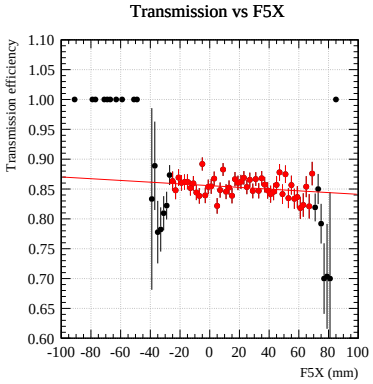

(e) F5X dependence.

Figure D.11: Transmission distributions of ^{45}K with the reaction target.

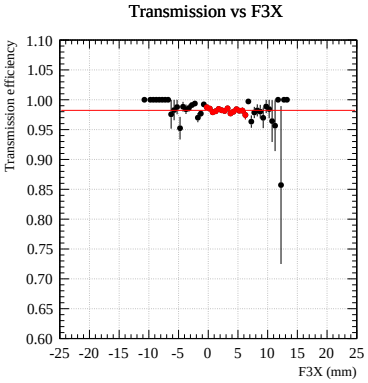

(a) F3X dependence.

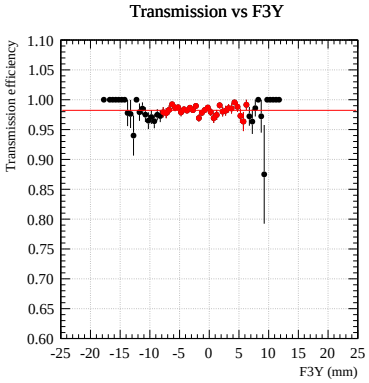

(b) F3Y dependence.

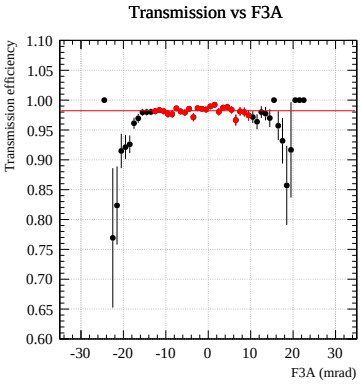

(c) F3A dependence.

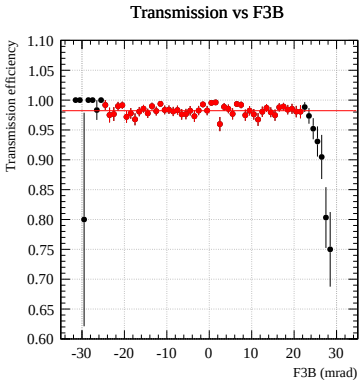

(d) F3B dependence.

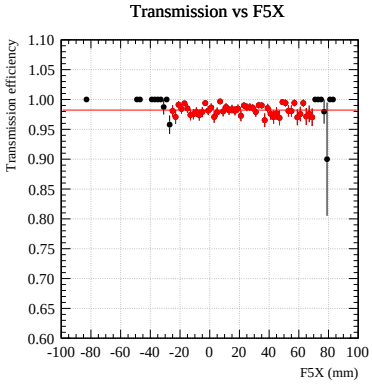

(e) F5X dependence.

Figure D.12: Transmission distributions of ^{45}K without the reaction target.

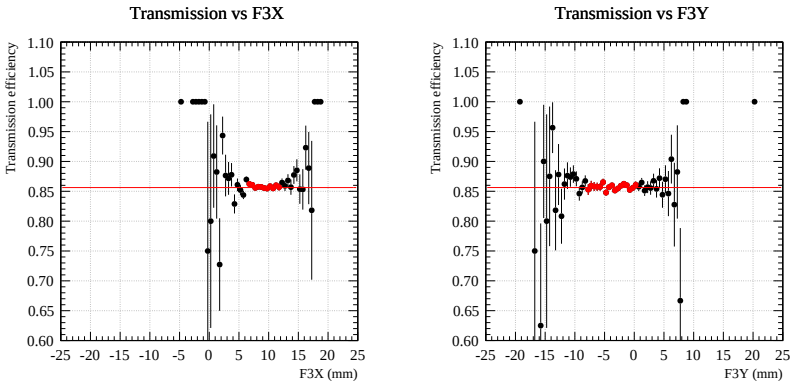

(a) F3X dependence.

(b) F3Y dependence.

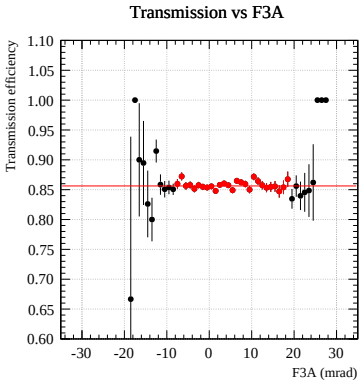

(c) F3A dependence.

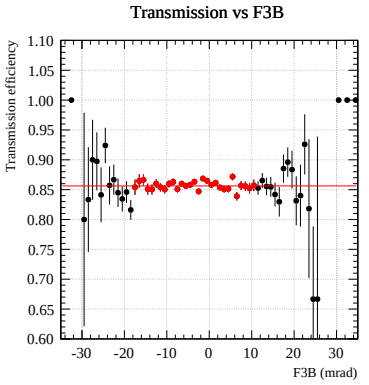

(d) F3B dependence.

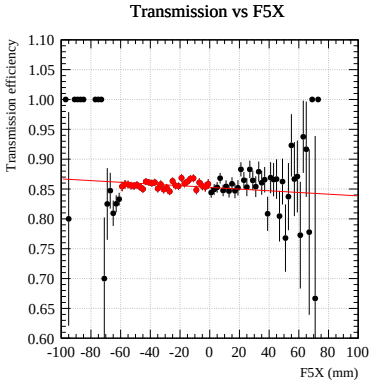

(e) F5X dependence.

Figure D.13: Transmission distributions of ^{46}K with the reaction target.

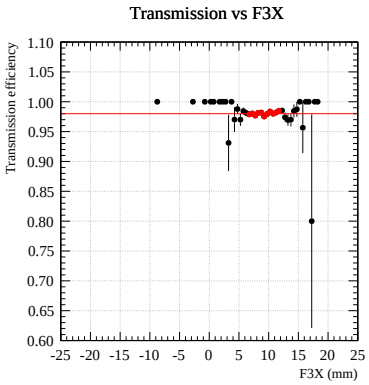

(a) F3X dependence.

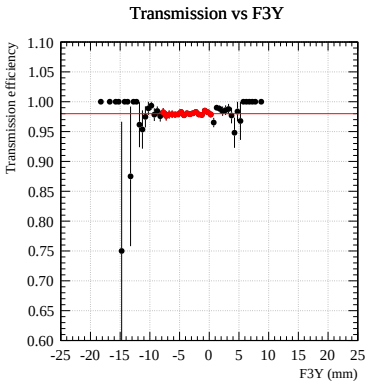

(b) F3Y dependence.

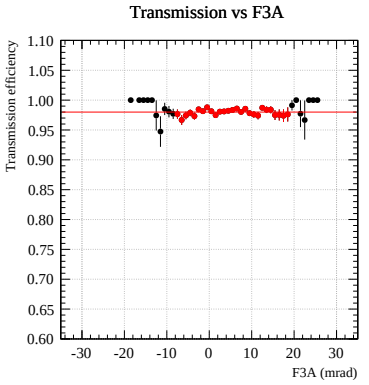

(c) F3A dependence.

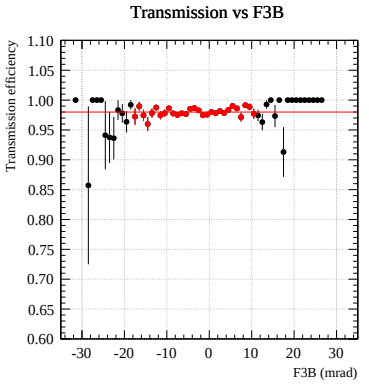

(d) F3B dependence.

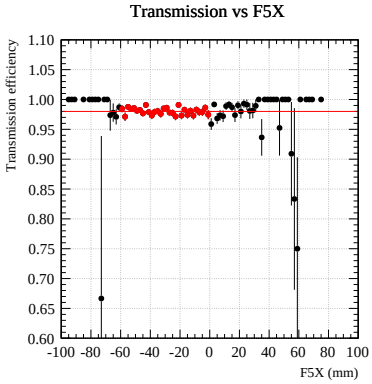

(e) F5X dependence.

Figure D.14: Transmission distributions of ^{46}K without the reaction target.

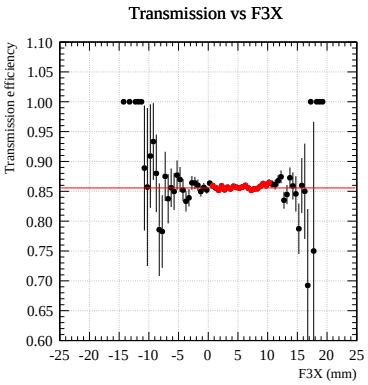

(a) F3X dependence.

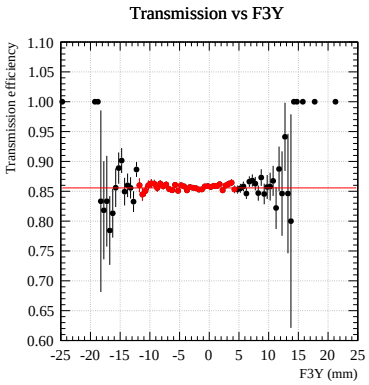

(b) F3Y dependence.

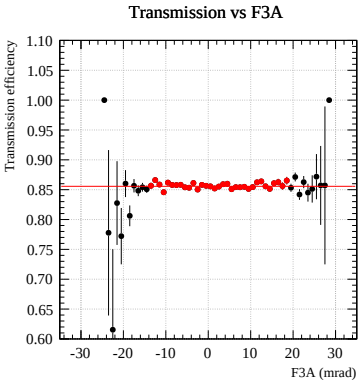

(c) F3A dependence.

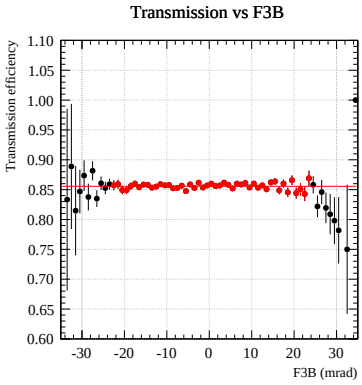

(d) F3B dependence.

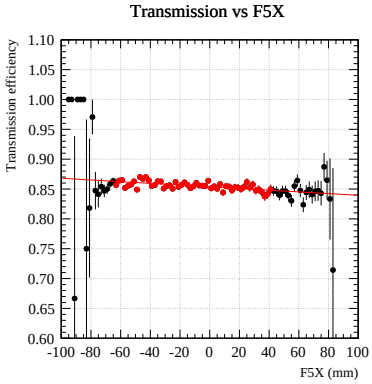

(e) F5X dependence.

Figure D.15: Transmission distributions of ^{47}K with the reaction target.

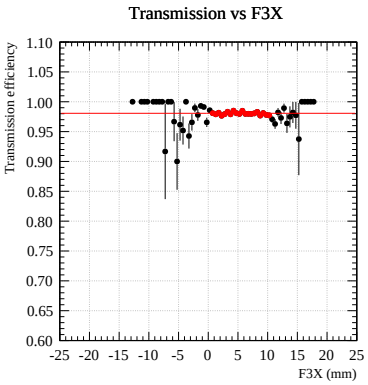

(a) F3X dependence.

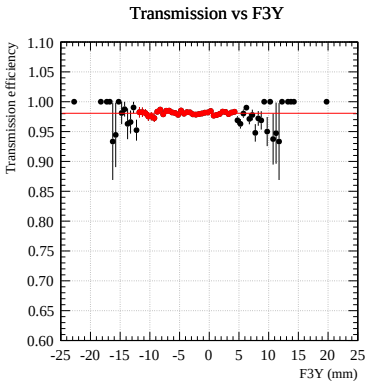

(b) F3Y dependence.

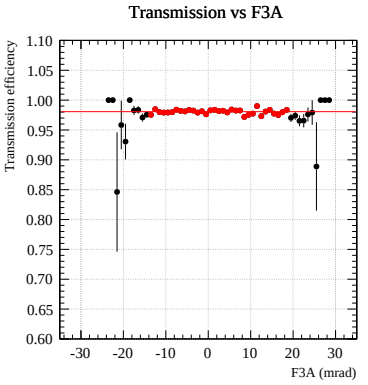

(c) F3A dependence.

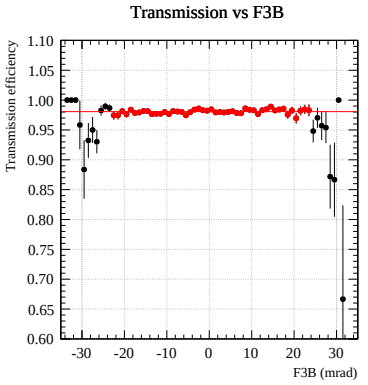

(d) F3B dependence.

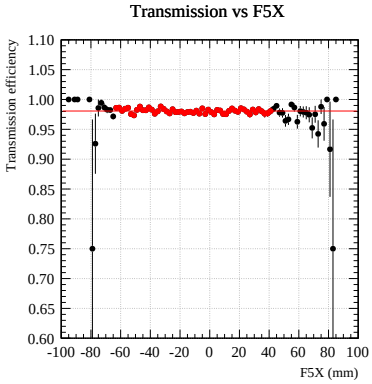

(e) F5X dependence.

Figure D.16: Transmission distributions of ^{47}K without the reaction target.

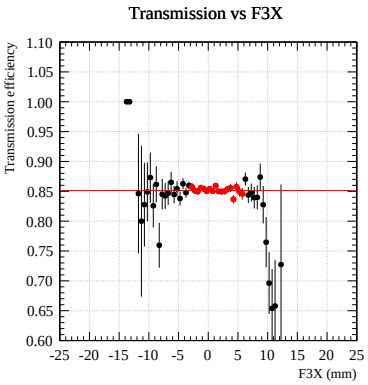

(a) F3X dependence.

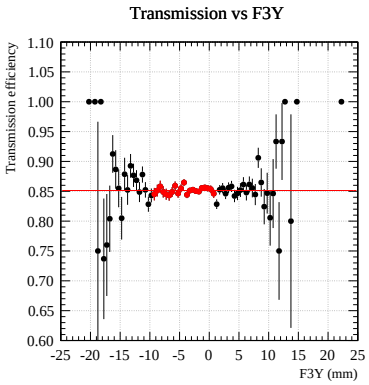

(b) F3Y dependence.

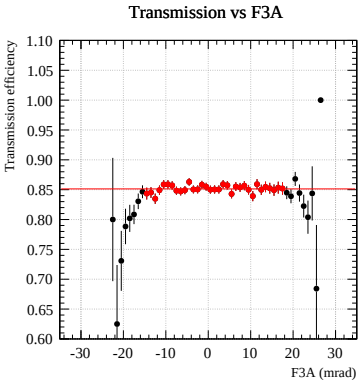

(c) F3A dependence.

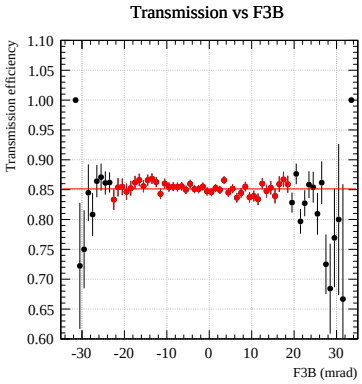

(d) F3B dependence.

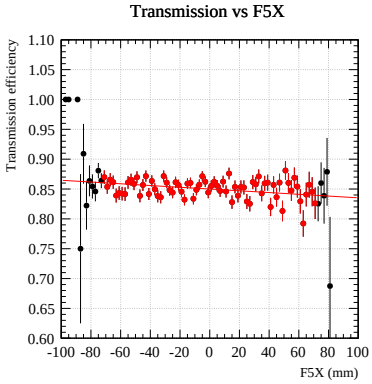

(e) F5X dependence.

Figure D.17: Transmission distributions of ^{48}K with the reaction target.

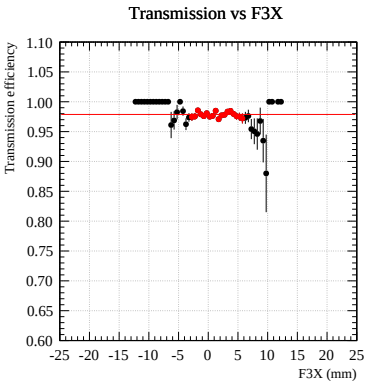

(a) F3X dependence.

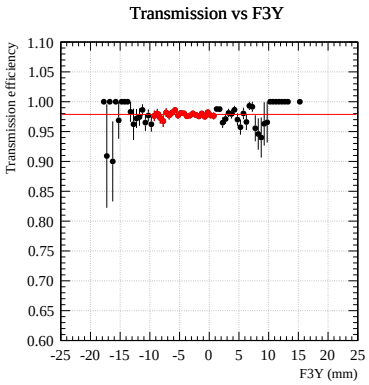

(b) F3Y dependence.

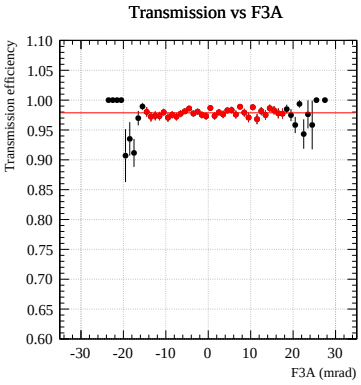

(c) F3A dependence.

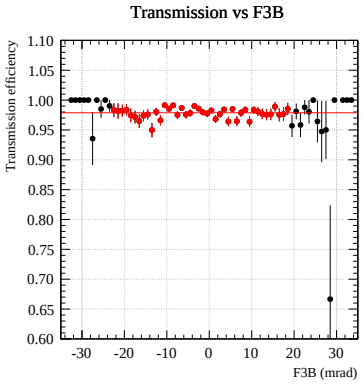

(d) F3B dependence.

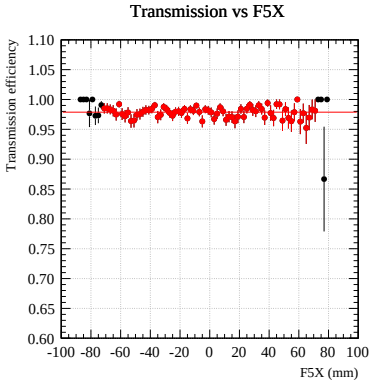

(e) F5X dependence.

Figure D.18: Transmission distributions of ^{48}K without the reaction target.

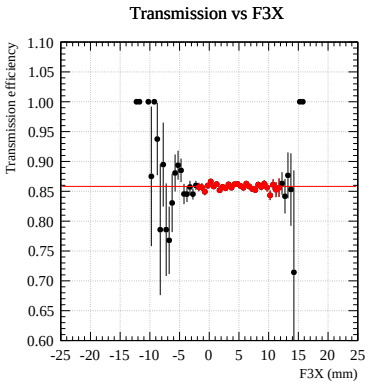

(a) F3X dependence.

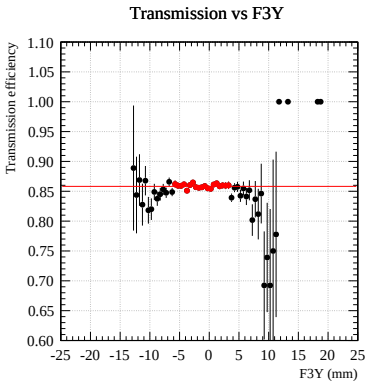

(b) F3Y dependence.

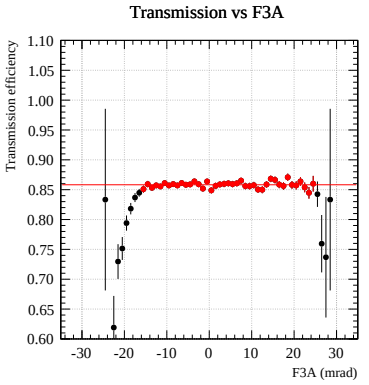

(c) F3A dependence.

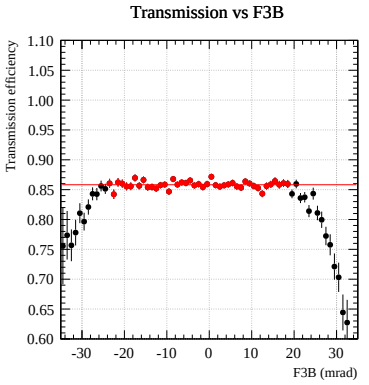

(d) F3B dependence.

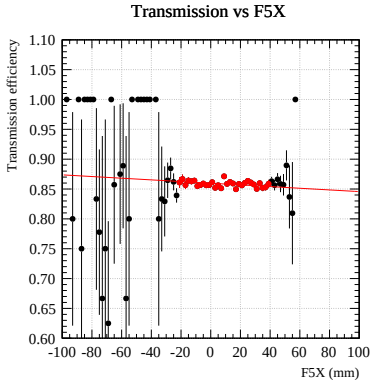

(e) F5X dependence.

Figure D.19: Transmission distributions of ^{42}Ca with the reaction target.

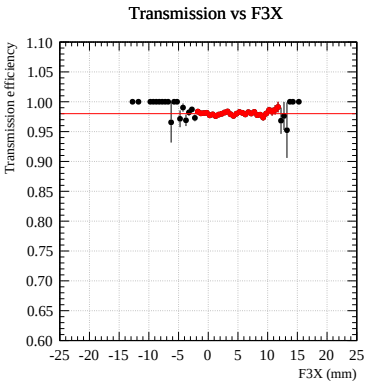

(a) F3X dependence.

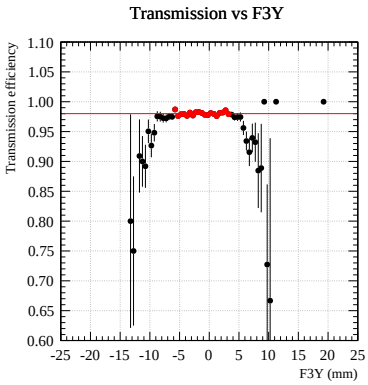

(b) F3Y dependence.

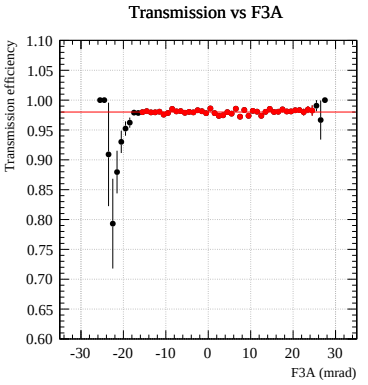

(c) F3A dependence.

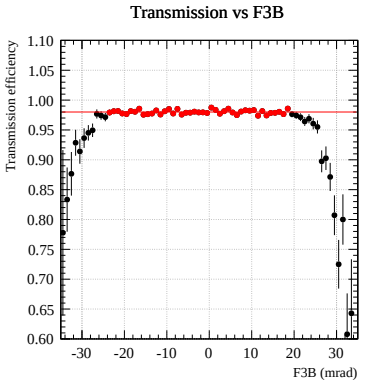

(d) F3B dependence.

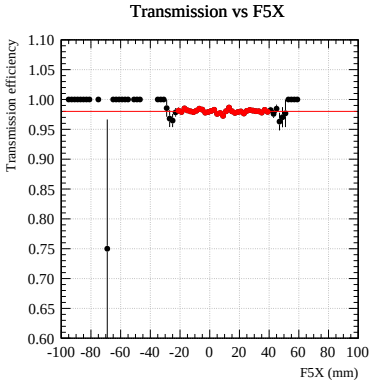

(e) F5X dependence.

Figure D.20: Transmission distributions of ^{42}Ca without the reaction target.

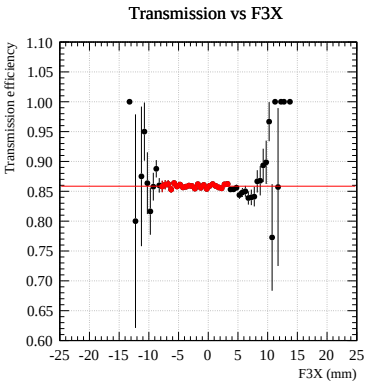

(a) F3X dependence.

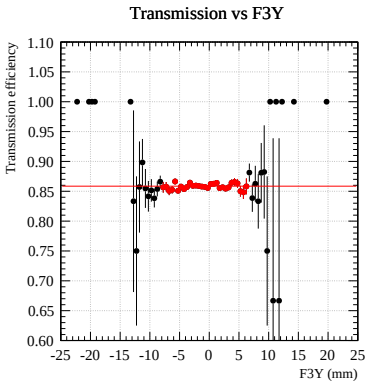

(b) F3Y dependence.

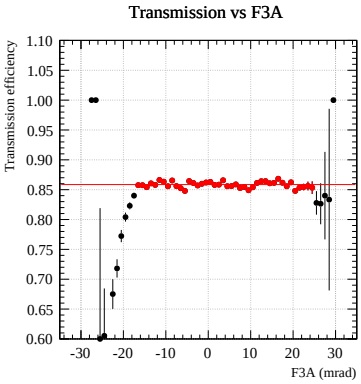

(c) F3A dependence.

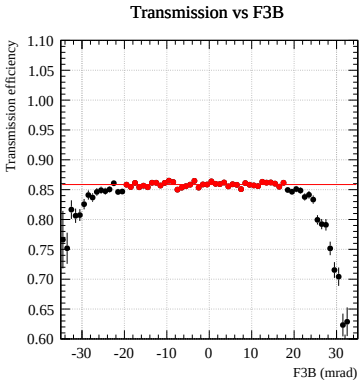

(d) F3B dependence.

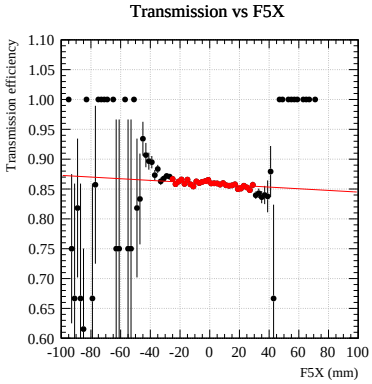

(e) F5X dependence.

Figure D.21: Transmission distributions of ^{43}Ca with the reaction target.

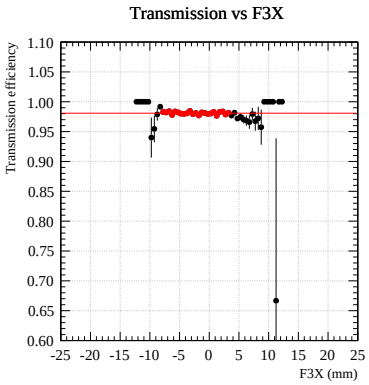

(a) F3X dependence.

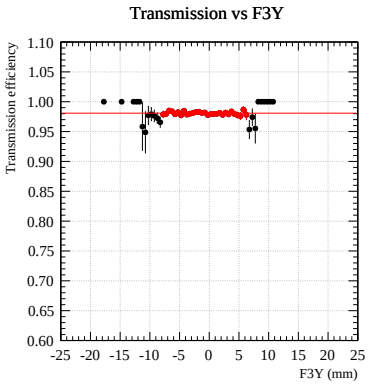

(b) F3Y dependence.

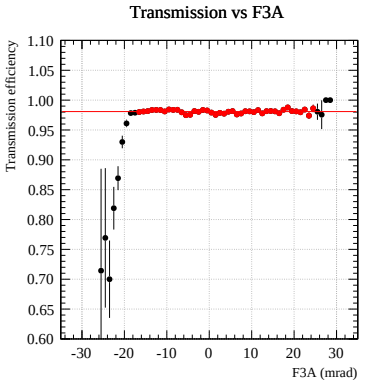

(c) F3A dependence.

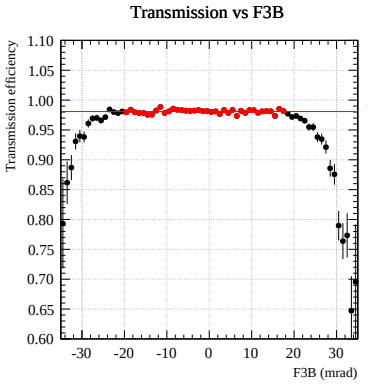

(d) F3B dependence.

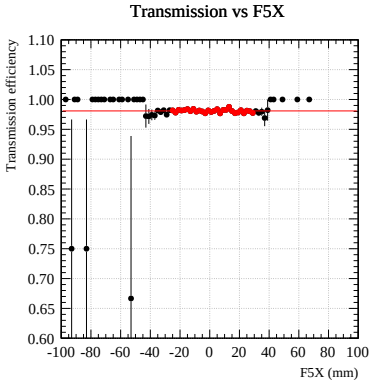

(e) F5X dependence.

Figure D.22: Transmission distributions of ^{43}Ca without the reaction target.

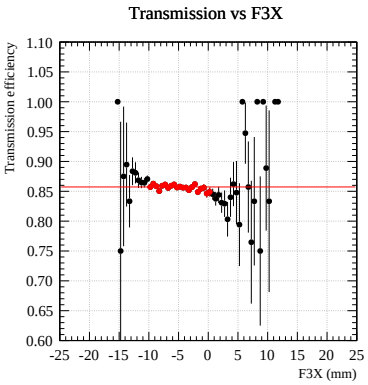

(a) F3X dependence.

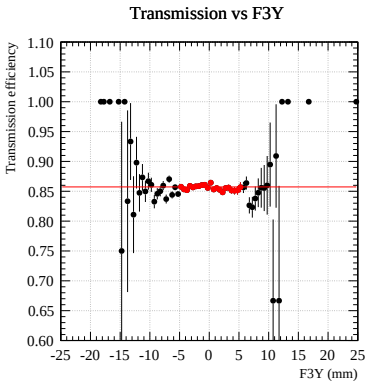

(b) F3Y dependence.

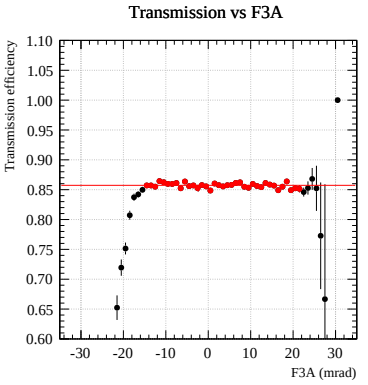

(c) F3A dependence.

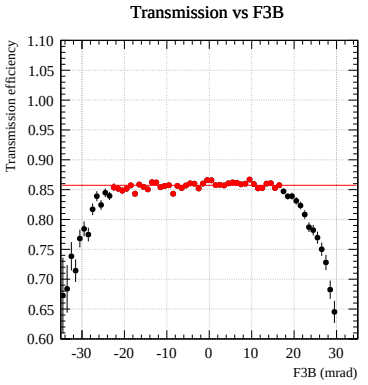

(d) F3B dependence.

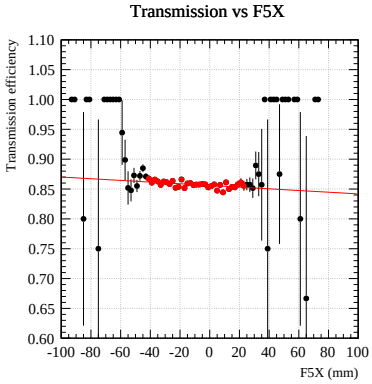

(e) F5X dependence.

Figure D.23: Transmission distributions of ^{44}Ca with the reaction target.

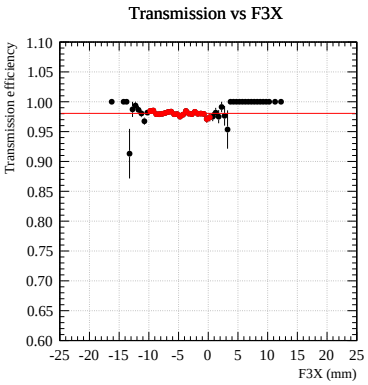

(a) F3X dependence.

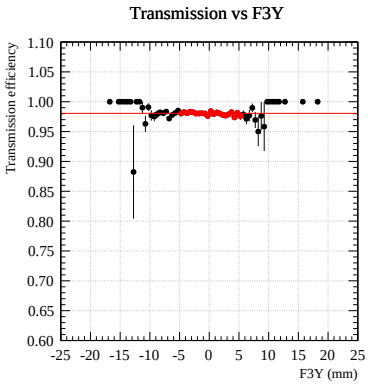

(b) F3Y dependence.

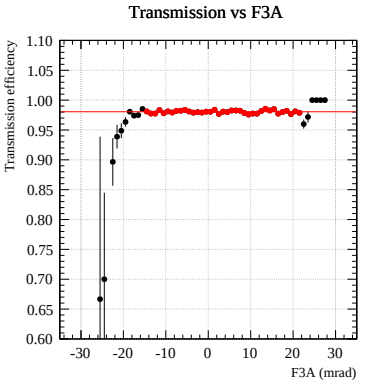

(c) F3A dependence.

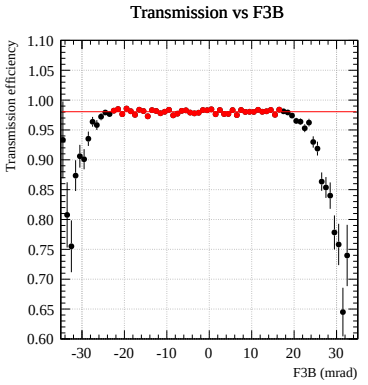

(d) F3B dependence.

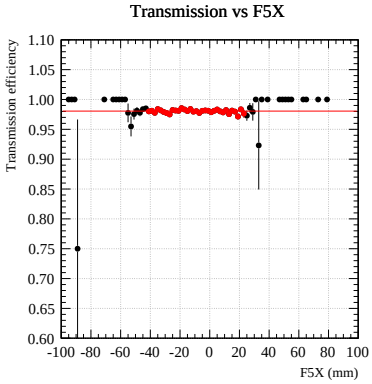

(e) F5X dependence.

Figure D.24: Transmission distributions of ^{44}Ca without the reaction target.

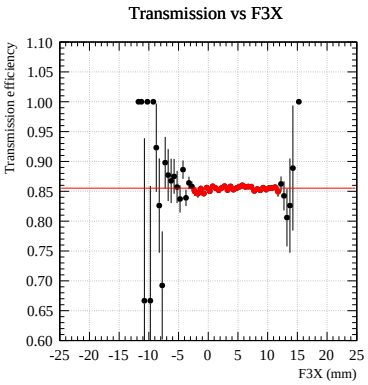

(a) F3X dependence.

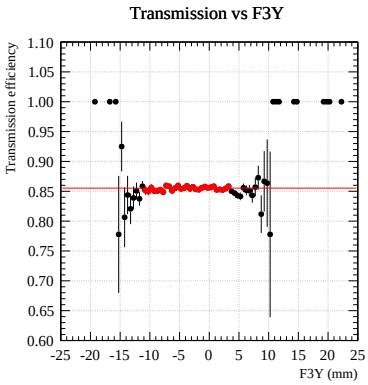

(b) F3Y dependence.

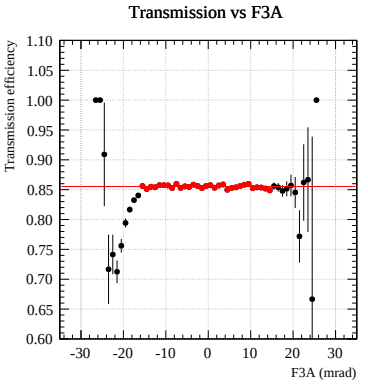

(c) F3A dependence.

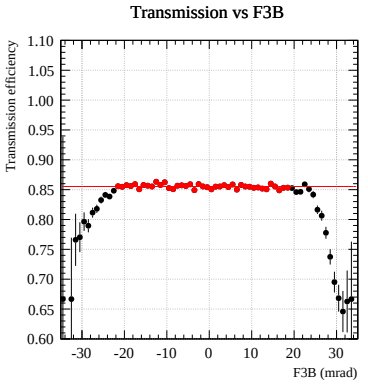

(d) F3B dependence.

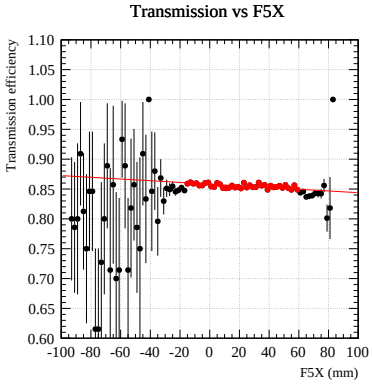

(e) F5X dependence.

Figure D.25: Transmission distributions of ^{45}Ca with the reaction target.

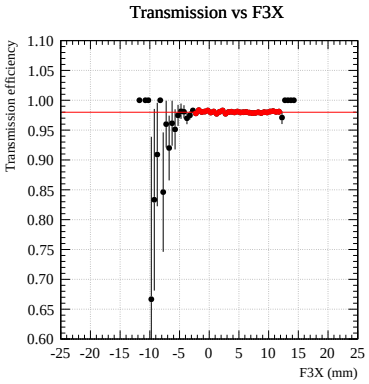

(a) F3X dependence.

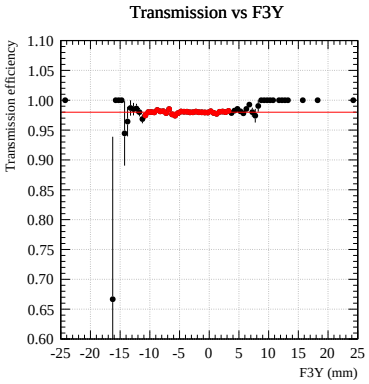

(b) F3Y dependence.

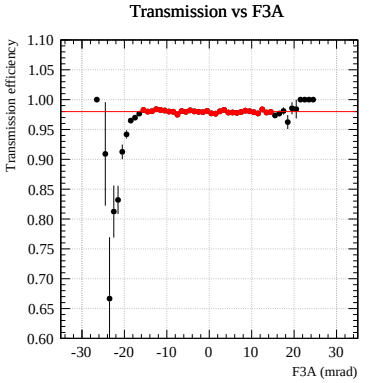

(c) F3A dependence.

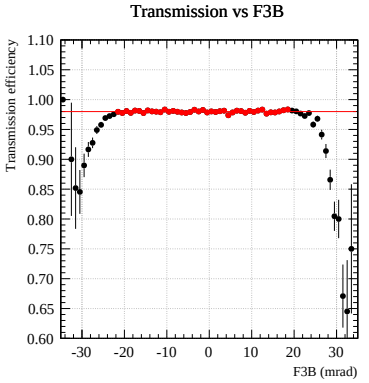

(d) F3B dependence.

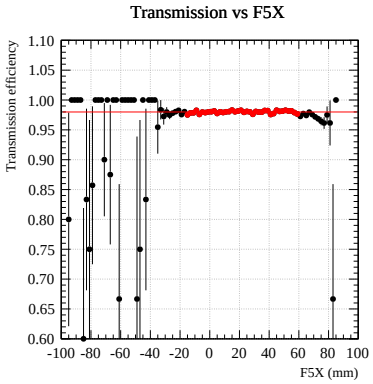

(e) F5X dependence.

Figure D.26: Transmission distributions of ^{45}Ca without the reaction target.

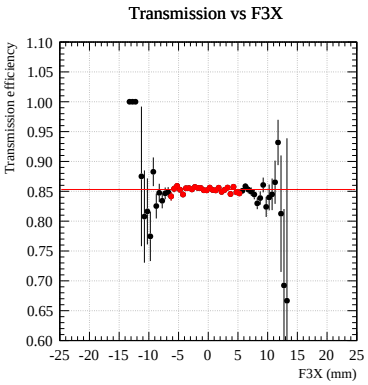

(a) F3X dependence.

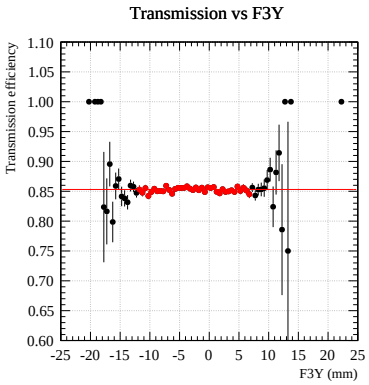

(b) F3Y dependence.

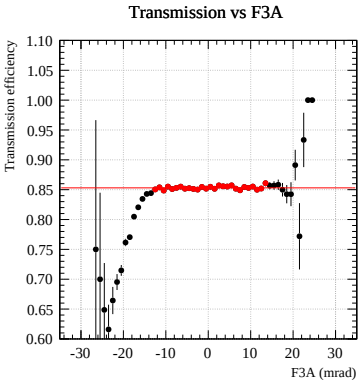

(c) F3A dependence.

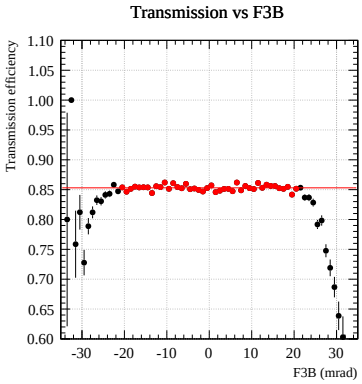

(d) F3B dependence.

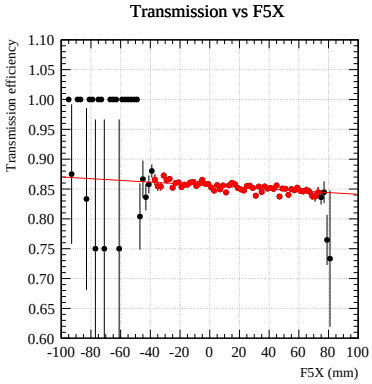

(e) F5X dependence.

Figure D.27: Transmission distributions of ^{46}Ca with the reaction target.

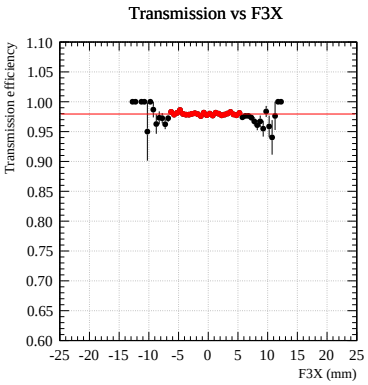

(a) F3X dependence.

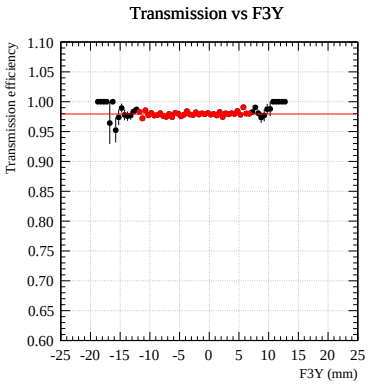

(b) F3Y dependence.

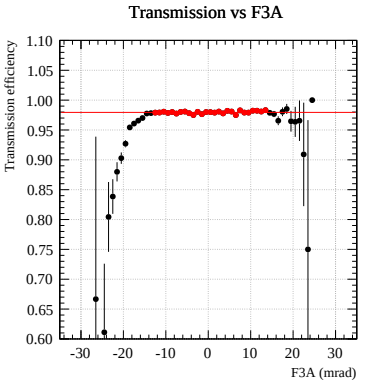

(c) F3A dependence.

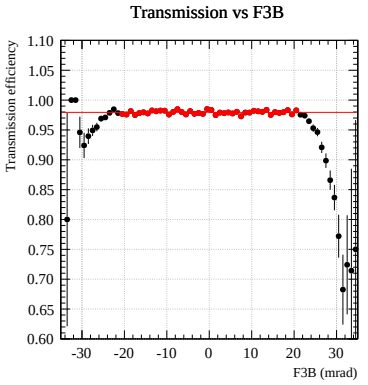

(d) F3B dependence.

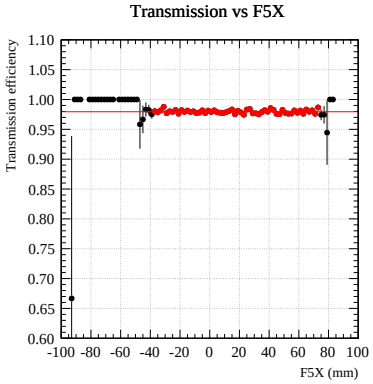

(e) F5X dependence.

Figure D.28: Transmission distributions of ^{46}Ca without the reaction target.

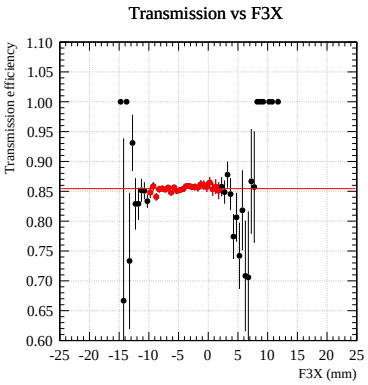

(a) F3X dependence.

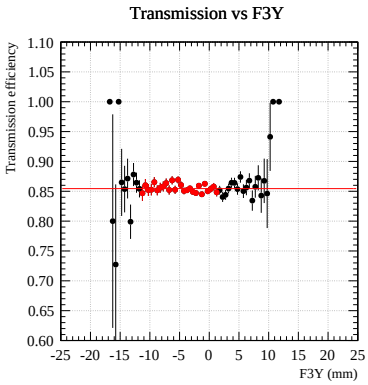

(b) F3Y dependence.

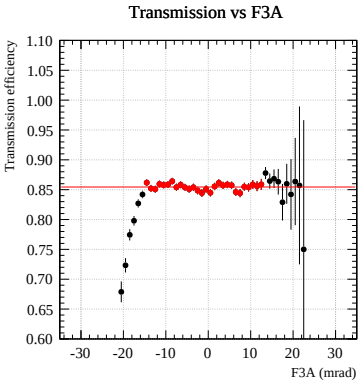

(c) F3A dependence.

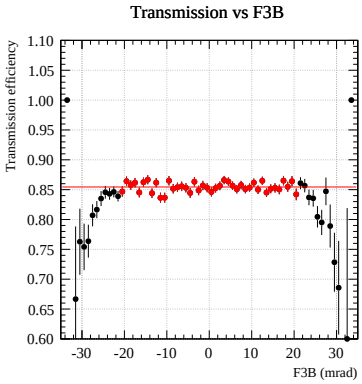

(d) F3B dependence.

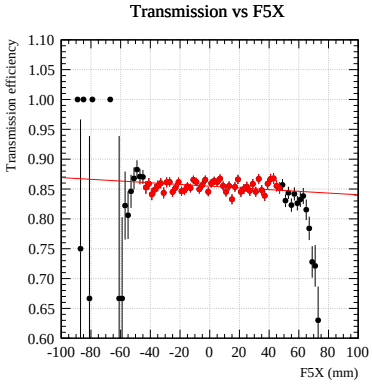

(e) F5X dependence.

Figure D.29: Transmission distributions of ^{47}Ca with the reaction target.

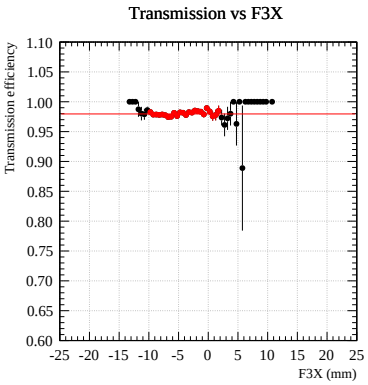

(a) F3X dependence.

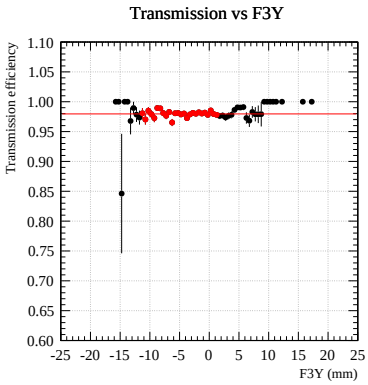

(b) F3Y dependence.

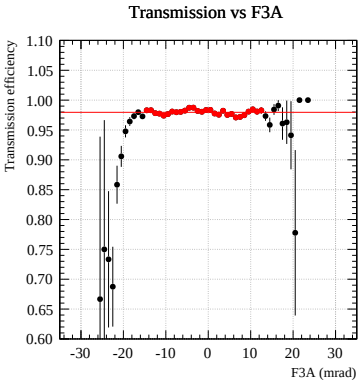

(c) F3A dependence.

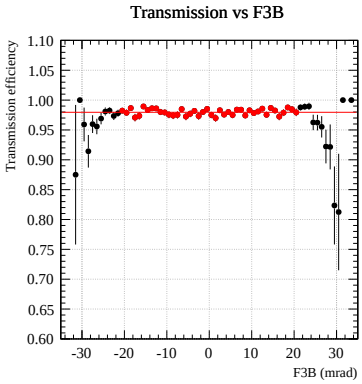

(d) F3B dependence.

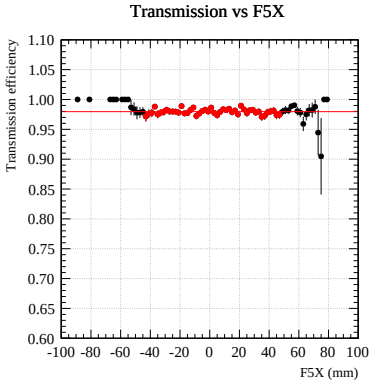

(e) F5X dependence.

Figure D.30: Transmission distributions of ^{47}Ca without the reaction target.

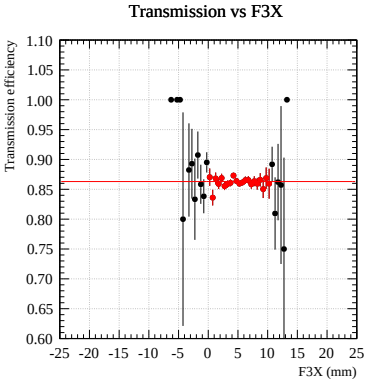

(a) F3X dependence.

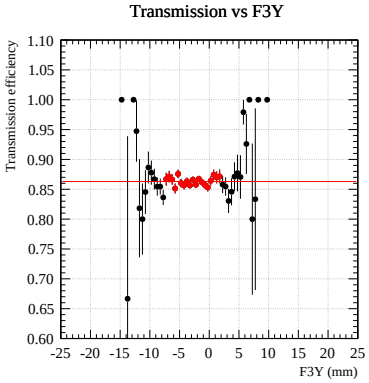

(b) F3Y dependence.

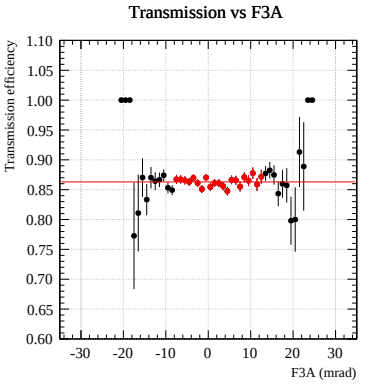

(c) F3A dependence.

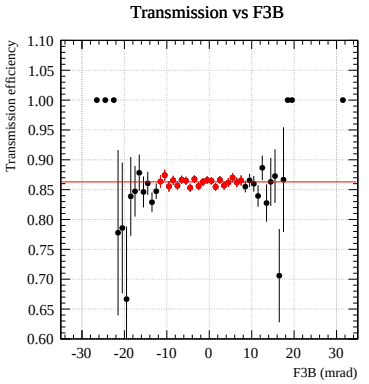

(d) F3B dependence.

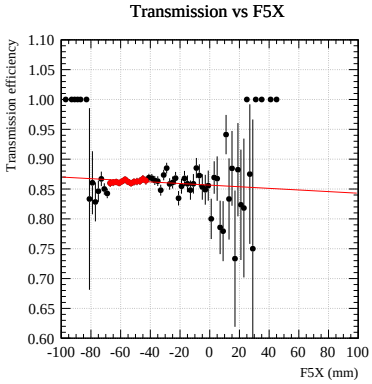

(e) F5X dependence.

Figure D.31: Transmission distributions of ^{48}Ca with the reaction target.

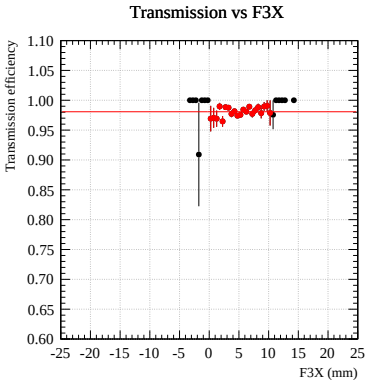

(a) F3X dependence.

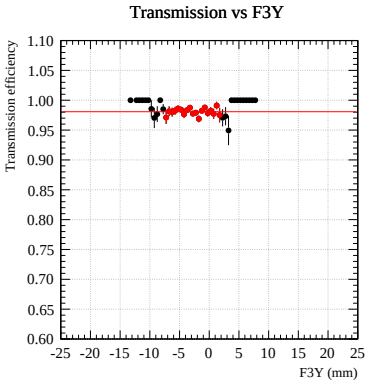

(b) F3Y dependence.

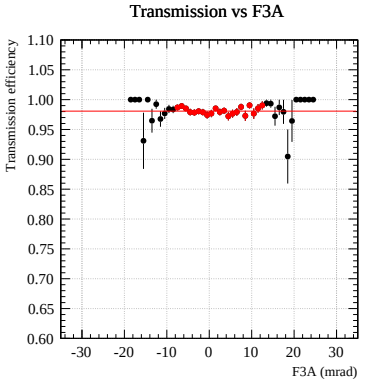

(c) F3A dependence.

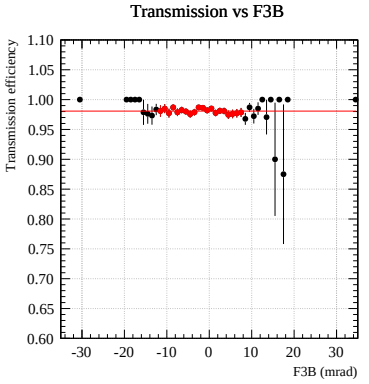

(d) F3B dependence.

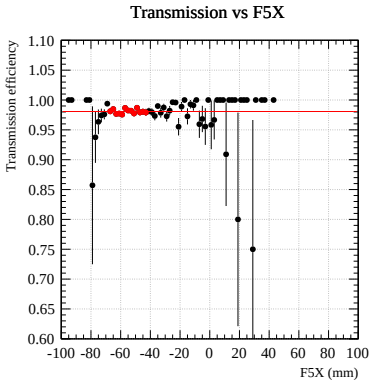

(e) F5X dependence.

Figure D.32: Transmission distributions of ^{48}Ca without the reaction target.

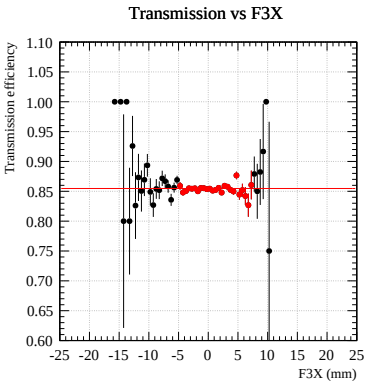

(a) F3X dependence.

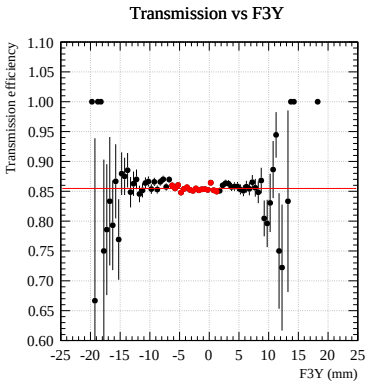

(b) F3Y dependence.

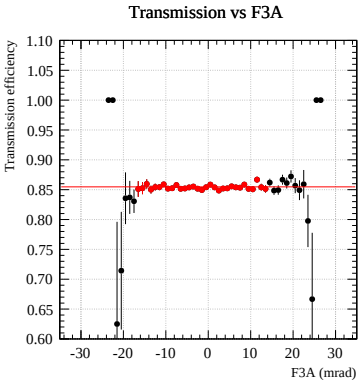

(c) F3A dependence.

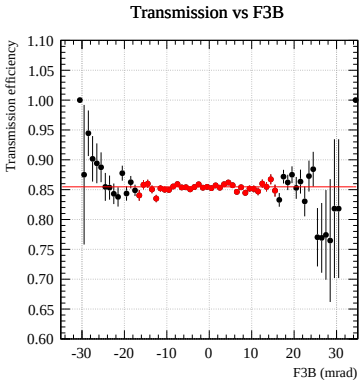

(d) F3B dependence.

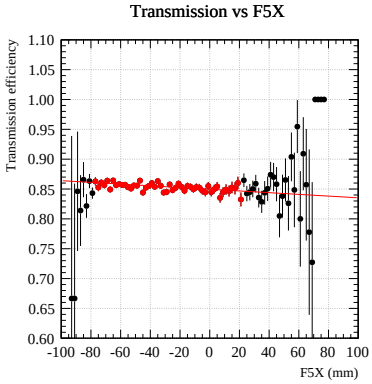

(e) F5X dependence.

Figure D.33: Transmission distributions of ^{49}Ca with the reaction target.

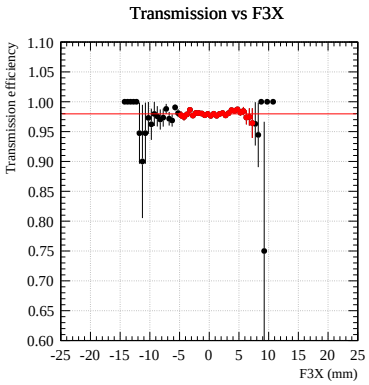

(a) F3X dependence.

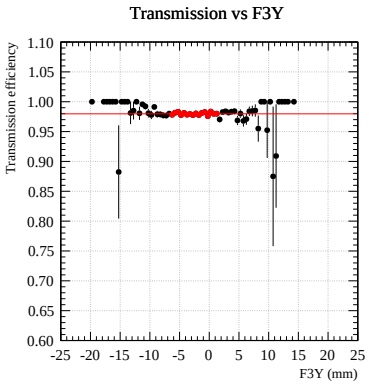

(b) F3Y dependence.

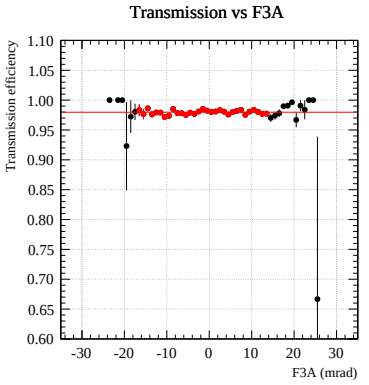

(c) F3A dependence.

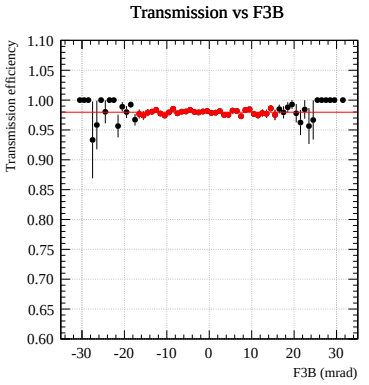

(d) F3B dependence.

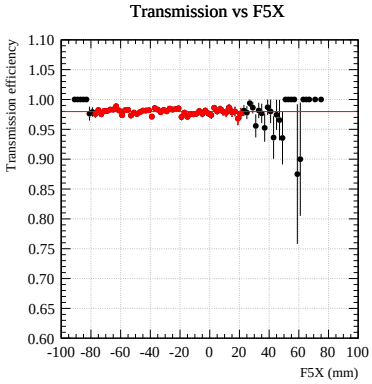

(e) F5X dependence.

Figure D.34: Transmission distributions of ^{49}Ca without the reaction target.

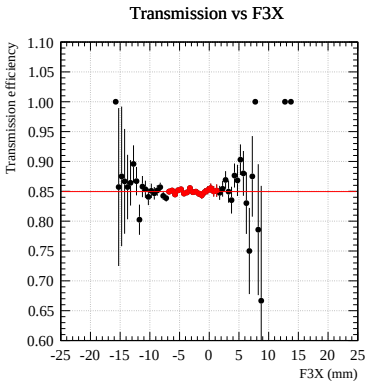

(a) F3X dependence.

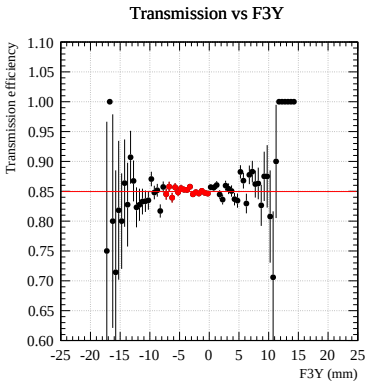

(b) F3Y dependence.

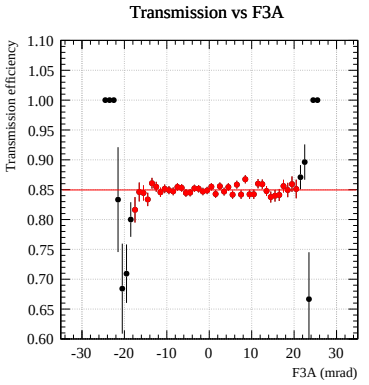

(c) F3A dependence.

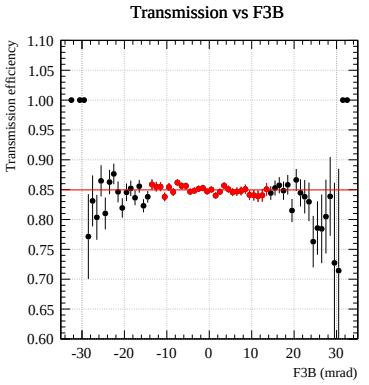

(d) F3B dependence.

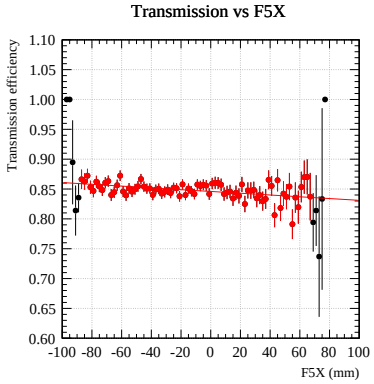

(e) F5X dependence.

Figure D.35: Transmission distributions of ^{50}Ca with the reaction target.

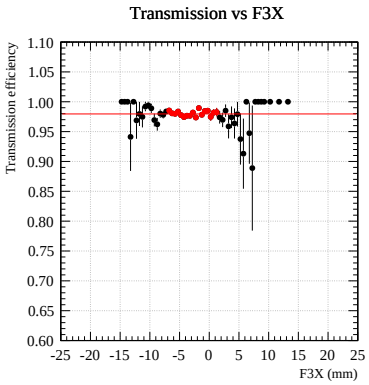

(a) F3X dependence.

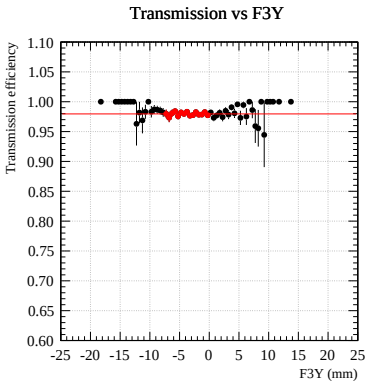

(b) F3Y dependence.

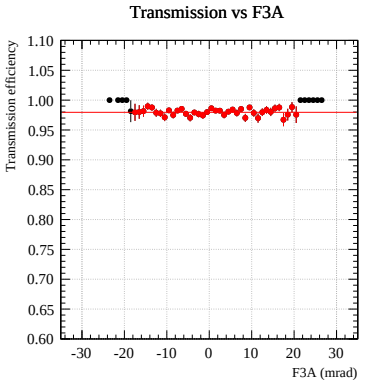

(c) F3A dependence.

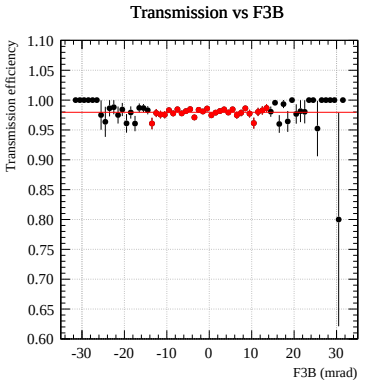

(d) F3B dependence.

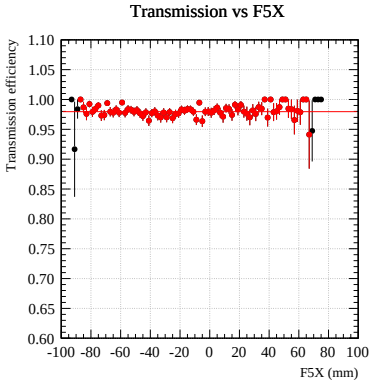

(e) F5X dependence.

Figure D.36: Transmission distributions of ^{50}Ca without the reaction target.

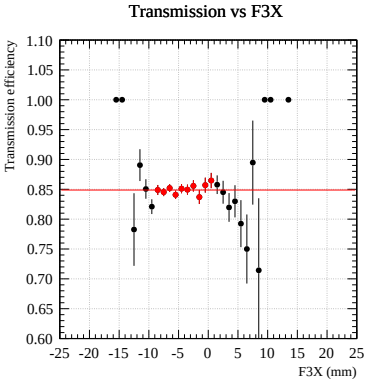

(a) F3X dependence.

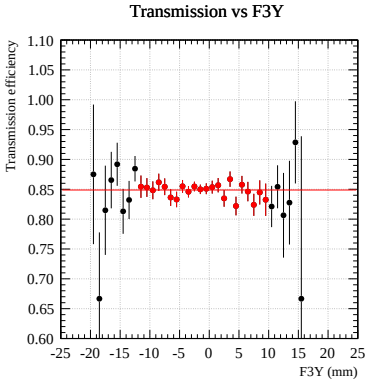

(b) F3Y dependence.

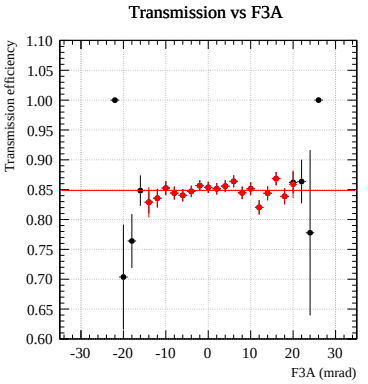

(c) F3A dependence.

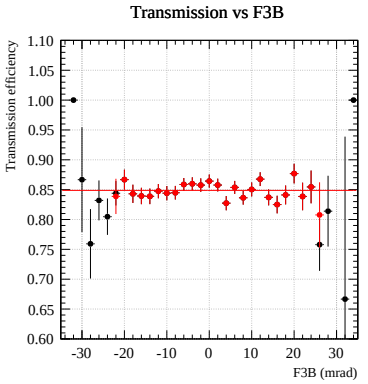

(d) F3B dependence.

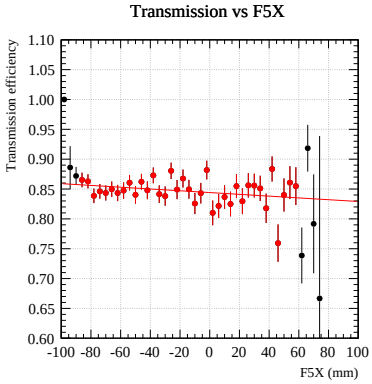

(e) F5X dependence.

Figure D.37: Transmission distributions of ^{51}Ca with the reaction target.

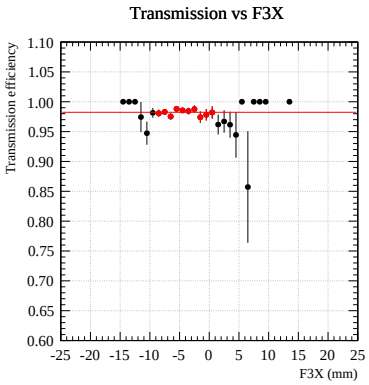

(a) F3X dependence.

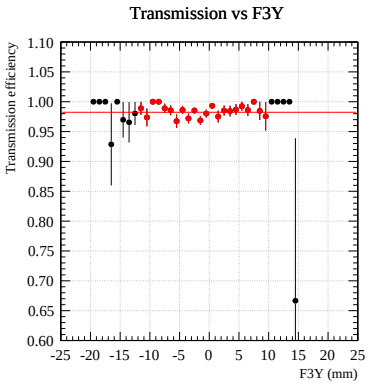

(b) F3Y dependence.

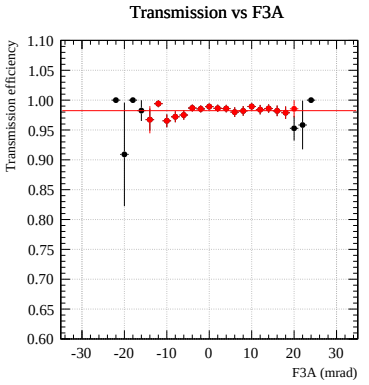

(c) F3A dependence.

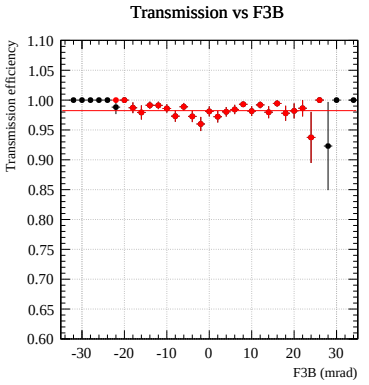

(d) F3B dependence.

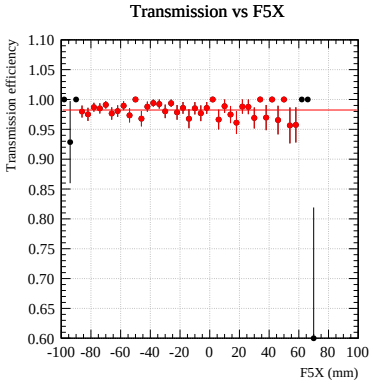

(e) F5X dependence.

Figure D.38: Transmission distributions of ^{51}Ca without the reaction target.

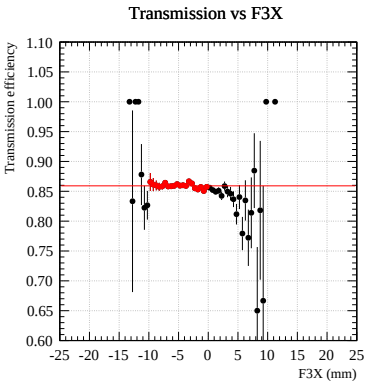

(a) F3X dependence.

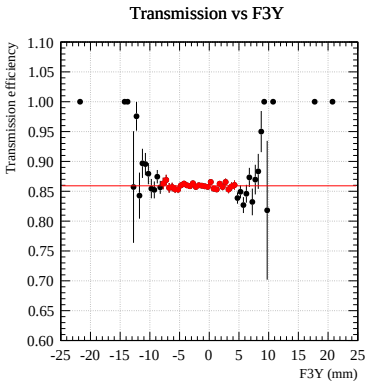

(b) F3Y dependence.

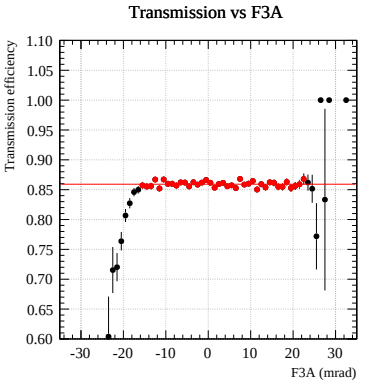

(c) F3A dependence.

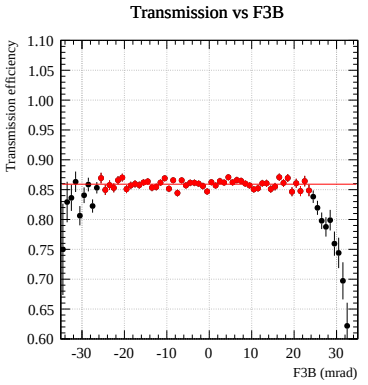

(d) F3B dependence.

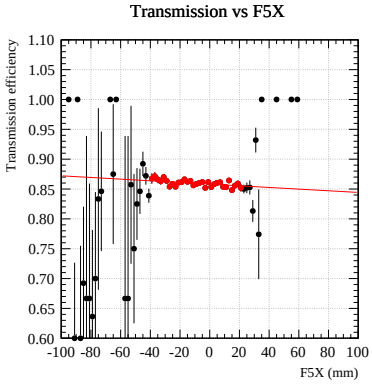

(e) F5X dependence.

Figure D.39: Transmission distributions of ^{44}Sc with the reaction target.

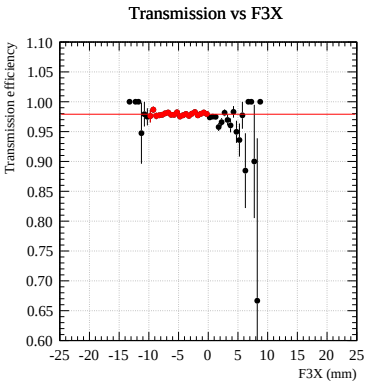

(a) F3X dependence.

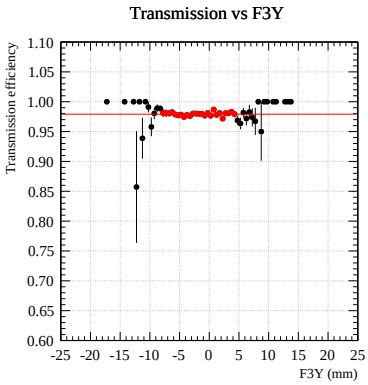

(b) F3Y dependence.

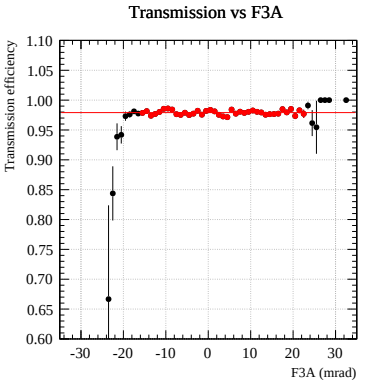

(c) F3A dependence.

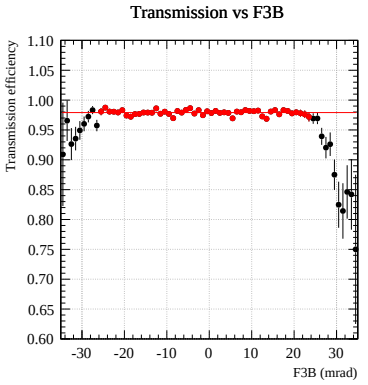

(d) F3B dependence.

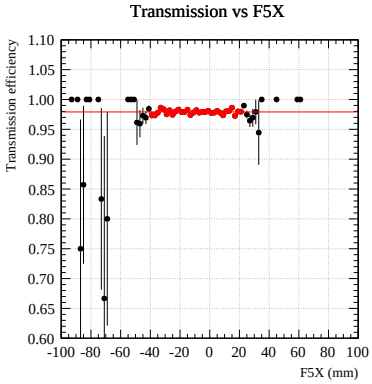

(e) F5X dependence.

Figure D.40: Transmission distributions of ^{44}Sc without the reaction target.

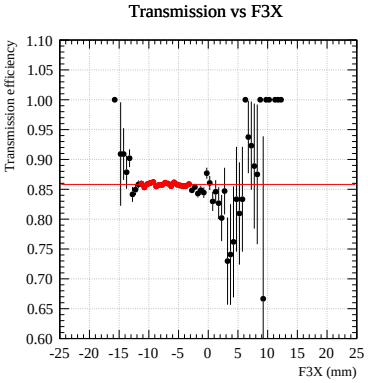

(a) F3X dependence.

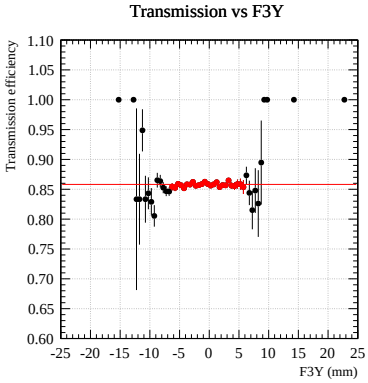

(b) F3Y dependence.

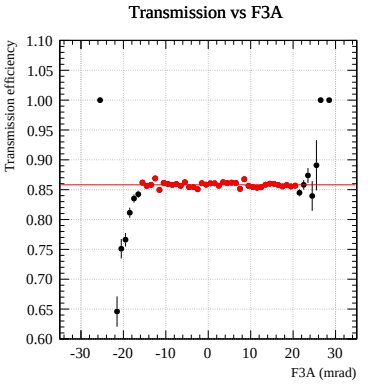

(c) F3A dependence.

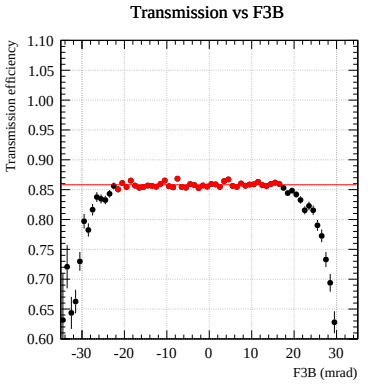

(d) F3B dependence.

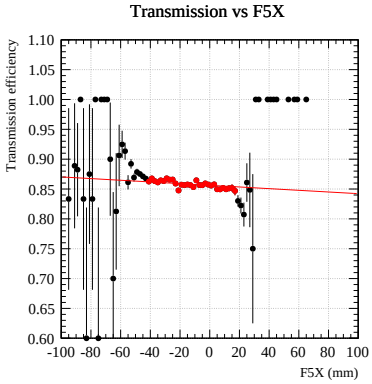

(e) F5X dependence.

Figure D.41: Transmission distributions of ^{45}Sc with the reaction target.

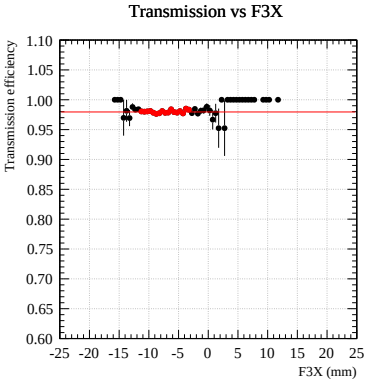

(a) F3X dependence.

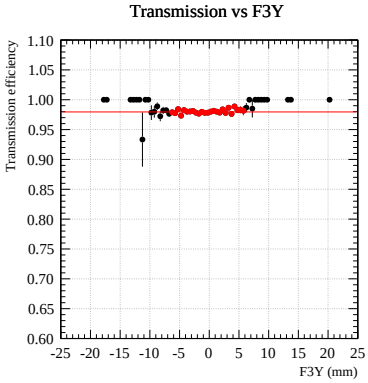

(b) F3Y dependence.

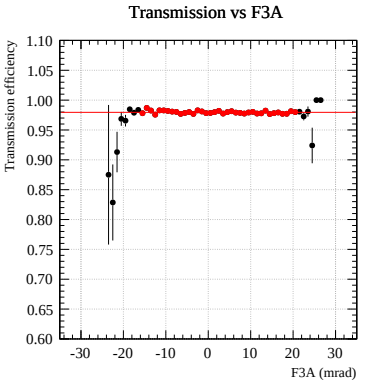

(c) F3A dependence.

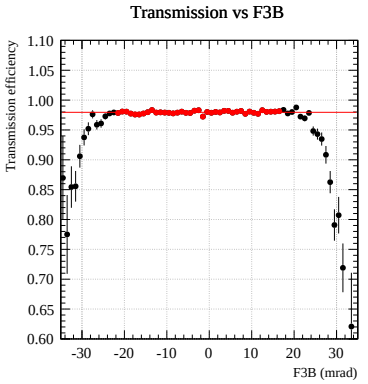

(d) F3B dependence.

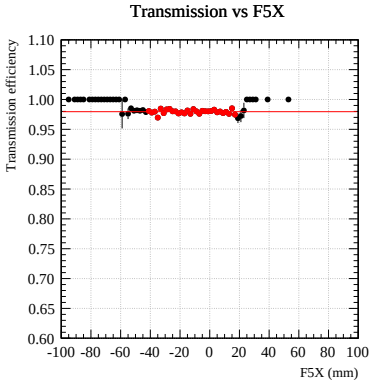

(e) F5X dependence.

Figure D.42: Transmission distributions of ^{45}Sc without the reaction target.

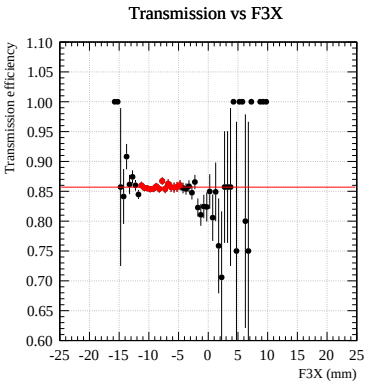

(a) F3X dependence.

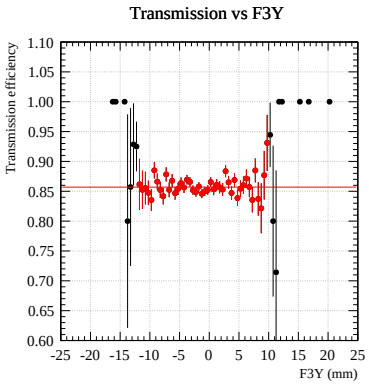

(b) F3Y dependence.

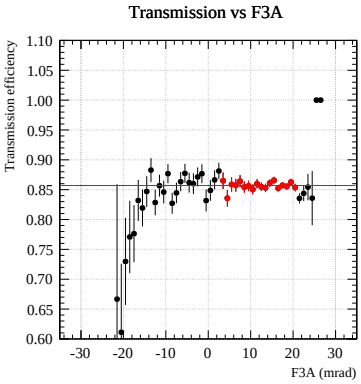

(c) F3A dependence.

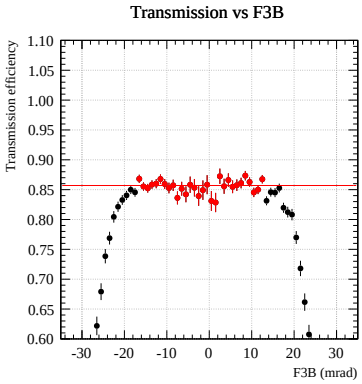

(d) F3B dependence.

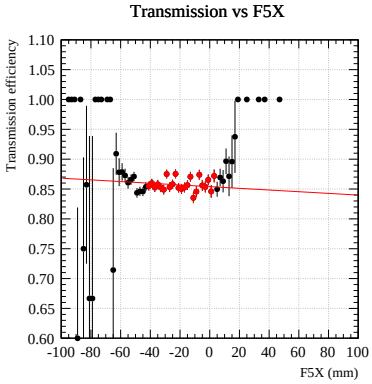

(e) F5X dependence.

Figure D.43: Transmission distributions of ^{46}Sc with the reaction target.

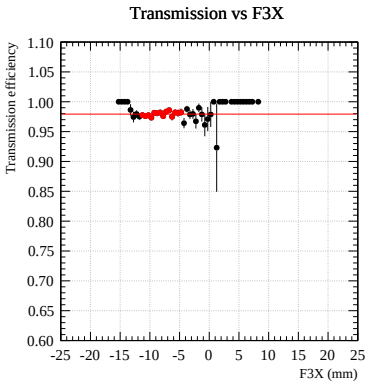

(a) F3X dependence.

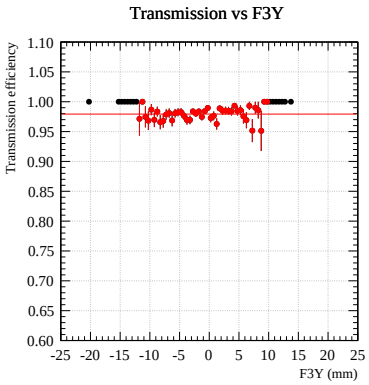

(b) F3Y dependence.

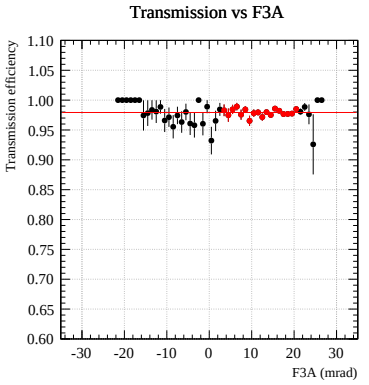

(c) F3A dependence.

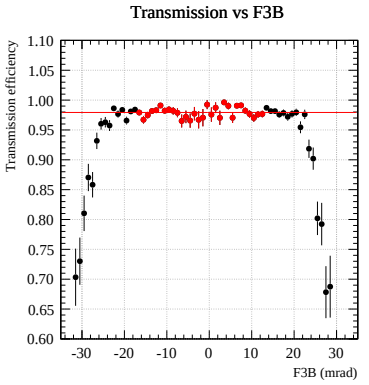

(d) F3B dependence.

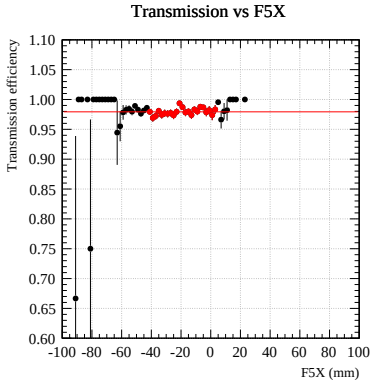

(e) F5X dependence.

Figure D.44: Transmission distributions of ^{46}Sc without the reaction target.